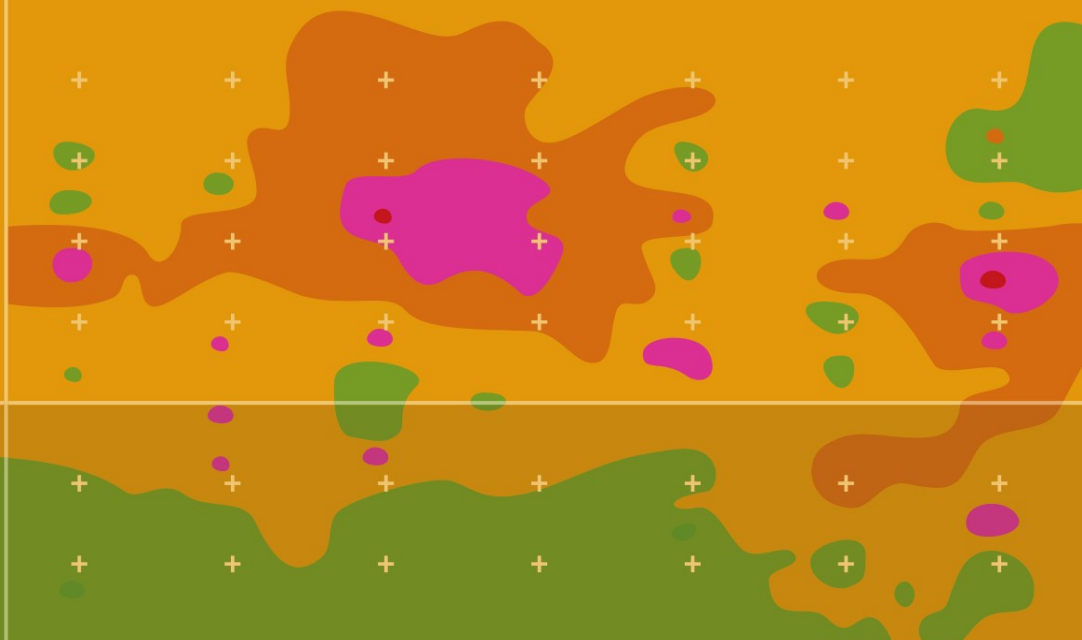# F. Jerry Lucia

Carbonate Reservoir Characterization

An Integrated Approach

2nd Edition

Springer

F. Jerry Lucia

Carbonate Reservoir Characterization

F. Jerry Lucia

Carbonate Reservoir Characterization

An Integrated Approach

Second Edition

With 233 Figures

Springer

F. Jerry Lucia
Bureau of Economic Geology
University Station Box X
Austin, Texas 78713
USA

E-Mail:
jerry.lucia@beg.utexas.edu

Preface

This book is intended for the use of geologist, geophysists, petrophysists, and engineers interested in building geologic models that can be converted into realistic reservoir flow models of carbonate reservoirs. The first edition of this book was focused on methods and approaches for constructing improved carbonate reservoir models. In this second edition these methods are enlarged based on research results since the first edition was published. Each chapter contains new information, particularly in the area of wireline logs and geostatistics. Importantly, several new field studies are included that illustrate the application of these methods in building reservoir models.

As in the first edition, the integration of geological and engineering data is at the center of the approach described in this edition. The fundamental link between geologic models and engineering fluid-flow models is the relationship between petrophysical properties and rock fabrics. Pore geometries control the flow properties and geologic history, as observed in rock fabrics, controls the pore geometries. Therefore, it is the study of rock fabrics that integrates geological and engineering data.

Not surprisingly, the approach is referred to as the "rock-fabric method." This method is an outgrowth of the published works of G.E. Archie (Gus), and the reader is encouraged to read the few reference to his work presented at the end of this Preface. The author is well acquainted with his work because Gus hired the author into Shell Oil in 1954 and work for him at Shell Development's research laboratory in Houston for a number of years. Gus pioneered the idea of relating petrophysical properties to rock fabrics, an idea that was further developed by Ray Murray and myself in carbonates, and Robert Sneider in clastics.

In this book I present a current picture of how this method can be applied in limestone, dolostone, and touching-vug reservoirs. The chapters have been reorganized to accommodate the research advances in the past nine years. Reservoir characterization is first and foremost concerned with developing 3D images of petrophysical properties suitable for input into fluid-flow computer simulators. Therefore, as in the first edition, the first chapter is a review of petrophysical data and how the data are obtained. The second chapter discusses relationships between rock fabric, porosity,

permeability, and saturation, and is the soul of the rock fabric method for reservoir characterization. Chapter 3 discusses methods for calculating interparticle porosity, permeability, and initial water saturation using the rock-fabric approach, permeability transforms, and capillary pressure models. New in this chapter is a thorough discussion of using wireline logs to identify geologic and rock-fabric facies. Chapter 4 discusses using sequence stratigraphy and depositional models to distribute rock fabrics in 3D space. Diagenesis, as well as deposition, is a major contributor to pore-size distribution and an overview of limestone diagenesis, dolomitization, and meteoric diagenesis is included in Chapters 6, 7, and 8. Chapter 5 is a new chapter that focuses on distributing petrophysical properties in 3D space using geostatistical methods constrained by rock fabric flow layers and sequence stratigraphy. Examples of how this approach is used to describe limestone reservoirs are presented in Chapter 6, to describe dolostone reservoirs in Chapter 7, and to describe touching-vug reservoirs in Chapter 8.

This book would never have been published without the able assistance of my editor, Amanda Masterson. If there are errors in this book it is because I failed to make the corrections she highlighted.

Austin, Texas   F. Jerry Lucia
May, 2007

References

Archie GE. 1952 Classification of carbonate reservoir rocks and petrophysical considerations. AAPG Bull 36, 2:278-298

Archie GE 1942 The electrical resistivity log as an aid in determining some reservoir characteristics. Trans AIME, 146:54-62

Archie GE 1950 Introduction to petrophysics of reservoir rocks. AAPG Bull 34, 5:943-961

Contents

Chapter 3 Wireline Logs

Chapter 4 Depositional Textures & Petrophysics

Chapter 5 Reservoir Models for Input into Flow Simulators

Chapter 8 Touching-Vug Reservoirs

Chapter 1 Petrophysical Rock Properties

1.1 Introduction

The principal goal of reservoir characterization is to construct three-dimensional images of petrophysical properties. The purpose of this chapter is to review basic definitions and laboratory measurements of the petrophysical properties porosity, permeability, relative permeability, capillarity, and saturation. Pore-size distribution is presented as the common link between these properties.

1.2 Porosity

Porosity is an important rock property because it is a measure of the potential storage volume for hydrocarbons. Porosity in carbonate reservoirs ranges from 1 to 35% and, in the United States, averages 10% in dolomite reservoirs and 12% in limestone reservoirs (Schmoker et al. 1985).
   Porosity is defined as pore volume divided by bulk volume.

$$Porosity = \frac{\text{Pore volume}}{\text{Bulk volume}} = \frac{\text{Bulk volume - Mineral volume}}{\text{Bulk volume}} \qquad (1)$$

   Fractional porosity is used in engineering calculations. Geologists, however, most commonly refer to porosity as a percentage (porosity x 100). The term "effective porosity" or "connected" pore space is commonly used to denote porosity that is most available for fluid flow. However, at some scale all pore space is connected. The basic question is how the pore space is connected, which will be the principal focus of this book.

Porosity is a scalar quantity because it is a function of the bulk volume used to define the sample size. Therefore, whereas the porosity of Carlsbad Caverns is 100% if the caverns are taken as the bulk volume, the porosity of the formation including Carlsbad Caverns is much less and depends upon how much of the surrounding formation is included as bulk volume. Calculating the porosity of caves using a "boundary volume" for bulk volume results in porosity values for the caves in the 0.5% range (Sasowsky, personal communication). Thus, porosity is always a number, and the value is a function of the bulk volume chosen. The term "porosity" is often misused in place of "pore space," which is the proper term for describing voids in a rock. Porosity is a measurement and cannot be seen, whereas what is observed is pore space, or pores. The misuse of these terms often leads to confusion, especially when discussing the "origin of porosity," which is the origin of the pore space or the history of changes in porosity.

Porosity is determined by visual methods and laboratory measurements. Visual methods of measuring total porosity are estimates at best because the amount of porosity visible depends on the method of observation: the higher the magnification, the more pore space is visible. Porosity is commonly estimated by visual inspection of core slabs using a low-power microscope. The Archie classification (Archie 1952) provides a method of combining textural criteria and visible porosity to determine total porosity. Visible porosity in thin section can be measured by point counting the visible pores or by using image analysis software to calculate pore space. The thin section is taken as the bulk volume. Visual estimates can be very inaccurate unless calibrated against point-counted values. Commonly, visual estimates of porosity are twice as high as point-counted values. Laboratory porosity values are normally higher than visual estimates because very small pore space cannot be seen with visual observational techniques. When all the pore space is large, such as in grainstones, however, point-counted values are comparable with measured values.

Measurement of porosity of rock samples in the laboratory requires knowing the bulk volume of the rock and either its pore volume or the volume of the matrix material (mineral volume). Bulk volume is usually measured by volumetric displacement of a strongly nonwetting fluid, such as mercury, or by direct measurement of a regularly shaped sample. Pore volume can be obtained in a number of ways. If the mineralogy is known, mineral volume can be calculated from grain density and the sample weight; pore volume is bulk volume minus mineral volume. The most accurate method of measuring porosity is the helium expansion method. A dried sample is placed in a chamber of known volume and the pressure is measured with and without the sample, keeping the volume of gas constant. The

difference in pressure indicates the pore volume. A grain density is reported for each sample, and the accuracy of the porosity value can be judged by how close the density is to a known mineral density. If the density values reported are less than 2.8 for dolostone samples, for example, the porosity values are probably too low. The injection of mercury under very high pressure (the porosimeter) is also used to measure porosity. However, this is a destructive method and is normally used only under special circumstances. Summations-of-fluids is an old technique that attempts to use the fluids removed from the core to measure pore volume. It is very inaccurate and no longer in use. However, old porosity measurements may have been made using this inaccurate technique.

The complete removal of all fluids is critical for accurate measurements of porosity. Any fluid that is not removed will be included as part of the mineral volume, resulting in porosity values being too low. An example of incomplete removal of all fluids is taken from the Seminole San Andres field (Lucia et al. 1995). The whole-core analysis porosity values were suspected of being too low, and 11 whole-core samples were reanalyzed by drilling three 1-in plugs from each sample and cleaning the plugs in an industry laboratory in which special care was taken to remove all water and oil. The average porosity of all but one of the samples was higher than the whole-core porosity by an average of 2 porosity units (Fig. 1).
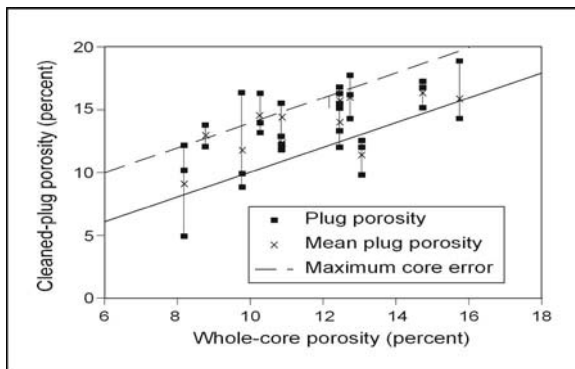
Fig. 1.1. Plot of whole-core porosity values versus porosity values of plug samples taken from the whole-core samples and recleaned. Whole-core porosity is too small by 0 – 4 porosity percent

Subjecting samples that contain gypsum to high temperatures in laboratory procedures results in dehydrating gypsum to the hemihydrate form Bassanite (see Eq. 2) and creating pore space and free water, both of which produce large errors in the porosity measurements (Table 1). Pore space is created because Bassanite (density 2.70) has a smaller molar volume than

does gypsum (density 2.35) (Bebout et al. 1987). It is important to keep temperatures below 70°C during core analysis to keep this porosity reaction from occurring (Hurd and Fitch 1959).

$$\text{Gypsum (CaSO}_4\cdot 2\text{H}_2\text{O)} + \text{heat} = \text{Bassanite (CaSO}_4\cdot 0.5\text{H}_2\text{O)} + 1.5\text{H}_2\text{O} \qquad (2)$$
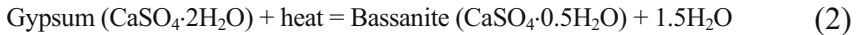
Table 1. Increase in porosity of gypsum-bearing dolomite samples due to heating (After Hurd and Fitch 1959)

	Low-temperature analysis	High-temperature analysis	Increase in porosity
Gypsum (%)	Porosity (%)	Porosity (%)	Porosity (%)
4.3	2.8	3.7	0.9
14.6	2.5	8.4	5.9
14.9	3.4	8.9	5.5
11.0	6.4	11.2	4.8

Porosity measurements should be made at in situ stress conditions because carbonate rocks are compressible, and porosity decreases with increasing effective stress. The common laboratory method is to increase confining pressure while maintaining a constant pore pressure. The resulting decrease in porosity is normally very small (2%) in Paleozoic and many Mesozoic reservoirs (Fig. 2), and porosity measurements at ambient conditions are usually adequate (Harari et al. 1995). Porosity values of all high-porosity carbonates, however, should be checked for porosity loss with increasing confining pressure.

The common pore type in sedimentary rocks is intergrain. Intergrain porosity is not a function of grain size but is a function of sorting. The percent intergrain porosity in a unit volume of cubic packed spherical grains can be calculated to be 47.6% (Fig. 3A). Cubic packing is the most open arrangement of grains. Rhombohedral packing is the closest arrangement of spherical grains and has a porosity of 25.9 percent per unit volume (Fig. 3B). The effect of sorting on porosity can be seen in unconsolidated sandstone. The porosity of extremely well sorted unconsolidated sandstone is 42%, whereas the porosity of poorly sorted sandstone is 27% (Beard and Weyl 1973).
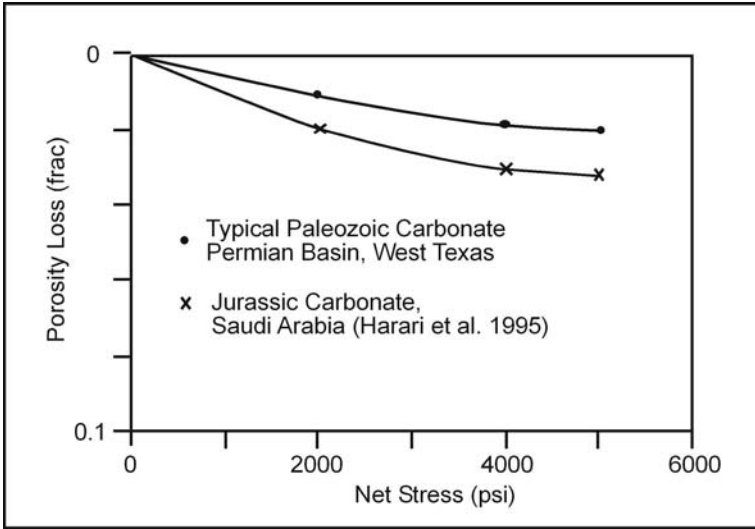
Fig. 1.2. Effect of confining pressure on porosity in Paleozoic and Jurassic carbonate reservoirs. Porosity loss is defined as confined porosity/unconfined porosity
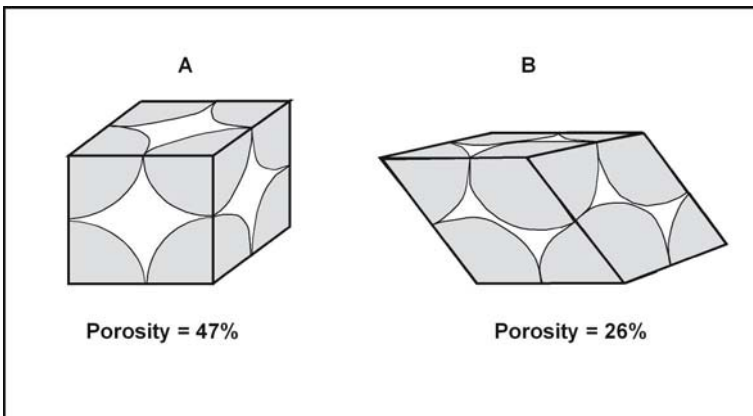
Fig. 1.3. Comparison of porosity in **(A)** cubic packed spheres and **(B)** rhombohedral-packed spheres. The porosity is a function of packing, and pore size is controlled by the size and packing of spheres

    In carbonate sediment the shape of the grains and the presence of intragrain porosity as well as sorting have a large effect on porosity. The presence of pore space within shells and peloids that make up the grains of carbonate sediments increases the porosity over what would be expected from intergrain porosity alone (Dunham 1962). The effect of sorting on porosity is opposite from that found in siliciclastics. The porosity of modern

ooid grainstones averages 45% but porosity increases to 70 percent as sorting decreases (Enos and Sawatski 1981). This increase is largely related to the needle shape of the mud-sized aragonite crystal. As a result, there is no simple relationship among porosity, grain size, and sorting in carbonate rocks.

Although there is no simple relation between porosity and fabric, it is apparent by inspection that intergrain pore size decreases with smaller grain size and with closer grain packing. Porosity also decreases with closer packing, resulting in intergain pore size being related to grain size, sorting, and intergrain porosity. The size and volume of intragrain pore space are related to the type of sediment and its post-depositional history.

1.3 Permeability

Permeability is important because it is a rock property that relates to the rate at which hydrocarbons can be recovered. Values range considerably from less than 0.01 millidarcy (md) to well over 1 darcy. A permeability of 0.1 md is generally considered minimum for oil production. Highly productive reservoirs commonly have permeability values in the Darcy range.

Permeability is expressed by Darcy's Law:

$$\text{Darcy's Law:} \quad Q = A\left(\frac{k}{\mu}\right)\left(\frac{\Delta P}{L}\right), \tag{3}$$

where Q is rate of flow, k is permeability, μ is fluid viscosity, $(\Delta P)/L$ is the potential drop across a horizontal sample, and A is the cross-sectional area of the sample. Permeability is a rock property, viscosity is a fluid property, and $\Delta P/L$ is a measure of flow potential.

Permeability is measured in the laboratory by encasing a sample of known length and diameter in an air-tight sleeve (the Hasseler Sleeve) in a horizontal position. A fluid of known viscosity is injected into a sample of known length and diameter while mounted in a horizontal position. The samples are either lengths of whole core, typically 6 inches long, or 1-in plugs drilled from the cores. The pressure drop across the sample and the flow rate are measured and permeability is calculated using the Darcy equation (Fig. 4). Normally, either air or brine is used as a fluid and, when high rates of flow can be maintained, the results are comparable. At low rates, air permeability will be higher than brine permeability. This is because gas does not adhere to the pore walls as liquid does, and the slippage of gases along the pore walls gives rise to an apparent dependence of permeability on

pressure. This is called the Klinkenberg effect, and it is especially important in low-permeability rocks.
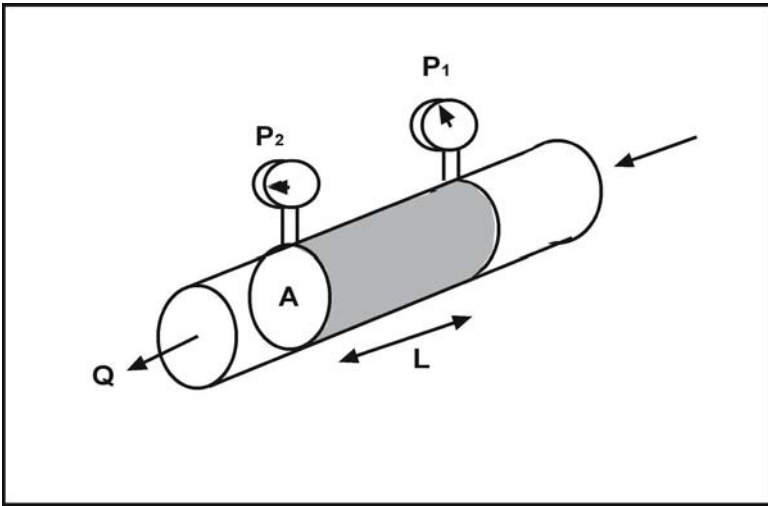
Fig. 1.4. Method of measuring permeability of a core plug in the laboratory. Samples are oriented horizontally to eliminate gravity effects; see text for explanation

Permeability can also be measured using a device called the miniairpermeameter (Hurst and Goggin 1995). This device is designed for use on flow surfaces such as outcrops or core slabs, and numerous permeability values can be obtained quickly and economically. This method, however, is not as accurate as the Hasseler Sleeve method. The equipment consists of a pressure tank, a pressure gauge, and a length of plastic hose with a special nozzle or probe designed to fit snugly against the rock sample. The gas pressure and the flow rate into the rock sample are used to calculate permeability.

Measurements should be made when the samples are under some confining pressure, preferably a confining pressure equivalent to in situ reservoir conditions. This is particularly important when the samples contain small fractures and stylolites because in unconfined conditions these features tend to be flow channels that result in unreasonably high permeability values.

Permeability is a vector and scalar quantity. Horizontal permeability varies in different directions, and vertical permeability is commonly less than horizontal permeability. Therefore, permeability is often represented as a vector in the x, y, and z directions. Core analysis reports give three permeability values when whole-core samples are used, two horizontal and one vertical, and a single horizontal value when core plugs are used. The two horizontal measurements are taken at 90 degrees from each other and are

commonly represented as maximum permeability and permeability 90 degrees from maximum.

Permeability depends upon the volume of the sample as well as the orientation. Darcy's Law shows permeability as a function of the cross-sectional area of the sample and pressure drop along a fixed length. In carbonate reservoirs permeability varies depending upon the size of the sample. An extreme example of the sampling problem is illustrated by a core sample with a large vug from a Silurian carbonate buildup (Fig. 5). The permeability of this sample is most likely very large because of the large touching vug, but the core analysis reports permeability at <0.1 md. This value is based on a 1-in plug, which was used because it would be very difficult to measure the permeability of the whole-core sample. Therefore, it is important to know how the formation was sampled before using the laboratory results. As a rule, *never use core data from a carbonate reservoir unless you have seen the core and observed how the core was sampled.*

Fig. 1.5. Core sample of a large vug from a Silurian reef, Michigan. The measured permeability from a core plug taken from this sample is <0.1md, which is an obvious understatement of the permeability of this sample

A measure of permeability can be obtained from production tests using pressure buildup analyses. The pressure in the well is drawn down by production, the well is shut in, and the rate of pressure increase is measured.

The rate of pressure increase is a function of the effective permeability of the reservoir. The effective, average permeability of the interval tested is calculated using the following equation:

$$\text{Slope (psi/log cycle)} = 162.6(q\mu B_o/kh), \qquad (4)$$

where q is the flow rate in stock-tank-barrels/day, μ = viscosity in centipoises, B_o is reservoir-barrels/stock-tank-barrels, k is permeability in millidarcys, and h is the net reservoir interval in feet.

Pressure buildup tests are used to calculate reservoir pressure and well bore damage (skin effect, Fig. 6) as well as effective permeability. A pressure buildup curve can be obtained by measuring the flow into a drill stem test tool or into a producing well after the well has been shut in for a period. Flow rates and pressure changes are analyzed using the Horner pressure buildup plot, which is a graph of pressure versus the log of dimensionless time, $(t+\Delta t)/\Delta t$. Reservoir pressure is determined by extrapolating the straight-line portion to 0 (log of 1). The skin calculation is related to the deviation of the buildup curve during the initial pressure buildup. Permeability is expressed as "fluid transmissibility", which is
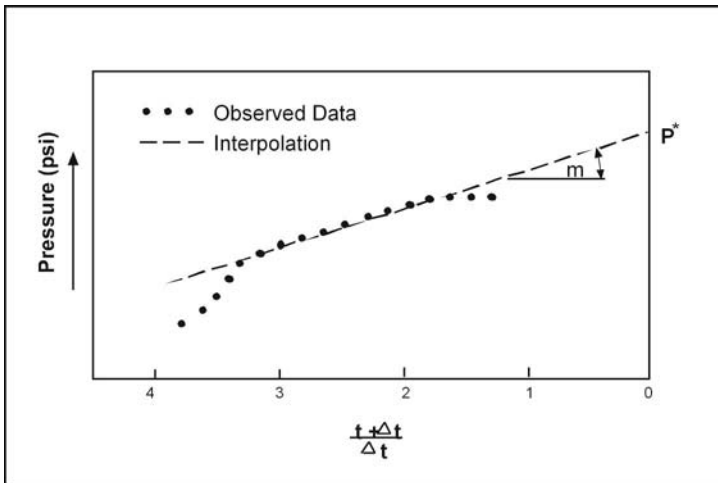
Fig. 1.6. Typical Horner pressure buildup plot (after Dake 1978). The slope of the line is a function of permeability-feet (kh)

expressed as permeability-feet (kh), and effective permeability values are normally obtained by dividing kh by the vertical height of the test interval. A large error in effective permeability can result if the proper height and reservoir volume sampled are not understood.

1.4 Pore Size and Fluid Saturation

Pore-size is the common factor between permeability and hydrocarbon saturation. Permeability models have historically described pore space in terms of the radius of a series of capillary tubes. The number of capillary tubes has been equated to porosity so that permeability is a function of porosity and pore-radius squared (Eq. 5 from Amyx et al. 1960, p. 97). Kozeny (1927) substituted surface area of the pore space for pore radius and developed the well-known Kozeny equation relating permeability to porosity, surface-area squared, and the Kozeny constant (Eq. 6).

$$k = \pi r^2/32, \text{ or } k = \phi r^2/8 \tag{5}$$

$$k = \phi/k_z S_p{}^2 \tag{6}$$

It is common practice to estimate permeability using simple porosity-permeability transforms developed from core data. However, porosity-permeability cross plots for carbonate reservoirs commonly show large variability (Fig. 7), demonstrating that factors other than porosity are important in modeling permeability. These equations illustrate that the size and distribution of pore space, or pore-size distribution, is important along with porosity in estimating permeability. In general it can be concluded that *there is no relationship between porosity and permeability in carbonate rocks unless pore-size distribution is included*.

A measure of pore-size can be obtained from mercury capillary pressure curves, which are acquired by injecting mercury (nonwetting phase) into a sample containing air (wetting phase). Mercury is injected at increments of increasing pressure and a plot of injection pressure against the volume of mercury injected (Hg saturation) is made (Fig. 8). The Hg saturation can be plotted as a percent of pore volume or bulk volume. This curve is referred to as the drainage curve. As the injection pressure is reduced, wetting fluid (air or water) will flow into the pore space and the nonwetting fluid will be expelled. This process is called imbibition, and a plot of pressure and saturation during the reduction of injection pressure is referred to as the imbibition curve (Fig. 8).

The pore size obtained by this method is referred to as the pore-throat size. Pore-throat size is defined as the pore size that connects the larger pores. It is based on the concept that interparticle pore space can be visualized as rooms with connecting doors. The doors are the pore-throats that connect the larger pores, or rooms.

Hg saturation is dependent on (1) the interfacial tension between mercury and water, (2) the adhesive forces between the fluids and the minerals that
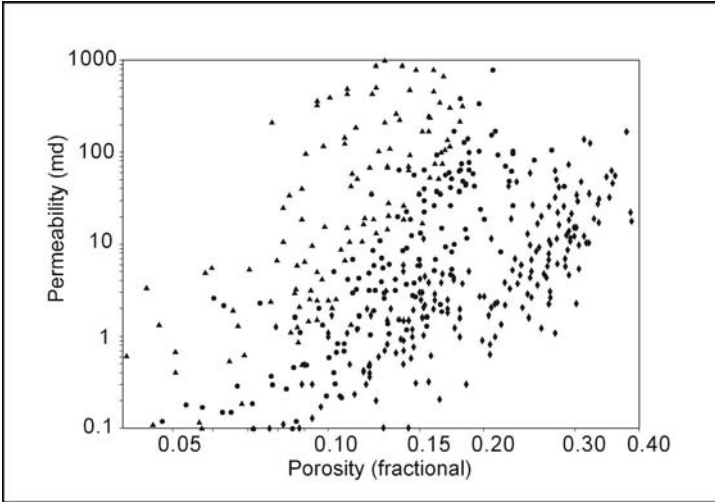
Fig. 1.7. Plot of porosity and permeability for carbonate rocks, illustrating that there is no relationship between porosity and permeability in carbonate rocks without including pore-size distribution
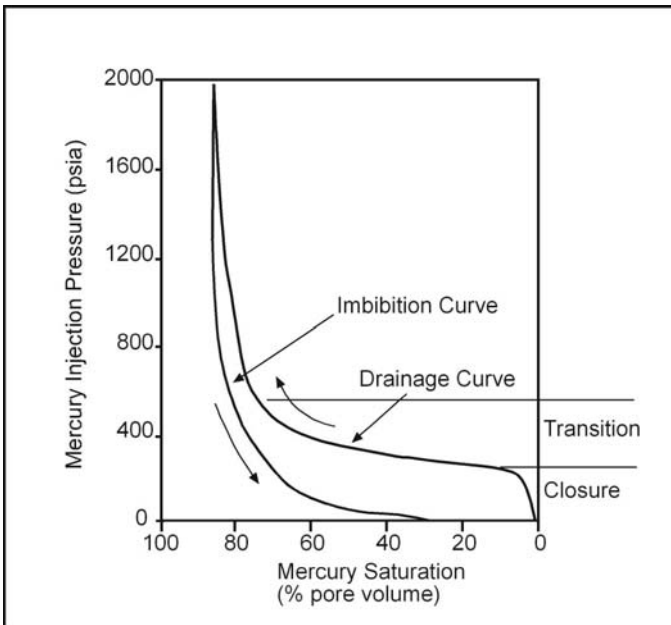
Fig. 1.8. Typical capillary pressure curves showing drainage and imbibition curves. Data for the drainage curve are obtained by increasing pressure, whereas data for the imbibition curve are obtained by reducing pressure

make up the pore walls, (3) the pressure differential between the mercury and water phases (capillary pressure), and (4) pore-throat size. Pore-throat size is calculated using the following equation:

$$r_c = 0.145(2\sigma\cos\theta/P_c), \tag{7}$$

where r_c is the radius of the pore throat in microns,
             σ is the interfacial tension in dynes/cm,
             P_c is the capillary pressure in psia (not dynes/cm^2), and
             0.145 is a conversion factor to microns

Interfacial tension results from the attraction of molecules in a liquid to each other. It can be defined in terms of the pressure across the fluid boundary and the radius of curvature of that boundary, as shown in Eq. (8).

$$2\sigma = (P_1-P_2)\, r_1, \tag{8}$$

where P_1-P_2 is the pressure differential across the meniscus (capillary pressure), σ is surface tension, and r_1 is the radius of curvature of the liquid.

Equation (8) can be derived by considering the hemispherical bottom part of a drip of water coming out of a small faucet just before it drops. The molecules within the drip attract each other equally, but the molecules on the surface are attracted toward the center of the drip and to the other molecules on the surface, creating a net inward force (Fig. 9).

If $F\downarrow$ = total downward force pulling on drip,
then:

$$F\downarrow = \pi r_1^2\, (P_1-P_2), \tag{9}$$

where πr_1^2 = cross-sectional area of drip and
       (P_1-P_2) = difference between the pressure inside the drip (water pressure) and pressure outside the drip (atmospheric pressure).

If $F\uparrow$ = upward cohesive forces holding drip together,
then $F\uparrow = 2\pi\, r_1\, \sigma$,

$$F\uparrow = 2\pi\, r_1\, \sigma, \tag{10}$$

where r_1 = radius of curvature of liquid,
       $2\pi\, r_1$ = circumference of drip and
       σ = surface tension.

At equilibrium, $F\uparrow = F\downarrow$

$\qquad 2\pi\, r_l\, \sigma = \pi r_l^2\, (P_1\text{-}P_2)$

$\qquad$ or:

$$2\sigma/\, r_l = (P_1\text{-}P_2). \qquad\qquad (11)$$
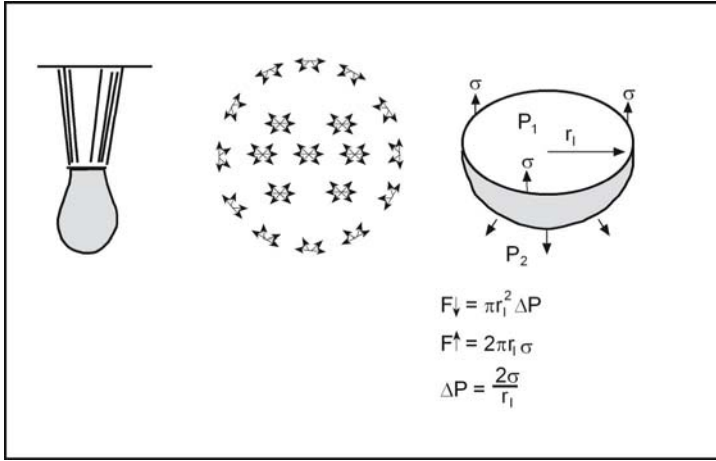
Fig. 1.9. Cohesive forces and the definition of surface tension

Whereas cohesive forces hold the liquid together, adhesive forces between solid and liquid tend to spread the liquid out. When a fluid encounters a solid surface, it tends either to spread over that surface or to form a ball on the surface, and the angle between the solid and liquid meniscus is a measure of the adhesive force. The contact angle between the fluid and the surface will be less than 90° for fluids that spread over the surface and greater than 90° for fluids that tend to form a ball. If the contact angle is less than 90°, the fluid is said to be wetting and if the angle is greater than 90°, nonwetting (Fig. 10).

The adhesive forces between a solid and water are greater than those between a solid and air in a water/air/solid capillary system and cause water to rise in a capillary tube (Fig. 11). The adhesive force is equal to cos θ, and is equal to the radius of the capillary tube divided by the radius-of-curvature of the liquid meniscus (Eq 12):

$$\cos\theta = r_c/r_l\,, \text{ or } r_l = r_c/\cos\theta, \qquad\qquad (12)$$

where r_l is the radius of the liquid meniscus, r_c is the radius of the capillary tube, and cos θ is the adhesive force (solid/liquid).
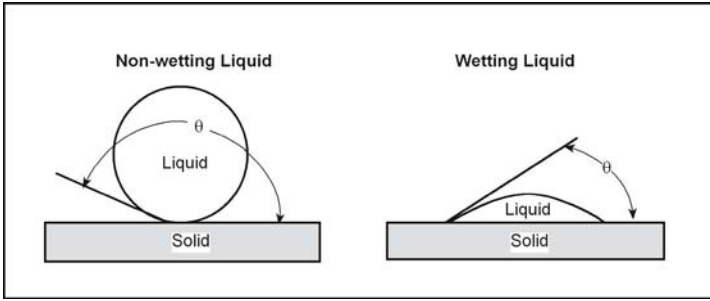
Fig. 1.10. Adhesive forces and the definition of wettability. If the adhesive forces are less than cohesive forces, $(\theta > 90°)$, the liquid is said to be nonwetting. If adhesive forces are greater than cohesive forces, $(\theta < 90°)$, the liquid is said to be the wetting phase
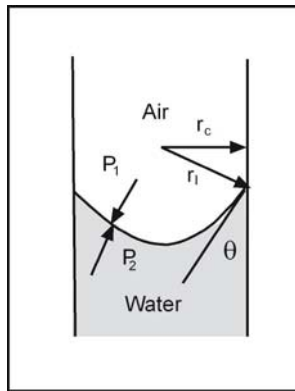
Fig. 1.11. Capillary pressure relations in a capillary tube

A pressure difference (capillary pressure) exists across the air/water interface, and this pressure can be defined in terms of the surface tension (σ) and the radius of curvature of the meniscus (r_l):

$$r_l = 2\sigma /(P_1-P_2) \text{ (see Eq. 7).}$$

Substituting Eq. (12) for r_l results in:

$$2\sigma \cos\theta/r_c = (P_1-P_2) = \text{capillary pressure } (P_c),$$

or:

$$r_c = 0.145(2\sigma \cos\theta/P_c), \tag{13}$$

where r_c is the radius of the pore throat in microns,
             σ is the interfacial tension in dynes/cm,
             P_c is the capillary pressure in psia (not dynes/cm^2), and
             0.145 is a conversion factor to microns

Pore-throat sizes are calculated for each point on the capillary pressure curve and presented a frequency or cumulative frequency plot as shown in Fig. 12. These plots characterize the statistical distribution of pore-throat sizes in the sample but do not characterize their spatial distribution. Also, these curves do not characterize all the pore sizes that are in the sample, only the pore-throat size. However, techniques have been developed to obtain a measure of larger pore sizes as well as pore-throat sizes from mercury injection. *Pore-size distribution as used in this book is defined as the spatial distribution of all the pore sizes in the rock, which includes pore-throat sizes.*

In order to relate pore-throat size, determined from mercury capillary pressure data, to permeability and porosity as discussed above, a normalizing pore size must be chosen (Swanson 1981). The pore-throat size at a mercury saturation of 35% has been determined to be most useful (Kolodizie 1980; Pittman 1992). Generic equations relating porosity, permeability, and pore-throat size at various mercury saturations for siliciclastics have been published by Pittman (1992). A plot using 35% mercury saturation to calculate pore-throat size (Fig. 13) demonstrates that pore-throat size has a larger effect on permeability than does porosity. Because these equations are derived for siliciclastic rocks, the porosity is restricted to intergrain porosity and not necessarily to total porosity.
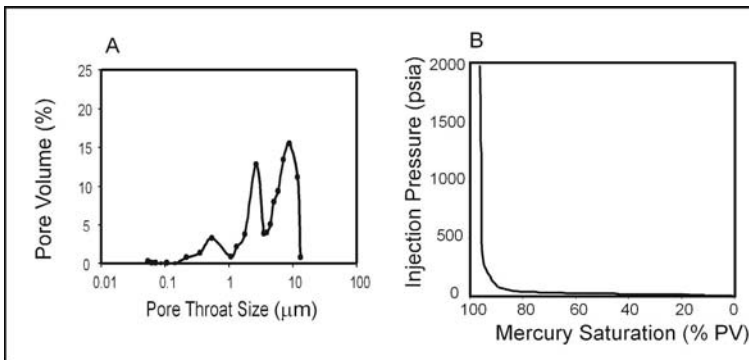
Fig. 1.12. A frequency diagram of pore-throat sizes **(A)** is calculated from the mercury capillary pressure curve **(B)**
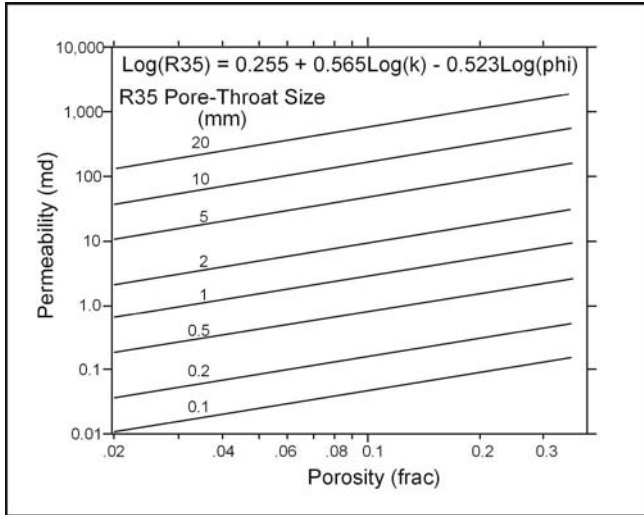
Fig. 1.13. Plot of porosity, permeability, and pore-throat size for siliciclastic rocks using 35% mercury saturation to calculate pore-throat size from mercury capillary pressure curves (Pittman 1992)

$$Log(r_{35}) = 0.255 + 0.565Log(k) - 0.523Log(\phi)$$

where r_{35} = pore-throat radius at 35% mercury saturation in microns,
            k = permeability in millidarcys, and
            ϕ = interparticle porosity as a fraction.

A similar equation has been published by Kolodizie (1980) and is presented here. It is referred to as the Winland equation and is used more commonly in the petroleum industry than is Pittman's equation.

$$k = 49.5\phi^{1.470} r_{35}^{1.701}$$

Hydrocarbon saturation in a reservoir is related to pore size as well as capillary pressure and capillary forces.   For oil to accumulate in a hydrocarbon trap and form a reservoir, the surface tension between water and oil must be exceeded. This means that the pressure in the oil phase must be higher than the pressure in the water phase. If the pressure in the oil is only slightly greater than that in the water phase, the radius of curvature will be large and the oil will be able to enter only large pores. As the pressure in the oil phase increases, the radius of curvature decreases and oil can enter smaller pores (Fig. 14).
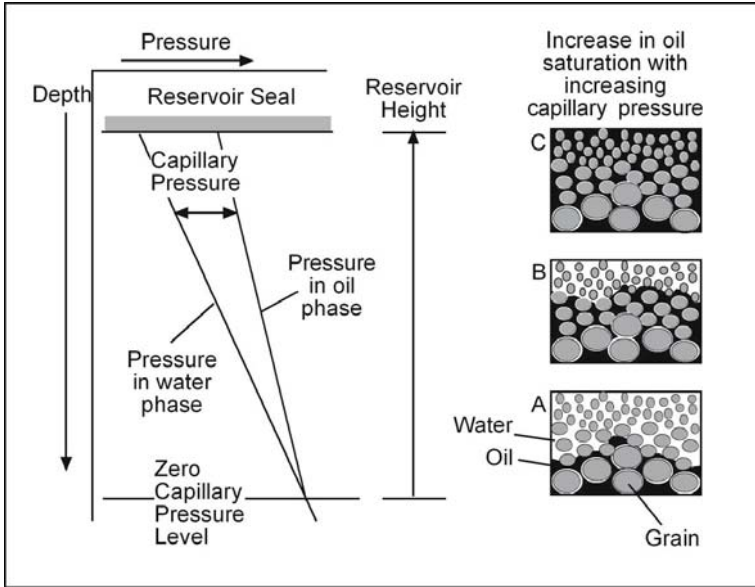
Fig. 1.14. Diagram showing smaller pores being filled with a non-wetting fluid (oil) displacing a wetting fluid (water) as capillary pressure increases linearly with reservoir height. Pore size is determined by grain size and sorting. **(A)** Only the largest pores contain oil at the base of the reservoir. **(B)** Smaller pores are filled with oil as capillary pressure and reservoir height increase. **(C)** Smallest pores are filled with oil toward the top of the reservoir

In nature, the pressure differential (capillary pressure) is produced by the difference in density between water and oil; the buoyancy effect. At the zero capillary pressure level (*zcp*), the reservoir pressure is equal to pressure in the water phase (depth times water density). Above the *zcp* level the pressure in the water phase will be reduced by the height above the *zcp* times water density, and the pressure in the oil phase will be reduced by the height above the *zcp* times oil density.

$$\text{Pressure in water phase} \quad P_w = P_{zcp} - H\rho_w \qquad (14)$$

$$\text{Pressure in oil phase} \quad P_o = P_{zcp} - H\rho_o \qquad (15)$$

At any height in an oil column, the pressure difference between the oil phase and the water phase (capillary pressure) is the difference between the specific gravity of the two fluids multiplied by the height of the oil column:

$$P_O - P_W = 0.434H(\rho_w - \rho_o), \qquad (16)$$

where H is the height above zero capillary pressure level, ρ_o is the density of the oil phase, ρ_w is the density of the water phase, and 0.434 is the unit conversion constant to feet.

Mercury capillary pressure measurements can be converted to height above the zero capillary pressure level (reservoir height) by converting the surface tension and contact angle for the fluids used in the laboratory to the values for the specific subsurface fluids in a given reservoir. The equation for this conversion can be derived from capillary theory:

$$H = \frac{(\sigma\cos\theta)_{o/w/s} \times (P_c)_{hg/a/s}}{0.434(\rho_w - \rho_o) \times (\sigma\cos\theta)_{hg/a/s}}, \tag{17}$$

where $o/w/s$ is the oil/water/solid system, and $hg/a/s$ is the mercury/air/solid system.

Typical values for converting mercury/air capillary pressure curves to reservoir conditions of oil/water are given in Table 2.

Table 2. Typical values for converting mercury/air capillary pressure curves to reservoir conditions of oil/water

LABORATORY mercury/air/solid	Reservoir oil/water/solid	Reservoir density (g/cc)	
σ 480 dynes/cm	σ 28 dynes/cm	Water (ρ_w)	1.1
θ 140°	θ 33 - 55°	Oil (ρ_o)	0.8

The capillary pressure curve characterizes the saturation profile of the nonwetting phase as well as the pore-throat sizes. The curve is often divided into an initial phase (closure) where voids on the surface of the sample are filled, a transition phase where most of the pore space is filled, and an irreducible phase where only the smallest pores remain empty of the nonwetting phase (Fig. 8). These concepts are used in reservoir description as well. However, the advent of high-pressure mercury porosimeters has demonstrated that above the transition zone the nonwetting saturation continues to increase by filling the smallest pore but at a much slower rate than filling the larger pores in the transition zone.

The base of a reservoir may be described by the drainage curve or by the imbibition curve depending upon the pressure history (Lucia 2000). If the reservoir pressure has been reduced for geologic reasons, the reservoir water will flow into the pore space and oil will be expelled. Some of the oil will be trapped in the pores because there is insufficient pressure in the oil phase to overcome capillary forces. The trapped oil is referred to as residual oil. The

reservoir will be in imbibition mode, and the imbibition curve must be used to describe the fluid distribution at the bottom of the reservoir. The drainage transition zone is replaced by a thinner imbibition transition zone and a residual oil zone.

The difference in density between water and hydrocarbons, the buoyancy force, produces pressures in hydrocarbon columns that exceed pressures in the water column. The pressure gradient in reservoirs can be used to determine the distance above the *zcp* level. Multiple reservoir pressures can be obtained from the repeat formation tester, a wireline formation tester capable of multiple settings downhole (Smolen and Litsey 1977). It can retrieve several fluid samples per trip, but its primary advantage is its multiple-level pressure-measuring capability. This tool allows a number of pressures to be taken from selected intervals, thus providing data to determine reservoir gradients. This data can be used to define *zcp* levels and define reservoir compartments (Fig. 15).
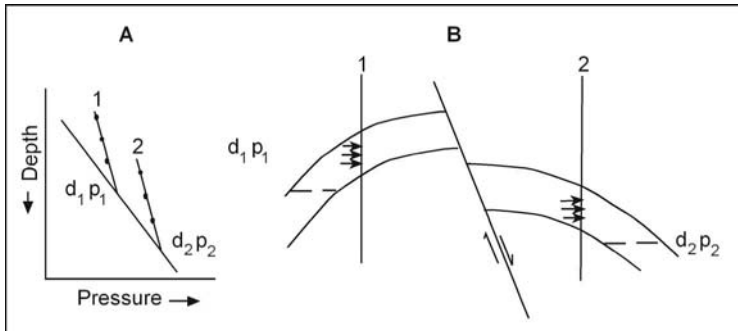
Fig. 1.15. Diagram illustrating the use of pressure gradients to define reservoir compartments and water levels. **(A)** Depth plot of pressure from wells 1 and 2 shown in **(B)**. Intersections of depth plots with the regional fluid-pressure gradient are at depths d_1 and d_2, suggesting separate reservoirs with different water-oil contacts. **(B)** Cross section showing well locations, sampling depths, and sealing fault dividing the hydrocarbon accumulation into two reservoirs

The pressure in the water phase depends upon the degree to which the fluid column is connected to the Earth's surface. In an open system, the fluid pressure is equal to depth times the density of the fluid and is called hydrostatic (Fig. 16). The hydrostatic pressure gradient is about 0.434 psi/ft; overburden pressure equals the weight of the overburden sediment and has a gradient of about 1 psi/ft. Deviations from hydrostatic pressure, abnormal pressures, occur when the formation fluid is confined and cannot equilibrate with surface pressure. Overpressuring is the most common abnormal pressure and is produced by (1) compaction during rapid burial, (2) tectonic

compression, and (3) hydrocarbon generation and migration (Osborne and Swarbrick 1997). In extreme cases, fluid pressures can equal and even exceed overburden pressures. Uncommonly, pressures can be lower than hydrostatic. Underpressure is often related to erosional unloading that results in an increase in pore volume due to the elastic rebound of the sediment as the overburden is reduced (Bachu and Underschultz 1995).
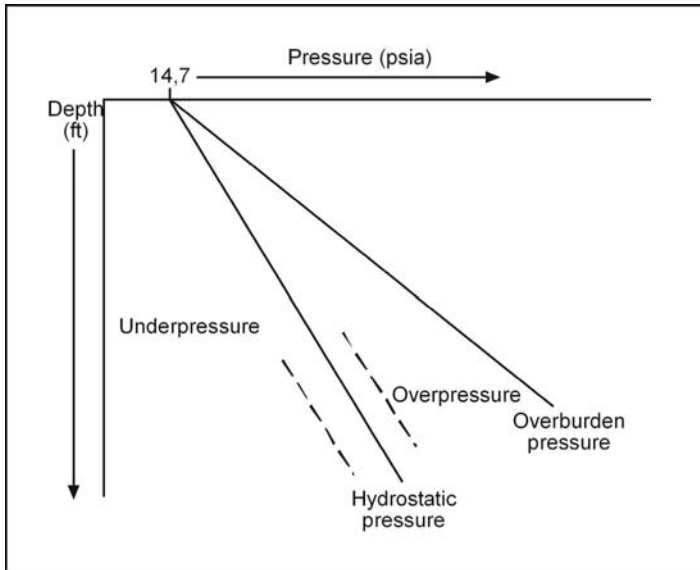
Fig. 1.16. Diagram illustrating overburden, normal hydrostatic, and abnormal over- and underpressure regimes. (After Dake 1978)

1.5 Relative Permeability

Oil, water, and gas are found in hydrocarbon reservoirs in varying propor- tions. Permeability measurements, however, are typically done using a single fluid, commonly air or water, and the permeability values must be corrected for the varying saturations of water, oil, and gas that occur in the reservoir. The correction is necessary because when a non-wetting fluid, such as oil, enters a water-wet pore system, the oil fills the centers of the largest, well connected pores whereas the water is found lining the pore walls and filling the smallest pores. This fluid distribution reduces the pore space available for flow of either water or oil. When water is injected or imbibed into the water-wet pore system, oil is trapped in pores with the

smallest portals due to capillary forces. This oil is referred to as residual oil to water flooding (Fig. 17).
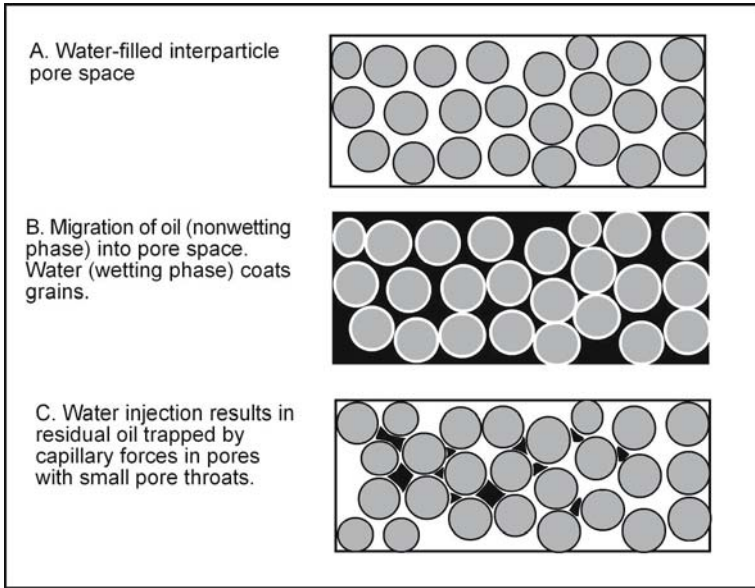
Fig. 1.17. Diagram of oil and water distribution in a water-wet rock under three conditions: (**A**) 100% water saturation, (**B**) injection of a nonwetting fluid (oil), and (**C**) injection of a wetting fluid (water)

Relative permeability is simply the permeability measured at a specific fluid saturation expressed as a fraction of the total or absolute permeability. *Absolute permeability* is the permeability of a rock that is 100% saturated with a single fluid. In a water-wet rock only water can totally saturate the pore system, and brine permeability is normally taken as the absolute permeability.   However, hydrocarbon permeability at residual water saturation is often used as absolute permeability in reservoir engineering studies. *Effective permeability* is the permeability of one fluid in the presence of another fluid measured at a specific saturation state. Effective permeability is always lower than the absolute permeability and will change as the saturation changes. Thus, if a rock 100% saturated with brine has a permeability of 50 md whereas the brine permeability in the presence of 50% oil saturation is 10 md, the relative permeability of brine at 50% oil saturation is said to be 0.2. Graphs of relative permeability versus saturation (Fig. 18) are very important because they can be used to predict changes in production rates with changes in water saturation. They are fundamental in fluid flow

simulation, and changing the relative permeability characteristics has a major effect on the resulting performance prediction.
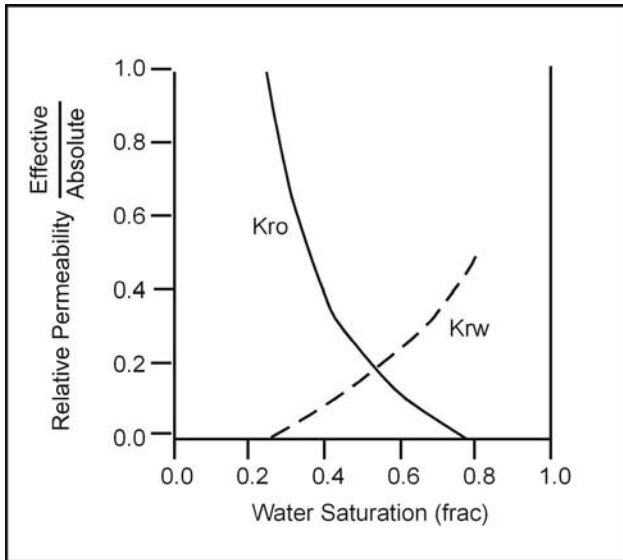
Fig. 1.18. Typical relative permeability plot where absolute permeability is taken as oil permeability at lowest water saturation. Kro is the relative permeability to oil and Krw is the relative permeability to water

There are two methods for measuring permeability at various saturation states to obtain relative permeability, steady state and unsteady state (Fig. 19). The steady-state method is the most accurate method, but it is time consuming and expensive because it involves injecting both oil and water simultaneously until the output rates match the input rates. The unsteady-state method is less accurate but faster because it involves saturating the core with oil and flooding with water. The relationships between relative permeability and saturation obtained by these two methods are commonly very different. A third method that is rapid and less expensive is to measure effective permeabilities at irreducible water and residual oil. This is called the end point method, and it assumes that a reasonable estimate of the curvature can be made.

A significant problem in measuring relative permeability in the laboratory is restoring samples to reservoir conditions. Pore surfaces, especially in carbonate rocks, are reactive to changes in fluids, and these reactions can alter the wettability state. Elaborate methods have been devised to preserve the original wettability state of core material, and the accuracy of any relative permeability data is dependent on the success of these methods.
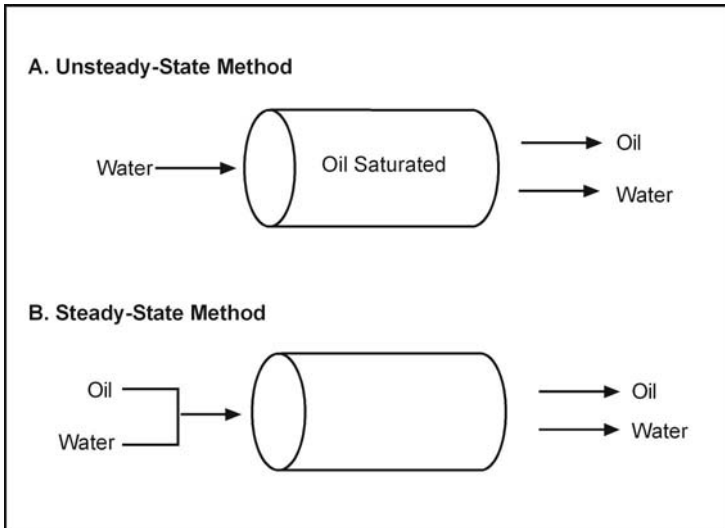
Fig. 1.19. Illustration of unsteady-state and steady-state methods of measuring two-phase oil and water relative permeability

Many carbonate reservoirs are considered to have mixed wettability at present; some pore walls are oil wet and some water wet. However, it is most likely that the reservoirs were water wet at the time of oil migration.

Reservoir height (capillary pressure), relative permeability, and saturation are interrelated, as illustrated in Fig. 20 (Arps 1964). The oil becomes mobile only after attaining a saturation defined by the relative permeability curve that equates to a reservoir height defined by the capillary pressure curve. This level often defines the field oil/water contact. Oil and water are produced above this reservoir height until the relative permeability to water becomes extremely low and only oil will flow. The reservoir height at which this occurs is defined by the capillary pressure curve. This depth interval is commonly referred to as the transition zone between water production and oil production. Above this interval, water-free oil production can be expected.
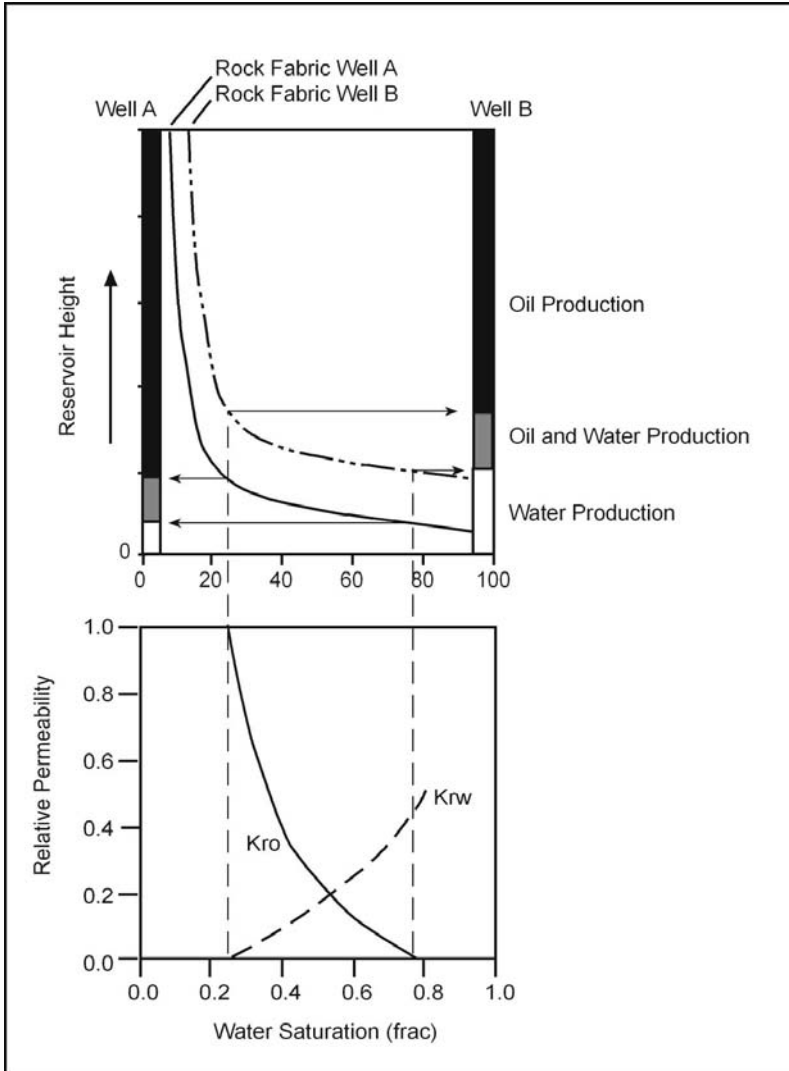
Fig. 1.20. Simplified illustration showing the relationship between relative permeability to oil and water, capillary pressure converted to reservoir height, water saturation, and pore size. The effect of pore size is illustrated by considering two capillary pressure curves **(rock-fabric A**, **rock-fabric B)** from carbonate rocks with different pore-size distributions. The change in pore size results in the possibility of intervals where (1) clean oil is produced from rock-fabric A and oil and water from rock-fabric B , and (2) oil and water is produced from rock-fabric A and water from B

1.6 Summary

The petrophysical properties of porosity, permeability, relative permeability, and fluid saturations are linked through pore-size. *Porosity* is a fundamental property of reservoir rocks. It is a number calculated by bulk volume divided by pore volume. Visible pores are referred to as pore space and not porosity because porosity is a number and is not visible. Pore-size is related to the size and sorting of the particles that make up the fabric of the rock, as well as to the porosity. *Fluid saturations*, such as water and oil saturations, are a function of pore size, porosity, and capillary pressure. Capillary pressure is directly linked to reservoir height through the density difference of the fluids involved. *Permeability* is a function of porosity and pore-size. *Relative permeability* is a function of absolute permeability and fluid saturation, which are both linked to pore-size.

Pore-size can be measured in a number of different ways. Although some pore-sizes and shapes can be measured visually, the most reliably method is injecting the sample with mercury at varying pressures. The radius-of-curvature of the connecting pores (pore throats) is a function of the injection pressure, the interfacial tension of the liquid, and the adhesive forces between the fluid and the pore wall. The relationship is given in equation 13 and repeated here.

$$r_c = 0.145(2\sigma \cos\theta / P_c), \tag{13}$$

Capillary pressure in a hydrocarbon reservoir is a function of the difference between the pressure in the water and hydrocarbon phases, which is a function of the height above the zero capillary pressure level. Using the densities of water and hydrocarbon together with the above equation a capillary pressure curve can be converted into reservoir height. The resulting curve will express the changing water saturation with increasing reservoir height.

A critical activity in reservoir characterization is distributing petrophysical properties in 3D space. Laboratory measurements of petrophysical properties have no spatial information at the reservoir scale. Measuring permeability in different directions provides spatial information at the core scale, but not at the reservoir scale. One-dimensional information can be obtained by the detailed sampling along the length of the core but that data does not provide spatial information at the reservoir scale. Petrophysical properties must be tied to geological descriptions and geophysical data in order to display these properties in 3D space. The link is through pore-size,

which is a function of porosity and rock fabric. Porosity is measured using various visual and laboratory methods and can be obtained indirectly from wireline logs and seismic surveys. Rock fabric descriptions are key to distributing properties in 3D because rock fabric can be tied directly to 3D geologic models. Methods of obtaining this information are discussed in Chapter 2.

References

Amyx JW, Bass DM Jr, Whiting RL 1960 Petroleum reservoir engineering. McGraw-Hill, New York, 610 pp

Archie GE 1952 Classification of carbonate reservoir rocks and petrophysical considerations. AAPG Bull 36, 2: 278-298

Arps JJ 1964 Engineering concepts useful in oil finding. AAPG Bull 43, 2: 157-165

Bachu S, Underschultz JR 1995 Large-scale underpressuring in the Mississippian-Cretaceous succession, Southwestern Alberta Basin. AAPG Bull 79, 7: 989-1004

Beard DC, Weyl PK 1973 Influence of texture on porosity and permeability in unconsolidated sand. AAPG Bull 57: 349-369

Dake LP 1978 Fundamentals of reservoir engineering: developments in petroleum science, 8. Elsevier, Amsterdam, 443 pp

Dunham RJ 1962 Classification of carbonate rocks according to depositional texture. In: Ham WE (ed) Classifications of carbonate rocks – a Symposium. AAPG Mem 1:108–121

Enos P, Sawatsky LH 1981 Pore networks in Holocene carbonate sediments. J Sediment Petrol 51, 3: 961-985

Harari Z, Sang Shu-Tek, Saner S 1995 Pore-compressibility study of Arabian carbonate reservoir rocks. SPE Format Eval 10, 4: 207-214

Hurd BG, Fitch JL 1959 The effect of gypsum on core analysis results. J Pet Technol 216: 221-224

Hurst A, Goggin D 1995 Probe permeametry: an overview and bibliography. AAPG Bull 79, 3: 463-471

Kolodizie S Jr 1980 Analysis of pore throat size and use of the Waxman-Smits equation to determine OOIP in Spindle Field, Colorado. SPE paper 9382 presented at the 1980 SPE Annual Technical Conference and Exhibition, Dallas, Texas

Kozeny JS 1927 (no title available). Ber Wiener Akad Abt Iia, 136: p 271

Lucia FJ 1995 Rock fabric/petrophysical classification of carbonate pore space for reservoir characterization. AAPG Bull 79, 9: 1275-1300

Lucia FJ 2000 San Andres and Grayburg imbibition reservoirs. SPE paper SPE 59691, 7 p.

Osborne MJ, Swarbrick RE 1997 Mechanisms for generating overpressure in sedimentary basins: a reevaluation. AAPG Bull 81, 6: 1023-1041

Schmoker JW, Krystinic KB, Halley RB 1985 Selected characteristics of limestone and dolomite reservoirs in the United States. AAPG Bull 69, 5: 733-741

Smolen JJ, Litsey LR 1977 Formation evaluation using wireline formation tester pressure data. SPE paper 6822, presented at SPE-AIME 1977 Fall Meeting, Oct 6-12, Denver, Colorado

Swanson BJ 1981 A simple correlation between permeability and mercury capillary pressures. J Pet Technol Dec: 2488-2504

Chapter 2 Rock-Fabric Classification

2.1 Introduction

The goal of reservoir characterization is to describe the spatial distribution of petrophysical parameters such as porosity, permeability, and saturation. In Chapter 1 we showed that porosity, permeability, and fluid saturations are linked through pore size. In this chapter we will expand simple pore size to pore-size distribution, that is, the spatial distribution of pore sizes within the rock, and show how pore-size distribution can be linked to rock fabrics. Wireline logs, core analyses, production data, pressure buildups, and tracer tests provide quantitative measurements of petrophysical parameters in the vicinity of the wellbore, but they generally provide only one-dimensional spatial information. Therefore, wellbore data must be integrated with geologic models to display the petrophysical properties in three-dimensional space. Studies that relate rock fabric to pore-size distribution, and thus to petrophysical properties, are key to quantification of geologic models in numerical terms for input into computer simulators (Fig. 1).
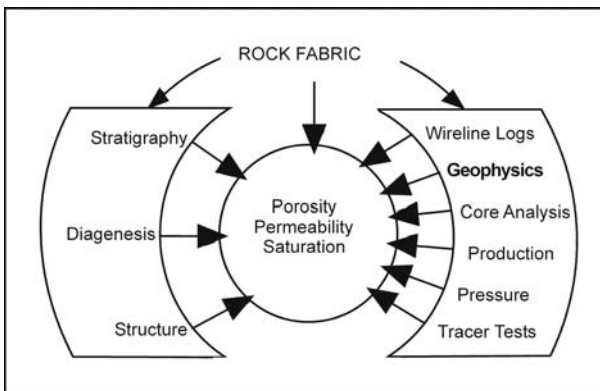
Fig. 2.1. Integration of spatial geologic data with numerical engineering data through rock-fabric studies

Geologic models are generally based on observations that are interpreted in terms of depositional models and sequences. In the subsurface, cores, wireline logs, and seismic data are the main sources of information for these interpretations. Engineering models are based on wireline log calculations and average rock properties from core analyses. Numerical engineering data and interpretive geologic data are linked by rock fabrics because the pore structure is fundamental to petrophysical properties, and the pore structure is the result of spatially distributed depositional and diagenetic processes.

The purpose of this chapter is to define important geologic parameters to be described and mapped to allow accurate petrophysical quantification of carbonate geologic models by (1) describing the relationship between carbonate rock fabrics and petrophysical properties and (2) presenting a generic petrophysical classification of carbonate pore space.

2.2 Pore Space Terminology and Classification

Pore space must be defined and classified in terms of rock fabrics and petrophysical properties in order to integrate geological and engineering information. Archie (1952) made the first attempt at relating rock fabrics to petrophysical rock properties in carbonate rocks. The Archie classification focuses on estimating porosity but is also useful for approximating permeability and capillary properties. Archie (1952) recognized that not all the pore space can be observed using a 10 power microscope and that the surface texture of the broken rock reflected the amount of matrix porosity. Therefore, pore space is divided into matrix and visible porosity (Fig. 2). *Chalky texture* indicates a matrix porosity of about 15 percent, *sucrosic texture* indicates a matrix porosity of about 7 percent, and *compact texture* indicates matrix porosity of about 2 percent. Visible pore space is described according to pore size; A for no visible pore space and B, C, and D for increasing pore sizes from pinpoint to larger than cutting size. Porosity/permeability trends and capillary pressure characteristics are also related to these textures.

Although the Archie method is still useful for estimating petrophysical properties, relating these descriptions to geologic models is difficult because the descriptions cannot be defined in depositional or diagenetic terms. A principal difficulty is that no provision is made for distinguishing between visible interparticle pore space and other types of visible pore space such as moldic pores. Research on carbonate pore space (Murray 1960; Choquette and Pray 1970; Lucia 1983) has shown the importance of relating pore space to depositional and diagenetic fabrics and of distinguishing between

interparticle (intergrain and intercrystal) and other types of pore space. Recognition of the importance of these factors prompted modification of Archie's classification.
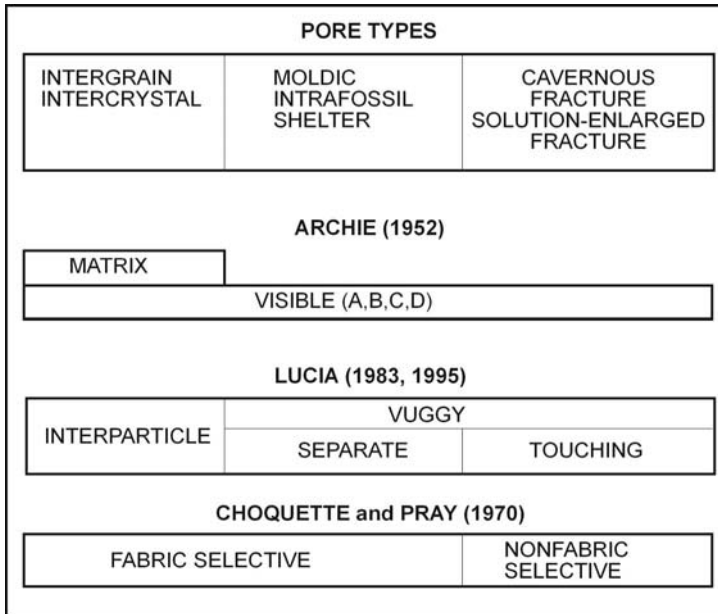
Fig. 2.2. Petrophysical classification of carbonate pore types used in this report (Lucia 1983) compared with Archie's original classification (1952) and the fabric selectivity concept of Choquette and Pray (1970)

The petrophysical classification of carbonate porosity presented by Lucia (1983, 1995) emphasizes petrophysical aspects of carbonate pore space, as does the Archie classification.   However, by comparing rock fabric descriptions with laboratory measurements of porosity, permeability, capillarity, and Archie m values, Lucia (1983) showed that the most useful division of pore types was between pore space located between grains or crystals, called interparticle porosity, and all other pore space, called vuggy porosity (Fig. 2). Vuggy pore space is further subdivided by Lucia (1983) into two groups based on how the vugs are interconnected: (1) vugs that are interconnected only through the interparticle pore network are termed *separate vugs* and (2) vugs that form an interconnected pore system are termed *touching vugs*.

Choquette and Pray (1970) discussed the geologic concepts surrounding carbonate pore space and presented a classification that is widely used. They emphasize the importance of pore space genesis, and the divisions in their

classification are genetic and not petrophysical. They divide all carbonate pore space into two classes: fabric selective and nonfabric selective (Fig. 2). Moldic and intraparticle pore types are classified as fabric selective porosity by Choquette and Pray (1970) and grouped with interparticle and intercrystalline pores. However, Lucia (1983) demonstrated that moldic and intraparticle pores have a different effect on petrophysical properties than do interparticle and intercrystalline pores and, thus should be grouped separately. Pore-type terms used in this classification are listed in Figure 3 and compared with those suggested by Choquette and Pray. Although most of the terms

Term	Abbreviations	
	Lucia	Choquette and Pray (1970)
Interparticle	IP	BP
Intergrain	IG	-
Intercrystal	IX	BC
Vug	VUG	VUG
Separate Vug	SV	-
Moldic	MO	MO
Intraparticle	WP	WP
Intragrain	WG	-
Intracrystal	WX	-
Intrafossil	WF	-
Intragrain microporosity	$ig\mu\phi$	-
Shelter	SH	SH
Touching Vug	TV	-
Fracture	FR	FR
Solution-enlarged fracture	SF	CH*
Cavernous	CV	CV
Breccia	BR	BR
Fenestral	FE	FE

*Channel.

Fig. 2.3. Pore-type terminology used in this report compared with terminology of Choquette and Pray (1970)

defined by Choquette and Pray are also used here, interparticle and vug porosity have different definitions. Lucia (1983) demonstrated that pore spaces located both between grains (intergrain porosity) and between crystals (intercrystal porosity) are petrophysically similar, and a term is need to identify these petrophysically similar pore types. The term "interparticle" was selected because of its broad connotation. The classification of Choquette and Pray (1970) does not have a term that encompasses these two petrophysically similar pore types. In their classification, the term "interparticle" is used instead of "intergrain."

Vuggy porosity, as defined by Lucia (1983), is pore space that is within grains or crystals or that is significantly larger than grains or crystals; that is, pore space that is not interparticle. Vugs are commonly present as dissolved grains, fossil chambers, fractures, and large irregular cavities. Although fractures may not be formed by depositional or diagenetic processes, fracture porosity is included because it defines a unique type of porosity in carbonate reservoir rocks. This definition of vug deviates from the restrictive definition of vugs used by Choquette and Pray (1970) as nondescript, nonfabric selective pores, but it is consistent with the Archie terminology and with the widespread and less restrictive use in the oil industry of the term "vuggy porosity" to refer to visible pore space in carbonate rocks.

2.3 Rock Fabric/Petrophysical Classification

The foundation of the Lucia classification, as well as of the Archie classification, is the concept that pore-size distribution, that is the spatial distribution of pore sizes within the rock, controls permeability and saturation and that pore-size distribution is related to rock fabric. In order to relate carbonate rock fabrics to pore-size distribution, it is important to determine if the pore space belongs to one of the three major pore-type classes, interparticle, separate-vug, or touching-vug. Each class has a different type of pore-size distribution and interconnection. As presented in Chapter 1, the pore size of interparticle pores is controlled by particle size and sorting, and by the volume of interparticle cement; for a given particle size and sorting the interparticle pore size will be reduced in proportion to the volume of cement. The pore size of separate vugs will vary depending upon origin and can vary from large to micro pores within grains.

2.3.1 Classification of Interparticle Pore Space

In the absence of vuggy porosity, pore-size distribution in carbonate rocks can be described in terms of particle size, sorting, and interparticle porosity (Fig. 4). Lucia (1983) showed that particle size can be related to mercury capillary displacement pressure in nonvuggy carbonates with more than 0.1 md permeability, suggesting that particle size describes the size of the largest pores (Fig. 5). Whereas the displacement pressure characterizes the largest pores sizes, the shape of the capillary pressure curve characterizes the smaller pore sizes and is dependent on interparticle porosity (Lucia 1983).
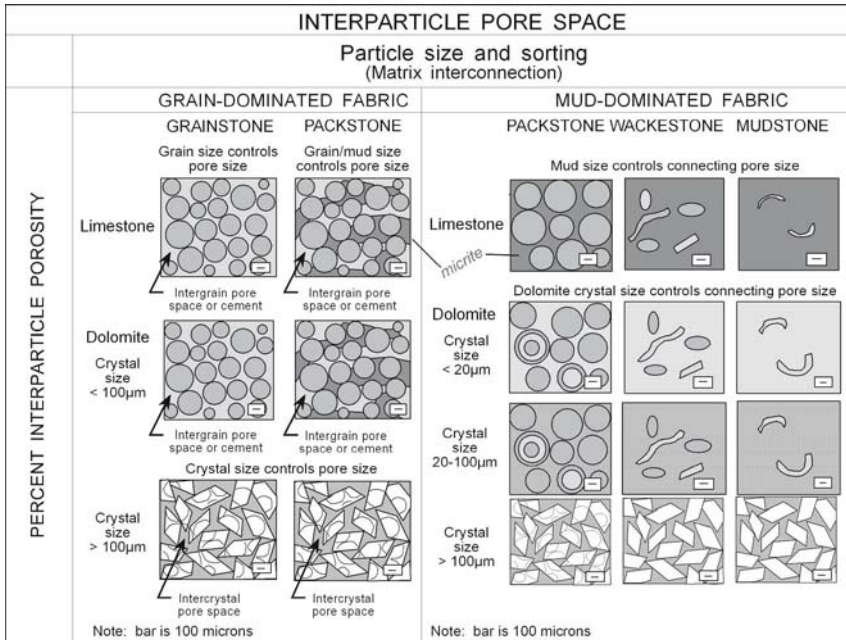
Fig. 2.4. Geological/petrophysical classification of carbonate interparticle pore space based on size and sorting of grains and crystals. The volume of interparticle pore space is important because it relates to pore-size distribution

The relationship between displacement pressure and particle size (Fig. 5) is hyperbolic and suggests important particle-size boundaries at 100 and 20 microns. Lucia (1983) demonstrated that three permeability fields can be defined using particle-size boundaries of 100 and 20 microns, a relationship that appears to be limited to particle sizes less than 500 microns (Fig. 6).

These three permeability fields were based on intercrystalline porosity in dolostones primarily.   Recent work that includes considerably more limestone fabrics has shown that permeability fields can be better described in geologic terms if sorting as well as particle size is considered.   The approach to size and sorting used in this petrophysical classification is similar to the grain/mud-support principle upon which Dunham's (1962) classification is built. Dunham's classification, however, is focused on depositional texture, whereas petrophysical classifications are focused on contemporary rock fabrics which include depositional and diagenetic textures.   Therefore, minor modifications must be made in Dunham's classification before it can be applied to a petrophysical classification.

Instead of dividing fabrics into grain support and mud support as in Dunham's classification, fabrics are divided into grain-dominated and mud-
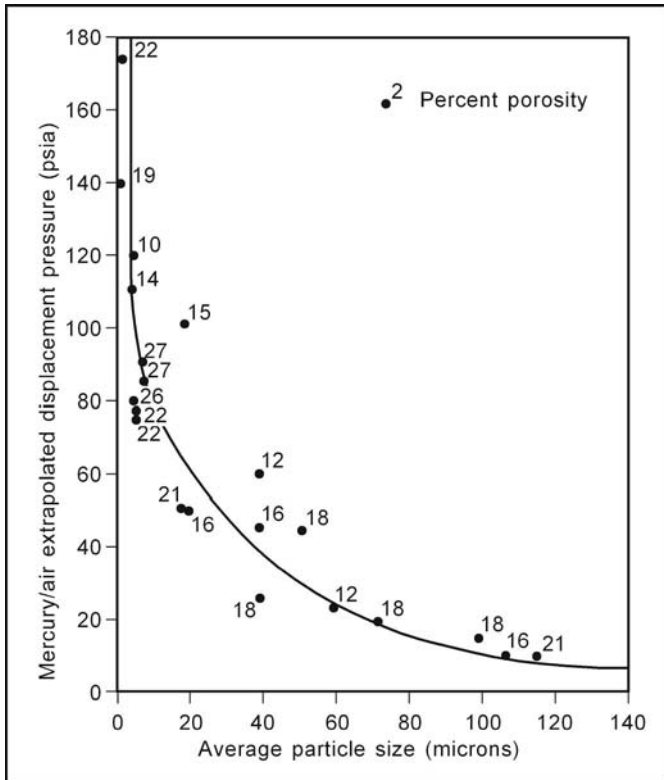
Fig. 2.5. Relationship between mercury displacement pressure and average particle size for nonvuggy carbonate rocks with permeability greater than 0.1 md (Lucia 1983). The displacement pressure is determined by extrapolating the capillary pressure curve to a mercury saturation of zero

dominated; terms meant to emphasize the fabric elements that control pore size (Fig. 4). The important attributes of grain-dominated fabrics are the presence of open or occluded intergrain porosity and a grain-supported texture. The important attribute of mud-dominated fabrics is that the areas between the grains are filled with mud even if the grains appear to form a supporting framework.

Grainstone is clearly a grain-dominated fabric, but Dunham's packstone class bridges a boundary between large intergrain pores in grainstone and small interparticle pores in wackestones and mudstones. Some packstones have both intergrain pore space and mud and some have the intergrain spaces filled with mud. The packstone textural class must be divided into two rock-fabric classes: grain-dominated packstones that have intergrain pore space or
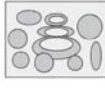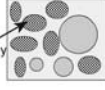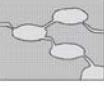
cement and mud-dominated packstones that have intergrain spaces filled with mud (Fig. 4).
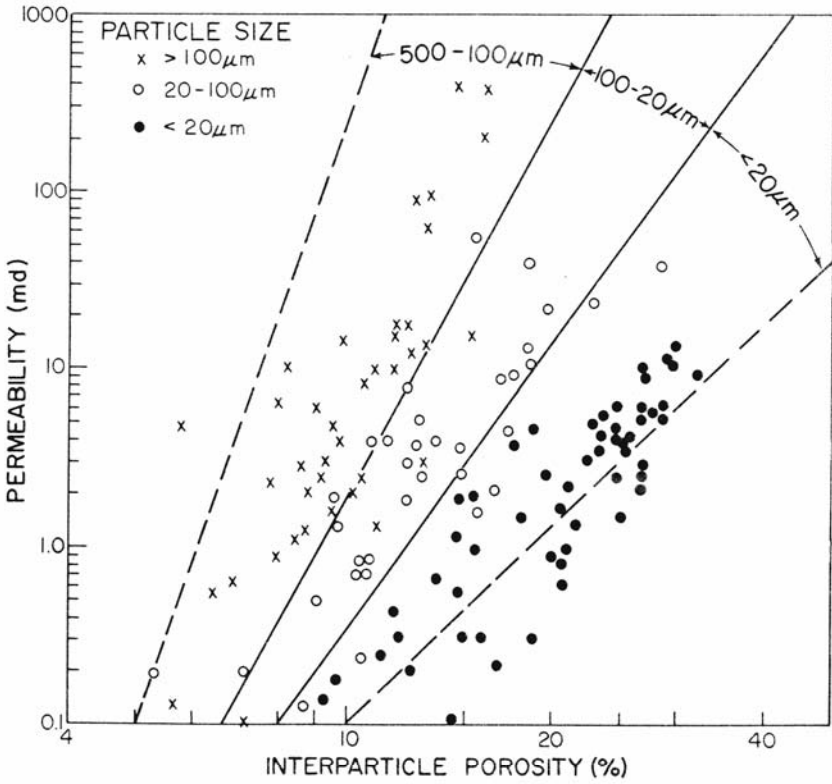
Fig. 2.6. Porosity-air permeability relationship for various particle-size groups in nonvuggy carbonate rocks (Lucia 1983)

2.3.2 Classification of Vuggy Pore Space

The addition of vuggy pore space to interparticle pore space alters the petrophysical characteristics by altering the manner in which the pore space is connected, all pore space being connected in some fashion. Separate vugs are defined as pore space that is interconnected only through interparticle pore space. Touching vugs are defined as pore space that forms an interconnected pore system independent of interparticle pore space (Fig. 7).

Fig. 2.7. Geological/petrophysical classification of vuggy pore space based on vug interconnection. The volume of separate-vug pore space is important for characterizing the pore-size distribution

Separate-Vug Pore Space

Separate-vug pore space is defined as pore space that is 1) either within particles or is significantly larger than the particle size (generally >2x particle size) and 2) interconnected only through interparticle pore space (Fig. 7). Separate vugs are typically fabric-selective in their origin. Intrafossil pore space, such as the living chambers of a gastropod shell; grain molds, such as oomolds or skeletal molds; and intragrain microporosity are examples of intraparticle, fabric-selective separate vugs. Molds of evaporite crystals and fossil-molds found in mud-dominated fabrics are examples of fabric-selective separate vugs that are significantly larger than the particle size. In mud-dominated fabrics, shelter pore space is typically much larger than the particle size and is classified as separate-vug porosity, whereas in grain-dominated fabrics, shelter pore space is related to particle size and is considered intergrain porosity.

In grain-dominated fabrics, crushing of grains with large intragrain pores by overburden pressure may improve the connection between intragrain and intergrain pore space by fracturing the walls of the grains. In the extreme case the grains may be crushed beyond recognition and the distinction between intra- and inter-grain pore space blurred, in which case the grain fragments become particles of diagenetic origin. Similarly, the centers of dolomite crystals may be selectively dissolved and the skeletal dolomite

crystals crushed to form diagenetic particles composed of pieces of dolomite crystals.

Grain-dominated fabrics may contain grains with intragrain microporosity (Pittman 1971, Keith and Pittman, 1983, Moshier et al. 1988). Even though the pore size is small, intragrain microporosity is classified as a type of separate vug because it is located within the particles of the rock. Mud-dominated fabrics may also contain grains with microporosity, but they present no unique petrophysical condition because of the similar pore sizes between the microporosity in the mud matrix and in the grains.

Touching-Vug Pore Space

Touching-vug pore systems are defined as pore space that (1) is significantly larger than the particle size and (2) forms an interconnected pore system of significant extent (Fig. 7). Touching vugs are typically nonfabric selective in origin. Cavernous, collapse breccia, fracture, and solution-enlarged fracture pore types commonly form an interconnected pore system on a reservoir scale and are typical touching-vug pore types. Fenestral pore space is commonly connected on a reservoir scale and is grouped with touching vugs because the pore size is not related to particle size or sorting (Major et al. 1990).

Fracture porosity is included as a touching-vug pore type because fracture porosity is an important contributor to permeability in many carbonate reservoirs and, therefore, must be included in any petrophysical classification of pore space. Although fracturing is often considered to be of tectonic origin, and thus not a part of carbonate geology, diagenetic processes common to carbonate reservoirs, such as karsting (Kerans 1989), can produce extensive fracture porosity. The focus of this classification is on petrophysical properties rather than genesis, and must include fracture porosity as a pore type irrespective of its origin.

2.4 Rock-Fabric/Petrophysical Relationships

2.4.1 Interparticle Porosity/Permeability Relationships

Limestone Rock Fabrics

Examples of limestone rock fabrics with little vuggy pore space are illustrated in Figure 8. In grainstone fabrics (Fig. 8 A, B), the pore-size distribution is controlled by grain size and sorting and by the volume of intergrain cement, which is reflected in the amount of interparticle porosity.
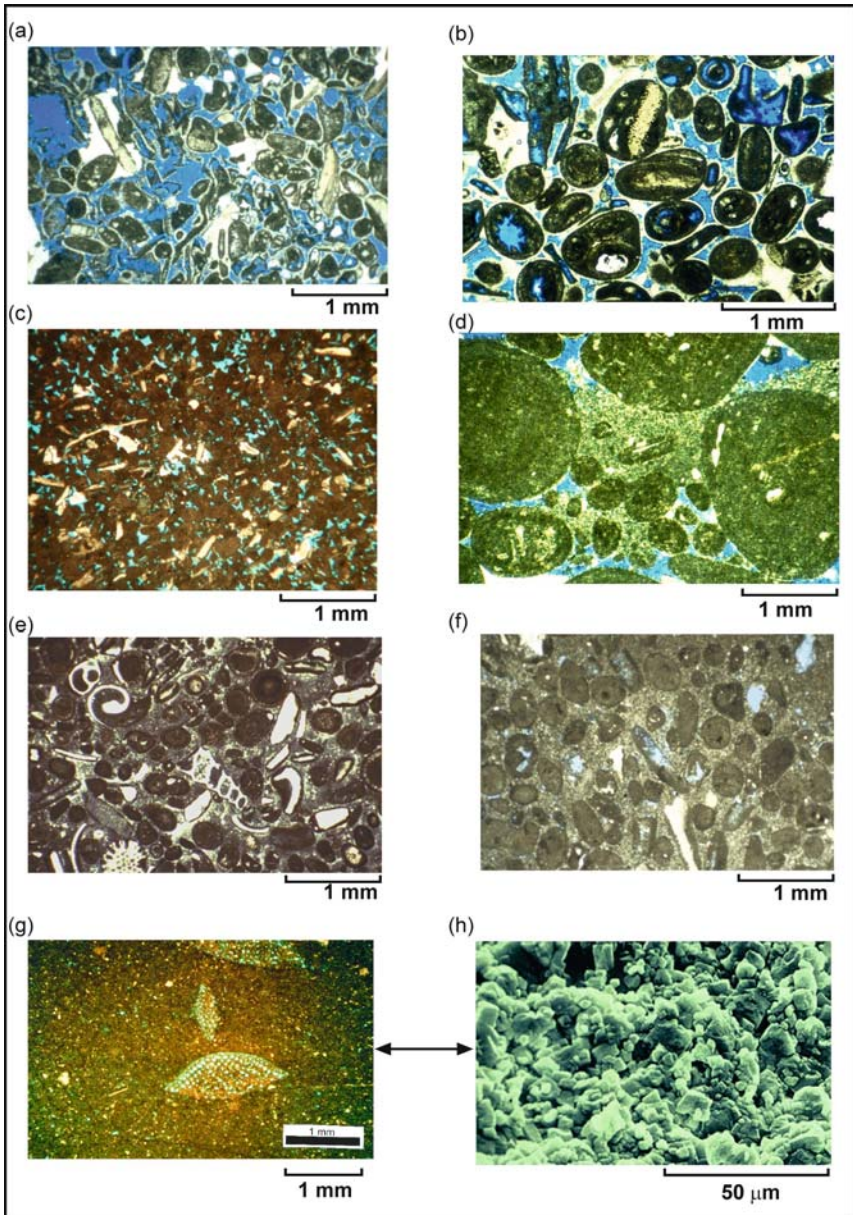
Fig. 2.8. Examples of nonvuggy limestone rock fabrics. **(a)** Grainstone. **(b)** Grainstone with some separate-vug pore space. **(c)** Grain-dominated packstone. **d)** Large grain grain-dominated packstone. **(e)** Mud-dominated packstone. **(f)** Mud-dominated packstone with some separate-vug pore space. **(g)** Wackestone with microporosity. **(h)** Scanning electron microscope photo of microporosity in a wackestone

In grain-dominated packstones the pore-size distribution is controlled by grain size, intergrain cement, and the size and porosity of the intergrain micrite (Fig. 8 C, D).   In mud-dominated packstones, wackestones, and mudstones (Fig. 8 E, F, G), the size of the micrite particles and the amount of interparticle porosity in the mud controls the pore-size distribution.   The small pore size is often referred to as microporosity and is visible with a scanning electron microscope (SEM) (Fig. 8H).

Figure 9a illustrates a cross plot between air permeability and intergrain
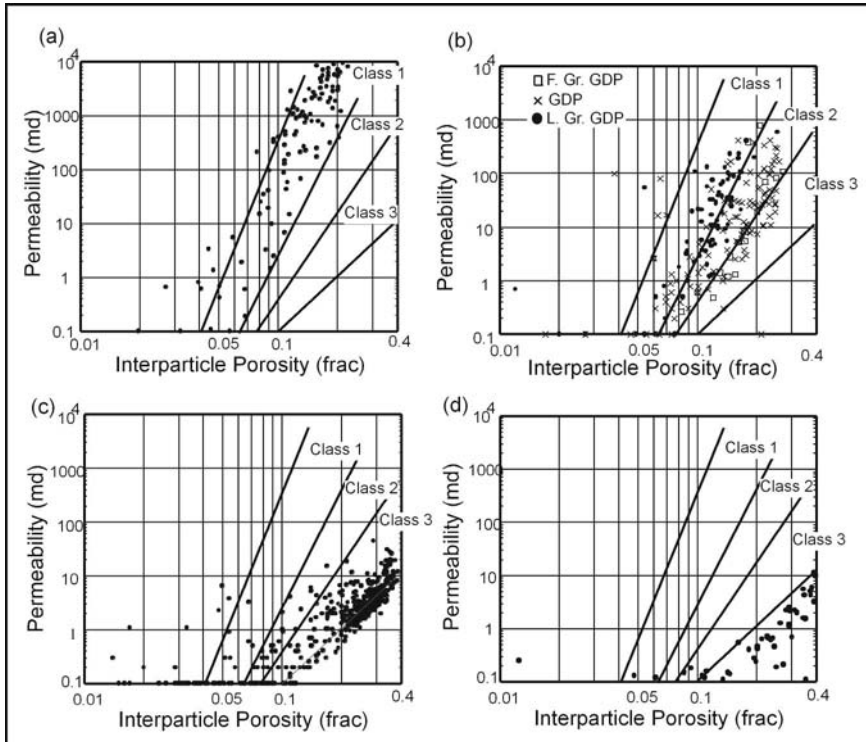
Fig. 2.9. Porosity-air permeability cross plots for nonvuggy limestone rock fabrics compared with the three permeability fields illustrated in Fig. 2.6. **(a)** Mississippian ooid grainstone (Choquette and Steiner 1985) and Jurassic grainstone (Lucia et al. 2001). **(b)** Jurassic peloid grain-dominated packstone (Lucia et al. 2001) Cretaceous oncoid grain-dominated packstone (Cruz, 1997), Wolfcamp peloid grain-dominated packstone (Lucia and Conti 1987). **(c)** Cretaceous wackestones and mudstones (unpublished data, Moshier et al. 1988). **(d)** Coccolith chalk, Cretaceous (Scholle 1977)

porosity for grainstones. The data are from Choquette and Steinem's (1985) publication on the Ste. Genevieve oolite (Mississippian) and from Lucia et

al.'s (2001) publication on the Arab D (Jurassic). The grain size of the oolites ranges from 500 to 200 microns. The points on this graph are concentrated within the >100 micron permeability field. Within the grainstone field the pore size and permeability are reduced in proportion to the decrease in intergrain porosity resulting from cementation and compaction.

Figure 9b illustrates a cross plot of porosity and interparticle porosity for grain-dominated packstones. The data are from Lucia et al. (2001), Lucia and Conti (1987), and Cruz (1997). Data from the Ghawar field (Lucia et al., 2001) plot within the 20-micron to 100-micron permeability field. The fabric is a peloid grain-dominated packstone with a grain size of 150 microns to 300 microns. The volume of intergrain lime mud varies from a few percent to 40 percent of bulk volume. Data reported by Lucia and Conti (1987) from a core of Wolfcamp age in West Texas plot on the boundary between 100- to 20-micron and the <20-micron permeability fields, and are described as a fine-grained grain-dominated packstone with a grain size of 80-100 microns. Data reported by Cruz (1997) for a Cretaceous reservoir, offshore Brazil, are described as an ooid-oncoid grain-dominated packstone. The ooids are 400 microns in diameter, the oncoids 1-2 mm in diameter, and the intergrain lime mud is composed of 5-micron particles. Data from this fabric scatter about the upper limit of the 100-micron to 20-micron permeability field because of the large size of the oncoids. The grain size and volume of intergrain lime mud vary considerably within grain-dominated packstone fabrics and control the location of the data within the 100-micron to 20-micron field. Within the grain-dominated-packstone field the pore size and permeability are reduced in proportion to the decrease in interparticle porosity resulting from cementation and compaction.

Figure 9c illustrates a cross plot between air permeability and interparticle porosity from wackestones, mudstones, and mud-dominated packstones from Arab D reservoirs (Lucia et al. 2001) and unpublished data from Middle East Cretaceous reservoirs. The textures range from mudstone with an average crystal size of about 5 microns to mud-dominated packstone with peloids ranging in size from 80 microns to 300 microns. The data are concentrated in the <20 micron permeability field. The mudstones define the lower limit of this field whereas the mud-dominated packstones define the upper limit. Within the mud-dominated field the pore size and permeability are reduced in proportion to the decrease in interparticle porosity resulting from cementation and compaction.

Figure 9d illustrates a cross plot between air permeability and total porosity for North Sea coccolith chalk (Scholle 1977). The average size of the coccoliths is about 1 micron. The data points plot below the <20-micron

permeability field because the particle size is less than 5 microns, resulting in a much smaller pore size.

Figure 10 illustrates all the data for limestones compared with the permeability fields. Grainstone and mud-dominated wackestones and mud-
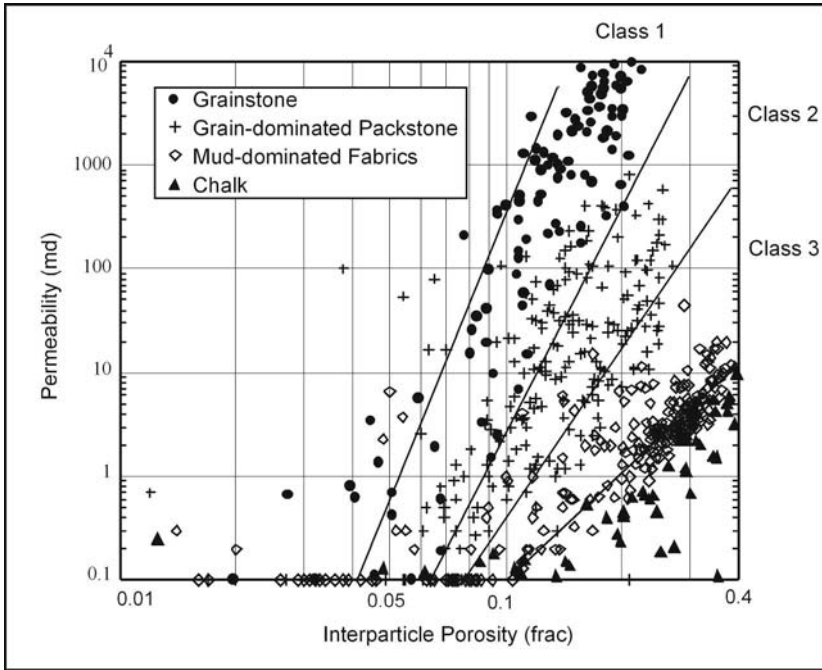
Fig. 2.10. Composite porosity-air permeability cross plot for nonvuggy limestone fabrics compared with the three permeability fields illustrated in Fig. 2.6. The chalk data suggest that an additional porosity-permeability field should be added

stones define reasonably well constrained permeability fields. Grain-dominated packstone fabrics plot at an intermediate location between grainstones and mud-dominated limestones. They overlap with the grainstone field when the grain size is larger than about 500 microns. Grain-dominated packstones tend to overlap with the mud-dominated field when the grains are less than 100 microns and where the distinction between grain-dominated and mud-dominated packstone is not clear. The deep sea chalks plot below the mud-dominated fabrics and define a separate porosity-permeability field.

Despite the considerable scatter in the data, grainstone, grain-dominated packstone, and mud-dominated fabrics are reasonably well constrained to the three permeability fields. Whereas grain size and sorting define the permeability fields, the interparticle porosity defines the permeability within

the field because pore size is related to the volume of interparticle pore space as well as particle size and sorting. Systematic changes in intergrain porosity by cementation, compaction, and dissolution processes will produce systematic changes in the pore-size distribution and result in systematic changes in permeability. Therefore, permeability in limestones with little vuggy porosity is a function of interparticle porosity, grain size, and sorting.

Dolostone Rock Fabrics

Examples of dolostone rock fabrics with little vuggy porosity are illustrated in Figure 11. Dolomitization can change the rock fabric significantly. Limestones fabrics can usually be distinguished with little difficulty. If the rock has been dolomitized, however, the overprint of dolomite crystals often obscures the precursor limestone fabric. Precursor fabrics in fine-crystalline dolostones are easily recognizable. However, as the crystal size increases, the precursor fabrics become progressively more difficult to determine.

Dolomite crystals (defined as particles in this classification) commonly range in size from several microns to >200 microns. Micrite particles are usually <20 microns in size. Thus, dolomitization of a mud-dominated carbonate fabric can result in an increase in particle size from <20 microns to >200 microns and the increase in dolomite crystal size results in a proportional increase in pore size (Fig. 11 E-H). The cross-plot of interparticle-porosity and permeability (Fig. 12a) illustrates the principle that, in mud-dominated fabrics, permeability increases as dolomite crystal size, and resulting pore size, increases. Finely crystalline (average 15 microns) mud-dominated dolostones from Farmer and Taylor Link fields (Lucia and Kerans 1992) in the Permian Basin and from Choquette and Steiner (1985) plot within the <20 micron permeability field. Medium crystalline (average 50 microns) mud-dominated dolostones from the Dune field, Permian Basin (Bebout et al. 1987) plot within the 100- to 20-micron permeability field. Large crystalline dolostones from the Haradh sector of the Ghawar field (Lucia et al. 2001) and large crystalline mud-dominated dolostones from Andrews South Devonian field, Permian Basin (Lucia 1962), plot in the >100-micron permeability field.

Grainstones are usually composed of grains much larger than the dolomite crystal size (Fig. 11 A,B) so that dolomitization does not have a significant effect on the pore-size distribution. This principle is illustrated in Figure 12b, where interparticle porosity and permeability measurements from dolomitized grainstones are cross plotted.   The grain size of the dolograinstones is 200 microns. The finely crystalline dolograinstone from Taylor Link field, Permian Basin, the medium crystalline dolograinstone
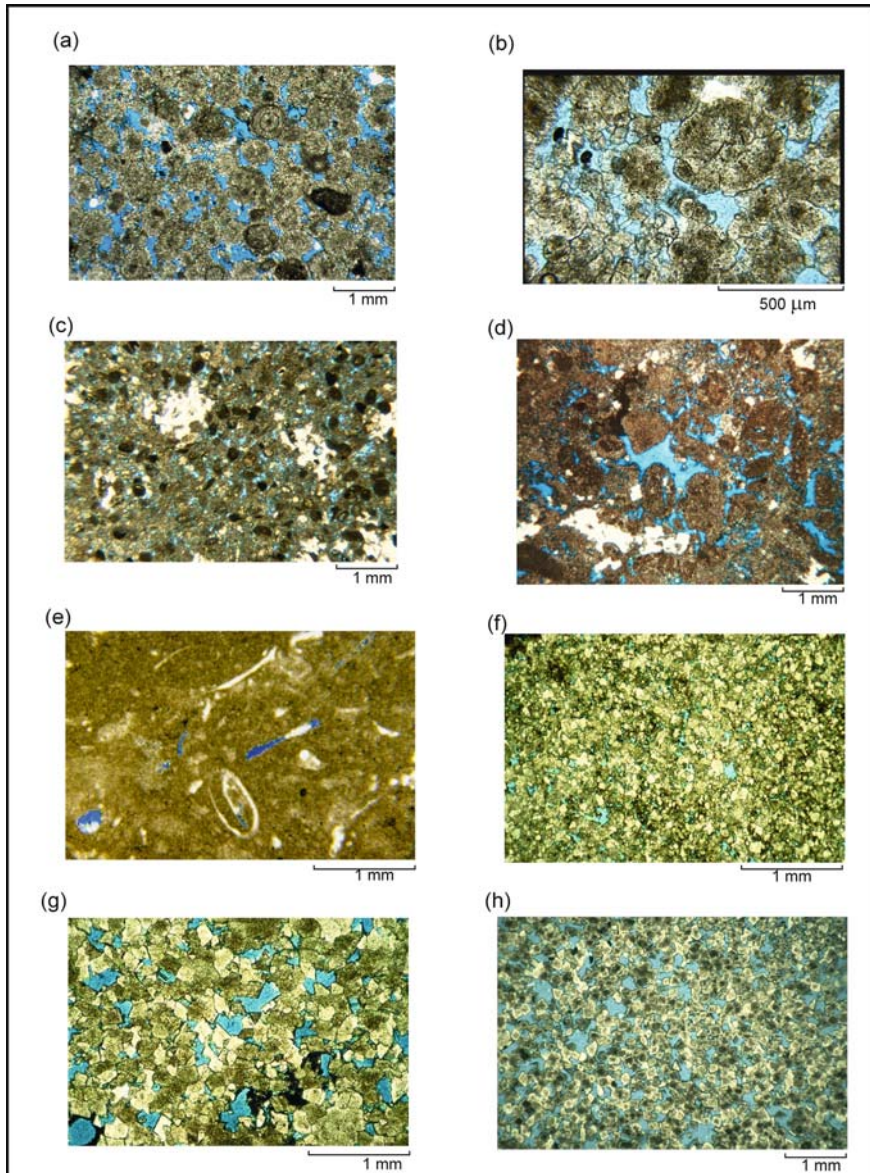
Fig. 2.11. Examples of nonvuggy dolostone fabrics. **(a)** Medium crystalline ooid dolograinstone. **(b** Large crystalline dolograinstone. **(c)** Fine peloid medium crystalline grain-dominated dolopackstone with poikilotopic anhydrite (white). **(d)** Peloid medium crystalline grain-dominated dolopackstone with poikilotopic anhydrite (white). **(e)** Fine crystalline dolowackestone. **(f)** Medium crystalline dolowackestone.   **(g)** Large crystalline dolowackestone. **(h)** Large crystalline dolostone
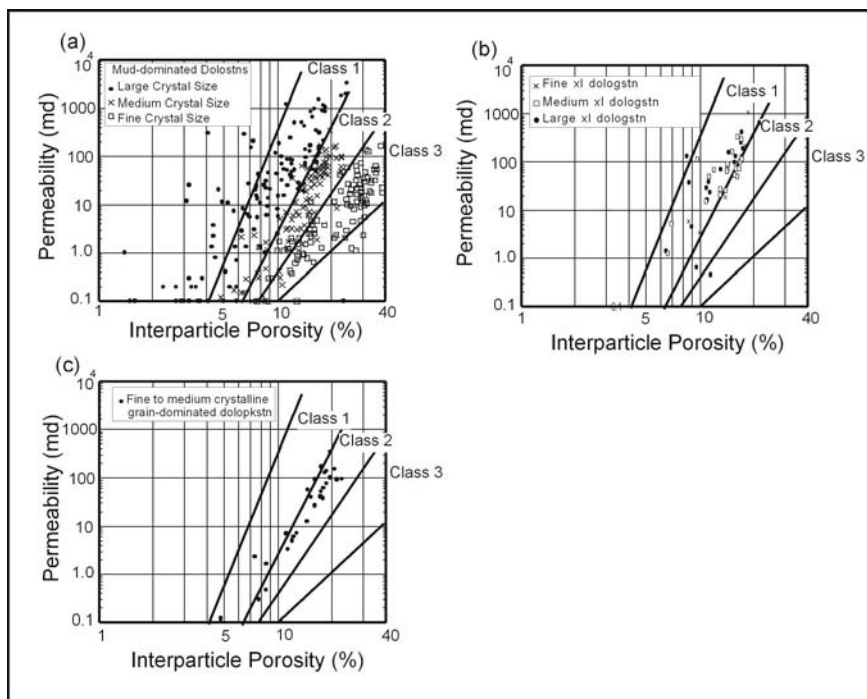
Fig. 2.12. Porosity-air permeability cross plots of nonvuggy dolostone fabrics compared with the three permeability fields illustrated in Fig. 6. **(a)** Mud-dominated dolostones with dolomite crystal sizes ranging from 10 to 500 microns. **(b)** Dolograinstones (average grain size is 200 microns) with dolomite crystal sizes ranging from 15 to 150 microns. **(c)** Grain-dominated dolopackstones with fine to medium dolomite crystal sizes

from Dune field, Permian Basin, and the large crystalline dolograinstone from an outcrop on the Algerita Escarpment, New Mexico, all plot within the >100-micron permeability field.

Interparticle porosity and permeability measurements from fine to medium crystalline grain-dominated dolopackstones are crossplotted in Figure 12c. The average grain size is 200 microns. The samples are from the Seminole San Andres Unit (Wang et al. 1998) and the Dune (Grayburg) field (Bebout et al. 1987), Permian Basin. The data plot in the 100- to 20-micron permeability field.

Figure 13 illustrates all dolomite data compared with permeability fields. Dolograinstones and large crystal dolostones constitute the >100-micron permeability field. Grains are very difficult to recognize in dolostones with >100 micron crystal size. However, because all large crystalline dolostones plot in the >100 micron permeability field, the precursor fabric makes little

difference petrophysically.   Fine and medium crystalline grain-dominated dolopackstones and medium crystalline mud-dominated dolostones constitute the 100- to 20-micron permeability field.   Fine crystalline mud-dominated dolostones constitute the <20-micron field.
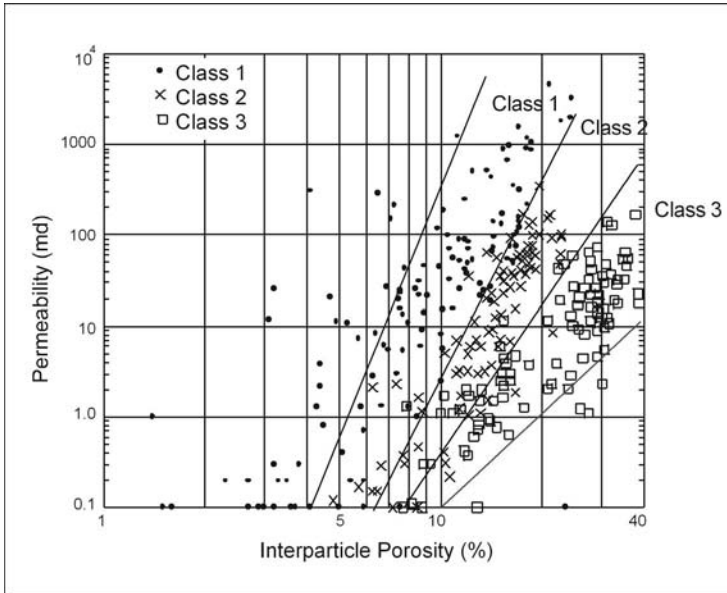
Fig. 2.13. Composite porosity-air permeability cross plot for nonvuggy dolostone fabrics compared with the three permeability fields illustrated in Fig. 6

The dolostone permeability fields are defined by dolomite crystal size as well as by grain size and sorting of the precursor limestone. Within the field, pore size and permeability are defined by interparticle porosity. Systematic changes in intergrain and intercrystal porosity by dolomite cementation and by burial compaction will systematically change the pore-size distribution, resulting in a systematic change in permeability. Therefore, interparticle porosity defines the permeability within the permeability field defined by dolomite crystal size, grain size, and sorting.

Limestone and Dolomite Comparison

Data from limestone and dolomite rock fabrics are combined into one porosity-permeability cross plot in Fig. 14.   The permeability fields are referred to as rock-fabric petrophysical class 1, class 2, and class 3. The class fields are similar to the original permeability fields, but the upper limit of the >100 micron permeability field and the lower limit of the <20 micron field
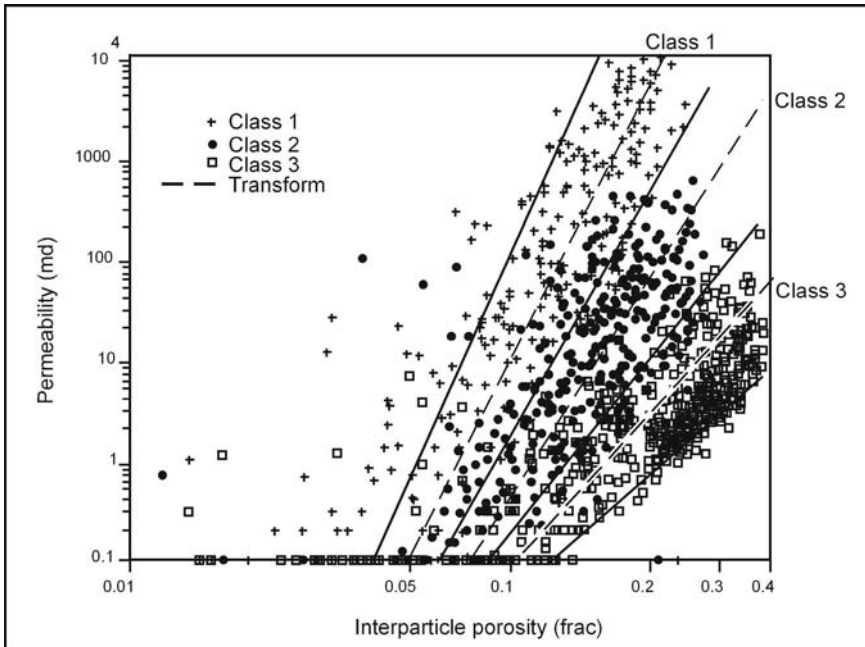
Fig. 2.14. Composite porosity-air permeability cross plot for nonvuggy limestones and dolostones showing statistical reduced-major-axis transforms for each class (dashed lines). See text for equations

had to be moved to accommodate the new data. Three rock fabrics that make up the class 1 field are: (1) grainstones, (2) dolomitized grainstones, and (3) large crystalline dolostones, which may be dolograinstones, grain-dominated dolopackstones or mud-dominated dolostones. In general, grain size and crystal size increase from right to left across this field from 100 microns to 500 microns. The upper particle size limit of 500 microns is not well defined. An upper limit to this permeability field is imposed because as the particle size increases the slope of the porosity-permeability transform approaches infinity and porosity has little relationship to permeability.

Three rock fabrics make up the class 2 field: (1) grain-dominated packstones, (2) fine to medium crystalline grain-dominated dolopackstones, and (3) medium crystalline mud-dominated dolostones. Grain size of the grain-dominated packstones/dolopackstones ranges from 400 to 80 microns. Crystal sizes in the mud-dominated dolostones range from 20 to 100 microns.

Two rock fabrics make up the class 3 field: (1) mud-dominated fabrics (mud-dominated packstone, wackestone, and mudstone) and (2) fine crystalline mud-dominated dolostones. Thin section observations suggest that permeability increases as the grain content increases within this field.

Permeability Estimation

Transforms between permeability and interparticle porosity can be defined for each of the three petrophysical classes. Reduced major axis (RMA) transforms, calculated based on data presented by Lucia (1999), are presented below for each petrophysical class (Fig. 14). Although the new data presented in Fig. 14 suggest slightly different transforms, the original transforms are still useful.

$$\text{Class 1 } k = \left(45.35 \times 10^8\right)\phi_{ip}^{8.537}$$

$$\text{Class 2 } k = \left(2.040 \times 10^6\right)\phi_{ip}^{6.38}$$

$$\text{Class 3 } k = \left(2.884 \times 10^3\right)\phi_{ip}^{4.275}$$

where k is permeability in md and ϕ_{ip} is porosity as a fraction.

Although eight rock fabrics are divided into three petrophysical classes, in nature there is no sharp boundary between the rock fabrics. Instead, there is a continuum of grain size and sorting from mudstone to grainstone, as reflected in the proportion of mud to grains and in grain size (Fig. 15a). Similarly, there is a continuum of dolomite crystal size from 5 μm to 500 μm in mud-dominated dolostones (Fig. 15b). Therefore, there is also a complete continuum of porosity-permeability transforms within the petrophysical class fields.

To model such a continuum the boundaries of each petrophysical class are assigned a value (0.5, 1.5, 2.5, and 4) (Fig. 15c) and porosity-permeability transforms generated. These transforms, together with the three petrophysical-class transforms, were used to develop an equation relating permeability and interparticle porosity to a continuum of petrophysical classes using multiple linear regressions. The continuum of petrophysical classes is called *rock-fabric numbers (rfn)*. The resulting global transform is given below (Lucia et al. 2001; Jennings and Lucia 2003).

$$Log(k) = \left(A - BLog(rfn)\right) + \left(\left(C - DLog(rfn)\right)Log\left(\phi_{ip}\right)\right)$$

where $A = 9.7982$, $B = 12.0838$, $C = 8.6711$, $D = 8.2965$ and rfn is the rock fabric number ranging from 0.5 – 4, and ϕ_{ip} is the fractional interparticle porosity.

Mud-dominated limestones and fine crystalline mud-dominated dolostones occupy rfn's from 4 to 2.5 (Fig. 15c). The rfn decreases with
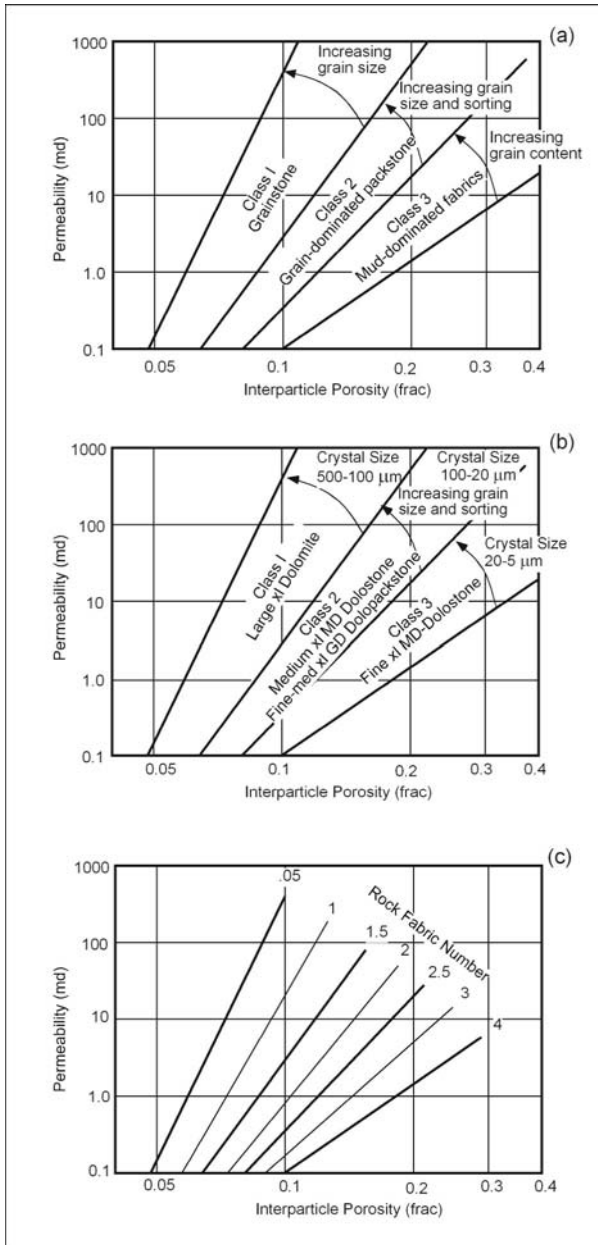
Fig. 2.15. Continuum of rock fabrics and associated porosity-permeability transforms. **(a)** Fabric continuum in nonvuggy limestone. **(b)** Fabric continuum in nonvuggy dolostone. **(c)** Rock-fabric numbers ranging from 0.5 - 4 defined by class-average and class-boundary porosity-permeability transforms

increasing dolomite crystal size from 5 to 20 microns in mud-dominated dolostones and with increasing grains in mud-dominated limestones. Grain-dominated packstones, fine-to-medium crystalline grain-dominated dolopackstones, and medium crystalline mud-dominated dolostones occupy rfn's from 2.5 to 1.5 (Fig. 15c). The rfn's decrease with increasing dolomite crystal size from 20 to 100 microns in mud-dominated dolostones and with increasing grain size and decreasing amounts of intergrain micrite. Grainstones, dolograinstones, and large crystalline dolomites occupy rfn's 1.5 to 0.5 (Fig. 15c). The rfn's decrease with increasing grain size and dolomite crystal size from 100 microns to 500 microns.

As discussed in Chapter 1, Pittman (1992) and Winland (Kolodizie 1980) have published petrophysical relationships between interparticle porosity, permeability, and capillary pressure, principally for siliciclastics, but applied to carbonates as well. They conclude that pore-throat size measured at 35% mercury saturation gives the best relationship to porosity and permeability, and Pittman's equation (1992) is presented below.

$$Log(R35) = 0.255 + 0.565log(k) - 0.523log(\phi)$$

where R35 is the pore-throat size calculated at 35% mercury saturation, k is permeability in md, and ϕ is porosity. Because the published data are from siliciclastics, porosity is best considered as interparticle porosity.

The above equation is plotted in Figure 16 and compared with the petrophysical-class fields described in this report.   It is apparent that Pittman's relationship between pore-throat size, porosity, and permeability does not conform to the petrophysical classes defined in this classification. It is also apparent that, within a petrophysical class, pore-throat size decreases as interparticle porosity decreases. The eight basic rock fabrics defined here are constrained to specific petrophysical-class fields and not to a specific pore-throat size. Therefore, *there is no direct link between pore size and rock fabrics in carbonate rocks*.

2.4.2 Rock-Fabric/Porosity/Water Saturation Relationships

As stated in Chapter 1, fluid saturations are related to pore-throat size and capillary pressure (reservoir height). Several methods have been proposed for relating pore size, water saturation and reservoir height (Leverett 1941; Aufricht et al. 1957; Heseldin 1974; Alger et al. 1989). These methods equate pore size with the ratio of permeability and porosity (k/ϕ) and attempt to average the capillary pressure curves into one relationship by using k/ϕ as normalizing parameter. The Leverett "J" function is a common method of
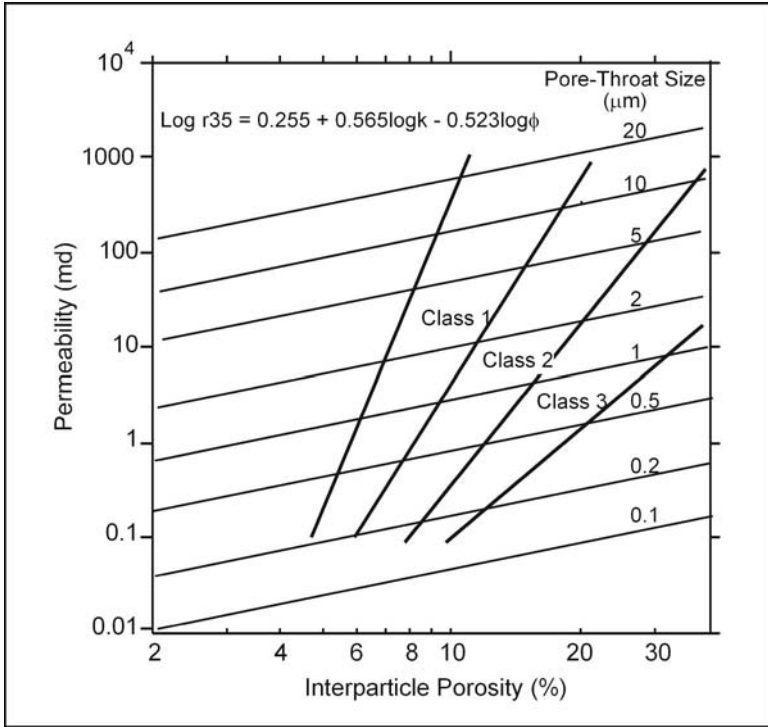
Fig. 2.16. Comparison of petrophysical-class fields and pore-throat sizes versus interparticle porosity and permeability

averaging capillary pressure data. A common form of the J function is given below.

$$J(Sw) = \left(\frac{Pc}{\sigma}\right)\left(\frac{k}{\phi}\right)^{\frac{1}{2}}$$

where Pc = capillary pressure in psia, σ = interfacial tension in dynes/cm, k = permeability in md, and ϕ = fractional porosity.

The Leverett J function relates water saturation to capillary pressure, which is a function of reservoir height, and $(k/\phi)^{1/2}$, which is a function of pore size. Figure 16 suggests that pore size can be related to petrophysical class and interparticle porosity as well as to $(k/\phi)^{1/2}$. Therefore, changes in interparticle porosity within each petrophysical field represent a change in pore size, and water saturation should be related to reservoir height (H), porosity (ϕ), and petrophysical class (PC).

$$Sw = f(H, \phi, PC)$$

These equations are not suitable for carbonates with large volumes of vuggy porosity, such as moldic grainstones or grain-dominated fabrics with extensive intragrain microporosity.

To quantify the saturation characteristics of the three petrophysical classes, a suite of capillary pressure curves was collected from each petrophysical class with varying values for porosity. The data includes limestones and dolostones. Curves for each class were grouped into porosity bins, and average porosity was calculated. Mercury saturation values were averaged for each injection pressure, and plots of reservoir height (capillary pressure), mercury saturation, and porosity were constructed for each class. Injection pressure was converted to reservoir height using generic values and the equations described in Chapter 1. Equations relating water saturation to porosity and reservoir height were developed using a multiple linear regression with the log of water saturation as the dependent variable and the logs of capillary pressure and porosity as independent variables. The water saturation described by these equations is the initial, or original, water saturation assuming a reservoir in drainage, not imbition, mode.

The resulting equations are listed below and illustrated in Figure 17.

Class 1: $Sw_i = 0.02219 \times H^{-0.316} \times \phi^{-1.745}$

Class 2: $Sw_i = 0.1404 \times H^{-0.4.07} \times \phi^{-1.440}$

Class 3: $Sw_i = 0.6110 \times H^{-0.505} \times \phi^{-1.210}$

where Sw_i is the initial fractional water saturation, H is reservoir height in feet, and ϕ is fractional porosity (mostly interparticle). Reservoir height can be converted to capillary pressure by $CP = H/0.7888$.

A fourth equation developed for rfn-4 fabrics using data from the Cretaceous Shuaiba formation in the Middle East is presented below.

Rfn 4 $Sw_i = 5 \times H^{-0.7} \times \phi^{-1.0}$

The relationship between porosity, initial water saturation and petrophysical class can be demonstrated by selecting a reservoir height of 500 ft (equates to a mercury capillary pressure of about 650 psia) and plotting saturation against porosity for each petrophysical class. The results (Fig. 18) show that, in carbonates with little vuggy porosity, a plot of porosity versus water saturation can separate the three petrophysical classes into saturation
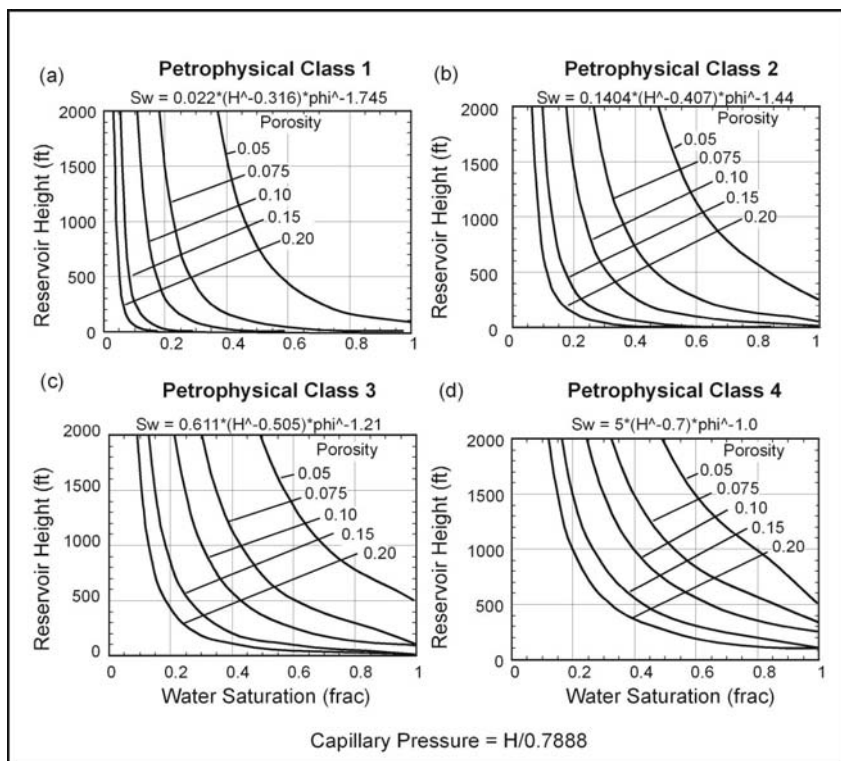
Fig. 2.17. Initial water saturation models based on capillary pressure data for specific petrophysical classes. **(a)** Class 1 saturation model based on data from dolograinstones. **(b)** Class 2 saturation model based on data from medium crystalline dolowackestones. **(c)** Class 3 saturation model based on data from fine crystalline dolowackestones. **(d)** Class 4 saturation model based on data from microcrystalline mudstones and wackestones from Shuaiba reservoirs in the Middle East

fields similar to permeability fields. *This observation confirms the premise that both permeability and fluid saturations are controlled by pore-size distribution and that pore-size distribution can be described by rock fabric descriptions and porosity in carbonates with little vuggy porosity.*

2.4.3 Rock-Fabric/Petrophysical Classes

Three rock fabric groups define the three petrophysical classes. Figure 19 illustrates the relationship between rock fabric and petrophysical classes. Grainstones, dolograinstones, and large crystalline dolostones all have similar petrophysical properties that are characterized by petrophysical class 1. Grain-dominated packstones, fine and medium crystalline grain-dominated
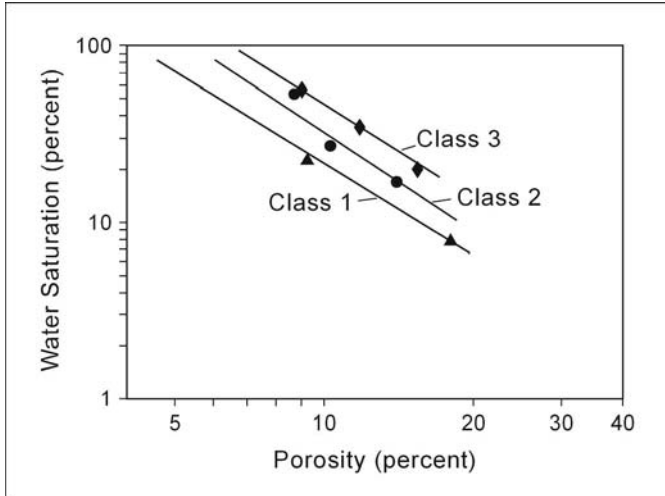
Fig. 2.18. Cross plot of porosity and water saturation for the three rock-fabric petrophysical classes at a reservoir height of 150 m (500 ft). Water saturation (1-Hg saturation) and porosity values are taken from capillary pressure curves illustrated in Fig. 2.17
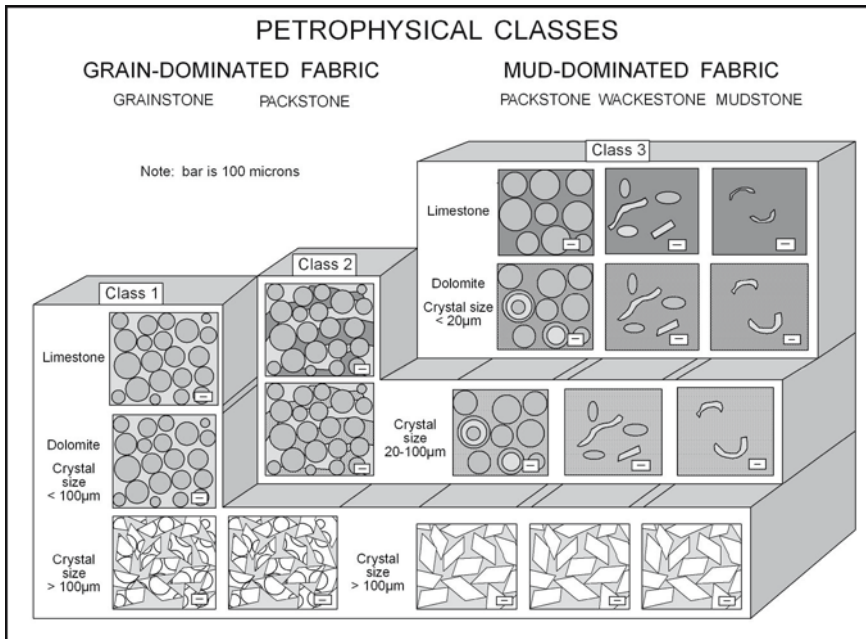
Fig. 2.19. A block diagram illustrating the relationship between rock fabrics and petrophysical classes. There are three rock fabrics in class 1, three rock fabrics in class 2, and two rock fabrics in class 3

dolopackstones, and medium crystalline mud-dominated dolostones all have similar petrophysical properties that are characterized by petrophysical class 2. Mud-dominated limestones (mud-dominated packstone, wackestone, and mudstone) and fine crystalline mud-dominated dolostones all have similar petrophysical properties that are characterized by petrophysical class 3. The equations relating porosity, permeability, water saturation, and reservoir height (capillary pressure) are summarized below.

Class 1

$$k = \left(45.35 \times 10^8\right)\phi_{ip}^{8.537}$$

$$Sw_i = 0.02219 \times H^{-0.316} \times \phi^{-1.745}$$

Class 2

$$k = \left(2.040 \times 10^6\right)\phi_{ip}^{6.38}$$

$$Sw_i = 0.1404 \times H^{-0.4.07} \times \phi^{-1.440}$$

Class 3

$$k = \left(2.884 \times 10^3\right)\phi_{ip}^{4.275}$$

$$Sw_i = 0.6110 \times H^{-0.505} \times \phi^{-1.210}$$

Global permeability transform

$$Log(k) = \left(A - BLog(rfn)\right) + \left(\left(C - DLog(rfn)\right)Log\left(\phi_{ip}\right)\right)$$

2.4.4 Petrophysics of Separate-Vug Pore Space

The addition of separate-vug porosity to interparticle porosity alters the petrophysical characteristics by altering the manner in which pore space is connected, all pore space being connected at some level.   Examples of separate-vug pore space are illustrated in Figure 20. Separate vugs are not connected to each other. They are connected only through the interparticle pore space and, although the addition of separate vugs increases total porosity, it does not significantly increase permeability (Lucia 1983). Figure 21a illustrates this principle. Permeability of a moldic grainstone is less than would be expected if all the total porosity were interparticle and, at constant porosity, permeability increases with decreasing separate-vug porosity (Lucia and Conti 1987).   The same is true for a large crystalline dolowackestone (Fig. 21b) in that the data plot to the left of the class 1 field in proportion to the separate-vug porosity (Lucia 1983). The same principle is illustrated by
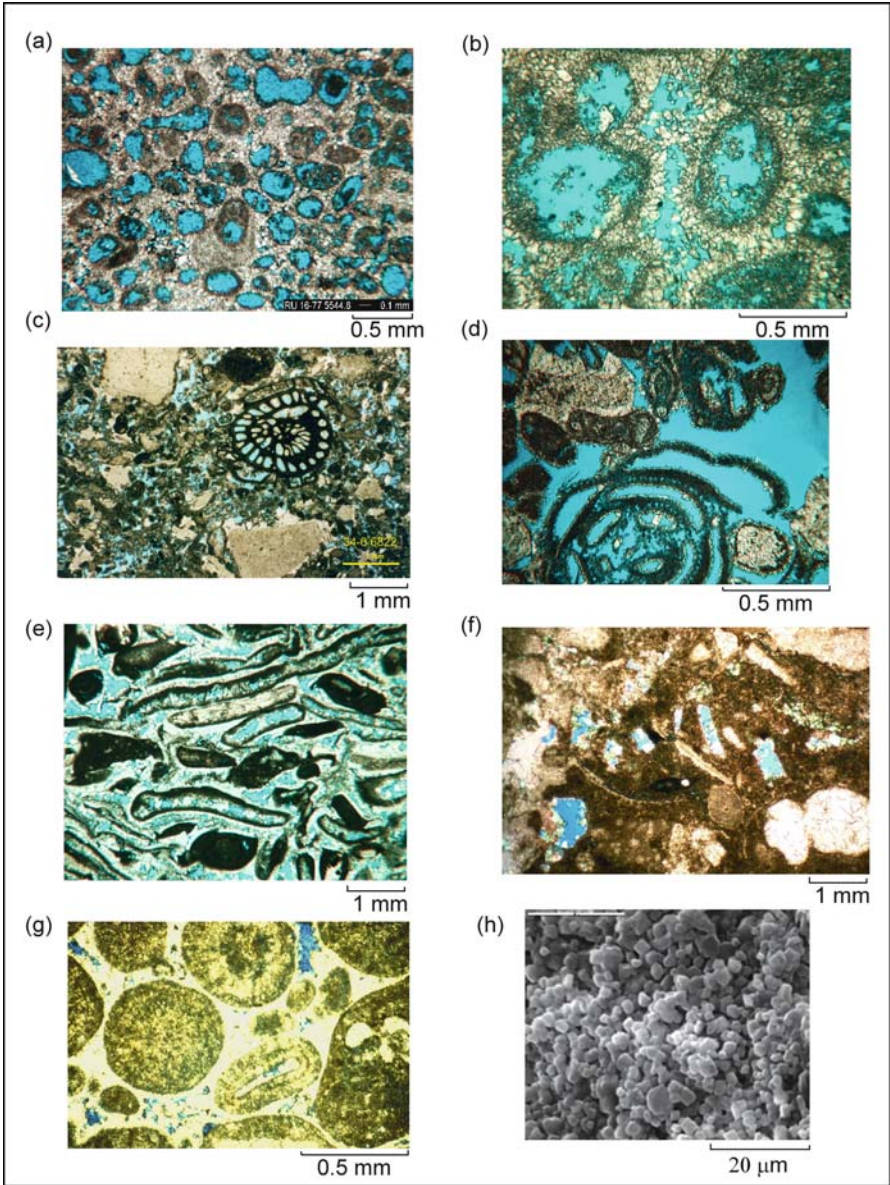
Fig. 2.20. Examples of separate-vug pore types. **(a)** Oomolds in oomoldic grainstone. **(b)** Oomolds and intergrain pore space in a grainstone. **(c)** Intrafossil pore space in a fusulinid grain-dominated packstone. **(d)** Intrafossil pore space in a foram with a large opening to interparticle pore space. **(e)** Skeletal grain molds in moldic skeletal grainstone. **(f)** Grain molds in a wackestone. **(g)** Ooid grainstone with intragrain microporosity. **(h)** Scanning electron photomicrograph of intragrain microporosity showing micropores in a 5-micron rhombic calcite matrix
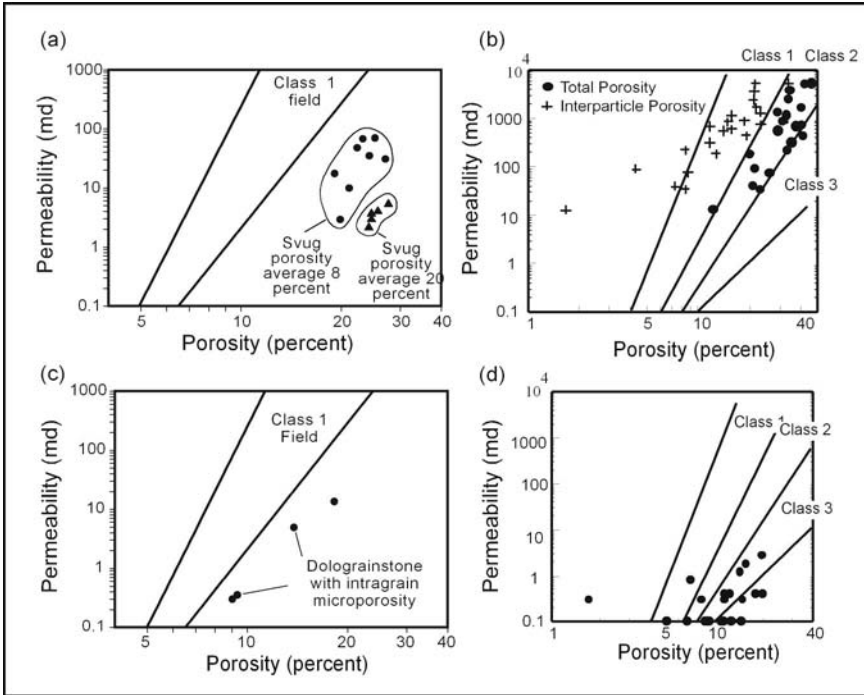
Fig. 2.21. Cross plot illustrating the effect of separate-vug porosity on air permeability. **(a)** Grainstones with separate-vug porosity in the form of grain molds plot to the right of the grainstone field in proportion to the volume of separate-vug porosity. **(b)** Grainstones with intrafossil and intragrain microporosity plot in the class 2 field when plotted against total porosity. **(c)** Dolograinstones with intragrain microporosity plot in the class 2 field. **(d)** Grainstones with intragrain microporosity plot in the class 3 field

data from an Eocene grainstone described by Budd (2002). Interparticle porosity is estimated from thin section by detailed point counts. The data plots in the class 1 field when interparticle porosity is used and in the class 2 field when total porosity is used (Fig. 21c). In this example, total porosity includes intrafossil, intragrain microporosity, and intergrain pore types. An ooid grainstone from a Cretaceous reservoir, offshore Brazil (Cruz 1997) is composed of some intergrain porosity and considerable intragrain microporosity (Fig. 21d). The data plot in the class 3 field and below because intergrain porosity is very low.

Initial water saturation in carbonates with separate vugs depends upon the interparticle pore size and, in grain-dominated fabrics, the size of the pores connecting the separate-vug and interparticle pore space. The pores in intragrain microporosity are small, and the connection to interparticle pore

space is always through microporosity. Grain molds and intrafossil vugs are usually large and the connection depends upon the size of the pore space in the rim surrounding the grain mold or fossil chamber. Pore spaces within gastropods and forams are usually large and have some large openings to the intergrain pore space. Grain molds, such as oomolds, are normally rimmed by microporosity, unless the grains have been dolomitized, in which case the rimming pore size will depend upon the dolomite crystal size. Overburden crushing of grains can produce microfractures that enhance the connection between grain molds and interparticle pores.

An example drainage capillary pressure curve from an oomoldic limestone (Fig. 22a) shows that the pores connecting the grain molds to the
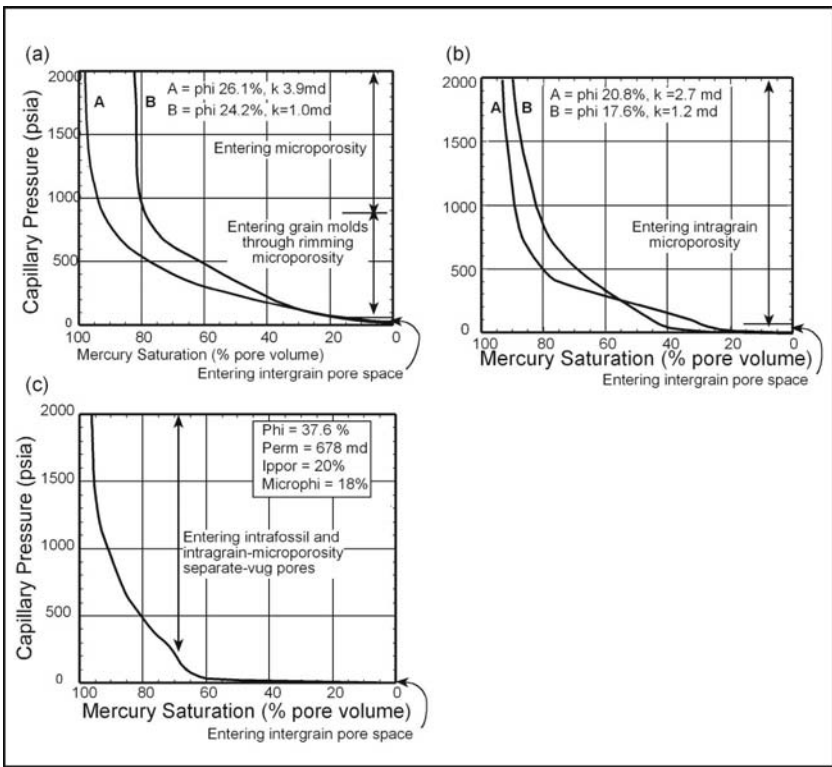
Fig. 2.22. Capillary pressure curves illustrating the effect of separate vugs on capillary properties. (a) High-porosity, low-permeability oomoldic grainstone with little intergrain pore space. Most of the curve reflects entry into the large oomolds through micro pores lining the oomolds. (b) High-porosity, low- permeability ooid grainstone with intragrain microporosity. Most of the curve reflects entry into the micropores located within the grains. (c) Grainstone with a high intergrain porosity

interparticle pores are very small. However, once a capillary pressure (reservoir height) is obtained that will force oil into the molds, the molds rapidly become oil saturated. Within the transition zone the oil will be concentrated in the interparticle pores and grain molds with water saturation concentrated in the small connecting pores.

The distribution of initial water saturation in intragrain microporosity is different because of small pore sizes. Example capillary pressure curves from grainstones with significant amounts of intragrain microporosity (Fig. 22b) show that considerable amounts of water can be trapped water within the grains by capillary forces within the transition zone. Initial oil saturation is concentrated in the intergrain pore spaces, and water is concentrated in the intragrain microporosity. Within the transition zone, this fabric will be characterized by high initial water saturation trapped by capillary forces within the grains and producible hydrocarbons in the intergrain porosity. This results in the possibility of having water-free production in an interval that calculates high water saturation (Pittman 1971; Dixon and Marek 1990).

An example capillary pressure curve from a grainstone with intergrain porosity, intragrain microporosity, and crushed intrafossil pores shows little effect of the intrafossil porosity on initial water saturation because it is connected to the intergrain pores by microfractures and large openings typical of gastropods and forams. The water is trapped primarily in the intragrain microporosity (Fig. 22c).

2.4.5 Petrophysics of Touching-Vug Pore Space

Examples of touching-vug pore types are illustrated in Figure 23 and have little relationship to rock fabrics. Touching vugs can increase permeability well above what would be expected from the interparticle pore system. Lucia (1983) illustrated this fact by comparing a plot of fracture permeability versus fracture porosity to the three petrophysical fields (Fig. 24). This graph shows that permeability in touching-vug pore systems cannot be characterized by rock fabrics or petrophysical classes.

Estimating the permeability of touching-vug systems is difficult because the pores are often larger than the well bore. The best information about flow properties comes from production data. In general, core measurements are not meaningful because of the large size of most touching-vug systems. The core analysis of the cavernous core from northern Michigan (Fig. 23A) reports a permeability < 0.1 md, which is clearly not a useful value. However, the permeability of small touching-vug fabrics composed of micro-fractures and grain molds can be measured by routine methods. Porosity-permeability cross-plots f rom two microfracture fabrics are illustrated in
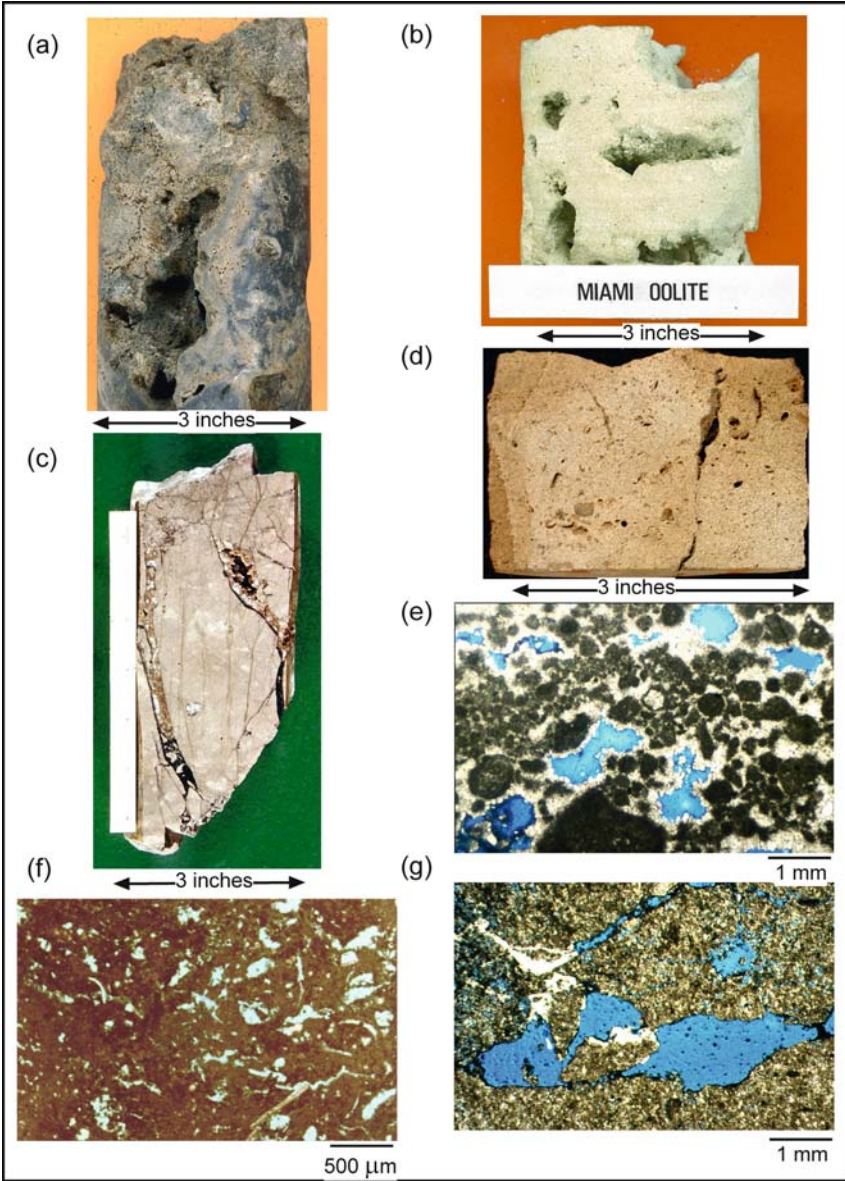
Fig. 2.23. Touching-vug pore types: **(a)** Cavernous pore space in a Niagaran reef, northern Michigan. **(b)** Cavernous pore space in Miami oolite, Florida. **(c)** Solution-enlarged fractures with saddle dolomite, Ellenburger, West Texas. **(d)** Solution-enlarged fracture, Permian, West Texas. **(e)** Fenestral pore space, Permian, West Texas. **(f)** Microfractures connecting grain molds in a wackestone, Cretaceous, Qatar. **(g)** Microfracturing and collapse of a fusumold, Permian, West Texas

Figure 25 and suggest a permeability enhancement of 5x to 10x over what would be expected from a simple interparticle pore system (Lucia and Ruppel 1996).
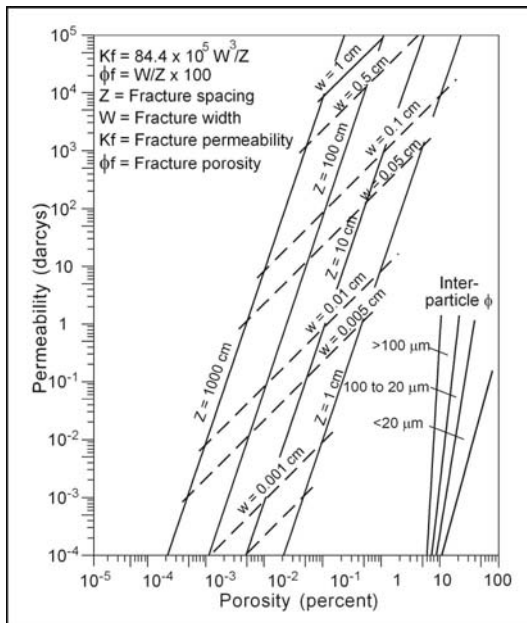
Fig. 2.24. Theoretical fracture air permeability-porosity relationship compared to the rock-fabric/petrophysical porosity, permeability fields (Lucia 1983). W = fracture width, Z = fracture spacing
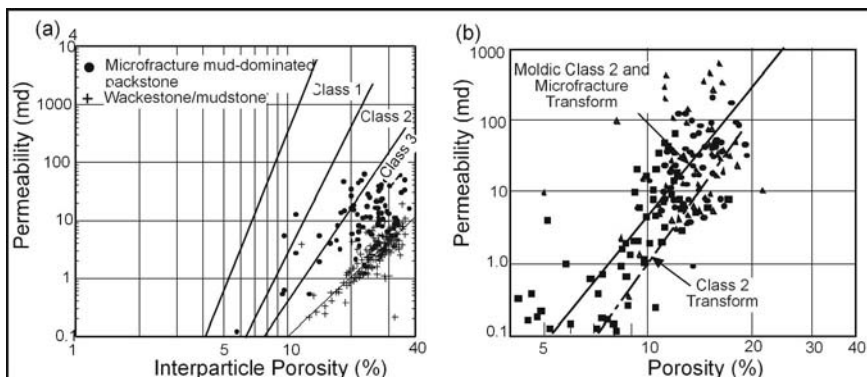
Fig. 2.25. Illustrations of permeability enhancement due to microfractures. **(a)** A factor of 5 permeability enhancement due to microfracturing of a mud-dominated limestone. **(b)** A factor of 5 permeability enhancement in a class 2 medium crystalline dolowackestone due to microfractures connecting fusumolds

There is no hard data on saturation characteristics of large touching vugs. It is thought that large touching vugs most likely have initial water saturations near zero. The initial water saturation of the microfracture fabrics, however, is probably similar to matrix saturation values because the microfractures occupy a small percentage of the pore volume.

2.5 Summary

The goal of reservoir characterization is to describe the spatial distribution of petrophysical parameters such as porosity, permeability, and saturation. In Chapter 1 we showed that permeability and water saturation are controlled by pore size. The rock fabric approach presented here is based on the premise that pore size and pore-size distribution can be expressed in terms of particle size, sorting, interparticle porosity, and separate vug porosity. Therefore, pore-size distribution is related to rock fabric, a product of geologic processes. Thus, rock fabric integrates geologic interpretation with engineering numerical measurements.

To determine the relationships between rock fabric and petrophysical parameters it is necessary to define and classify pore space as it exists today in terms of petrophysical properties. This is best accomplished by dividing pore space into pore space located between grains or crystals, called interparticle porosity, and all other pore space, called vuggy porosity. Vuggy pore space is further subdivided into two groups based on how the vugs are interconnected: (1) vugs that are interconnected only through the interparticle pore network are termed *separate vugs* and (2) vugs that are in direct contact with each other are termed *touching vugs*.

The petrophysical properties of interparticle porosity are related to particle size, sorting and interparticle porosity. Grain size and sorting of grains and micrite is based on Dunham's classification, modified to make it compatible with petrophysical considerations. Instead of dividing fabrics into grain support and mud support, fabrics are divided into grain-dominated and mud-dominated. The important attributes of grain-dominated fabrics are the presence of open or occluded intergrain porosity and a grain-supported texture. The important attribute of mud-dominated fabrics is that the volume between the grains is filled with mud even if the grains appear to form a supporting framework.

Grainstone is clearly a grain-dominated fabric, but Dunham's packstone class bridges an important petrophysical boundary. Some packstones, as we see them now, have intergrain pore space, and some have the intergrain spaces filled with mud. Therefore, the packstone textural class must be

divided into two rock-fabric classes: grain-dominated packstones that have intergrain pore space or cement as well as intergrain mud, and mud-dominated packstones where the intergrain spaces are filled with mud.

The important fabric elements to recognize for petrophysical classification of dolomites are precursor grain size and sorting, dolomite crystal size, and intergrain/intercrystal porosity. Important dolomite crystal size boundaries are 20 and 100 microns. Dolomite crystal size has little effect on the petrophysical properties of grain-dominated dolostones. The petrophysical properties of mud-dominated dolostones, however, are significantly improved when the dolomite crystal size is >20 microns.

Permeability and saturation characteristics of interparticle porosity can be grouped into three rock-fabric/petrophysical classes. Class 1 is composed of grainstones, dolograinstones, and large crystalline dolostones. Class 2 is composed of grain-dominated packstones, fine to medium crystalline grain-dominated dolopackstones, and medium crystalline mud-dominated dolostones. Class 3 is composed of mud-dominated limestone and fine crystalline mud-dominated dolostones.

Generic permeability transforms and initial water saturation, porosity, reservoir-height equations for each rock-fabric/petrophysical class are presented below. The Sw_i equations are valid only when little vuggy porosity is present.

Class 1 - Grainstones, dolograinstones, and large crystalline dolostones.

$$k = \left(45.35 \times 10^8\right)\phi_{ip}^{8.537}$$
$$Sw_i = 0.02219 \times H^{-0.316} \times \phi^{-1.745}$$

Class 2 - Grain-dominated packstones, fine and medium crystalline grain-dominated dolopackstones, and medium crystal mud-dominated dolostones.

$$k = \left(2.040 \times 10^6\right)\phi_{ip}^{6.38}$$
$$Sw_i = 0.1404 \times H^{-0.4.07} \times \phi^{-1.440}$$

Class 3 - Mud-dominated limestones and fine crystalline mud-dominated dolostones.

$$k = \left(2.884 \times 10^3\right)\phi_{ip}^{4.275}$$
$$Sw_i = 0.6110 \times H^{-0.505} \times \phi^{-1.210}$$

The three permeability transforms together with transforms describing the boundary of the petrophysical classes are combined into a global porosity-permeability transform presented below. Petrophysical class is replaced with a continuum of rock-fabric numbers (rfn).

$$Log(k) = (A - BLog(rfn)) + ((C - DLog(rfn))Log(\phi_{ip}))$$

where A = 9.7982, B = 12.0838, C = 8.6711, D = 8.2965 and rfn is the rock fabric number ranging from 0.5 – 4, and ϕ_{ip} is the fractional interparticle porosity.

The addition of separate-vug porosity to interparticle porosity increases total porosity but does not significantly increase permeability. Therefore, it is important to determine interparticle porosity by subtracting separate-vug porosity from total porosity and using interparticle porosity to estimate permeability. The effect of separate vugs on permeability and initial water saturation depends upon the size of the pores connecting the intra- and intergrain pore space.

Large separate vugs are normally filled with hydrocarbons above the transition zone. Intragrain microporosity will contain significant amounts of capillary-bound water within the transition zone, resulting in water-free production of hydrocarbons from intervals with high initial water saturations. The transition zone for grainstones with large volumes of separate vugs will be greater than that expected for a nonvuggy grainstone.

Touching-vug pore systems cannot be related to porosity but are related to the geometry of fracture pore space, large vugs, and collapse breccia. These pore systems are normally larger than the well bore and cannot be adequately studied using cores. Small touching-vug systems formed by microfractures and grain dissolution connecting grain molds can be characterized by core measurements. These systems enhance permeability 5x to 10x over that expected from matrix permeability.

The key to constructing a geologic model that can be quantified in petrophysical terms is to select facies or units that have unique petrophysical qualities for mapping. In non-touching vug reservoirs (matrix reservoirs), the most important fabric elements to describe and map are 1) grain size and sorting using the modified Dunham classification, 2) dolomite crystal size using 20 and 100 microns as size boundaries, 3) interparticle porosity, 4) separate-vug type with special attention to intragrain microporosity, and 5) separate-vug porosity.

In touching-vug reservoirs, characterizing the pore system is difficult because the pore system is not related to a precursor depositional fabric but is usually wholly diagenetic in nature. Whereas it may conform to bedding, as

in the case of evaporite collapse brecciation and associated fractures, it more often cuts across strata. However, recognition of the presence of a touching-vug pore system is paramount because it may dominate the flow characteristics of the reservoir.

Three basic steps in predicting the spatial distribution of petrophysical properties are 1) developing predictable models relating rock fabrics to petrophysical properties as described in this chapter, 2) describing the one-dimensional distribution of rock fabrics and petrophysical properties from core and wireline log data, and 3) extrapolating this information in three dimensions using geologic processes and stratigraphic principles. In the next chapter we will discuss describing rock fabrics and petrophysical properties in one dimension using core and wireline log data.

References

Alger RP, Luffel DL, Truman RB 1989 New unified method of integrating core capillary pressure data with well logs. Society of Petroleum Engineers Formation Evaluation 4, 2:145–152

Archie GE 1952 Classification of carbonate reservoir rocks and petrophysical considerations. AAPG Bulletin 36, 2:278–298

Asquith GB 1986 Microporosity in the O'Hara oolite zone of the Mississippian Ste. Genevieve Limestone, Hopkins County, Kentucky, and its implications for formation evaluation. Carbonates and Evaporites 1, 1:7–12

Aufricht WR, Koepf EH 1957, The interpretation of capillary pressure data from carbonate reservoirs. Transactions, AIME, v. 210, p. 402–405

Bebout DG, Lucia FJ, Hocott CF, Fogg GE, Vander Stoep GW 1987, Characterization of the Grayburg reservoir, University Lands Dune field, Crane County, Texas: The University of Texas at Austin, Bureau of Economic Geology Report of Investigations No. 168, 98 p

Budd DA 2002, The relative roles of compaction and early cementation in the destruction of permeability in carbonate grainstones: a case study of the Paleogene of west-central Florida, U.S.A. J of Sedimentary Research 72, 1:116-128

Choquette PW, Pray, LC 1970 Geologic nomenclature and classification of porosity in sedimentary carbonates. AAPG Bulletin 54, 2:207–250

Choquette PW, Steiner, RP 1985 Mississippian oolite and non-supratidal dolomite reservoirs in the Ste. Genevieve Formation, North Bridgeport Field, Illinois Basin. In Roehl PO, Choquette PW, (eds) Carbonate petroleum reservoirs. Springer-Verlag, p. 209–238.

Cruz WM 1997 Study of Albian carbonate analogs: Cedar Park Quarry, Texas, USA, and Santos Basin Reservoir, Southeast Offshore of Brazil. Unpubl PhD thesis, The University of Texas at Austin, Austin, Texas

Dixon FR, Marek BF 1990 The effect of bimodal pore size distribution on electrical properties of some Middle Eastern limestones. Society of Petroleum Engineers Technical Conference, September 1990, SPE 20601

Dunham RJ 1962 Classification of carbonate rocks according to depositional texture. In Ham WE (ed) Classifications of carbonate rocks—a symposium. AAPG Memoir 1:108–121

Heseldin GM 1974 A method of averaging capillary pressure curves. Society of Professional Well Log Analysts Annual Logging Symposium, June 2-5, paper E

Jennings JW, Lucia FJ 2003 Predicting permeability from well logs in carbonates with a link to geology for interwell permeability mapping. SPE Reservoir Evaluation & Engineering 6, 4:215–225

Keith BD, Pittman ED 1983 Bimodal porosity in oolitic reservoir—effect on productivity and log response, Rodessa Limestone (Lower Cretaceous), East Texas Basin. AAPG Bulletin 67, 9:1391–1399

Kerans C 1989 Karst-controlled reservoir heterogeneity in the Ellenburger Group carbonates of West Texas. AAPG Bulletin 72, 10:1160–1183

Kerans C, Lucia FJ, Senger RK 1994 Integrated characterization of carbonate ramp reservoirs using Permian San Andres Formation outcrop analogs. AAPG Bulletin 78, 2:181–216

Kolodizie S 1980 Analysis of pore throat size and use of the Waxman-Smits equation to determine OOIP in Spindle Field, Colorado. SPE paper 9382 presented at the 1980 SPE Annual Technical Conference and Exhibition, Dallas, Texas

Leverett MC 1941 Capillary behavior in porous solids. Transactions, AIME, 142:151–169

Lucia FJ 1962 Diagenesis of a crinoidal sediment. J of Sedimentary Petrol 32, 4:848–865

Lucia FJ 1983 Petrophysical parameters estimated from visual description of carbonate rocks: a field classification of carbonate pore space. J Pet Technology March:626–637

Lucia FJ 1993 Carbonate reservoir models: facies, diagenesis, and flow characterization, In Morton-Thompson D, Woods AM (eds) Development geology reference manual. AAPG Methods in Exploration 10, AAPG Tulsa, pp 269–274

Lucia FJ 1995 Rock fabric/petrophysical classification of carbonate pore space for reservoir characterization. AAPG Bulletin 79, 9:1275–1300

Lucia FJ, Conti RD 1987 Rock fabric, permeability, and log relationships in an upward-shoaling, vuggy carbonate sequence. The University of Texas at Austin, Bureau of Economic Geology Geological Circular 87-5, 22 p

Lucia FJ, Kerans C, Senger RK 1992a, Defining flow units in dolomitized carbonate-ramp reservoirs. Soc Petroleum Engineers Techn Conf. Washington, D.C., SPE 24702, pp 399-406

Lucia FJ, Ruppel SC 1996 Characterization of diagenetically altered carbonate reservoirs, South Cowden Grayburg reservoir, West Texas. Soc Petroleum Engineers Paper SPE 36650

Lucia FJ,. Kerans C, Vander Stoep GW 1992b, Characterization of a karsted, high-energy, ramp-margin carbonate reservoir: Taylor-Link West San Andres Unit, Pecos County, Texas. The University of Texas at Austin, Bureau of Economic Geology, Report of Investigations No. 208, 46 pp

Lucia FJ, Jennings JW, Meyer FO, Rahnis M 2001 Permeability and rock fabrics from wireline logs, Arab-D reservoir, Ghawar Field, Saudi Arabia. GeoArabia 6, 4:619–646

Major RP, Vander Stoep GW, Holtz MH 1990 Delineation of unrecovered mobile oil in a mature dolomite reservoir: East Penwell San Andres Unit, University Lands, West Texas. The University of Texas at Austin, Bureau of Economic Geology, Report of Investigations No. 194, 52 pp

Moshier SO, Handford CR, Scott RW, Boutell RD 1988 Giant gas accumulation in "chalky"-textured micritic limestones, Lower Cretaceous Shuaiba Formation, Eastern United Arab Emirates. In Lomando AJ, Harris PM (eds) Giant oil and gas fields. Society of Economic Paleontologists and Mineralogists (SEPM) Core Workshop No. 12, 1:229–272

Murray RC 1960 Origin of porosity in carbonate rocks. J of Sedimentary Petrol 30, 1:59–84

Pittman ED 1971 Microporosity in carbonate rocks: AAPG Bulletin 55, 10:1873–1881

Pittman ED 1992 Relationship of porosity and permeability to various parameters derived from mercury injection-capillary pressure curves for sandstone. AAPG Bulletin 72, 2:191–198

Scholle PA 1977 Chalk diagenesis and its relation to petroleum exploration: Oil from chalks, a modern miracle?. AAPG Bulletin 61, 7:982–1009

Senger RK, Lucia FJ, Kerans C, Ferris MA 1993 Dominant control of reservoir-flow behavior in carbonate reservoirs as determined from outcrop studies. In Linville B, Burchfield RE, Wesson TC (eds) Reservoir characterization III. Pennwell Books, Tulsa, Oklahoma, pp 107–150

Wang FP, Lucia FJ, Kerans C 1998 Integrated reservoir characterization study of a carbonate ramp reservoir: Seminole San Andres Unit, Gaines County, Texas. SPE Reservoir Evaluation & Engineering, 1, 3:105–114

Chapter 3 Wireline Logs

3.1 Introduction

Petrophysical measurements and rock-fabric descriptions provide a basis for quantifying geological descriptions with petrophysical properties but are point data and have no spatial information. These measurements and descriptions are expanded in one dimension by detailed sampling of core material. However, cores are normally available from only a few wells, whereas wireline logs are available from most wells. Therefore, rock fabric data and facies descriptions must be calibrated to wireline logs to expand the coverage of one-dimensional core data.

There are two basic requirements for constructing a petrophysical model. One is building a 3-D stratigraphic framework, which will be discussed later. The other basic requirement is quantifying the framework in petrophysical terms, which is accomplished through a knowledge of the spatial distribution of rock fabrics within the framework. These tasks begin with the one-dimensional description of rock fabrics and depositional facies from cores. As described in Chapter 2, the basic fabric parameters to describe are (1) rock fabrics, (2) dolomite crystal size, (3) petrophysical class, (4) interparticle porosity, (5) separate-vug porosity, and (6) touching-vug pore space.

The purpose of this chapter is to illustrate methods of obtaining rock-fabric and facies data from wireline logs through a technique referred to as core-log calibration. These data are then used to calculate vertical profiles of permeability and initial water saturation using algorithms established in Chapter 2. Core descriptions will be discussed first, followed by methods of obtaining rock-fabric and facies information from wireline logs.

3.2 Core Description

The first step in quantifying a geologic model is the description of rock fabrics from core material, using the Lucia classification methods and relating the descriptions to measured porosity, permeability, and capillary pressure curves, as described in Chapter 2. The best sampling method is to drill 1-inch-diameter core plugs for analysis from every foot of core and to prepare a thin section from the end pieces for detailed rock-fabric description. If whole core samples are used in the analysis, a thin section is made from a sample of the whole core. If samples other than those used for analysis are used, it will be difficult to match rock-fabric descriptions with core analysis data because of the high small-scale variability of porosity and permeability in carbonate reservoirs.

The critical observations to record when describing the core for petrophysical quantification are lithology, dolomite crystal size, rock fabric, petrophysical class, amount and type of separate vugs, and a description of touching vugs. Supplementary information includes grain types and visible interparticle porosity. This information is best obtained from thin sections and can be collected quickly by a trained observer. A suggested spreadsheet that includes the critical fabric information and the measured porosity and permeability is illustrated in Fig. 1. Rock fabric data are usually presented as a one-dimensional depth for easy comparison to wireline logs.

Depth		LITHOLOGY								TEXTURE		VISIBLE PORE SPACE				PET.	CALC Ippor	CORE ANALY.		NOTES
Sp. No.	Dolomite		Calc		Sulfate			Quartz		Acc.	Rock Fabric	Grain Size	Ippor	Svugs		Tvug	CLASS	Cpor-Svug	Cpor	Cperm	
	%	size µ	%	Anhy	Type	Gyp	Type	%	Size		Description	µm	%	%	Type	Type		%	%	md	

Fig. 3.1. Spreadsheet for rock fabric/petrophysical descriptions

3.3 Core Analysis

Petrophysical data obtained from core measurements are normally considered to be accurate and are used to calibrate log data. Routine core analysis data, however, can be very inaccurate for the reasons listed below.

1. Some methods of measuring porosity, such as the sum-of-fluids method, are very inaccurate. Only porosity values determined by using the Boyles Law method should be considered quantitative.
2. Biased sampling of the core can result in incorrect representations of porosity and permeability.
3. Permeability values obtained from routine whole-core analysis are typically too high on the low end and too low on the high end when compared with data from controlled laboratory procedures, probably because insufficient care was taken with the measurements.
4. Induced fractures and stylolites commonly result in unrealistically high permeability values because insufficient confining pressure is used.
5. Porosity values can be too low due to incomplete removal of hydrocarbons or other fluids.
6. Porosity and permeability values can be too high if high-temperature procedures are used on core material containing gypsum and clay minerals, because high temperatures can significantly alter these minerals.

3.4 Core/Log Calibration

The second step in quantifying a geologic model is to correlate rock-fabric data and facies descriptions with wireline log response. Vertical successions of facies and rock fabrics obtained from core descriptions must be calibrated with wireline logs to expand the coverage of one-dimensional data. Wireline logs that have been used for this purpose include gamma-ray, neutron, density, photoelectric (PEF), acoustic, resistivity, and formation imaging logs. The nuclear magnetic resonance log (NMR) may also have application here. A general discussion of these logs and their use in identifying rock fabrics, facies, petrophysical class, rock fabric number, interparticle porosity, separate-vug porosity, and touching vugs is presented below.

Wireline logs respond to physical properties and not to geologic attributes (see Dewan, 1983, for details of log interpretation). Logs cannot be used to distinguish between grainstone and wackestone or between

ooids and fusulinid, but they can differentiate between levels of natural gamma-ray radiation, which may uniquely distinguish between grainstones and wackestones. With the exception of the NMR tool, logs do not measure differences in pore sizes, but electric logs measure rock resistivities, which relate to saturations and, in turn, to pore size and rock fabrics. Wireline logs can distinguish different densities, which can be related to lithology. Such empirical relationships between log response and geological characteristics of the reservoir are used to extend core descriptions and measurements throughout the field.

3.4.1 Procedures for Core-Log Calibration

A key step in core-log calibration is depth shifting core depth to match log depth. There are always a number of core depths to consider, including 1) depths scribed at the well site, unless core recovery is incomplete and the location of the missing core is unknown, 2) core analysis depths that may or may not be scribed on the core but most likely agree with depths scribed at the well site, 3) depth intervals written on the core boxes, which are at best plus-or-minus 1 foot or worse if the boxes have been dropped and scrambled, 4) depths scribed on the core or core slabs other than the original depth markings, which may have been added over the years and can have large errors depending on how well the core has been handled.

The principal method of matching core and log depths is by comparing core porosity or gamma ray to wireline log porosity and gamma ray. Linking shale intervals with the gamma-ray log is commonly used, but the key link between log depths and core depths is the depths reported on the core analysis. Unfortunately, it is common for core depths to disagree with core analysis depths, for the reasons listed above. Therefore, core analysis sample numbers should be used to identify core depth wherever possible. However, if the core analysis sample number cannot be located, the depth scribed on the core or core box will have to be used, and the correlation between core and log depths will be only approximate.

Accurate depth shifting of core depths to wireline-log depths is a tedious but very important task. Depth shifting should be accurate to 1 foot for calibrating core descriptions to wireline logs because descriptions are normally on a foot-by-foot basis. This degree of accuracy, however, is difficult to achieve, and some manual shifting of core description logs will be necessary for proper calibration. After core depths are properly shifted to log depths, vertical profiles of rock fabric data and successions of depositional facies can be compared with various log responses and calibration algorithms developed. Next we will examine the potential for

each wireline log to identify rock fabrics, facies, petrophysical class, rock fabric number, interparticle porosity, separate-vug porosity, and touching vugs.

3.4.2 Gamma-Ray Logs

The gamma-ray log measures the natural radiation of uranium, potassium, and thorium. Potassium and thorium are concentrated in the minerals that constitute insoluble residue in carbonate rocks, such as rock fragments and clays. Uranium, however, is most often diagenetic and not related to depositional facies or rock fabric. Uranium radiation must be removed from the gamma-ray signal before the gamma-ray log can be used effectively to identify rock fabrics or facies. The gamma-ray spectroscopy tool distinguishes between uranium, thorium, and potassium sources of radiation and provides a means of separating diagenetic uranium from depositional thorium and potassium (Fig. 2). The spectral gamma-ray log is displayed as two logs: the spectral gamma-ray log (SGR), which combines all sources of radiation, and the computed gamma-ray log (CGR), which combines thorium and potassium sources. The CGR should be used for rock-fabric identification and lateral correlation of depositional events. Lithologies that typically have high potassium and thorium radiation are shaly intervals, quartz silt beds, and organic-rich beds. Sylvite (KCl) found associated with beds of halite (NaCl) has high gamma radiation from the potassium, as does feldspathic sandstone.

Gamma-ray logs run in old wells should be used with caution. Repeat runs of gamma-ray logs in cased-hole production wells have shown increased gamma-ray response over perforated intervals with time. This is probably the result of radioactive elements deposited along with well-bore scale that forms due to the flow of produced water through the perforated intervals.

Many carbonate facies can be correlated with current energy and thus with potassium and thorium radiation because the amount of insoluble residue is thought to be inversely proportional to current energy. Grainstones and grain-dominated packstones are deposited in high-energy environments and typically have low gamma-ray activity. Mud-dominated packstones, wackestones and mudstones are deposited in low-energy environments and typically have higher gamma-ray activity (Fig. 3). In many cases the response from potassium and thorium is too low to distinguish between fabrics (Fig. 3). In the presence of significant amounts of uranium the signal from potassium and thorium is masked, and the gamma-ray log is a poor tool for distinguishing rock fabrics or facies.
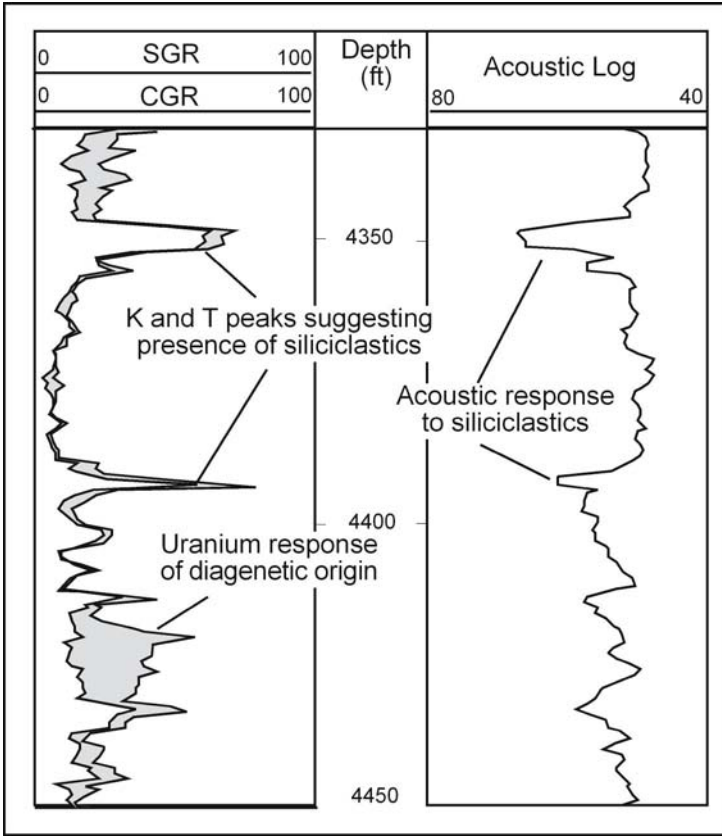
Fig. 3.2. Spectral gamma-ray log showing peaks caused by (1) high uranium content produced diagenetically and (2) high potassium and thorium content suggesting insoluble residue (siliciclastic) related to depositional energy conditions. Notice the response of the acoustic log to the presence of siliciclastic material. This is a lithology response that is often mistaken for high porosity

At best grain-dominated fabrics (classes 1 & 2), mud-dominated fabrics (class 3), and shaly/silty carbonates (class 3) can be distinguished using the gamma-ray log. However, depositional facies typically cannot be distinguished because they are commonly defined by grain type as well as by fabric. Grain type cannot be identified from logs; it can only be inferred from geologic knowledge.
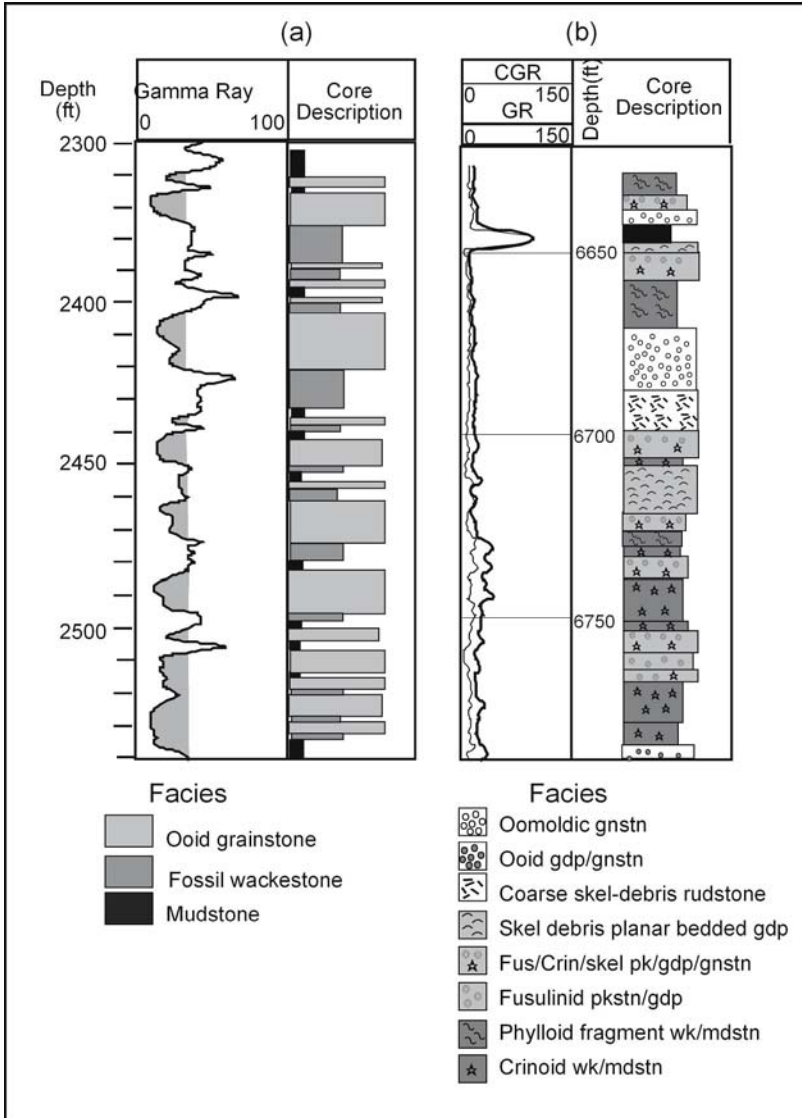
Fig. 3.3. Comparison of rock fabrics from core description with gamma-ray log. **(a)** An 80% agreement log response in distinguishing between grain-dominated from mud-dominated fabrics. **(b)** A lack of a robust relationship between facies of rock fabrics due to low levels of gamma-ray

3.4.3 Borehole Environment

Wireline log measurements respond to rock properties and the properties of the fluids in the pore space. The nature of the fluids in the pore space immediately surrounding the borehole depends upon the amount and type of mud filtrate that invades the formation. During the drilling process, drilling mud is pumped down the drill pipe and up the annulus between the drill pipe and the formation. In formations with sufficient permeability, water will infiltrate the formation, leaving mud cake on the side of the well bore. This occurs because the pressure in the mud column is greater than the formation pressure. The invaded zone is composed of a flushed zone and a transition zone, and the dimensions of the transition zone will vary with time due to diffusion. In a water-bearing formation, the mud filtrate will completely flush the formation water near the well bore, and there will be a transition zone between the flushed zone and undisturbed formation (Fig. 4A). In a hydrocarbon-bearing formation composed of connate water and oil or gas, the connate water will be flushed, but residual hydrocarbons will be trapped by capillary forces in the flushed zone. There will be a transition zone between the flushed zone and the undisturbed reservoir where oil saturation will increase and water saturation decrease (Fig. 4B).

The saturation profile of the invaded zone must be taken into account when interpreting wireline logs. For neutron, density, and acoustic logs, the difference between oil and water is not large and is often ignored in calculations. However, the presence of residual gas in the invaded zone has a significant effect, as will be discussed later. The saturation and resistivity of water in the invaded zone have a major effect on resistivity and conductivity measurements that must be considered when interpreting resistivity logs.

3.4.4 Neutron-Density Cross-Plot Porosity

Porosity is a basic value needed for volumetric calculations and for rock-fabric characterization. Porosity is generally calculated from neutron and density logs. There are many algorithms used for this but the general form of the equation is presented below.

$$\phi_{ND} = \left(\frac{\phi_N + \phi_D}{2} \right)$$

Where ϕ_N = neutron porosity corrected for lithology
ϕ_D = density porosity corrected for lithology
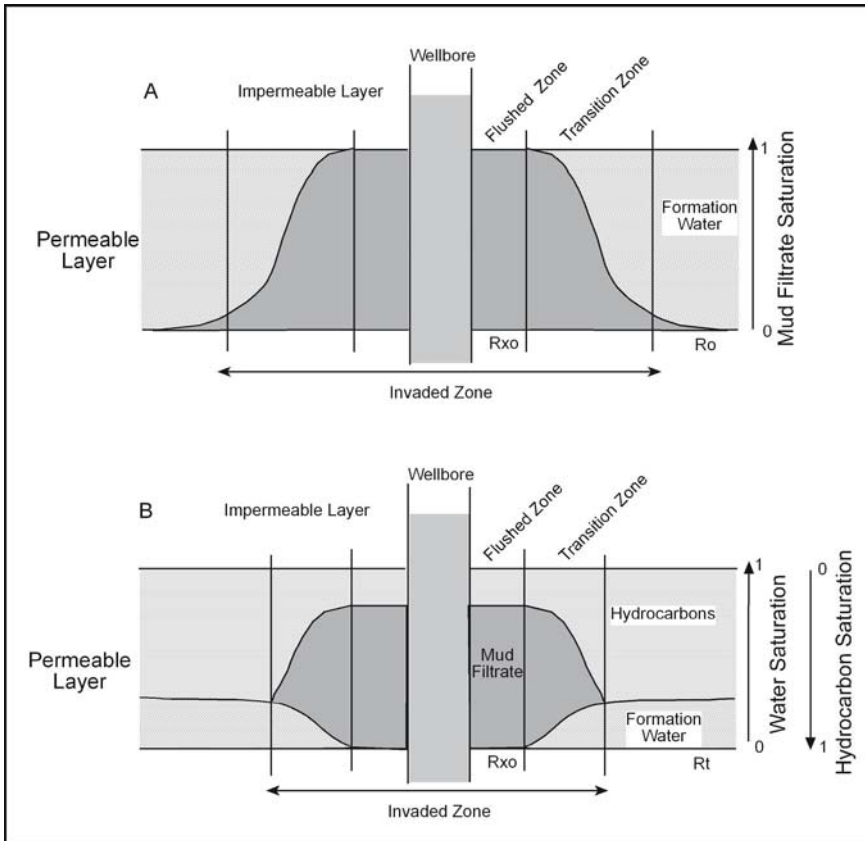
Fig. 3.4. Fluid composition of the invaded zone. In a permeable water-bearing formation, the mud filtrate will completely flush the formation water near the well bore, and there will be a transition zone between the flushed zone and the undisturbed formation (**A**). In a hydrocarbon-bearing formation composed of formation water and oil or gas, the flushed zone will be composed of mud filtrate and residual hydrocarbons trapped by capillary forces, the undisturbed reservoir will be composed of hydrocarbons and formation water, and the transition zone will be composed of hydrocarbons, mud filtrate and formation water (**B**)

Acoustic logs can also be used for calculating porosity, but only if the effects of vuggy porosity and lithology are accounted for.

Neutron and density logs have their own unique inaccuracies and should be calibrated with core porosity values whenever possible. However, as described in Chapter 1, core porosity values should not be accepted as "truth" until their accuracy is verified by examining laboratory

procedures and by checking the samples for uniformity, pore type, and complete removal of hydrocarbons.

Porosity data can often be used to identify grain-dominated and mud-dominated fabrics if calibrated with core descriptions. Mud-dominated limestone fabrics commonly have less porosity than do grain-dominated fabrics because muddy sediments are more susceptible to compaction than are grainy sediments.   This may also be found in dolostones if dolomitization occurs early and the precursor fabrics can be recognized.

Calibration of rock fabrics and porosity is accomplished in several ways. Histograms and average porosity for specific rock fabrics can be examined for statistically significant differences (Fig. 5). Depth profiles of porosity and rock fabrics can be compared and examined for meaningful
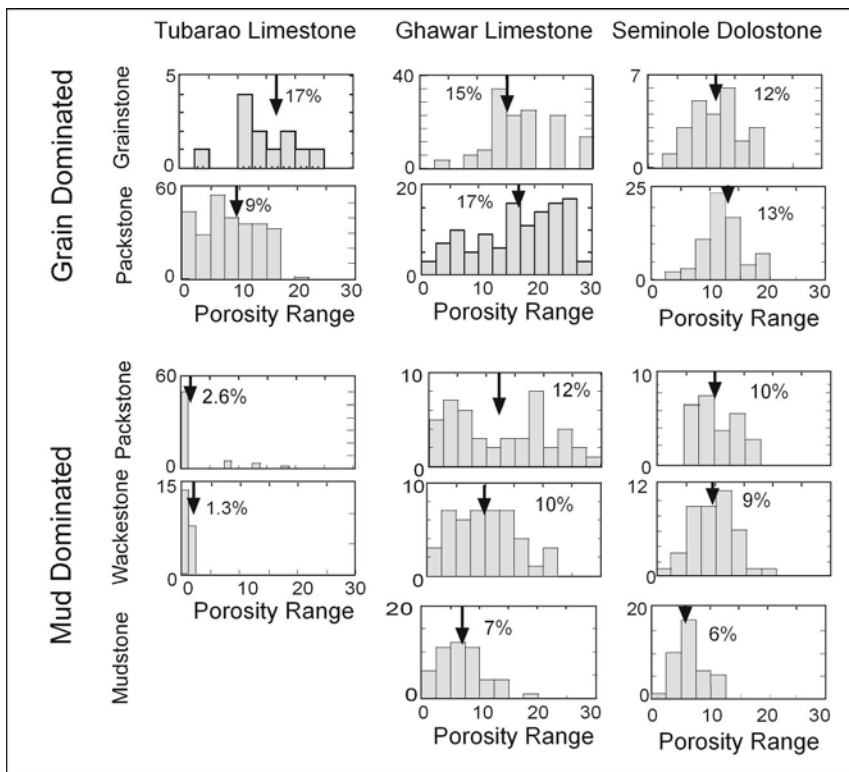
Fig. 3.5. A series of porosity histograms showing the difference between the basic rock fabrics. Average porosity decreases with increasing mud content in both limestones and in early dolostones

trends (Fig. 6).   In Paleozoic reservoirs, dolomite is commonly more porous than limestone, and dolomitization may selectively replace mud-
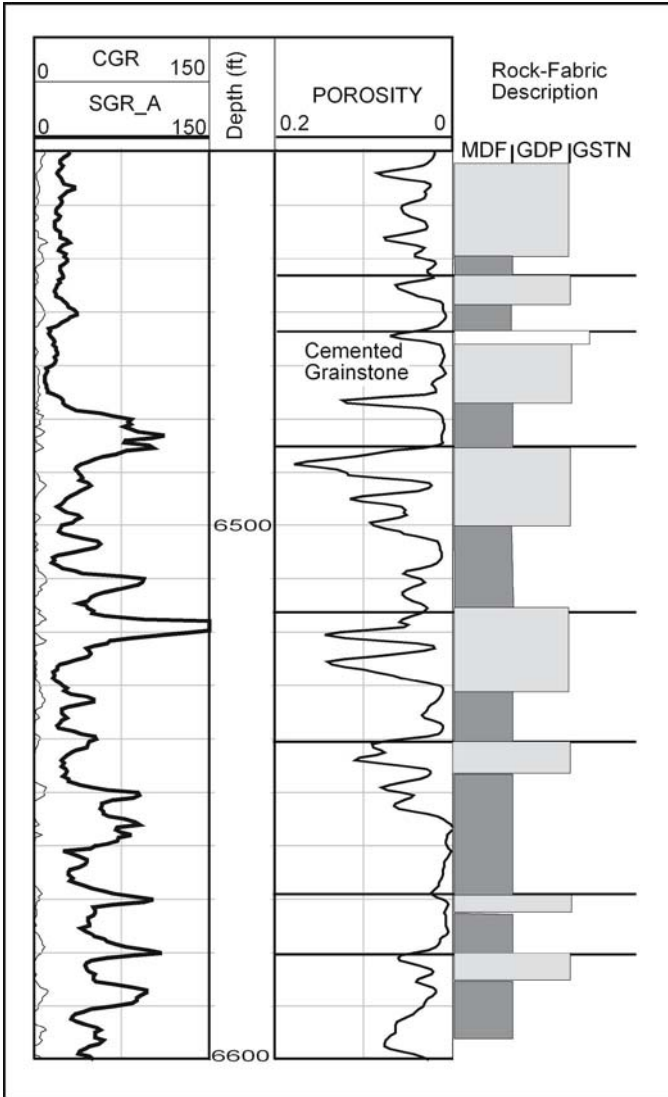
Fig. 3.6. A comparison of a gamm-ray/porosity log with dolostone rock fabrics from thin section descriptions. Grain-dominated dolostones tend to have higher porosity than mud-dominated dolostones. Note the large amount of diagenetic uranium indicated by the spectral log and the small amount of response to the CGR log

dominated fabrics (Lucia, 1962). Normally, only two groups of depositional facies can be recognized using the porosity log: grainstone/grain-

dominated packstone and mud-dominated packstone, wackestone, and mudstone. Facies based on allochems cannot be recognized.

Neutron logs measure the hydrogen ion concentration of the formation by measuring the capture of neutrons emitted by a neutron source. Common neutron tools are the compensated neutron and compensated dual spacing neutron logs, which are normally run in conjunction with a density log. Neutron logs are a centralized tool that require accurate corrections for borehole size; these corrections are usually automated into the final log display. The fact that this is a centralized tool and not a pad device leads to a degree of inaccuracy in porosity values. The sidewall neutron log is a borehole pad device that requires less correction for borehole size and is more accurate. It is no longer available, but it is often encountered when working with old wells.

The neutron log responds to fluids in the invaded zone of the well bore because the depth of investigation is only a few inches. Water and residual oil and gas are present in the invaded zone and contain hydrogen ions. The hydrogen index of water and oil is similar and is usually assumed to be 1. Because of its much lower density, gas has a significantly lower concentration of hydrogen, resulting in a lower reading than expected from water or oil for the same porosity. If the gas saturation is not accounted for, the porosity values will be erroneously low. This is referred to as *the gas effect* and is commonly used to detect gas, in combination with the density log described below.

Hydrogen ions are also present in some minerals as bound water Bound water will appear as porosity on the neutron log because it cannot distinguish between free and bound water. Common minerals that contain bound water are gypsum ($CaSO_4 \cdot 2H_2O$) and clay ($Al_2SO_5(OH)_4$). Organic material also contains hydrogen ions. The presence of these materials will result in erroneously high porosity values. Carbonate reservoir rocks do not usually contain enough clay or organic material to have a serious effect on the neutron log. Gypsum, however, can cause a serious problem for interpretation of neutron logs.

The following equation illustrates how common minerals found in carbonate reservoir rocks affect the neutron porosity value, assuming that no gas is present.

$$\phi_n = 0.02V_d + 0.00V_c + 0.00V_a + 0.49V_g - 0.04V_q$$

(Pirson, 1983), where V_d, V_c, V_a, V_g, and V_q equal the bulk volumes of dolomite, calcite, anhydrite, gypsum, and quartz in the formation. This equation reveals that the mineral gypsum ($CaSO_4 \cdot 2H_2O$) will appear as 49% porosity on a neutron log. This effect can result in erroneously high porosity values that may be misinterpreted as vuggy porosity when compared with the sonic log (Fig. 7). As a result, the neutron log is ineffective as a porosity tool in the presence of gypsum.
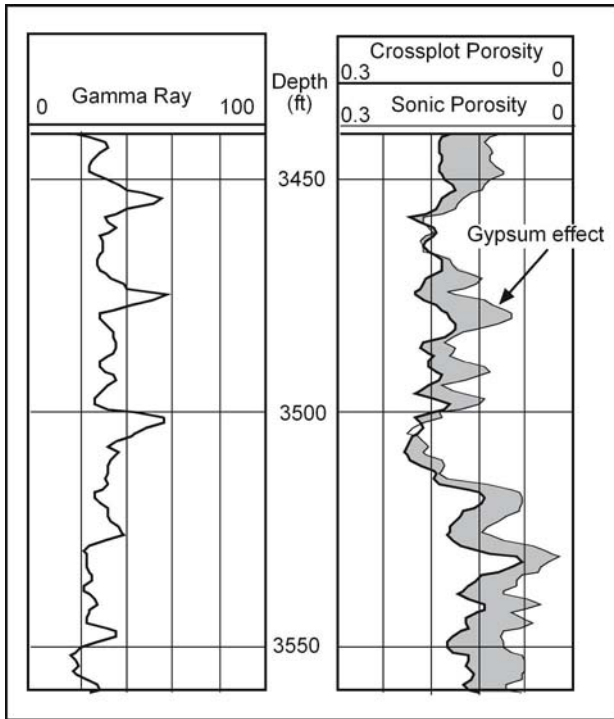
Fig. 3.7. Depth plot overlaying CNL porosity and acoustic porosity, showing the effect of bound water in gypsum on CNL porosity (underline)(shaded areas)(/underline)

The *formation density log* emits medium-energy gamma rays, which lose energy when they collide with the electrons in the formation. The number of collisions is related to the bulk density of the formation, and the bulk density is related to porosity and common minerals found in carbonate reservoirs through the following equation. This tool is a pad device that requires no borehole correction and provides more accurate

values than the compensated neutron log does. When the lithology is known this log gives the most accurate porosity values.

Bulk Density (ρ_{bulk}) =
$\rho_f \phi + 2.71V_c + 2.84V_d + 2.98V_a + 2.35V_g + 2.65V_q$ (Pirson, 1983)

or
$$\rho_{bulk} = \rho_{ma}(1-\phi) + \phi\rho_f$$
and
$$\phi = \frac{\rho_{ma} - \rho_{bulk}}{\rho_{ma} - \rho_f}$$

where ϕ is porosity, ρ_f is the fluid density, ρ_{bulk} is the bulk density, ρ_{ma} is the matrix density, and V_d, V_c, V_a, V_g, and V_q equal the bulk volumes of dolomite, calcite, anhydrite, gypsum, and quartz, respectively, in the formation.

Porosity can be calculated from the density log if the matrix and fluid densities are known. The density log is often displayed as porosity calculated assuming a limestone grain density of 2.71 and a fluid density of 1.1. The values used are recorded on the log header. If the formation is composed of minerals other than calcite, such as dolomite or anhydrite, the bulk volume must be calculated from the density porosity log by using a grain density of 2.71 and a fluid density of 1.1. The correct porosity can then be calculated using matrix densities for the minerals present.

The formation fluid that affects the density tool is the fluid in the invaded zone of the well bore because of the small radius of investigation. Oil and gas have lower densities than water, and their presence will result in lower bulk density values, and therefore erroneously high porosity values if fluid density is assumed to be 1.1. The largest effect is due to the presence of residual gas in the invaded zone. This is referred to as *the gas effect* and is commonly used, in combination with the neutron log, to detect gas.

3.4.5 Lithology

The density log is the basic lithology tool when used in conjunction with porosity values from the neutron log. The density log alone can be used to distinguish beds of anhydrite and halite from carbonate beds because they have unique densities of 2.97 and 2.0, respectively, and are typically dense (Fig. 8a). The combination of density and neutron logs is commonly used

to identify limestone and dolostone in a carbonate sequence. Given the correct log scales, the density and neutron logs will overlie for limestone and will be separated for dolostone (Fig. 8b).
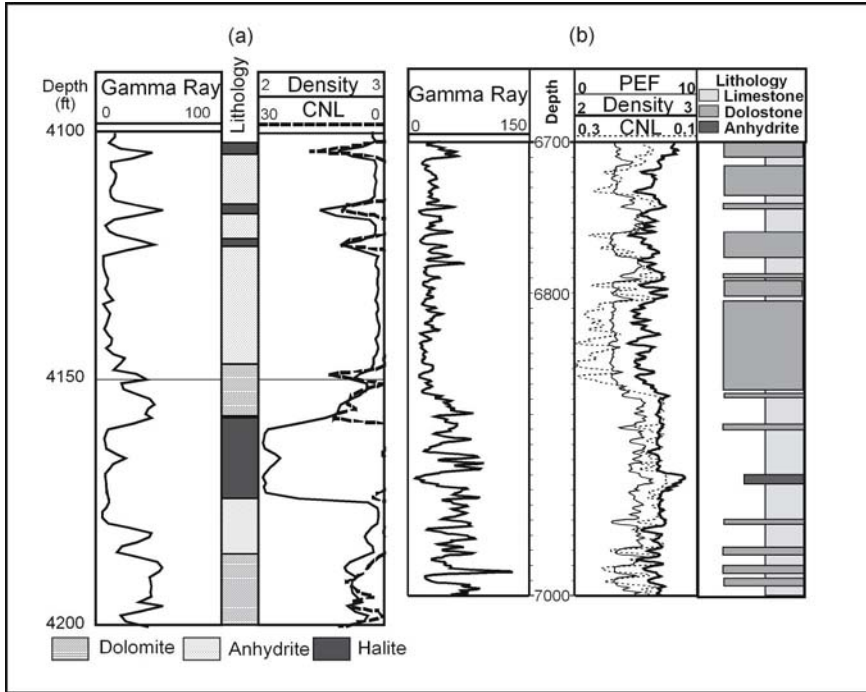
Fig. 3.8. Illustrations of lithology from wireline logs. **(a)** Depth plot overlaying density and CNL porosity logs showing identification of halite, anhydrite, and dolomite beds. **(b)** An illustration of identifyling limestone, dolostone, and anhydrite beds using overlays of neutron and density porosity augmented by the PEF curve

The *photoelectric log* (PEF) is also a basic log for determining lithology. This log focuses on low-energy gamma rays, and the energy loss can be related directly to lithology. Photoelectric factors for common carbonate minerals can be found in Schlumberger's Log Interpretation Charts (1989) and are listed below in Table 1.

Table 1. Photoelectric factors of five common minerals

Calcite	Dolomite	Anhydrite	Gypsum	Quartz
5.08	3.14	5.05	3.99	1.81

The PEF log is often used to distinguish between calcite and dolomite in the absence of large volumes of anhydrite and quartz (Fig. 8b). Together the PEF, neutron, and density logs provide a powerful combination to identify the three minerals most commonly found in carbonate reservoirs: calcite, dolomite, and anhydrite. *However, all mineral identification should be calibrated with local rock information to ensure accuracy.*

In reservoir modeling it is often important to separate limestone from dolostone. Limestone rock fabrics are often linked to petrophysical class, whereas the petrophysical class of dolostone fabrics is strongly affected by dolomite crystal size. In addition, the productive characteristics of dolostones are often quite different from those of limestones.

3.4.6 Acoustic Logs

Acoustic logs record the travel time of compressional sound waves through a 2-foot interval of the formation. Travel time is expressed as the interval transit time in μsec/ft or μsec/cm, which is the reciprocal of the sonic velocity (distance/time). Velocity is a function of rock rigidity, and rock rigidity is a function of a number of variables, including lithology, porosity, and pore type. The relationship between velocity and pore type is of most interest in reservoir characterization because it provides an approach for estimating interparticle porosity, which is needed as input into the global permeability transform. The approach is to use acoustic-porosity cross plots to estimate separate-vug porosity and to estimate interparticle porosity by subtracting separate-vug porosity from total porosity obtained from neutron and density logs.

The following equation is a form of the Wyllie time-average empirical formula. It shows the relationship between acoustic transit time (Δt), porosity (ϕ), matrix transit time (Δt_{ma}) and fluid travel time (Δt_f).

$$\Delta t = \Delta t_f \, \phi_{ip} + \left(1 - \phi_{ip}\right) \Delta t_{ma}$$

and

$$\phi_{ip} = \frac{\Delta t - \Delta t_{ma}}{\Delta t_f - \Delta t_{ma}}$$

or

$$\Delta t = \Delta_f \left(\phi_{ip}\right) + \left(1 - \phi_{ip}\right)\left(44 V_d + 49 V_c + 50 V_a + 52 V_g + 56 V_q\right)$$

(after Pirson, 1983), where

Δt is fluid transit time usually given as 189 μsec/ft,

ϕ is interparticle porosity (fraction), and

V_d , V_c , V_a , V_g ,and V_q equal the bulk volumes of dolomite, calcite, anhydrite, gypsum and quartz, respectively, in the formation preceded by their transit-time values.

Transit-time values for the common minerals in carbonate reservoirs are found in Schlumberger's manual and are given below in Table 2.

Table 2. Transit-time values for basic minerals found in carbonate reservoirs

Calcite	Dolomite	Anhydrite	Gypsum	Quartz
48.5	44	50	52	56

The Wyllie time-average equation is for nonvuggy carbonates and should not be used in the presence of more than a few percent of separate-vug porosity or in the presence of large touching vugs. The equation shows that transit time has a large lithology effect and can be used to determine lithology in combination with neutron, density, and PEF logs in the absence of vuggy porosity. Siliciclastic beds can be easily identified in a carbonate sequence because of the large velocity difference between quartz and carbonate minerals (Fig. 9). Care should be taken not to confuse high transit times with high porosity in mixed carbonate-clastic reservoirs.

Dolomite reservoirs commonly contain small amounts of sulfate in the form of anhydrite. However, small amounts of sulfate have little effect on transit time because the velocity difference between dolomite and anhydrite is not large. In shallow reservoirs, however, anhydrite is commonly converted to the hydrous form, gypsum. As discussed previously, the hydrogen ions in gypsum render neutron and density logs virtually useless for calculating porosity. However, the difference between the velocity of anhydrite and of gypsum is small and has only a negligible effect on porosity calculations obtained from acoustic logs. Therefore, acoustic logs can be used to calculate porosity in the presence of gypsum, assuming that the amount of separate-vug porosity is small (Bebout et al. 1987).

Acoustic velocity has been shown to be a function of pore type. When most of the porosity is confined to separate vugs, the Wyllie time-average porosity equation does not apply and the velocity is higher (travel time lower) than expected for interparticle porosity. The effect of moldic porosity on acoustic log response has long been expressed as the difference between porosity calculated from the acoustic log and porosity calculated from neutron and density logs. This difference is often expressed as "secondary" porosity, whereas neutron and density porosity is "primary" porosity. These terms have little geologic value and will not be used here. Several equations have been developed to quantify "secondary" porosity
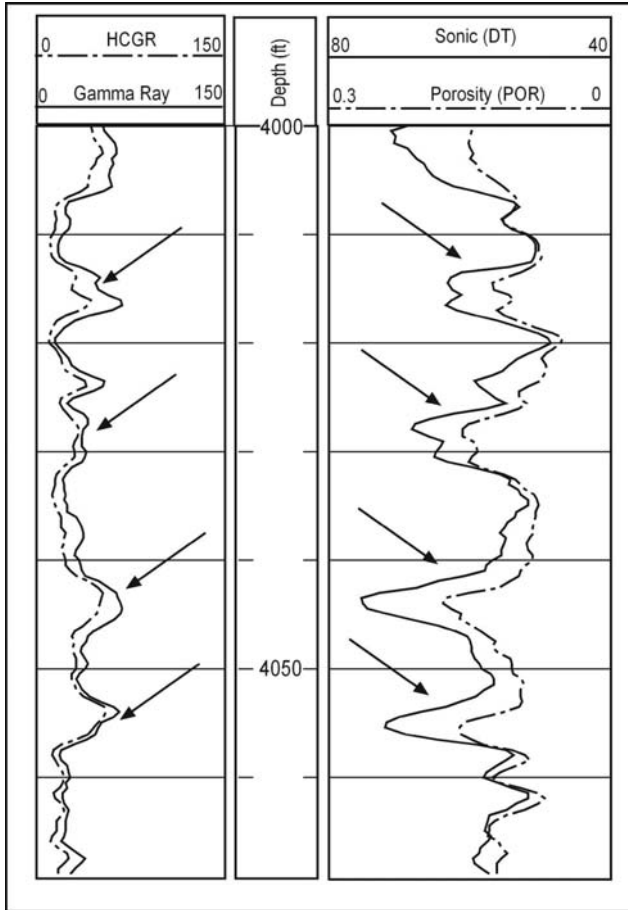
Fig. 3.9. Identifying silty/sandy carbonate using overlays of porosity and acoustic logs and based on the fact that quartz has a much higher transit time value than carbonate. Notice that the CGR is tracking the spectral gamma ray indicating that there is very little uranium in the system and the gamma-ray log is a good indicator of siliciclastic input

using a linear relationship between neutron and acoustic porosity (Nugent et al. 1978). Calibration of acoustic response with core descriptions of pore types does not support a linear relationship.

Calibration of pore types to acoustic log response is accomplished by making a detailed log of porosity types described from thin sections and constructing Z-plots of total porosity and transit time from logs and separate-vug porosity from thin sections (Fig. 10). It is assumed that for constant separate-vug porosity a plot of transit time and porosity will have the same slope as the Wyllie time average plot. Lines of constant separate-
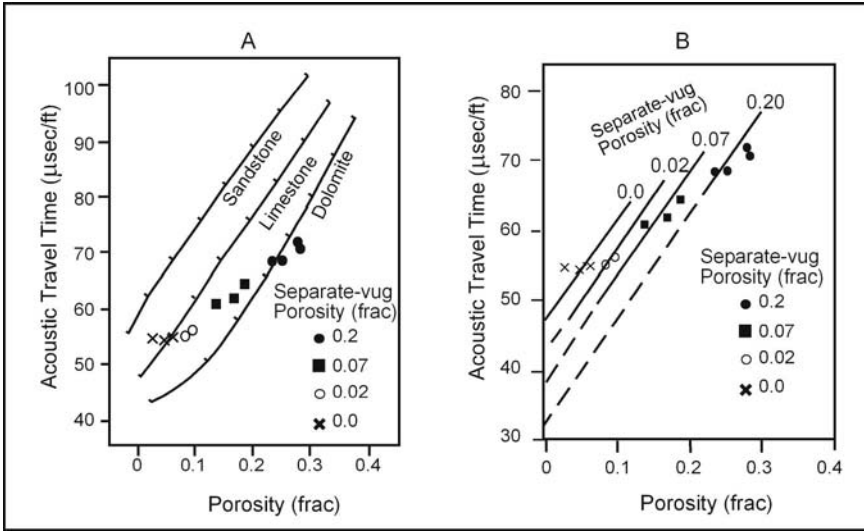
Fig. 3.10. Z-plot of acoustic travel time, total porosity, and separate-vug porosity from an oomoldic limestone.   **A** Comparison with Schlumberger lithology lines illustrating how an oomoldic limestone could be mistaken for dolomite.   **B** Parallel lines drawn through points with equal separate-vug porosity. The slope parallels the Wyllie time average curve for limestone
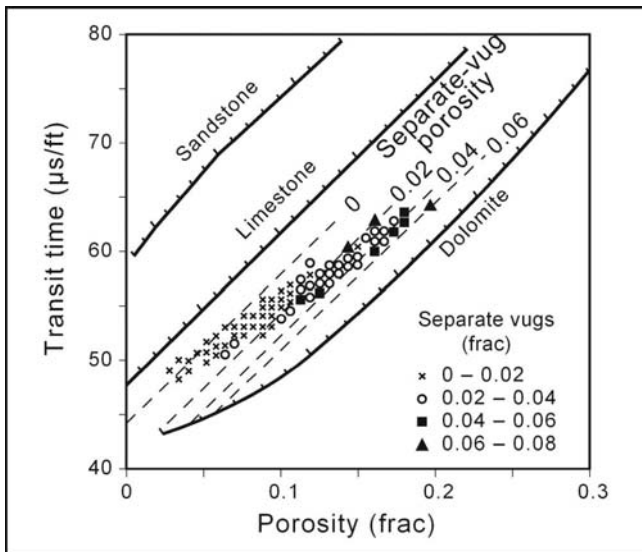
Fig. 3.11. Z-plot of acoustic travel time, total porosity, and separate-vug porosity from an anhydritic dolomite showing lines of equal separate-vug porosity constructed parallel to the Wyllie time average curve for dolostone

vug porosity can be constructed that are parallel to the Wyllie curve and extended to intersect the transit-time axis at zero porosity. The value at the intersection is normally the matrix transit time (Δt_{ma}) but here it is referred to as the pseudomatrix transit time (pseudomatrix Δt). An example from an oomoldic limestone is shown in Fig. 10 (Lucia and Conti, 1987), along with an example from an anhydritic dolostone in Fig. 11 (Lucia et al., 1995).

The pseudomatrix Δt is plotted against the log of separate-vug porosity (Fig. 12). The pseudomatrix Δt can be expressed in terms of Δt and
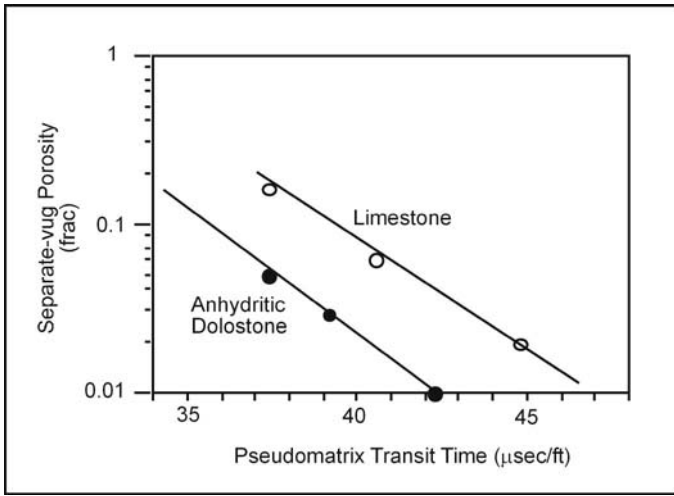
Fig. 3.12. Cross plot of the log of separate-vug porosity and pseudomatrix transit times for oomoldic limestone and anhydritic dolomite illustrated in Figs. 3.10, 3.11. The curves have similar slopes but different intercepts because of the lithology difference

porosity resulting in a relationship between total porosity, transit time, and separate-vug porosity.

$\Delta t = (\Delta t_f - \Delta t_{ma})\phi + \Delta t_{ma}$, and

$\Delta t_f = 189$ μsec/ft,

$\Delta t_{ma} = 48$ μsec/ft for limestones,

$\Delta t_{ma} = 44$ μsec/ft for dolostones.

For nonvuggy limestones

$\Delta t_{ma} = \Delta t - (189\text{-}48)\phi$, or $\Delta t - 141\phi$

For separate-vug limestones

Pseudomatrix $\Delta t = \Delta t - 141\phi$

For nonvuggy dolostones
$\Delta t_{ma} = \Delta t - (189\text{-}44)\phi$, or $\Delta t - 145\phi$
For separate-vug dolostones
Pseudomatrix $\Delta t = \Delta t - 145\phi$

The general form of the resulting equation is given below (Wang and Lucia, 1993).

$$Log(\phi_{sv}) = a - b[\Delta t - (pseudomatrix\Delta t)]$$

or

$$Log(\phi_{sv}) = a - b[\Delta t - (\Delta t_f - \Delta_{ma})\phi]$$

or

$$\phi_{sv} = 10^{a - b\left[\Delta t - \left(\Delta t_f - \Delta t_{ma}\right)\phi\right]}$$

where *a* and *b* are intercept and slope, which vary with lithology,
Δt = transit time from acoustic log (μsec/ft)
Δt_f = fluid transit time (μsec/ft)
Δt_{ma} = matrix transit time (μsec/ft)
ϕ = total porosity (frac), and
ϕ_{sv} = separate-vug porosity (frac).

The general equations derived for limestone and dolostone are given below. However, these equations should always be checked with core descriptions before using them to calculate separate-vug porosity and should be modified if necessary.

Limestone
$$\phi_{sv} = 10^{4.09 - 0.1298[\Delta t - 141\phi]}$$
Dolostone
$$\phi_{sv} = 10^{4.4419 - 0.1526[\Delta t - 145\phi]}$$

By calibrating the acoustic-porosity cross plot with thin section descriptions of separate vugs we develop a relationship that is log-linear rather than linear. More recently, relationships between sonic velocity, porosity, and pore type have been developed using laboratory velocity measurements, an approach that allows the results to be applied to seismic data more easily (Anselmetti and Eberly, 1999, Eberly et al., 2003).

There are numerous conditions where these equations are not applicable. The equations work best in the presence of grain molds such as oomoldic grainstone (Fig. 13). However, two types of separate vugs, intragrain microporosity and large grain molds, do not respond differently from interparticle porosity (Fig. 14). The rigidity of carbonates with these
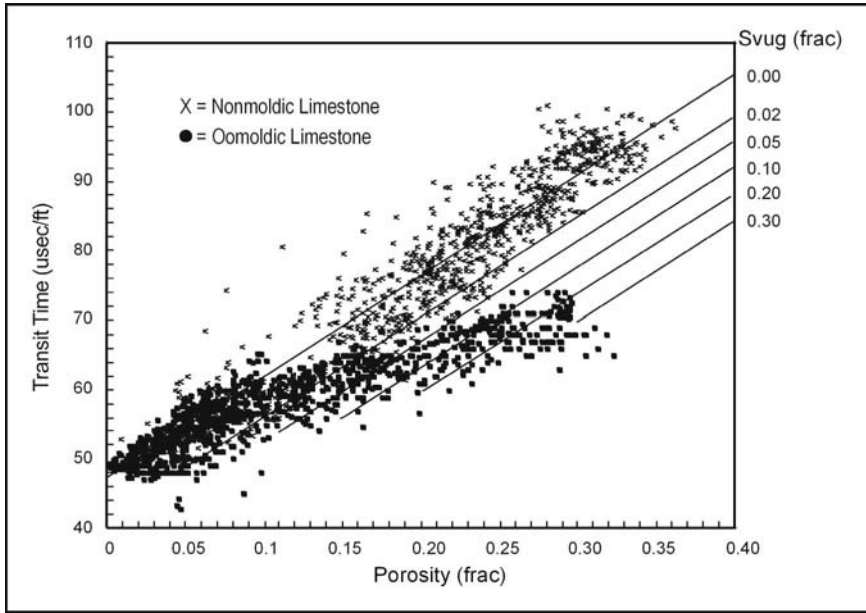
Fig. 3.13. Transit-time/porosity cross plot for several nonvuggy limestones and oomoldic limestones. Oomoldic limestones have a distinctly different response than nonvuggy limestones

types of separate vugs appears to be no different than that of carbonate where all the pore space is interparticle. In addition, there are cases in which the acoustic porosity is less than total porosity but no separate-vugs are present.   In one of these examples the acoustic log is responding to a microfracture touching-vug system and permeability is enhanced rather than reduced (Fig. 14c). Therefore, a calibration of the acoustic log with rock fabrics, lithology, and separate-vug pore types must be the first step in developing a relationship between acoustic logs and separate-vug porosity.
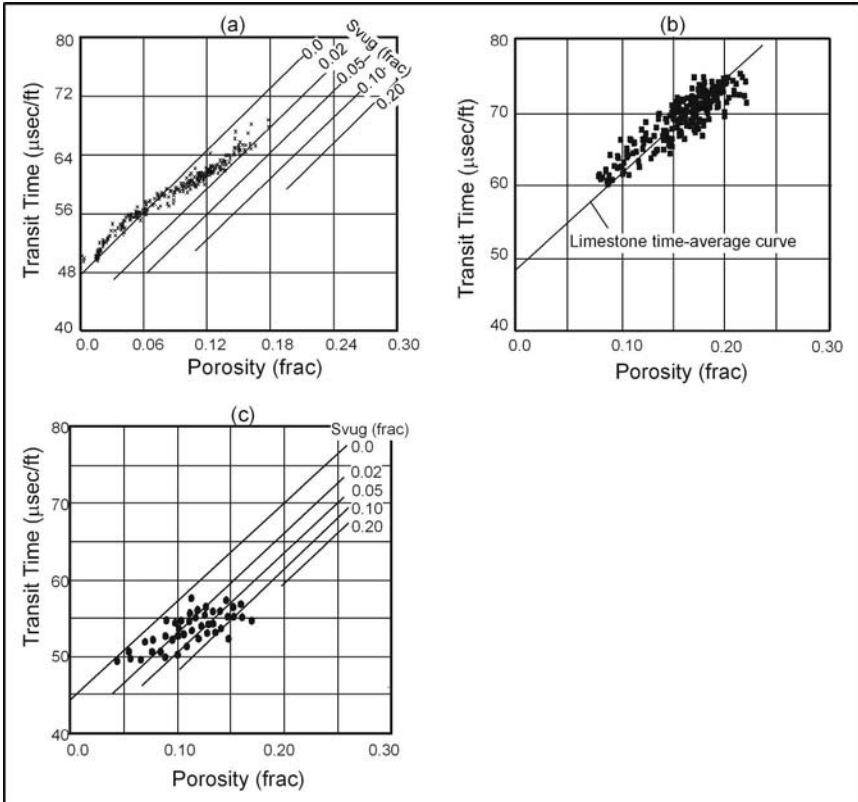
Fig. 3.14. Transit-time/porosity cross plots that are exceptions to conventional wisdom. **(a)** An ooid grainstone with large volumes of intragrain microporosity (a type of separate vug) that responds similarly to interparticle porosity. **(b)** A fossil grainstone with large grain molds and intrafossil pores that also respond similarly to interparticle porosity. **(c)** A dolowackestone with microfracture touching vugs that responds similarly to grain molds but indicates enhanced permeability rather than permeability reduction

3.4.7 Resistivity/Induction Logs

Initial-water-saturation/porosity (Swi-ϕ) relationships can be used to calculate rock-fabric number and petrophysical class for input into the global permeability transform.   Water saturation is calculated from resistivity, induction, and porosity logs using the Archie equation. Archie (1942) developed his famous equation by using water resistivity to normalize resistivity values. Archie demonstrated that in 100% water-

saturated rocks, rock resistivity (R_o) is related to (1) porosity (ϕ), (2) water resistivity (R_w), and (3) pore geometry (m). These factors are related in the Archie equation given below.

$$\text{Formation Resistivity Factor F} = \frac{R_o}{R_w} = \phi^{-m},$$

where R_o is the resistivity of 100% water-saturated rock,
               R_w is the resistivity of formation water,
               ϕ is the fractional porosity, and
               m is the lithology exponent or cementation factor.

Archie (1942) also showed that, when hydrocarbons are present, the volume of water in the pore space is reduced and the resistivity is increased in proportion to the amount of hydrocarbons present. The resistivity of the formation in the presence of hydrocarbons is given by the following equation:

$$\text{Resistivity Index I} = \frac{R_t}{R_o} = S_w^{-n},$$

where R_t is the resistivity of the rock containing hydrocarbons,
               R_o is the resistivity of the rock 100% water saturated,
               S_w is the fraction of pore space occupied by water, and
               n is the saturation exponent.

These two equations are combined to give the well-known Archie equation.

$$R_t = R_w \times \phi^{-m} \times S_w^{-n}$$

or

$$S_w = \left(\frac{R_w}{R_t \times \phi^m} \right)^{\frac{1}{n}}$$

The resistivity of the rock (R_t) is obtained from electric logs. Three logs are typically run: a deep investigation, a shallow investigation, and a micro device that investigates the area immediately around the well bore. Borehole corrections are applied and a value for the true resistivity of the formation is calculated. Resistivity of the formation water (R_w) is a

function of salinity and temperature, and it can be measured using produced waters and estimated from water-saturated intervals using cross plots of porosity and resistivity extrapolated to 100% porosity (Pickett, 1966). Porosity is obtained from neutron-density cross plots, as described earlier in this chapter. The "n" value is related to wettability and can be measured in the laboratory but is difficult to obtain from logs. Normally it is assumed to be "2", based on average laboratory values.

The "m" value (lithology exponent or cementation factor) is different from the other terms in the Archie equation in that it is related to rock fabrics, specifically to vuggy porosity. Laboratory (Lucia, 1983) and borehole (Lucia and Conti, 1987) data have demonstrated that the "m" value is a function of the ratio of separate-vug porosity to total porosity, a ratio referred to as the *vug porosity ratio* (VPR). This ratio can be calculated using separate-vug porosity estimated from acoustic logs, and total porosity calculated from neutron and density logs. Figure 15 shows
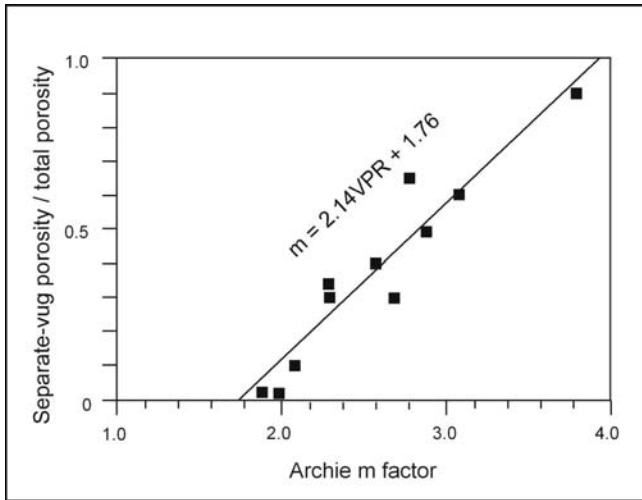
Fig. 3.15. Relationship between Archie m and the ratio of separate-vug porosity and total porosity (vug-porosity ratio, VPR) using laboratory data (Lucia, 1983) and log data. (Lucia and Conti, 1987)

the relationship between VPR and "m" varies based on laboratory measurements and log calculations, which is defined by the following equation:

$$\text{Cementation Factor } m = 2.14\left(\frac{\phi_{sv}}{\phi_t}\right) + 1.76,$$

where ϕ_{sv} is the separate-vug porosity, and
         ϕ_t is the total porosity.

A similar relationship has been developed by Brie et al. (1985) using a model composed of spherical pores. For other approaches see Focke and Munn (1987).

The value of "m" for nontouching-vug carbonates ranges from 1.8 to as high as 4. In the presence of fractures and other touching-vug pore types, the "m" value may be less than 1.8 (Wang and Lucia, 1993; Meyers, 1991). Conventional wisdom suggests using an m value of 2 when no other information is available. However, if the range in m values is not properly accounted for in saturation calculations, the resulting water saturations will be too low if m is larger than 2, and too high if m is smaller than 2. An example is shown in Table 3.

Table 3. The effect of "m" on water saturation calculations

R_t (ohm m)	Porosity	R_w	n	m	Calc S_w (%)
400	0.2	1.6	2	2.0	32
400	0.2	1.6	2	2.5	47
400	0.2	1.6	2	3.0	71

By changing the m value from 2 to 3, the water saturation changes from 32% to 71%, or from oil- to water-productive.   Oomoldic grainstones, for example, have large m factors, and routine Archie calculations using an m of 2 typically result in low water saturations even though the rock is 100% water bearing.

Separate-vug porosity can be calculated from resistivity measurements if water saturation and total porosity are known, because resistivity is a function of the Archie m factor, which is a function of separate-vug porosity. The pertinent equations for a water-bearing interval are given below (Lucia and Conti, 1987):

$$\phi_{SV} = \left(\frac{m - 1.76}{2.14} \right) \phi_t$$

and

$$\phi_{sv} = \left[\frac{\left[\dfrac{\log R_W - \log R_O}{\log \phi_t} \right] - 1.76}{2.14} \right] \times \phi_t$$

where R_o is the resistivity of the water-saturation rock,

R_W is the resistivity of the formation water,

ϕ_{sv} is the separate-vug porosity, and

ϕ_t is the total porosity.

Water saturation is a function of reservoir height, porosity, and petrophysical class or rock-fabric number, as discussed in Chapter 2. The effect of reservoir height and petrophysical class on water saturation is shown in Fig. 16 using generic rock-fabric specific saturation equations (see Chap. 2) and a typical porosity log from a Permian reservoir in West Texas. The three generic rock-fabric petrophysical classes are easily distinguished up to 500 ft above the zero capillary pressure level, and the distinction becomes more apparent at lower reservoir heights. Ideally, vertical successions of rock fabrics can be identified above the transition zone. An example of how this approach can be applied to a typical upward-shoaling cycle, assuming a limestone reservoir, is shown in Figure 16b. If S_{wi} matches the class 1 saturation, a grainstone fabric is indicated. Similarly, a grain-dominated packstone is suggested if S_{wi} matches the class 2 saturation, and a mud-dominated fabric is suggested when S_{wi} matches the class 3 saturation. In this manner, a vertical succession of rock-fabric facies can be calculated using the S_{wi}-ϕ cross plots.

Porosity/water-saturation/rock-type relationships were quantified by Buckles (1965). He showed that, for a given rock type, an equilateral hyperbola equation in the form of

$$\phi \times S_W = C$$

often fits porosity/irreducible-water-saturation data. This equation only applies above the transition zone in the zone of "irreducible water saturation". The correlation factor C has become known as *bulk volume water* and is commonly used to evaluate production potential (Asquith, 1985). In general, a reservoir at irreducible water saturation has a constant correlation factor and a variable factor when in the transition zone. In addition, the pore size decreases with increasing "C". Values higher than
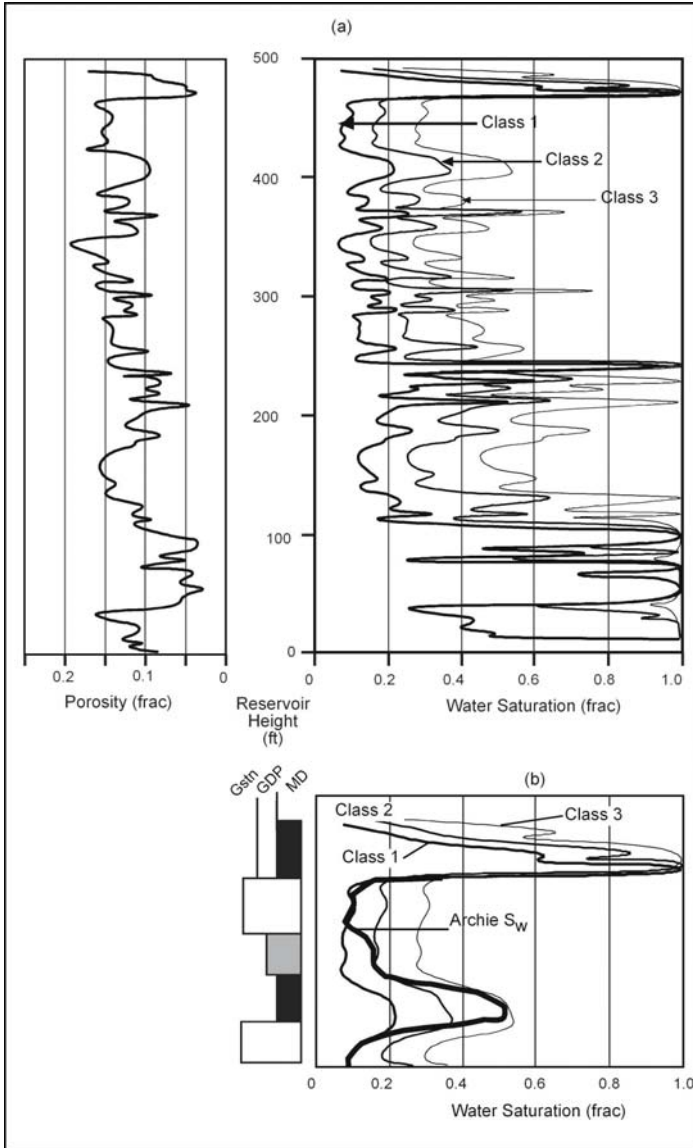
Fig. 3.16. Illustration of the effect of reservoir height and petrophysical class on water saturation. **(a)** A depth plot of water saturation for various classes based on the generic equations, a porosity curve and an assumed zero capillary pressure level. Note that the three generic classes can be distinguished up to 500 ft. **(b)** A vertical succession of rock fabrics interpreted from a comparison of Archie Sw and petrophysical-class Sw assuming a limestone lithology. A grainstone is indicated when Archie Sw matches class 1 Sw, a grain-dominated packstone when it matches class 2 Sw, and a mud-dominated fabric when class 3 Sw is matched

0.04 will tend to have low permeabilities and are likely to produce water (Asquith, 1985).

Rock fabric number (rfn) or petrophysical class can be obtained from Swi-ϕ cross plots in a manner similar to the Buckles formula. An example based on capillary pressure models developed in Chapter 2 is shown in Fig. 17. A general relationship has been developed based on core calibration of wireline log data. The cross plot of Swi-ϕ presented in Figure 18 was constructed using data from the Haradh sector of the Ghawar field (Lucia et al., 2001). Water saturations and porosity values are from wireline logs and rock-fabric descriptions are from thin sections. The cross plot shows a spread of data points that can be grouped by petrophysical class; class 1 large crystalline dolostone, class 2 peloid grain-dominated packstone, and class 3 mud-dominated fabrics. Trend lines and boundaries for these groups were used to develop a power law relationship between rock-fabric number, initial water saturation, and porosity above the transition zone (Lucia et al., 2001; Jennings and Lucia, 2003).
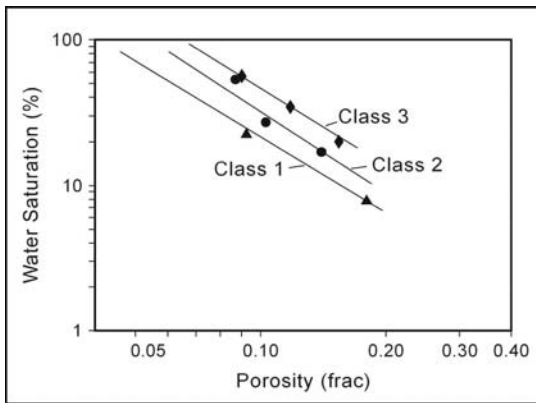
Fig. 3.17. Cross plot of porosity and water saturation for three generic capillary pressure curves a reservoir height of 150 m (500 ft)

$$Log(rfn) = [A + B\log(\phi) + \log(S_{wi})]/[C + D\log(\phi)],$$

where rfn = rock-fabric number ranging from 0.5 – 4,
             S_{wi} = initial water saturation above the transition zone,
             ϕ = porosity,
             and constants of
             $A = 3.1107$, $B = 1.8834$, $C = 3.0634$, $D = 1.4045$.
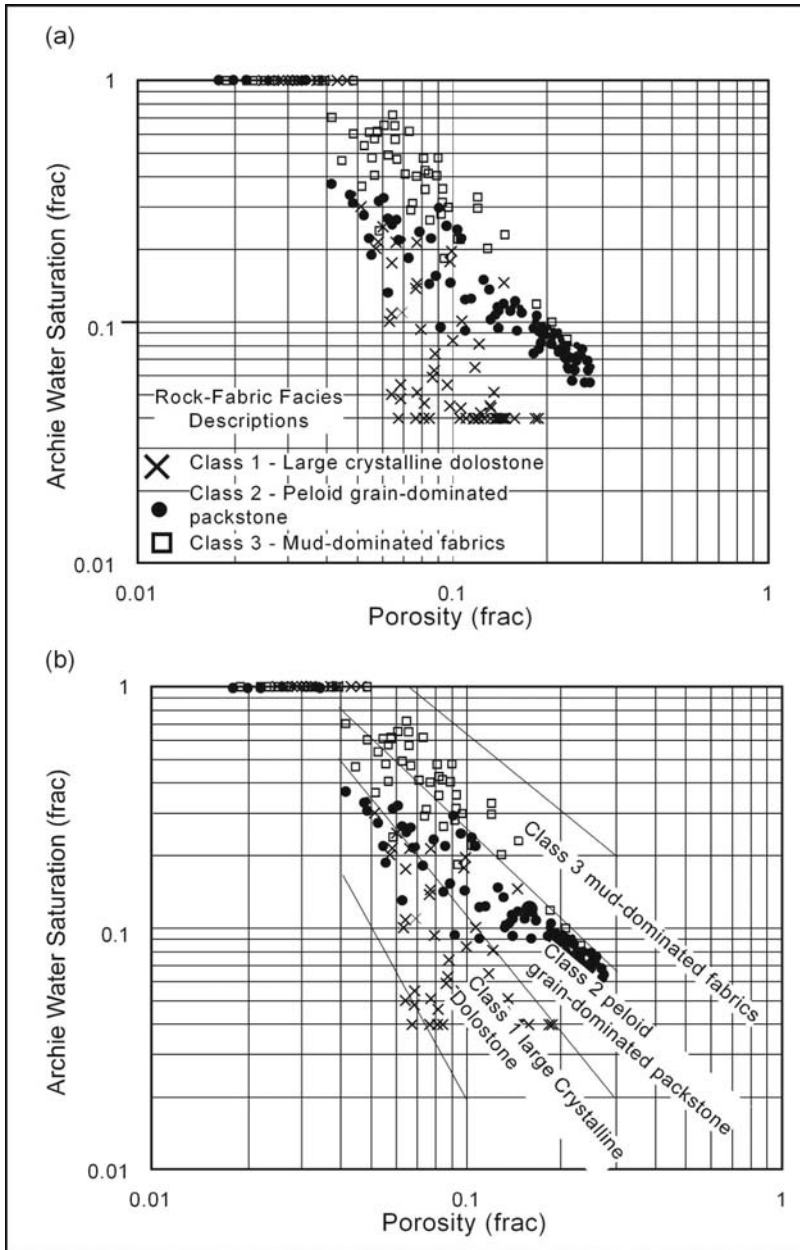
Fig. 3.18. Crossplot of porosity and Archie water saturation calibrated to rock-fabric petrophysical class from a Middle East Arab D well (Lucia et al, 2001). **(a)** A cross plot of the log and thin section data. **(b)** The cross plot showing petro-physical-class fields. This plot is used to construct the rock fabric equation discussed in the text

Limits to the use of this equation are 1) only above the transition zone, 2) where there is no effect of water flooding, and 3) where no intragrain microporosity or touching vugs are present.

This equation is similar to the Buckles equation (1965) and substitutes rfn for the correlation factor C. A comparison of the Sw$_i$-ϕ plots constructed using the rock fabric equation and the Buckles equation shows similarities in the high rfn's and high Buckles' factors and divergence in the low values (Fig. 19). This implies that Buckles factors and rfn's are similar in small pore sizes but that the Buckles relationship does not hold for large pore sizes.
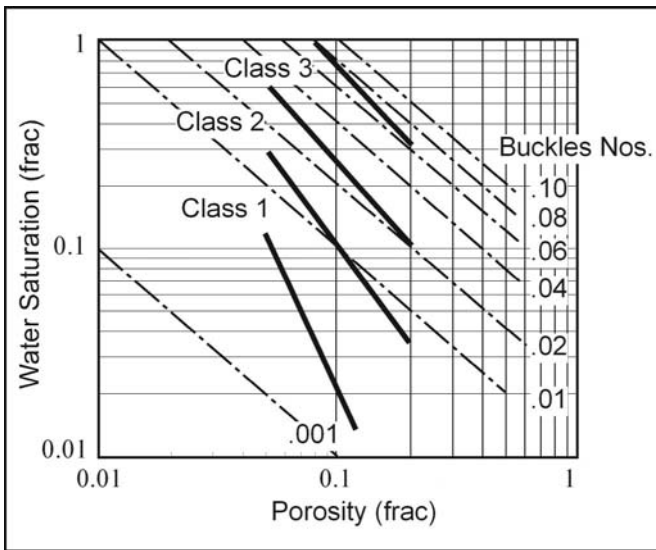
Fig. 3.19. Comparison of Buckles and petrophysical-class Sw$_i$ -ϕ plots

Studies of Permian reservoirs in West Texas and Cretaceous and Jurassic reservoirs in the Middle East have confirmed the usefulness of the rfn equation (Fig. 20). The lower limit of the class 3 field is defined by mudstones from the Cretaceous Shuaiba formation. Data used to constrain the class 3 field are from fine peloid mud- and grain-dominated packstones of the Cretaceous Shuaiba formation, wackestones and mud-dominated packstones from the Jurassic Arab D formation, and fine crystalline mud-dominated dolostones from the Permian of West Texas. The class 2 field is defined by grain-dominated packstones from the Jurassic Arab D formation and grain-dominated dolopackstones and medium crystalline mud-dominated dolostones from the Permian of West Texas. The class 1 field

is defined by large crystalline dolostones from the Jurassic Arab D formation and dolograinstones from the Permian of West Texas.

Although S_{wi}-ϕ cross plots are useful for obtaining rfn or petrophysical class they have limited use for rock fabric or facies identification. Grainstones, grain-dominated packstones, and mud-dominated facies or fabrics with little vuggy porosity can be distinguished using this method if composed of limestone or fine crystalline dolomite. The link between petrophysical class and rock fabric, however, decreases as the dolomite crystal size increases. Medium crystalline mud-dominated dolostones are class 2 and cannot be distinguished from class 2 grain-dominated packstones. In the extreme all the rock fabrics and facies could be class 1 grainstones and large crystalline dolostones.
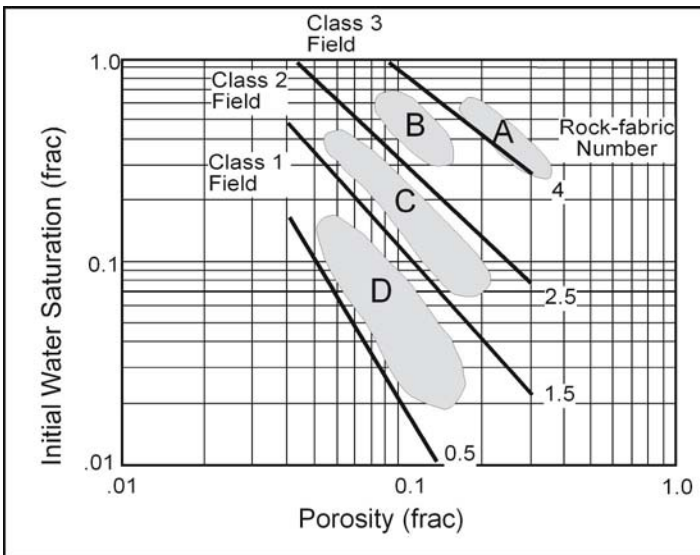
Fig. 3.20. This figure illustrates the generalized relationship between initial water saturation, porosity, and petrophysical class/rock-fabric number. Limitations are 1) above the transition zone, 2) no affect of water flooding, and 3) on intragrain microporosity of touching vugs. **Area A** is defined by Cretaceous Shuaiba mudstones. **Area B** is defined by Cretaceous Shuaiba fine peloid grain-dominated packstones, Jurassic Ghawar wackestones and mud-dominated packstones, and Permian fine crystalline mud-dominated dolostones. **Area C** is defined by Jurassic Ghawar grain-dominated packstones and Permian grain-dominated dolo packstones and medium crystalline mud-dominated dolostones. **Area D** is defined by Jurassic Ghawar large crystalline dolostones and Permian dolograinstones

Importantly, the S_{wi}-ϕ-rfn approach can be applied only when initial water saturation is known. In reservoirs that are under enhanced recovery

operations (water flood, CO_2 flood) current water saturations may be much higher than initial. In these situations intervals that plot in the class 3 field could be either class 3 rock fabrics or class 1 or 2 fabrics that have been flooded with fresher water than connate water. This situation can be resolved with prior knowledge of the petrophysical class profile. Some reservoirs are characterized by a single petrophysical class, so no prior knowledge is required. In reservoirs with more than one petrophysical class, knowledge of the vertical succession of rock fabrics obtained from stratigraphic models can be used to determine the petrophysical class (Fig. 21). With knowledge of petrophysical class profiles, the S_{wi} can be calculated from rock-fabric-specific capillary pressure models and compared with S_w from wireline logs for identifying intervals that have
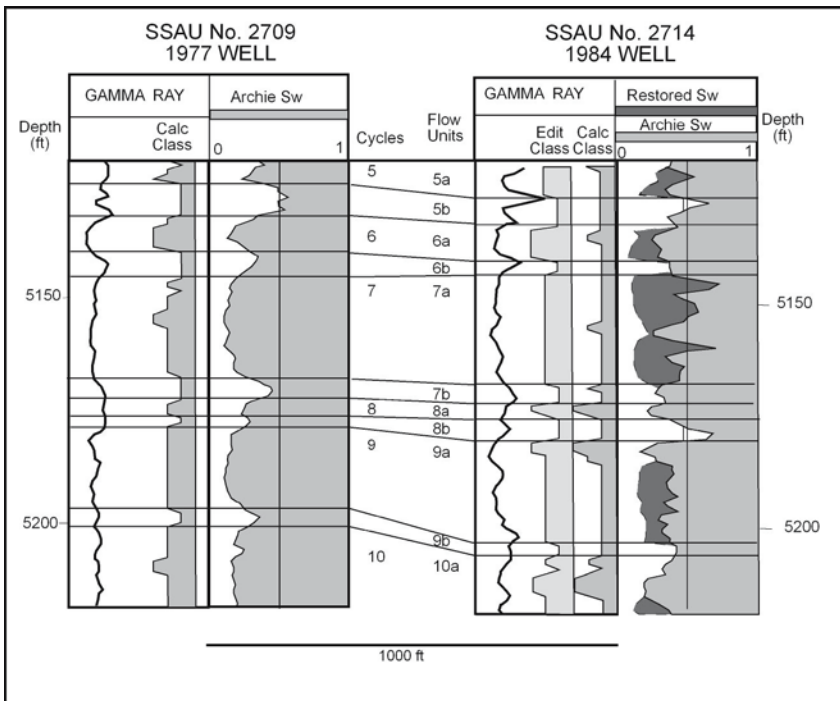
Fig. 3.21. Flooded zone are identified using stratigraphy to obtain petrophysical class for input into rock-fabric capillary pressure models. Well 2709 was completed free of water whereas well 2714 produced considerable flood water at completion. Correlation of petrophysical classes from 2709 to 2714 provides the information needed to use rock-fabric specific saturation-porosity-height equations to estimate initial water saturation. A comparison of Archie saturations with initial saturations indicates intervals invaded by flood water

been flooded. Intervals that have not been flooded are targets for new recovery programs.

In summary, the rfn or petrophysical class required for input into the global transform and rock-fabric-specific capillary pressure models can be obtained from Swi-ϕ relationships above the transition zone and in unflooded wells.

3.4.8 Formation Imaging Logs

Formation imaging tools are an important source of information about touching-vug pore types and have been used to identify depositional facies based on depositional textures (Figs. 22, 23). Most formation imaging logs
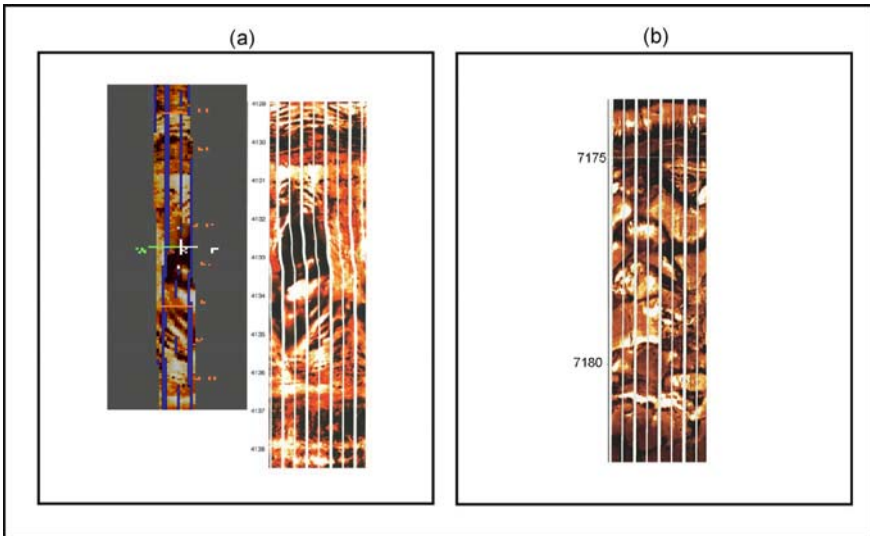
Fig. 3.22. Images indicating a touching-vug pore system. **(a)** Three foot cave in dolostone. **(b)** Collapse breccia in dolostone

provide microresistivity images in water-based mud. However, some tools based on acoustic measurements are also available.   Schlumberger developed the first tool (the FMS), which has evolved into the FMI tool. The FMI tool has four orthogonal arms with two pads. Each pad contains 24 microresistivity buttons for a total of 192 microresistivity readings. The buttons are spaced to give a resolution of 0.2 in. The tool provides borehole drift and direction that can be used to orient the formation images. The fluid in the invaded zone, formation sloughing, enlargement of the borehole, and tool sticking can affect the images.
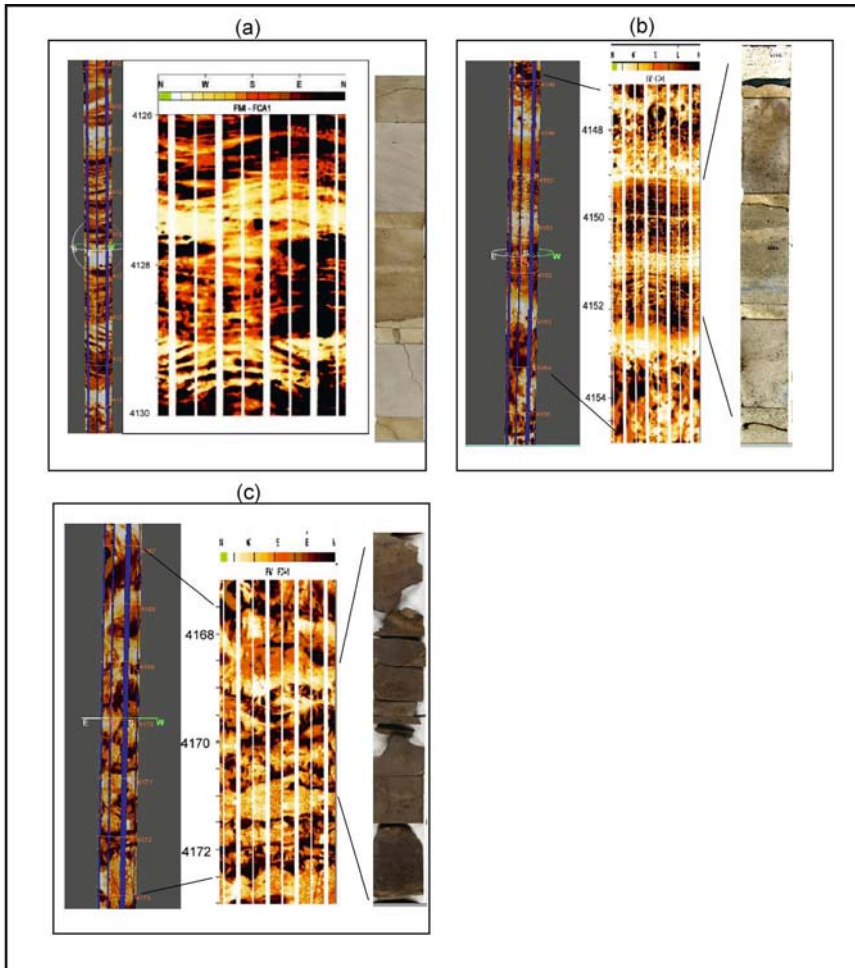
Fig. 3.23. Examples of fabrics from image logs. **(a)** Cross bedded dolograinstone compared with core. **(b)** Laminated tidal flat dolostone with core. **(c)** Patchy porosity in a subtidal dolostone, which could be mistaken for vuggy porosity

The image logs can provide images of fractures, breccias, large vugs, and sedimentary structures useful for correlation and characterizing touching-vug pore systems. Images of carbonates commonly appear as patchy patterns of black (low resistivity, high porosity) in a field of lighter browns (more resistive, lower porosity) (Fig. 23c). This pattern is often misinterpreted as a vuggy carbonate. However, most often no vugs are found in cores from the same interval. Therefore, the images should be calibrated with core descriptions to ensure accuracy. In addition to identifying depositional facies, dips and strikes from foreslope beds of

carbonate buildups have been used to assist in locating rudist mounds and pinnacle reefs.

3.5 Permeability from Wireline Logs

Permeability cannot be obtained directly from wireline logs. The routine method is to correlate core permeability and porosity measurements and to use the resulting porosity-permeability transform to calculate permeability from porosity logs. This method too often averages out the robust permeability variations that are characteristic of carbonate reservoirs.

A more accurate method is to use the global permeability transform using petrophysical class or rfn and interparticle porosity.

$$Log(k) = (a - bLog(rfn)) + (c - dLog(rfn))Log(\phi_{ip})$$

where   *rfn* = rock-fabric number (petrophysical class can also be used)

ϕ_{ip} = Interparticle porosity,
 $a = 9.7982$,
 $b = 12.0838$,
 $c = 8.6711$ and
 $d = 82965$.

This approach provides the key link between permeability and rock fabrics that is critical for 3D modeling. It also accommodates the fact that interparticle, not total porosity is directly correlated with permeability. Petrophysical class or rfn is obtained from gamma-ray logs, porosity logs, or S_{wi}-ϕ cross-plots under the correct conditions. Interparticle porosity is obtained from Δt-ϕ cross properly calibrated with core descriptions. An example of this approach is shown in Figure 23.

Relationships between initial saturation and porosity have been used to estimate permeability without the intermediate step of linking to rock fabric (Timur, 1968: Saner et al., 1997). The rock-fabric approach is similar to these relationships but uses the S_{wi}-ϕ cross plot to determine petrophysical class or rfn, which provides the critical link between petrophysical properties and geologic descriptions needed for quantifying 3D geologic models.

3.6 Initial Water Saturation

Initial water saturation is normally calculated from wireline logs using the Archie equation, or some derivative. However, in old fields under enhanced recovery operations Archie saturations may be affected by flood water and will not be initial water saturations. In these cases it is useful to use rock-fabric-specific capillary pressure models, such as those developed in Chapter 2, to estimate S_{wi}. The porosity required as input into these equations is derived from porosity logs. Petrophysical class may be determined to be constant, based on petrophysical studies. If variable,
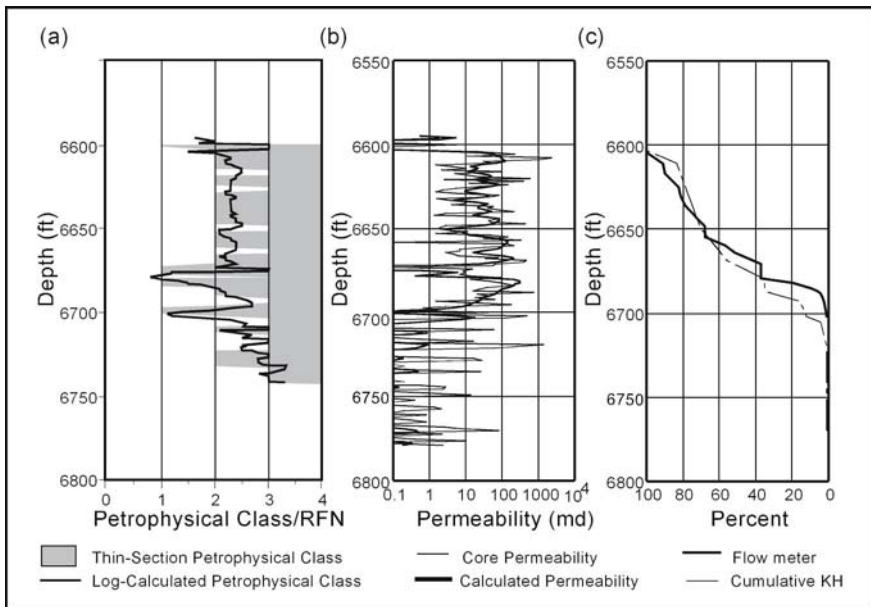
Fig. 3.24. Results of wireline permeability calculation in a Middle Eastern Arab D well (Lucia et al, 2001). **(a)** Calculated RFN from Sw_i-ϕ cross plot compared with thin section petrophysical class. **(b)** Calculated permeability compared with core permeability. **(c)** Comparision of cumulative horizontal calculated permeability (kh) profile with flow-meter data

spectral gamma-ray logs, porosity logs and rock-fabric geologic models may be useful. The difference between S_{wi} from capillary pressure models and Archie S_w from resistivity logs can indicate flooded zones in reservoirs under enhanced recovery programs (see Fig. 21).

3.7 Summary

The first step in constructing a reservoir model is to describe important stratigraphic and rock-fabric attributes seen in core material and to relate the rock fabrics to petrophysical data from core samples. The second step is to calibrate wireline logs with rock fabric and facies descriptions, and to calculate permeability and S_{wi} using rock fabric information and log porosity values. In this manner geologic and petrophysical data are distributed over the field area. The logs commonly used for calibration are gamma-ray, spectral gamma-ray, neutron, density, PEF, acoustic, resistivity/conductivity, and formation imaging logs. The NML log may be useful in some reservoirs.

The basic rock-fabric information required to calculate permeability using the global transform and initial water saturation using rock-fabric-specific capillary pressure models is interparticle porosity and rfn or petrophysical class. To obtain interparticle porosity it is necessary to have an estimate of separate-vug porosity to deduct from total porosity. In the presence of visible separate vugs, such as grain molds, separate-vug porosity can be estimated using an equation with the following form:

$$\phi_{sv} = 10^{a - b\left[\Delta t - \left(\Delta t_f - \Delta t_{ma}\right)\phi\right]}$$

However, experience has shown that the acoustic log response to intragrain microporosity and large separate vugs is similar to the response to interparticle porosity, and that deviations of acoustic porosity from density-neutron porosity can result from rock properties other than separate vugs. As a result, the above equation should not be used unless it has been calibrated with core data from a nearby well.

The rock-fabric number required for input into the global equation can be obtained from the following S_{wi}-ϕ relationship as well as from spectral gamma-ray and porosity logs under the correct conditions:

$$Log(rfn) = \left[A + B\log(\phi) + \log(S_{wi})\right] / \left[C + D\log(\phi)\right],$$

where rfn = rock-fabric number ranging from 0.5 to 4 (petrophysical
        class may also be used),
        S_{wi} = initial water saturation above the transition zone,
        ϕ = porosity,
        and constants of
        $A = 3.1107$, $B = 1.8834$, $C = 3.0634$, $D = 1.4045$.

This relationship is valid only above the transition zone and for values of initial water saturation. Initial water saturation can be obtained using the Archie equation in fields under primary depletion. In fields under enhanced recovery-operations, rfn and petrophysical class must be obtained from petrophysical studies, stratigraphic considerations, and other wireline logs. Unflooded zones can be identified by comparing Archie water saturations with S_{wi} calculated for rock-fabric-specific capillary pressure models.

Accurate values of the cementation factor m are required to calculate water saturations from resistivity logs. The m value is a function of the vug-porosity ratio, which can be estimated using separate-vug porosity calculated from acoustic logs, and total porosity using the following equation:

$$\text{Cementation Factor } m = 2.14\left(\frac{\phi_{sv}}{\phi_t}\right) + 1.76,$$

where ϕ_{sv} = separate-vug porosity and

ϕ_t = total porosity.

Formation imaging logs are used for identifying touching-vug pore systems, which are important in reservoirs because they can dominate fluid flow characteristics. They can also be used to identify facies, such as tidal flats and cross-bedded grainstones. However, the interpretation of FMI images is not simple and core calibration is highly desirable.

Improved permeability estimates are made by using the global permeability transform. The method is as follows.

1. Calculate total porosity using available porosity logs. Check results against core porosity values.
2. Calculate separate-vug porosity using travel-time/porosity/separate-vug relationships. Be sure to calibrate results with core descriptions.
3. Calculate interparticle porosity by subtracting separate-vug porosity from total porosity.
4. Determine the petrophysical class using gamma-ray, porosity logs, and lithology logs calibrated to core descriptions, or the rfn based on S_{wi}-ϕ cross plots.

$$Log(rfn) = \left[A + B\log(\phi) + \log(S_{wi})\right]/\left[C + D\log(\phi)\right],$$

5. Calculate permeability using the global transform.

$$Log(k) = (a - bLog(rfn)) + (c - dLog(rfn))Log(\phi_{ip})$$

Table 4 summarizes the rock fabric information that can be obtained from wireline logs.

Table 4. Calculation of rock-fabric petrophysical parameter from wireline logs.

Input	Output
Total porosity	Separate-vug porosity
Transit time	Interparticle porosity
True resistivity	Petrophysical class/rock-fabric number
R_w	Archie m value
Lithology	Variable m S_w
Saturation exponent (n)	Permeability

Extracting depositional facies and rock fabric information from wireline logs is fundamental to construction of stratigraphic models. Gamma-ray logs, porosity logs, lithology logs, S_{wi}-ϕ cross plots and, more recently, image logs are used for this purpose. The gamma-ray log is the most common log used by geologists, but it has limited use due to the presence of diagenetic uranium and the lack of resolution. However, it has been used to distinguish mud-dominated from grain-dominated fabrics. Neutron and density logs are the principal porosity tools. Porosity can also be used to identify mud-dominated and grain-dominated fabrics if properly calibrated with core descriptions. Under the best conditions S_{wi}-ϕ cross plots can identify grainstone, grain-dominated packstones, and mud-dominated fabrics. Image logs are useful for identifying facies with unique depositional textures, such as tidal flat laminations and cross beds in grainstones.

Neutron, density, PEF, and acoustic logs are the principal logs for extracting mineralogical information, and they are used to identify lithologic facies, such as sandy carbonates and dolostones. Importantly, facies defined by allochems cannot be identified from wireline logs because allochems do respond uniquely to wireline logs. At best, four or five facies can be identified from logs, and they are all rock-fabric facies. Facies likely to be recognized by wireline logs are listed in Table 5.

Table 5. Facies and rock fabrics likely to be recognized from wireline logs.

Wireline Log	Facies – Rock Fabrics
Spectral gamma-ray	Grain-dominated and mud-dominated
Porosity	Grain-dominated and mud-dominated
Acoustic-porosity cross plots	Moldic grainstone
S_{wi}-ϕ cross plots	Grainstone, grain-dominated packstone, mud-dominated limestone fabrics or fine crystalline dolostones
Lithology	Limestone, dolostone, anhydrite beds, salt beds, sandy and shaly carbonate
Image logs	Facies with distinct depositional textures

References

Anselmetti FS, Eberli GP 1999 The velocity-deviation log: A tool to predict pore type and permeability trends in carbonate drill holes from sonic and porosity or density logs. AAPG Bull 83, 3:450-467

Archie GE 1942 The electrical resistivity log as an aid in determining some reservoir characteristics. Trans AIME 146:54-62

Asquith GB 1985 Handbook of log evaluation techniques for carbonate reservoirs. AAPG Publ, Tulsa, Okla, Methods in Exploration Series No. 5, 47 pp

Bebout DG, Lucia FJ, Hocott CF, Fogg GE, Vander Stoep GW 1987 Characterization of the Grayburg reservoir, University Lands Dune field, Crane County, Texas. Report of Investigations No. 168, University of Texas at Austin, Bureau of Economic Geology, 98 pp

Brie A, Johnson DL, Nurmi RD 1985 Effect of spherical pores on sonic and resistivity measurements. Society of Professional Well Loggers Association 26th Ann Logging Symp, Paper W, Houston, Texas, June 17-20, 20 pp

Buckles RS 1965 Correlating and averaging connate water saturation data. Journal of Canadian Petroleum Technology Jan-March 1965:42-52

Dewan JT 1983 Essentials of modern open-hole log interpretation. PennWell Books, Tulsa, Oklahoma, 361 pp

Eberli GP, Maselmetti FS, Incze ML 2003 Factors controlling elastic properties in carbonate sediments and rocks. The Leading Edge, July 2003:654-660

Focke JW, and Munn D 1987 Cementation exponents in Middle Eastern Carbonate Reservoirs. SPE Formation Evaluation 2, 2:155-167

Jennings JW, Lucia FJ 2003 Predicting permeability from well logs in carbonates with a link to geology for interwell permeability mapping. SPE Reservoir Evaluation & Engineering 6, 4:215-225

Lucia FJ 1962 Diagenesis of a crinoidal sediment. J Sediment Petrol 32, 4:848-865

Lucia FJ 1983 Petrophysical parameters estimated from visual descriptions of carbonate rocks: a field classification of carbonate pore space. J Pet Technol, March 1983:629-637

Lucia FJ 1995 Rock-fabric/petrophysical classification of carbonate pore space for reservoir characterization. AAPG Bull 79, 9:1275-1300

Lucia FJ, Conti RD 1987 Rock fabric, permeability, and log relationships in an upward-shoaling, vuggy carbonate sequence. The University of Texas at Austin, Bureau of Economic Geology, Geological Circular 87-5, 22 pp

Lucia FJ, Kerans C, Wang FP 1995 Fluid-flow characterization of dolomitized carbonate ramp reservoirs: San Andres Formation (Permian) of Seminole field, and Algerita Escarpment, Permian Basin, Texas and New Mexico. In: Stoudt EL, Harris PM, (eds) Hydrocarbon reservoir characterization: Geologic framework and flow unit modeling. SEPM Short Course no. 34, pp 129-155

Lucia FJ, Jennings JW Jr, Meyer FO, Michael R 2001 Permeability and rock fabric from wireline logs, Arab-D reservoir, Ghawar Field, Saudi Arabia. GeoArabia 6, 4:619-646

Meyers MT 1991 Pore combination modeling: a technique for modeling the permeability and resistivity properties of complex pore systems. Society of Petroleum Engineers, Annual Techn Conf and Exhibition, Dallas, Texas, SPE 22662, p 77-88

Nugent WH, Coates G.R, and Peebler RP 1978 A new approach to carbonate analysis. Transactions of 19th Annual Logging Symposium, SPWLA, paper 0

Pickett GR 1966 A review of current techniques for determination of water saturation from logs. J Pet Technol November:1425-1433

Pirson JS 1983 Geologic well log analysis. Gulf Publishing Company, Houston, Texas, 475 pp

Saner S, Kissami M, and Al-Nufaili S 1997 Estimation of permeability from well logs using resistivity and saturation data. PE Formation Evaluation 12, 1:27-32

Schlumberger Log Interpretation Charts, 1989, 151pp

Timur A 1968 An investigation of permeability, porosity, and residual water saturation relationships. SPWLA Ninth Annual Logging Symposium, June 23-26, 1968:1-18

Wang FP, Lucia FJ 1993 Comparison of empirical models for calculating the vuggy porosity and cementation exponent of carbonates from log responses. The University of Texas, Bureau of Economic Geology, Geological Circular 93-4, 27 pp

Chapter 4 Depositional Textures & Petrophysics

4.1 Introduction

Petrophysical properties can best be distributed in the interwell space if constrained by a *chronostratigraphic framework.* Petrophysical data obtained from wireline logs and cores are one-dimensional and have no intrinsic spatial connotation other than the frequency and spacing of the data. To construct a three-dimensional image, the interwell volume must be filled with data using a correlation method. Because the volume of the reservoir traversed by wellbores is about one millionth of the total rock volume, 99.99% of the reservoir model is dependent upon the method used to correlate petrophysical data between wells. Geostatistical methods are available for filling the space between wells with a heterogeneous pattern of petrophysical properties, and this method will be discussed in a later chapter. Whereas unconstrained geostatistical methods are an improvement over using a few average properties to construct a model, the resulting images are unrealistic and produce unreliable performance predictions. Constructing a realistic model required that extrapolation methods be constrained by (1) a chronostratigraphic geological framework and (2) knowledge of geologic processes that form and modify petrophysical properties.

Key steps in constructing a petrophysical model are (1) relating rock fabrics to petrophysical parameters, (2) identifying the geological processes that formed the rock fabrics, (3) describing a cycle-based sequence stratigraphic framework, and (4) distributing petrophysically significant rock-fabric bodies within the stratigraphic framework.   In Chapter 2 we discussed the relationship of rock fabrics to pore-size distribution and to petrophysical parameters and identified key fabric elements to describe. In Chapter 3 we discussed the description of 1-D vertical successions of rock fabrics from cores and the relationship between rock fabrics and petrophysical properties to wireline log measurements. In this chapter we will discuss the origin of depositional textures, the

petrophysical properties of carbonate sediments, and the sequence stratigraphic framework. In the following chapters we will discuss the formation of carbonate reservoirs through diagenetic overprinting of the depositional texture and the resulting distribution of rock fabrics and petrophysical properties.

## 4.2 Properties of Carbonate Sediments

The initial process in the formation of a carbonate reservoir is sedimentation. Carbonate sediments are commonly produced in shallow, warm oceans either by direct precipitation out of seawater or by biological extraction of calcium carbonate from seawater to form skeletal material. The result is sediment composed of particles with a wide range of sizes, shapes, and mineralogies mixed together to form a multitude of textures, chemical compositions and, most importantly, associated pore-size distribution.

Carbonate sediments can be divided into loose sediment and sediment bound together as a result of organic activity. Sediment can be organically bound by filamentous algae to form algal stromatolites, or by encrusting organisms such as the modern coralline alga *Lithothamnium* or Devonian stromatoporoids to form reefs. The binding action can create large constructional cavities, which result in highly permeable sediment (Fig. 1).

More commonly, carbonate sediments are composed of loose grains. The grain size of the loose sediment is generally bimodal, being composed of a sand-sized (or larger) fraction and a mud-sized fraction. In general, sand-sized carbonate grains reflect the size of the calcareous skeletons or their calcified hard parts. Coral fragments, for example, are typically boulder-sized particles, whereas shell material is typically much smaller. Skeletal sediment undergoes various degrees of mechanical, biological, and chemical breakdown into smaller particles caused by exposure to strong marine currents, boring by fungi and algae, browsing by animals searching for food, and disintegration of organic material (Fig. 2). Skeletal breakdown can produce mud-sized particles (Gischler and Zingeler 2002). Most mud-sized particles, however, are aragonite crystals produced by calcareous algae organisms (Fig. 3) and by precipitation from sea water (Milliman et al. 1993). Calcareous planktonic cocolithids and forams are also mud size.
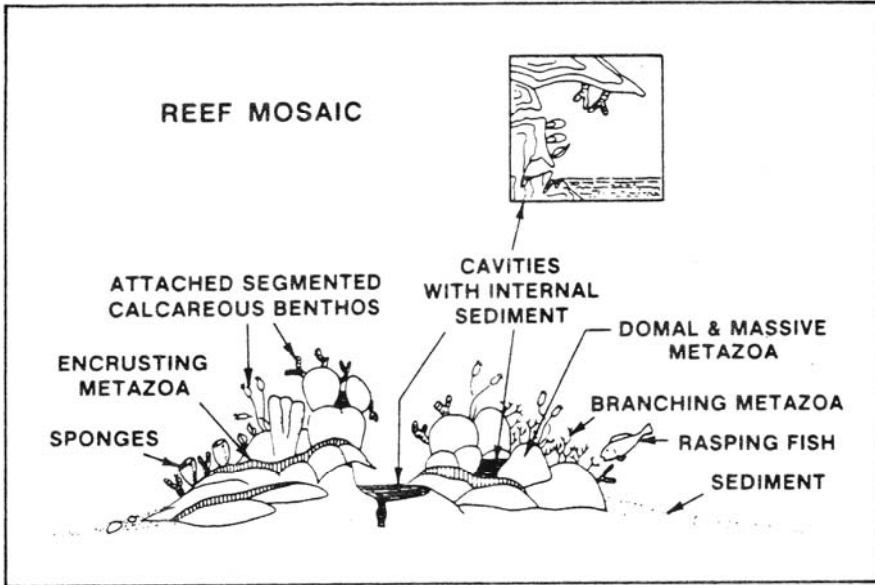
Fig. 4.1. Diagram of a reef assemblage showing large constructional cavities. The large constructional cavities and large coral fragments produce a depositional texture with large pore sizes. (after James 1984)
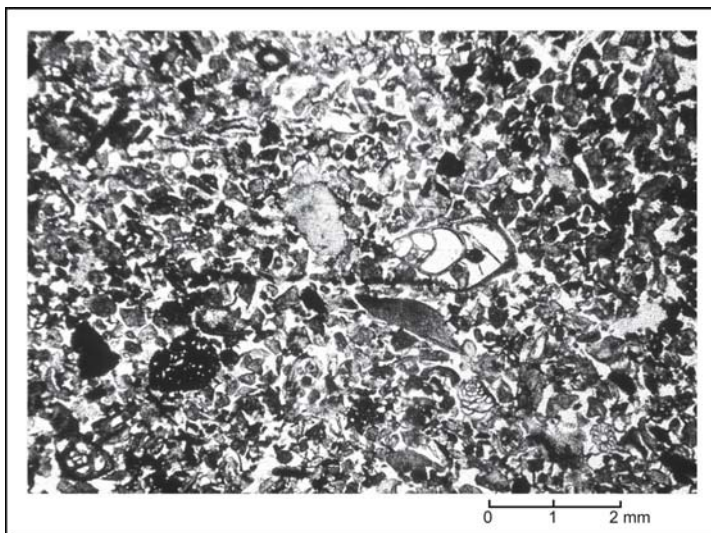
Fig. 4.2. Photomicrograph of a modern skeletal grainstone composed of coral, mollusks, coralline algae, and foram fragments. The size of the intergranular pores is controlled by the size of the grains. Note intragrain pore space within forams and gastropod
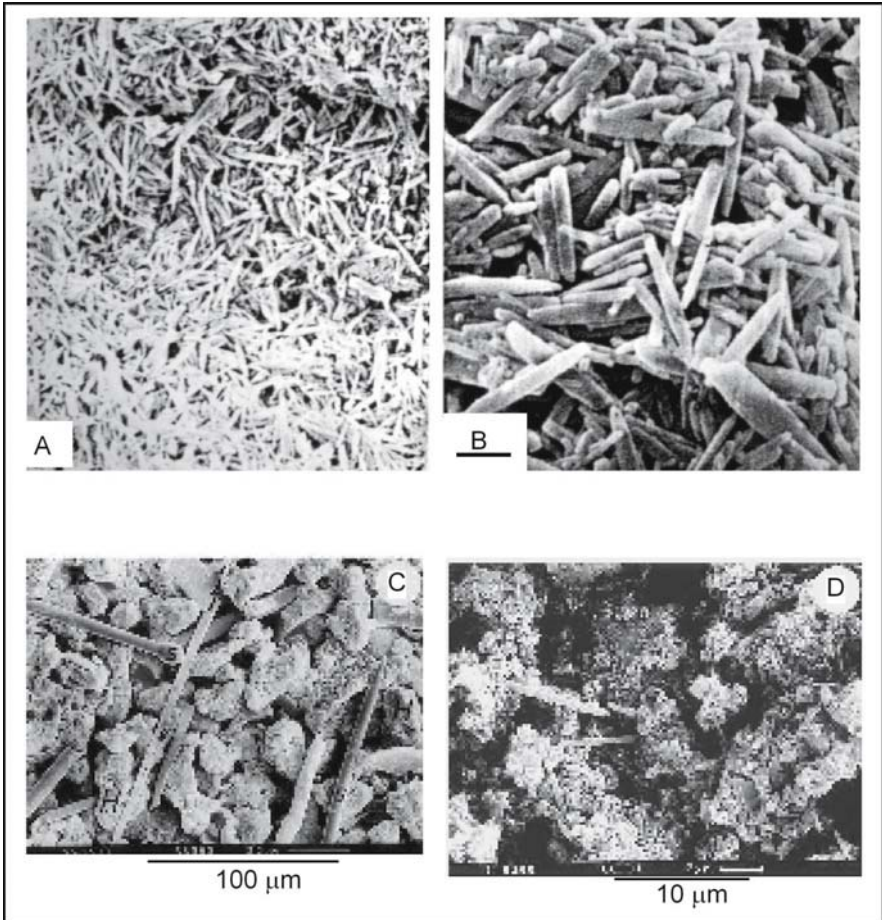
Fig. 4.3. Electron photomicrographs of carbonate mud. **A** and **B** Aragonite needles. The bar in **B** is 1 µm. (after Gebelein et al. 1980). **C** and **D** Mud–sized grains composed of skeletal material. (after Gischler and Zingeler 2002)  The size and shape of the pore space is controlled by the size and shape of the needles and grains, and the pore sizes are very small because the particles are very small

Biological and chemical processes can increase as well as decrease the particle size. Burrowing organisms pass mud-sized sediment through their digestive tract and produce sand-sized fecal pellets (Fig. 4), thus creating sand-sized particles out of mud-sized particles. Grain size can be enlarged by algal coatings forming oncoids. Forams can bind mud and pellets together to form grapestone particles.

Carbonate particles that are related to chemical processes include ooids, which are formed by chemical precipitation around a nucleus grain
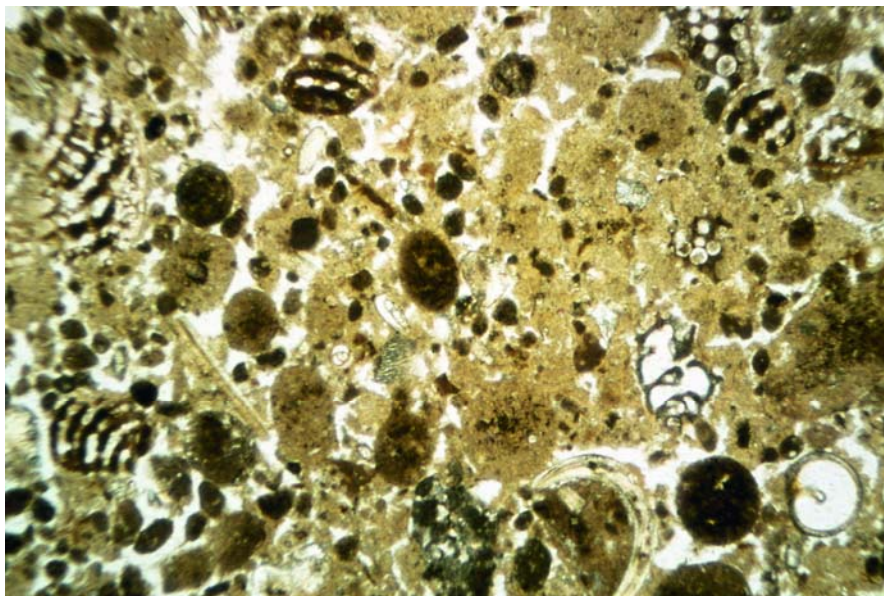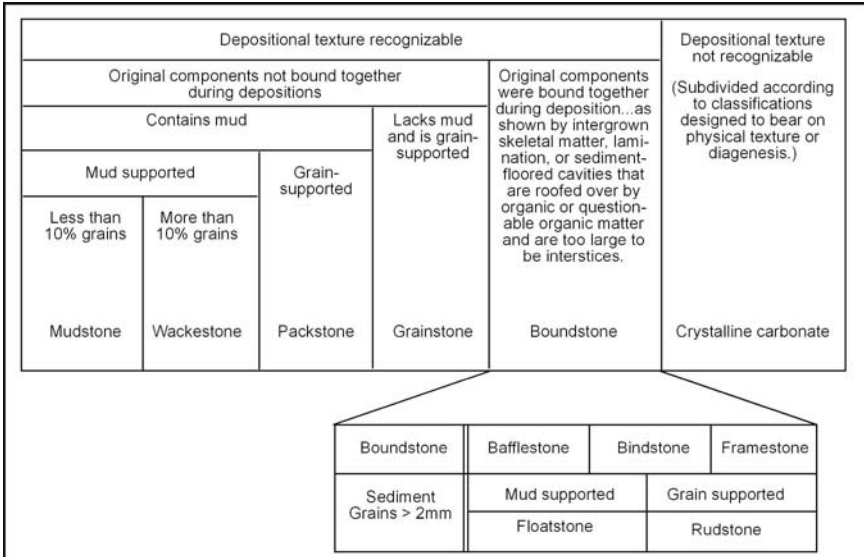
Fig. 4.4. Photomicrograph of modern pelleted carbonate mud. This sediment would be classified as a grain-dominated packstone because of the intergrain pore space. However, compaction may destroy the intergrain pore space, and the resulting fabric would be classified as a mud-dominated packstone or peloid wackestone. (courtesy of R. B. Perkins)

in the presence of strong current action; pisolites, which are a product of subaerial exposure (Gerhard 1985); and intraclasts, which are produced early by the breakup of lithified sediment in either the subaerial or subtidal environment.

Dunham's (1962) classification (Fig. 5) divides carbonates into organically bound sediments and loose sediments. A key consideration in Dunham's classification of loose sediment is the bimodal texture of carbonate sediment. Sediments are classified first by mud vs. grain support and then by amount of mud in the sediment. Generic names, such as wackestone and grainstone, are modified with grain type such as "trilobite wackestone" or "ooid grainstone."

Dunham's boundstone class was further divided by Embry and Klovan (1971) because carbonate reefs are commonly composed of large reef-building organisms, such as corals, sponges, and rudists, that are either bound together or transported, forming sediments composed of very large particles. Embry and Klovan devised a method of describing the complex

Depositional texture recognizable					Depositional texture not recognizable
Original components not bound together during depositions			Lacks mud and is grain-supported	Original components were bound together during deposition...as shown by intergrown skeletal matter, lamination, or sediment-floored cavities that are roofed over by organic or question-able organic matter and are too large to be interstices.	(Subdivided according to classifications designed to bear on physical texture or diagenesis.)
Contains mud		Grain-supported			
Mud supported					
Less than 10% grains	More than 10% grains				
Mudstone	Wackestone	Packstone	Grainstone	Boundstone	Crystalline carbonate

| Boundstone	Bafflestone	Bindstone	Framestone
Sediment Grains > 2mm	Mud supported		Grain supported
	Floatstone		Rudstone

Fig. 4.5. Dunham (1962) and Embry and Klovan (1971) classification of carbonate rocks

textural relationships, introducing the terms bafflestone, bindstone, and framestone to describe autochthonous (in-place) boundstone reef material, and the terms floatstone and rudstone to describe allochthonous (transported) reef sediment with particles larger than 2 mm in diameter. Rudstone is grain-supported whereas floatstone is mud-supported sediment.

This method of describing carbonate textures can also be used to describe pore geometries in carbonate sediments because "grain-supported" implies intergrain pore space between sand-sized grains whereas "mud-supported" implies microporosity between mud-sized particles.   However, petrophysical descriptions should divide the packstone class into mud-dominated and grain-dominated packstones, as described in Chapter 2, because the intergrain volume of a packstone may be filled with both intergrain pores and mud or with only mud. The pore-size distribution in bafflestones and bindstone is often not related to particle size and shape, and the pore types may best be grouped in the touching-vug class. The pore-size distribution of floatstone and rudstone depends upon the texture of the intergrain volume. If the intergrain volume is composed of lime mud (floatstone), the size of the mud particles will control pore size. If the intergrain volume is partially filled with or devoid of mud (rudstone), the size of the grains and intergrain mud will control the pore size.

Enos and Sawatsky (1981) measured the porosity and permeability of modern carbonate sediments. Their results show a general increase in porosity as the mud fraction increases (Fig. 6a). Average porosity of grainstone is about 45%, similar to extremely well sorted sandstone. Porosity increases up to 70% with increasing amounts of carbonate mud, a change that can be related to the open stacking of needle-shaped aragonite crystals found in carbonate mud (Fig. 3).
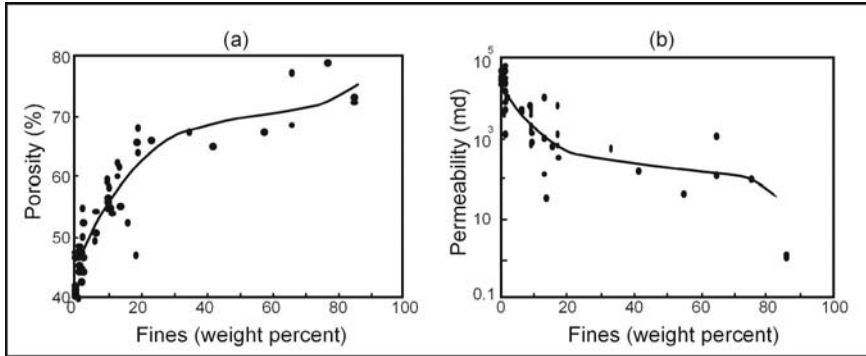

Fig. 4.6. Porosity and permeability data versus percent lime mud from Holocene carbonate sediments of the Bahamas and the Florida Keys. **a** Porosity increases as the percent fines increase to a value of 70%. **b** Permeability decreases as the percent fines increase because of the small pore size associated with mud-sized particles. (Enos and Sawatsky 1981)

Permeability is a function of pore-size distribution, which is directly related to the porosity, particle size, and sorting in Holocene sediments. The permeability of mud-dominated sediments is between 1 and 200 md because of the small size of the pores between the 5-10 μm aragonite crystals (Fig. 6b). Permeability increases as the volume of mud decreases from about 20 to 0%, indicating an increasing influence of grain size on pore size. The permeability of grain-dominated sediment with some intergrain mud averages about 2000 md

Pore space in carbonate sediment is found both between grains/crystals and also within grains. The sizes of the interparticle pore space are related to the size and shape of the sediment particles. Carbonate particles have a wide variety of shapes, such as spherical ooids, flat and coiled shell fragments, platy and rod-shaped algae, and needle-shaped aragonite crystals, and various sizes, such as 5-μm aragonite crystals, sand-sized ooids, and boulder-sized coral fragments. The sizes of intraparticle pore space are related to the structure of the grains. The living chambers of gastropods and forams are relatively large pores (Figs. 2, 4). Micro-

porosity is found between the aragonite needles that composed modern ooids (Folk and Lynch, 2001) (Fig. 7) and peloids. It is estimated that modern ooids and peloids contain 15% microporosity. Pore space located within grains is connected only through the interparticle pore space and is a type of separate-vug porosity. These factors result in a large variability of porosity and pore-size distribution in unconsolidated carbonate sediments. *However, the intergrain pore size and pore-size distribution are always a function of the size, shape, and sorting of particles.*
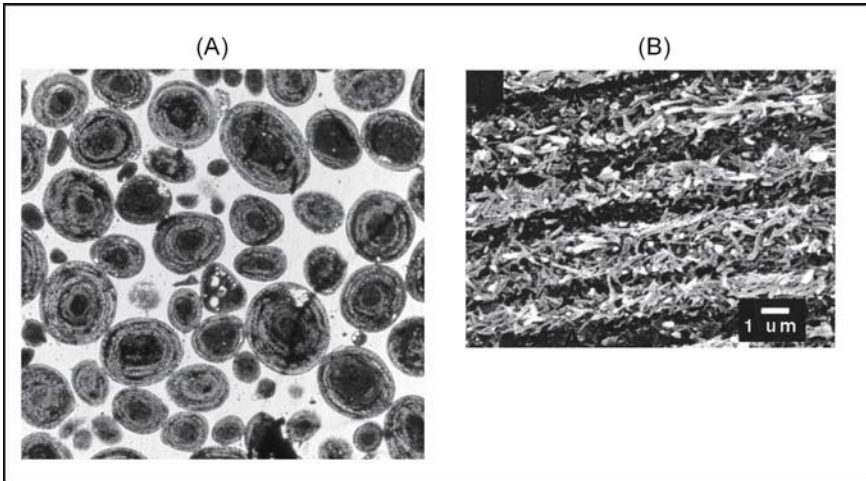
Fig. 4.7. Photomicrograph of a resedimented Bahamas oolite **(A)** and a detailed photo from a scanning electron microscope **(B)** showing micro pore space within the micro-size aragonite crystals that compose the ooid

A comparison of the porosity and permeability between Holocene sediments and carbonate reservoirs reveals that modern sediments have much higher porosity and permeability. Average porosity for reservoirs in the United States is 12% and average permeability is about 50 md (Schmoker et al. 1985), whereas carbonate sediments have porosity values higher than 40% and typical permeability values higher than 100 md. Therefore, all modern carbonate sediments have reservoir-quality permeability.

An important consideration in diagenesis is the mineralogical composition of the carbonate sediment. Carbonate sediments are composed of three forms of carbonate that are variably stable (Walter 1985; Fig. 8). Aragonite has an orthorhombic crystal structure and is unstable at surface conditions. Calcite has a triclinic crystal structure and
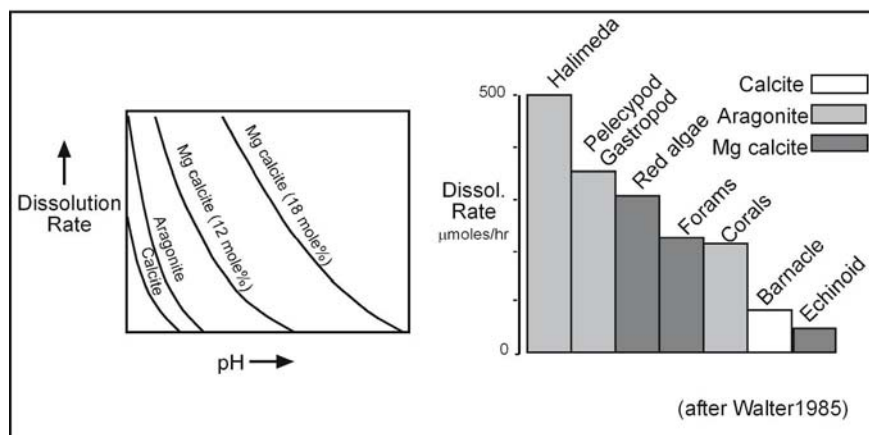
Fig. 4.8. Relationships between dissolution, texture, and mineralogy for carbonate sediments. (after Walter 1985)

is stable at surface conditions in its pure form. However, magnesium can substitute for calcium in the crystal lattice, and stability decreases with increasing amounts of magnesium. Holocene calcite has as much as 20% magnesium carbonate; calcite with significant magnesium substitution is referred to as high-magnesium calcite.

The mineralogy of marine organisms varies with phyla and over geologic time (Fig. 9). For instance, modern red algae are composed of high-magnesium calcite, brachiopods are composed of low-magnesium calcite, and coral is composed of aragonite. Most modern ooids are composed of aragonite, but many ancient oolites were composed of low-magnesium calcite. Carbonate mud is normally composed of a mixture of the three minerals, aragonite commonly being the most abundant.

4.3 Sequence Stratigraphic Framework

The spatial distribution of petrophysical properties in carbonate sediments is controlled by the distribution of depositional textures, which is best described in terms of a chronostratigraphic, sequence stratigraphic framework composed of high-frequency cycles (HFC), high-frequency sequences (HFS), and composite sequences (Kerans and Fitchen 1995). A HFC is a chronostratigraphic unit defined as a succession of genetically related textures (beds or bedsets) bounded by marine flooding surfaces and their correlative surfaces. A HFS is an unconformity-bound series of HFCs that show transgression and progradation. A composite sequence is
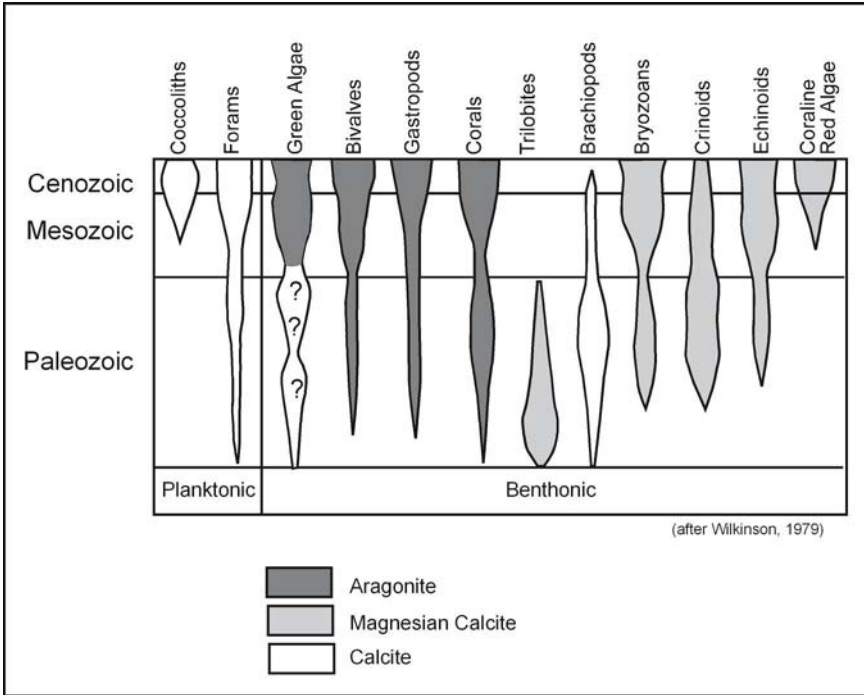
Fig. 4.9. Mineralogy of marine organisms. (Wilkinson 1979)

an unconformity-bound depositional sequence composed of multiple HFSs.

Marine flooding events and associated unconformities are believed to be the result of eustatic sea-level fluctuations. Assuming a constant rate of subsidence, each HFC begins with a flooding event produced by a sea-level rise, resulting in a transgressive, retreating shoreline and an increase in space available for carbonate sediment to accumulate (referred to as accommodation space, Fig. 10). Sea-level rise is followed by a stillstand during which sediment partially or completely fills accommodation space. The stillstand is followed by a sea-level fall, reducing accommodation space, and resulting in a prograding, regressive shoreline and transport of sediment from the shelf into the basin (Fig. 10). During the sea-level fall, the carbonate platform may be exposed, sedimentation may cease, and erosion may occur. A sea-level rise produces another flooding event, and the depositional cycle is repeated. *Flooding events approximate chronostratigraphic surfaces and define the HFC as a time-stratigraphic unit.*

The causes of repeated flooding events include cessation of carbonate sediment production due to filling of accommodation space (autocyclic),
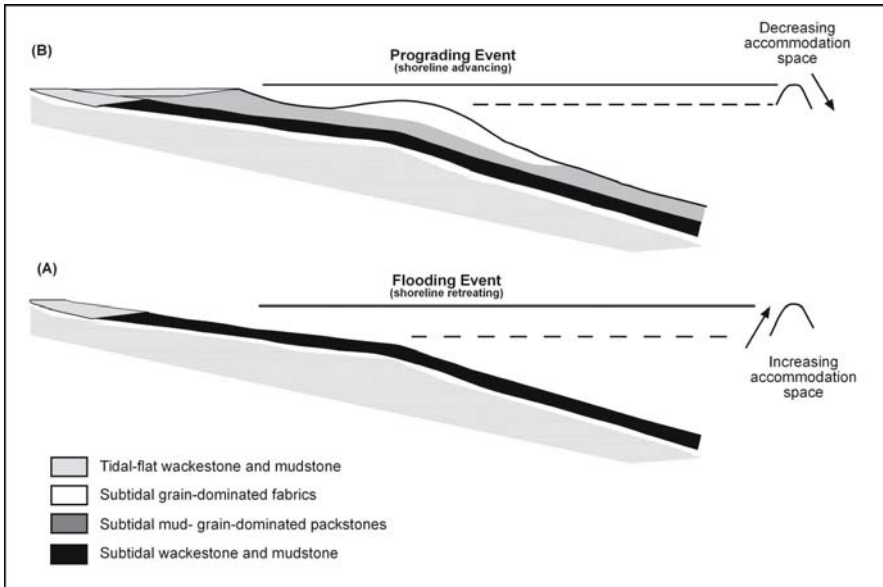
Fig. 4.10. Diagram illustrating the development of a depositional cycle through a combination of structural subsidence and eustatic sea-level fluctuations. **(a)** flooding of the shelf occurs with sea-level rise, which increases accommodation space for sediment to fill. **(b)** Progradation occurs when sea level falls. Decreasing accommodation space results in sediments building to sea-level, higher energy environments, and transport of sediment on and off the shelf

episodic subsidence, and externally forced fluctuations in sea level (allocyclic). Externally forced fluctuations are thought to be produced by changes in continental ice volume due to climatic changes, possibly related to systematic changes in the Earth's orbit (eustasy) (Kerans and Tinker 1997). It is well known that during the Pleistocene, the sea level fluctuated in response to the waxing and waning of continental glaciers. For our purposes, the origin of the HFC is not an issue, and we will assume a eustatic origin for the cyclicity commonly observed in carbonate reservoirs.

The high-frequency cycle concept has direct application to reservoir characterization and flow-modeling studies in carbonate reservoirs and is the most significant stratigraphic element in the stratigraphic framework. The upward and lateral succession of rock fabrics within the HFC can be translated into predictable patterns of petrophysical values that aid in log interpretation and in quantifying the framework in petrophysical terms for performance prediction.

4.3.1 High-frequency Cycles

High-frequency cycles are defined in one dimension by vertical successions of depositional textures and in two dimensions by lateral facies progressions. The two classic vertical successions that define cycles are (1) a subtidal cycle composed of a succession of textures that increase in grain size and sorting upward, and (2) a tidal-flat-capped succession of subtidal textures.

The vertical succession of texture reflects changes in current energy, and cycle thickness reflects accommodation space and sedimentation rate. The lateral distribution of depositional facies reflects energy levels, topography, and organic activity. These changes can be related to the geometry of the carbonate platform. Carbonate platform geometry has been divided into ramps and rimmed shelves (Reed 1985). Ramps have a gently dipping profile (0 to about a 2° dip; Fig. 11) and depositional rimmed shelves are those that have actively aggraded to form a steep shelf margin (15° dip to near vertical). Ocean currents are produced by tides and waves and are concentrated at major topographic features, such as ramp and rimmed shelf margins, islands, and shorelines (Fig. 11B). The combination of topography and ocean currents produces a facies progression from landward to basinward of (1) peritidal mud- to grain-dominated textures and evaporite facies, (2) middle-shelf mud-dominated and occasional grain-dominated packstone facies, (3) shelf-crest grain-dominated facies and reefs, (4) outer-shelf mud- to grain-dominated facies, and 5) basinal mud-dominated facies and debris flows (Figs. 10a and 11).

The peritidal facies is composed of tidal-flat capped cycles and is normally found in the most landward position of a carbonate shelf. The cycles are formed by filling accommodation space to sea level and deposition of sediment above sea level by transport of carbonate sediment onto the mud flat by tidal and storm currents. Therefore, tidal-flat capped cycles demonstrate a seaward movement of the shoreline by prograding intertidal and supratidal sediments over subtidal sediments (Fig. 13B).

Tidal-flat capped cycles are normally formed where the shoreline is sheltered from wave action, and the subtidal sediments are dominated by carbonate mud with grains concentrated in channels and beach ridges. The tidal flat environment is divided into the intertidal zone, which is defined as the vertical interval between mean-high and mean-low tides and is covered by sea water twice a day, and the supratidal zone, which is defined as the area beyond the reach of the daily tides and is covered by normal sea water only during spring and storm tides.
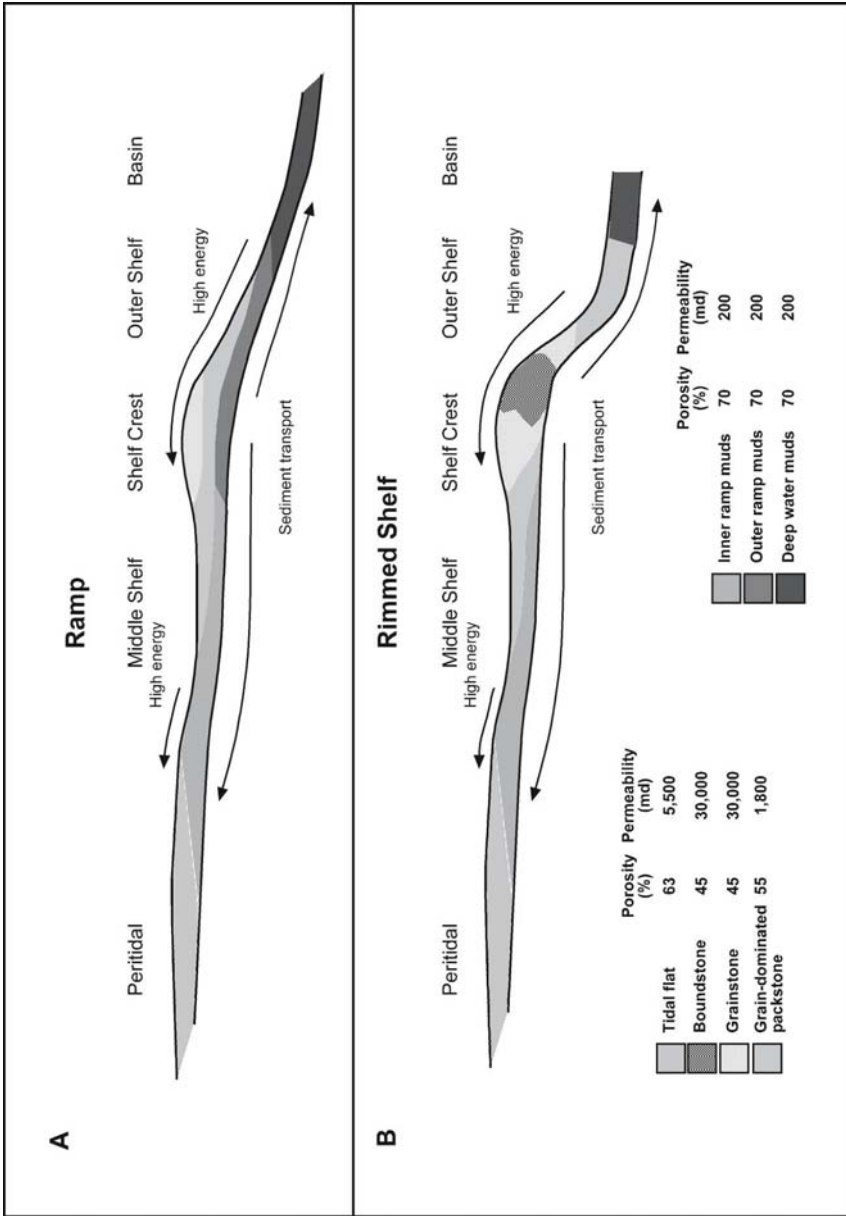
Fig. 4.11. Facies progression of depositional environments from land to basin for **A** ramp profile and **B** rimmed-shelf profile. The facies are systematically arranged based on topography and current energy. Characteristic Holocene porosity and permeability values for depositional textures from Enos and Sawatsky (1981) are listed

Sediment of the intertidal zone is characterized by burrowed, pelleted muddy sediment with no characteristic sedimentary structures and is best identified by its location immediately below a supratidal unit (see Table 1). Algal laminates are concentrated at the boundary between the intertidal and supratidal zones. The supratidal zone, sometimes referred to as the sabkha, referring to the extensive Persian Gulf supratidal flats (Patterson and Kinsman 1981) is easily recognized by characteristic irregular laminations, pisolites, mud cracks, intraclasts, and fenestral fabrics formed in response to short bursts of sediment deposition followed by long periods of desiccation (Table 1; see Shinn 1983 for a detailed description of the tidal-flat environment).

Where wave energy dominates the shoreline environment, the tidal-flat environment is replaced by the beach environment. This commonly occurs in high-energy environments where grainstone shoals build out of water to form islands as well as along high-energy coastlines isolated from clastic sedimentation. The beach environment is divided into the shoreface environment, which is located above low tide and influenced by tidal action and wind velocity, and the foreshore environment, which is located below low tide and influenced by longshore currents. An upward-increase in grain size and sorting is typical for shoreline deposits, which results from an increase in current energy produced by shallowing as the shoreline is approached (see Inden and Moore 1983, for detailed description).

In arid climates, evaporite deposits may form by precipitation from standing bodies of marine water isolated from the ocean by tidal floats or grainstone bars (Lucia 1968, 1972; Lloyd et al. 1987). A hypersaline lagoon that is restricted from the ocean by a discontinuous barrier is the depositional model most commonly used to explain evaporite deposits. Sea water must be evaporated to about one-third its original volume in order for gypsum to be deposited and to about one-tenth of its volume in order for halite to be deposited.   The amount of evaporation is a function of the net rate of evaporation, the amount of exchange between the hypersaline lagoon and the ocean, and the amount of hypersaline water that flows down in the underlying strata (reflux; Deffeyes et al. 1965). If there is no outflow, the salinity will be high and halite will be deposited; if there is a moderate amount of exchange, the salinity will be less and gypsum will be deposited; and if there is good exchange, no evaporites will form.

Hypersaline lagoons vary in size and origin. The Gulf of Karabugas, which is part of the Caspian Sea, has an area of about 14,000 km^2 and is restricted from the Caspian Sea by a barrier bar. Coastal salinas are much smaller; the Pekelmeer on the island of Bonaire, Netherlands Antilles, has a surface area of about 3 km^2 and is isolated from the ocean by a coral beach. The types of restrictions vary as well. The Pekelmeer is fed by a flow of

ocean water through the coral beach, whereas the Gulf of Karabugas is fed through a narrow channel connecting it to the Caspian Sea. In all known examples, however, the connection between hypersaline bodies of water and the open ocean is very small compared with the surface area of the hypersaline lagoon (Lucia 1972).

Depositional evaporites are recognized by laminated and coalesced-nodular textures. Laminated anhydrite suggests the deposition of gypsum crystals that precipitate within a body of water and fall to the bottom as sediment and are later altered to anhydrite during burial. Coalesced-nodular textures suggest the growth of gypsum crystals attached to the bottom and later modified by diagenetic processes, such as the alteration from gypsum to anhydrite with burial (Warren and Kendall 1985). Beds of depositional evaporites are found immediately above subtidal deposits and within supratidal deposits. When anhydrite occurs within a subtidal sequence it most likely represents a change in sea level and marks the top of a high-frequency cycle. The occurrence of evaporites within supratidal deposits can suggest a change in sea level or a growing restriction related to sedimentary processes, such as the construction of a barrier bar.

Table 1. Sequence of sedimentary features in tidal-flat capped cycles (Lucia 1972)

Interpreted sedimentary environment	Sedimentary structures	Fossils	Texture
Supratidal	Irregular laminations Lithoclasts Mud Cracks Fenestrae Pisolites Bedded anhydrite	Rare	Grain-dominated packstone to wackestone
Intertidal	Algal stromatolites Burrowing	Few Gastropods, forams, ostracods	Grain-dominated packstone to wackestone
Tidal channel	Current lamination Cross-bedding	Few Echinoids, mollusks	Lithoclasts, fine sand-sized pellets and some mud
Subtidal	Burrowing	Locally abundant Typically a restricted fauna of gastropods, forams, and lamellibranchs	Grainstone to wackestone

Subtidal cycles deposited in the quiet waters of the middle-shelf environment are typically mud-dominated textures with an upward change in faunal content and increasing volume of allochems. As sedimentation fills accommodation space, however, the sediment surface is moved closer to wave and storm currents and grain-dominated packstones cap the cycles. Burrowing organisms churn the muddy sediment and produce pellets that, together with shell material, compose the grain fraction of the sediment. Local topography may produce sufficient current energy to produce grain-dominated fabrics and patch reefs. Whereas sediments deposited in this environment may have interpellet pore space, compaction of the pellets with burial commonly alters the fabric to a pelleted wackestone or mud-dominated packstone (see Enos 1983 and Wilson and Jordan 1983 for more detailed descriptions).

Grain-dominated packstones and grainstones generally are produced in the high-energy conditions found in the shelf crest by winnowing of lime mud (Figs. 11, 12). The classic upward shoaling succession of mud-dominated to ooid grainstone textures typifies this environment (Fig. 13A; Ball 1967; Harris 1979). Typical high-energy deposits are (1) shelf margin sands, where funneling of tidal energy by the shelf slope produces widespread tidal-bar and marine sand belts, (2) back-reef sands associated with landward transport of sediment from a rimmed-shelf fringing reef, and (3) local middle-shelf deposits associated with inner-island gaps or tidal inlets forming lobate tidal deltas.
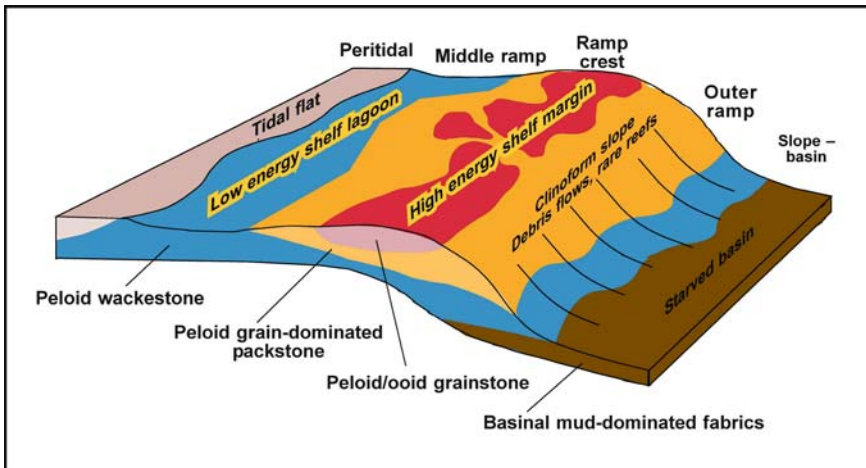
Fig. 4.12. Generalized block diagram illustrating carbonate-ramp facies patterns and topography
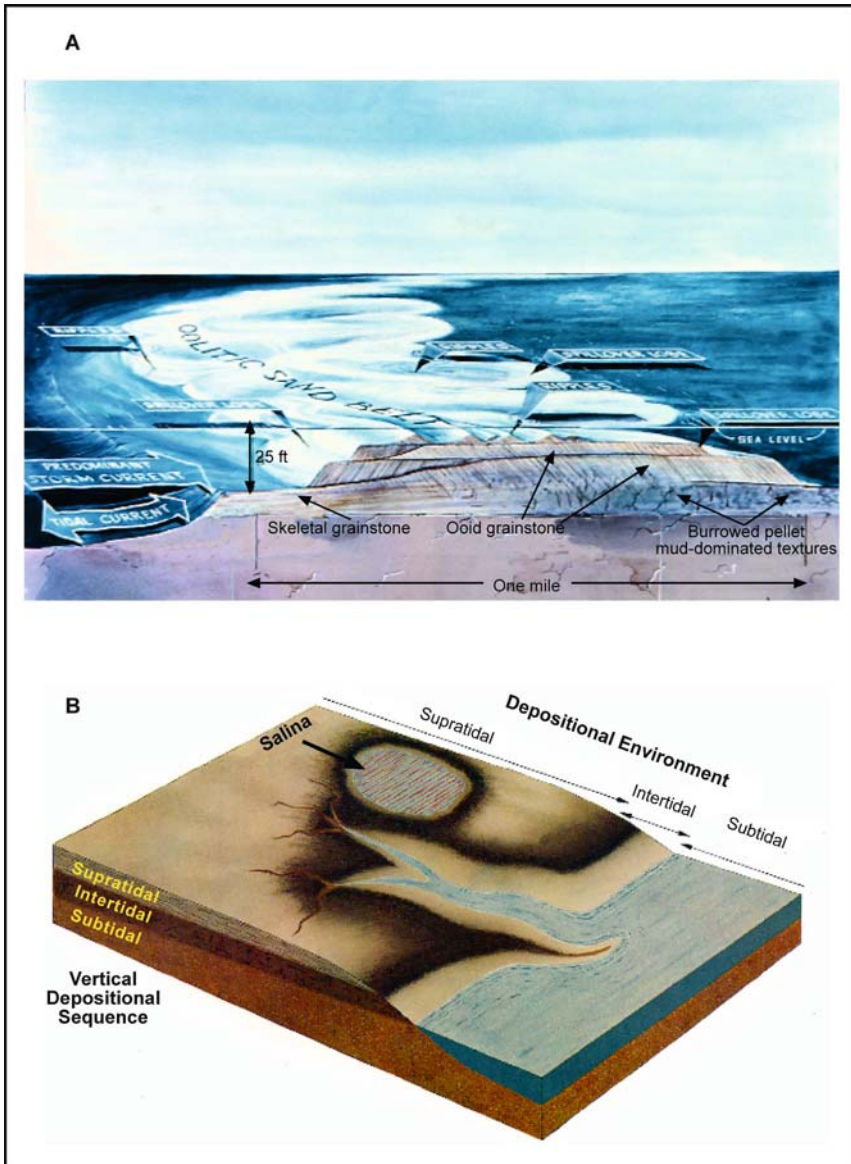
Fig. 4.13. Illustration of two typical depositional sequences. **A)** Schematic block diagram of the Cat Cay oolitic sand belt, Bahama Bank, showing a vertical sequence from burrowed pelleted mud to ooid grainstone (Ball 1967). **B** Diagrammatic view of a prograding evaporitic tidal flat showing general depositional environments and vertical sequence. (Lucia 1972)

Grain-dominated packstones are typically churned by burrowing organisms and do not show evidence of current transport. However, it is possible that some grain-dominated packstones result from the addition of carbonate mud by the mixing of muddy and grainstone sediments by burrowing. Cross bedding of all types and scales, from ripple bedding to large festoons, and commonly with multiple dip directions, indicating deposition out of tidal currents, is typically found in grainstone beds (see Halley et al. 1983 for detailed descriptions).

Reefs are concentrated at the high-energy margins of rimmed shelves where they can benefit from nutrients rising from the associated deep basins. The term "reef" has been much misused in the petroleum industry. At one time it was used as a general term for all carbonate reservoirs. Here, the term "reef" will be used to describe carbonate bodies composed of bindstone or bafflestone because they may have unique pore structures related to the binding nature of the organisms. Reefs are the physical expression of a community of organisms that live and grow together and have little to do with physical depositional processes. Reefs, however, are a major source of carbonate sediment, and sedimentary deposits associated with reefs are usually grainstones because reefs are typically found in high-energy environments. The organisms that form the reefs have evolved with time: Precambrian stromatolite reefs, Silurian coral reefs, Devonian stromatoporoid reefs, Permian sponge reefs, and Cretaceous rudist reefs, to name a few. The result is a robust variety of reef textures and geometries.

A second type of carbonate accumulation that is commonly referred to as a reef is more correctly termed a carbonate buildup, mound, or bioherm. These are features with topographic relief that are formed in response to pre-existing topography or localized organic activity. They are composed of sediment with only minor bind- and bafflestone, and their petrophysical characteristics can be described in terms of depositional textures. They can start in shallow or deep water but tend to grow to sea level (see James 1983 for detailed descriptions of reefs and bioherms).

Subtidal cycles in low-energy environments found in slope and basin environments may be composed entirely of mud-dominated textures. The cycles may contain an upward increase in the percentage of allochems or they may contain graded beds and Bouma-type turbidity sequences. HFCs are difficult to identify in these environments, and the cyclicity observed may not be related to the same process that produces cyclicity on the shelf.

Shelf slopes and basins adjacent to carbonate platforms receive carbonate sediment by mass transport from the shelf and by fallout of calcareous zooplankton and phytoplankton. The typically muddy sediment is punctuated with coarser grained sediment flows. Debris flows, slump deposits, reef

talus, grain flows, and turbidites are typical transportation mechanisms. The type of sediment flow depends in part on the degree of slope. Breccia beds composed of reef talus and other debris flows are typically found associated with the steep slopes of a rimmed shelf, whereas slump deposits and grain flows are more typical of gentle carbonate ramp slopes. Turbidite deposits are found in lower slope and basin environments (see Enos and Moore 1983; Cook and Mullins 1983, Scholle et al. 1983 for more detail).

The porosity and permeability profiles in an HFC will reflect the vertical succession of depositional textures (Fig. 14). The base of the HFC is commonly a mud-dominated texture having 70% porosity and 200 md permeability.   Grain-dominated packstone typically overlies mud-dominated strata and has 60% porosity and 2,000 md permeability. In high-energy environments, grainstone will cap the cycle with 45% porosity and 30,000 md permeability. The 2-D distribution of petrophysical properties is controlled by the lateral facies progression. The resulting 2-D pattern of petrophysical properties is shown in Fig. 10. Although there is a large spread in the permeability values, all the porosity and permeability values are sufficiently high to qualify as reservoir rock.

4.3.2 High-Frequency Sequence

Repeated eustatic sea-level cycles result in the vertical stacking of HFC (Fig. 15). Cycles are stacked vertically into retrogradational cycles, aggradational cycles, and progradation cycles. Retrogradational cycles are formed when the eustatic sea-level fall for each cycle is much less than the rise. The shoreline will move farther landward with each successive cycle, a pattern described as backstepping or transgression. The sediments are said to be deposited in the transgressive systems tract (TST). Aggradational cycles are formed when the eustatic rise and fall is equal, and the resulting facies will stack vertically. These cycles are defined as part of the highstand system tract (HST). Progradational cycles form when the eustatic fall for each cycle is greater than the rise. The shoreline for each successive cycle will move seaward, a pattern described as progradation or regression, and the sediments are said to be deposited in the highstand systems tract (HST). Sediments deposited when relative sea level is lowest are said to be deposited in the lowstand systems tract (LST). The sequence from TST to HST to LST defines a larger sea level signal referred to as a high-frequency sequence (HFS; Fig. 15).

Cycles deposited in the transgressive systems tract (TST) will typically be subtidal cycles with rare tidal-flat-capped cycles. Textures may coarsen

upward, becoming grain-dominated in association with topographic slope
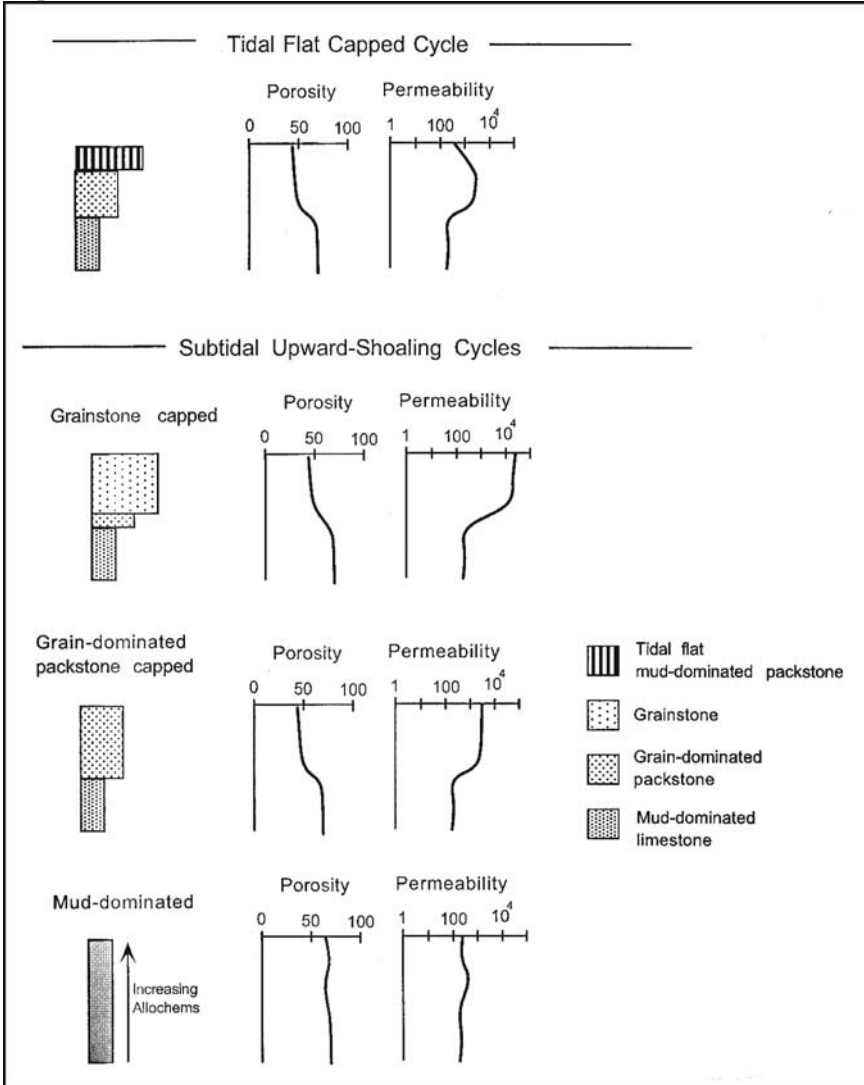
Fig. 4.14. Illustrations of typical depositional upward-coarsening cycles. Subtidal upward-shoaling cycles may be capped by grainstone, grain-dominated packstone, or mud-dominated packstone depending on the depositional environment. Tidal-flat capped cycles are most important because the tidal flat environment marks sea level. The vertical porosity and permeability profile is correlated with depositional texture

changes. Tidal flats will be restricted to the shoreline and will not prograde far seaward because of the overall transgressive nature of the shoreline. The overall sea-level rise results in each successive cycle starting at a more landward position, as shown by cycles 1, 2, and 3 in Fig. 15.   Cycles depos-
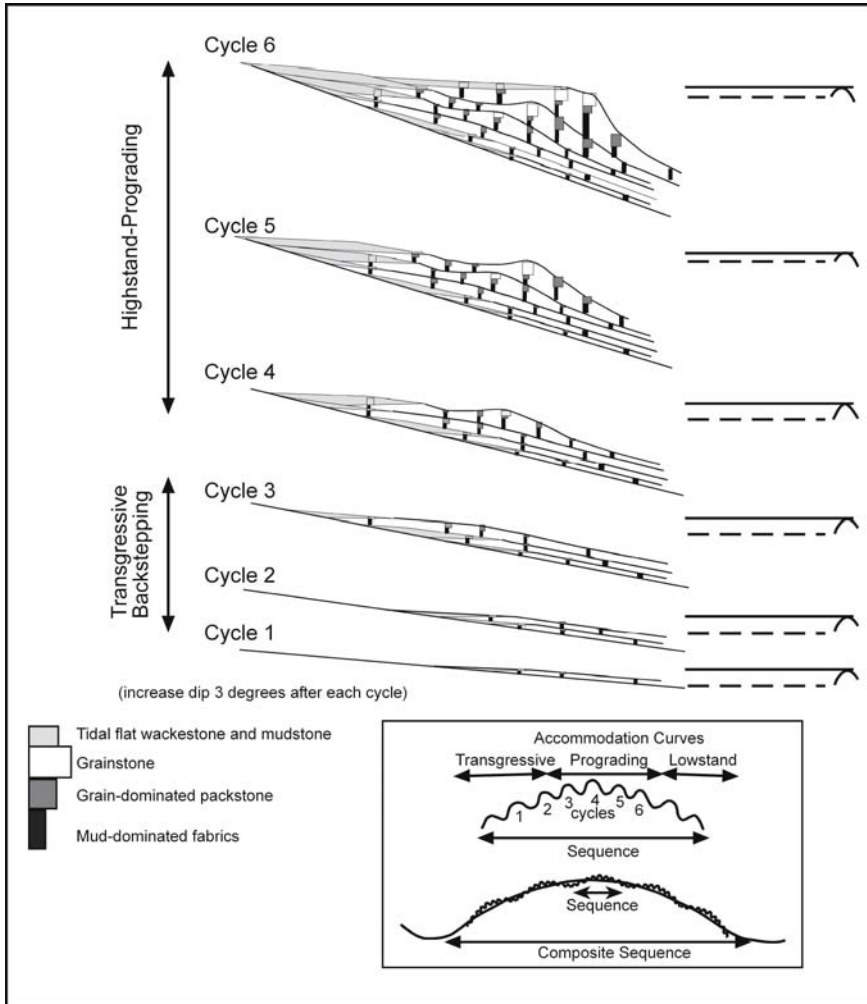
Fig. 4.15. Development of a carbonate high-frequency sequence (HFS). Cycles are grouped into longer term sea-level signals referred to as an HFS. Cycles backstep when long-term sea-level rise is greater than the long-term fall. Cycles prograde when long-term fall is greater than long-term rise. HFSs can be grouped into a longer-term sea-level signal referred to as a composite sequence

ited in the highstand systems tract are higher energy deposits because the amount of accommodation space is less due to more sea-level fall than rise. They typically have well-developed tidal-flat-capped cycles landward, lagoonal mud-dominated subtidal cycles, grain-dominated packstone and grainstone capped cycles and reefs at the shelf crest, and mud-dominated cycles in the outer shelf and basinal positions (see cycles 4, 5, and 6 in Fig. 15). Because sea-level fall is larger than rise in the HST, the cycles begin to onlap the shelf. Sedimentation fills accommodation space so that (1) tidal flats have ample opportunity to prograde seaward and (2) shelf sediment must be transported basinward, producing outer-shelf clinoform deposits.

This process produces a systematic pattern of depositional textures organized within the high-frequency sequence illustrated in Fig. 16.
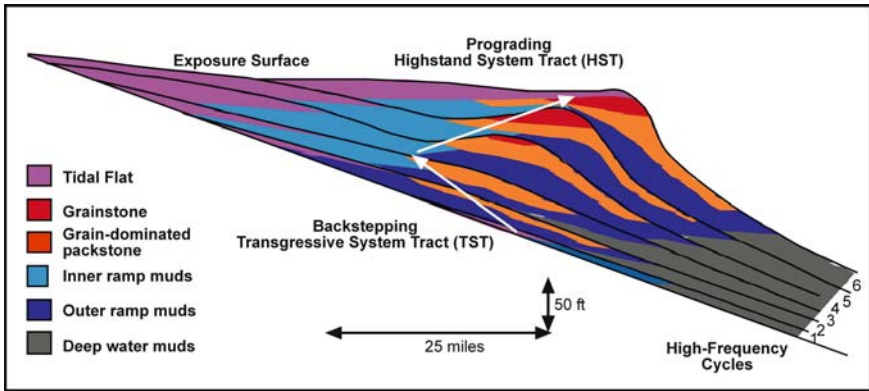
Fig. 4.16. Diagram of the HFS constructed in Fig. 13 showing the distribution of depositional textures and high-frequency cycles. Grainstones are concentrated in the ramp crest facies tract of the highstand systems tract

Petrophysical properties will be distributed according to the rock-fabric facies patterns, with the highest permeability in the grainstones and the lowest permeability in the carbonate muds. The resulting distribution of petrophysical properties is shown in Fig. 17. The result is a time-transgressive belt of highly permeable grain-dominated sediment bounded basinward by low-permeability mud-dominated slope and basin sediments, and landward by low-permeability mud-dominated middle-shelf sediment. The value of the HFC is to demonstrate the time-transgressive nature of the high-permeability grain-dominated facies and to illustrate that these facies are separated by layers of low-permeability, muddy sediment.
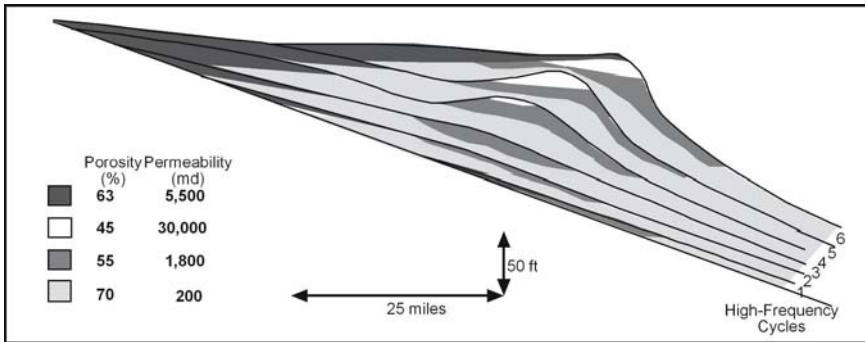
Fig. 4.17. Diagram of the HFS construction in Fig. 13 showing the distribution of petrophysical properties based on depositional textures. Highest permeability is concentrated in the ramp crest location and in the tidal flats

4.4 Example

An excellent example of the systematic distribution of rock-fabric facies in a carbonate sequence is found in the San Andres Formation that outcrops on the Algerita Escarpment, Guadalupe Mountains, Texas and New Mexico (Fig. 18; Kerans et al. 1994). Regional mapping shows that the 1500-ft-thick San Andres Formation can be divided into multiple high-frequency and composite sequences. Each sequence is composed of high-frequency cycles, and the facies patterns within the cycles and facies offset between cycles define the TST and HST. Petrophysical data collected from the outcrop show dolograinstones with 20 md permeability, grain-dominated dolopackstones with 4 md permeability, dolowackestones with 0.4 md permeability, and dolomudstones with less than 0.1 md permeability.

Detailed mapping was done on a reservoir-scale window within the formation that is a close analog for many San Andres reservoirs of the Permian Basin. The reservoir window is about 1 mile (1.6 km) long and 150 ft (30 m) high. Facies descriptions from numerous measured sections indicate nine high-frequency cycles that can be mapped along the length of the outcrop (Fig. 19). The cycles are predominantly asymmetric upward-shallowing cycles, and typically begin with basal mudstone, followed by wackestone or mud-dominated packstone, grain-dominated packstone, grainstone, and locally a fenestral (tidal flat) cap. In Fig. 19, cycles 3 and 8 have tidal-flat caps; cycles 1, 2, 3, 7, and 9 are subtidal cycles with thick

grainstone or grain-dominated packstone caps; and cycles 4, 5, and 6 have thin grain-dominated packstone caps. This vertical succession suggests
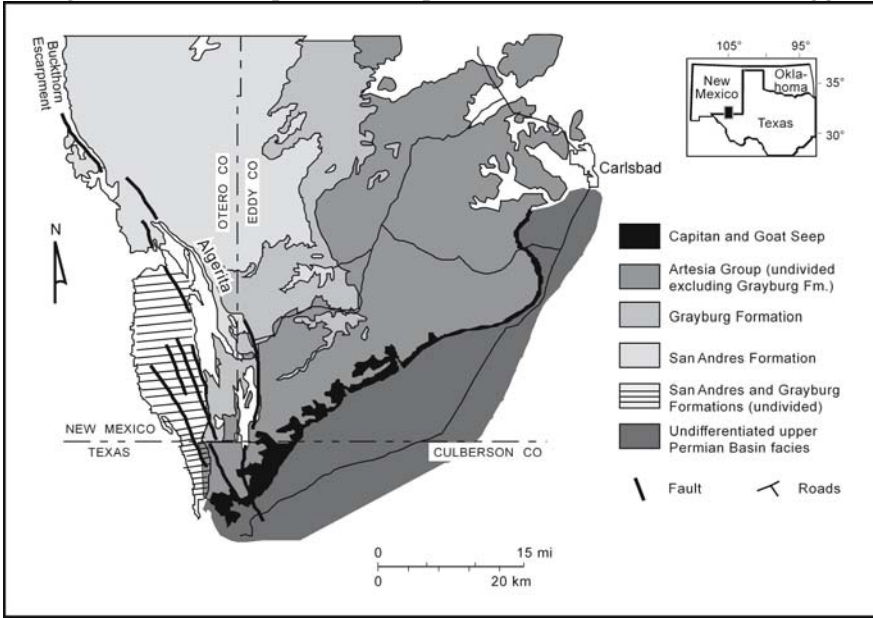

Fig. 4.18. Geological map of the Guadalupe Mountains area showing the location of the Algerita Escarpment San Andres outcrops. (Kerans et al. 1994)

a sequence boundary at the contact between cycles 3 and 4, and between cycle 9 and overlying cycles that onlap the cycle 9 exposure surface. Cycles 1-3 are prograding cycles of a lower highstand systems tract and cycles 7-9 are prograding cycles of an upper highstand systems tract. Cycles 4-6 are retrogradational cycles of the transgressive systems tract. These two sequence boundaries have been traced throughout the Guadalupe Mountains and formalized as Guadalupian 2 high-frequency-sequence, and Guadalupian 3 high-frequency-sequence, by Kerans et al. (1994) and Kerans and Fitchen (1995).

The measured sections provide one-dimensional data similar to a vertical development well. In excellent outcrops, however, two-dimensional data can be obtained by mapping the facies laterally between sections on the ground or by using oblique aerial photography. The cycle boundaries described here have been traced for 1 mile and the depositional facies mapped. The facies change laterally in a gradual manner and without sharp contacts, and they do not cross cycle boundaries. The vertical succession of facies in the middle ramp is typically more complicated than those of the ramp crest, and cycles of the outer ramp are

simple upward-coarsening cycles from mudstone and wackestone to mud- or grain-dominated packstones (Fig. 20). By mapping laterally, the vertical succession of facies
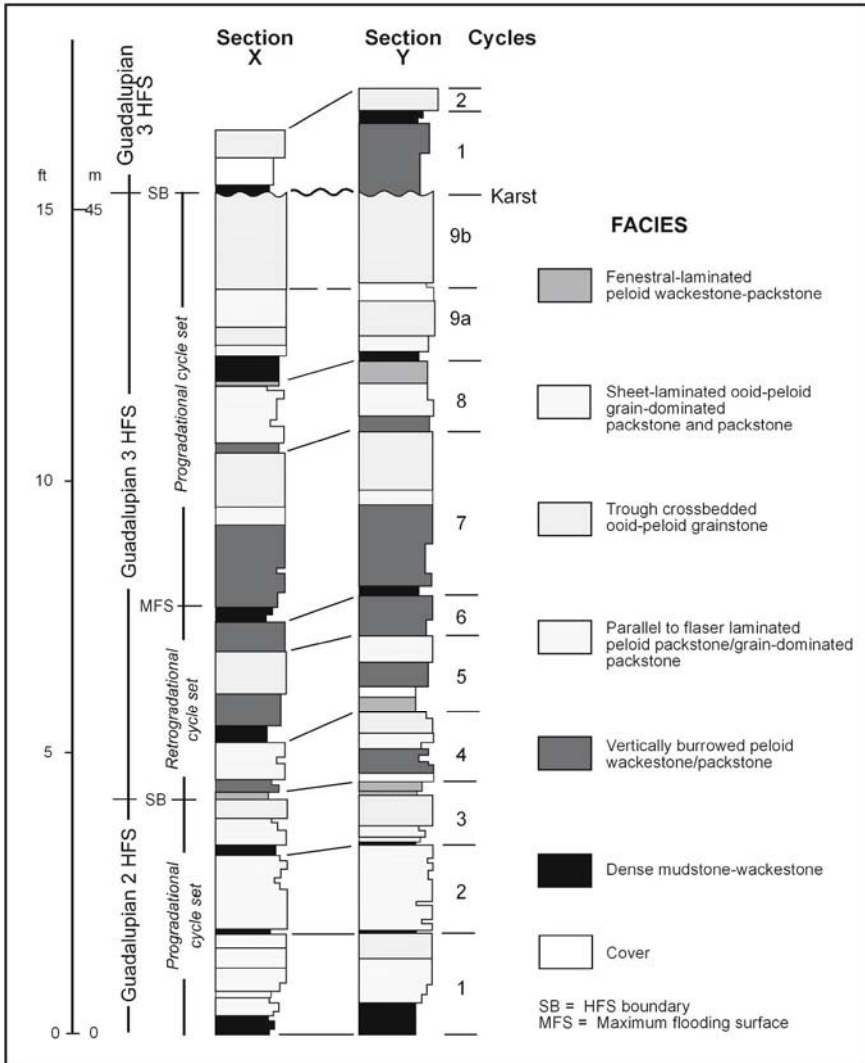
Fig. 4.19. Measured sections showing facies distribution within cycles and relationship of cycles to HFS framework in the Lawyer Canyon reservoir window. (Kerans et al. 1994)

within a cycle can be converted into a two-dimensional facies progression model (Fig. 20). Fossils that are water-depth indicators are important in interpreting the lateral facies progression, and fusulinids are key water-

depth indicators for the San Andres. As shown on the cross section, fusulinids are concentrated in the outer ramp and distal outer ramp. Cherty mudstones are also characteristic of the distal outer ramp.
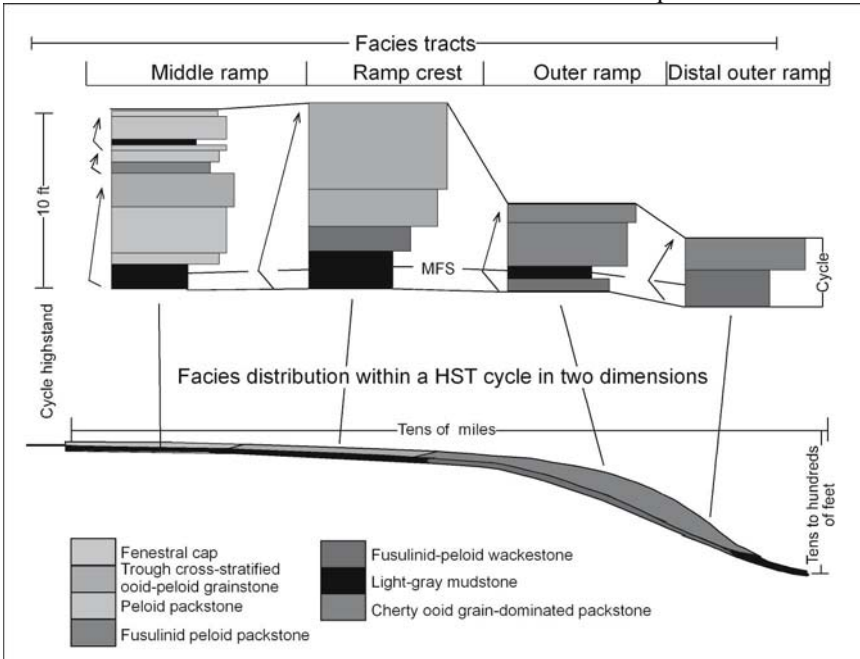
Fig. 4.20. Vertical facies successions and lateral facies progressions in a single cycle from the San Andres outcrop. (Kerans and Fitchen 1995)

Grainstones are of particular interest because they are the most permeable facies in modern sediments and in this outcrop. The detailed facies maps from the reservoir window show a partitioning of grainstone bodies between the transgressive and highstand systems tracts at the HFS scale (Figs. 21 and 22; Kerans et al. 1994). Grainstones are more common and have greater dimensions in the highstand than in the transgressive systems tracts. Also, grainstones are more common in the ramp-crest facies tract than in the inner-ramp or outer-ramp tracts.

This outcrop example illustrates the systematic distribution of depositional textures in a carbonate platform. Assuming the products of diagenesis conform reasonably well to depositional textures, predictions of petrophysical properties can be made based on predictions of the three-dimensional pattern of petrophysically significant depositional facies. Depositional patterns in carbonates are highly variable, and we have not attempted to discuss the extensive literature available on the subject. Instead, we have presented a simplified version of carbonate sedimentation

and cycle stacking. However, this approach can be applied to many major carbonate reservoirs in the world.
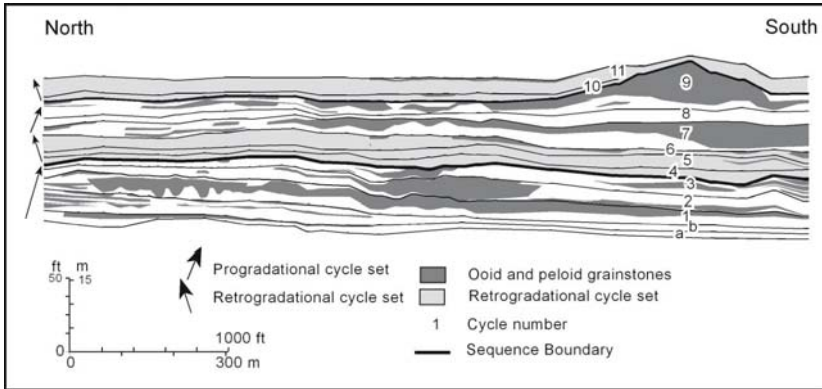
Fig. 4.21. Distribution of grainstone facies in the Lawyer Canyon, Algerita Canyon reservoir window, showing grainstones concentrated in progradational cycle sets in two HFSs. (Kerans et al. 1994)
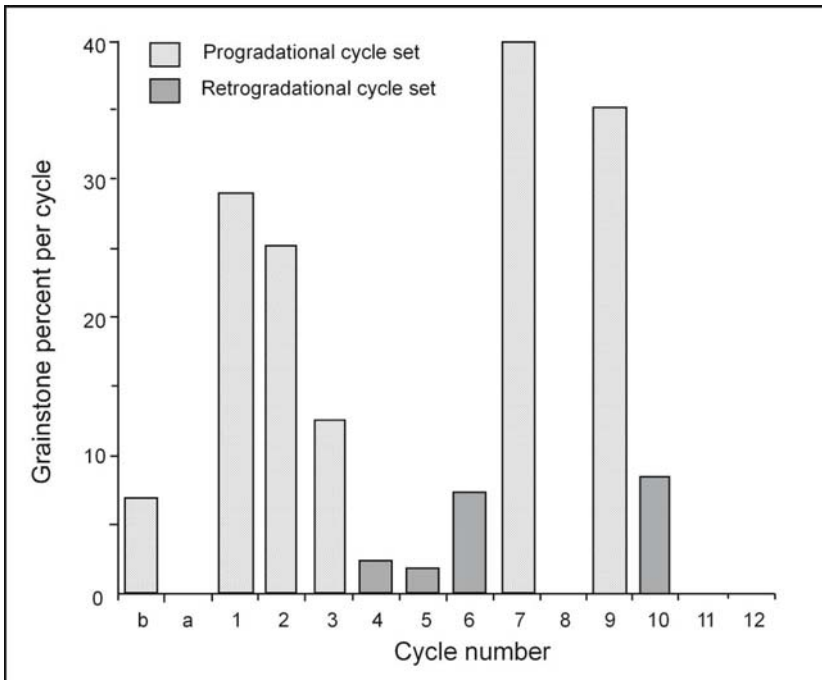
Fig. 4.22. Graph showing the partitioning of grainstones between progradational and retrogradational cycles. San Andres Formation, Algerita Escarpment. (Kerans et al. 1994)

4.5 Summary

Carbonate sediments have a wide range of particle size and sorting because they are formed by organic activity and redistributed by current transport. Porosity values range from 40% to 75% and permeabilities from 200 to 30,000 md. Mud-dominated fabrics average 70% porosity and 200 md permeability, grain-dominated packstones average 55% porosity and 1,800 md permeability, and grainstones average 45% porosity and 30,000 md permeability. Pore space is located between and within depositional grains. Interparticle pore-size is a function of the particle type, size, and sorting with particle sizes ranging form 5 micron mud to large ooids and coral fragments. Intraparticle pore sizes (separate vugs) range from microporosity in ooids and peloids to relatively large intraskeletal pores.

The spatial distribution of petrophysical properties is linked to facies patterns. Rock-fabric facies are systematically distributed within high-frequency cycles and within high-frequency sequences. These are chronostratigraphic units bounded by time surfaces that can be correlated from well to well. Depositional textures are vertically stacked into tidal-flat capped cycles and subtidal cycles that may be capped by bindstone, grainstone, grain-dominated packstone, mud-dominated packstone, or wackestone depending on the depositional energy. Depositional energy is controlled by topography and the types of ocean currents. The highest energy is generally located at the shelf margin and the cycles are typically capped by bindstone, grainstone, or grain-dominated packstone. Gentle currents are typically found over the middle shelf, except during storms, and mud-dominated cycles with thin mud- to grain-dominated packstones are cycle caps. The shoreline is a trap for sediment transported from the subtidal to the shore, forming beaches and tidal-flat-capped cycles. A variety of currents are found basinward of the shelf crest, depositing mud-dominated sediment as well as graded beds and boulder beds. The two basic cycles, however, are tidal-flat capped and subtidal, and subtidal cycles are commonly composed of two basic textures, a lower mud-dominated texture and an upper grain-dominated cap.

Each HFC begins with a flooding event produced by a relative sea-level rise. Flooding events approximate chronostratigraphic surfaces and define the HFC as a time-stratigraphic unit. High-frequency cycles stacked into retrogradational cycles indicate an overall sea-level rise, aggradational cycles indicate a sea level still stand, and progradational cycles indicate a general sea-level fall. The sequence from retrogradational to progradational defines a larger sea-level signal and is referred to as a high-frequency sequence. The systematic patterns of

depositional textures organized within the high-frequency sequence define the distribution of petrophysical properties at the cycle scale.

There are no nonproductive areas in the depositional model because very few sediments can be considered nonreservoir quality. However, bodies of high-permeability sediment are located in the vicinity of the shelf crest and are bounded seaward and landward by low-permeability mud-dominated sediments.   Petroleum reservoirs commonly have nonproductive areas because diagenetic processes modify depositional texture, most commonly reducing porosity and permeability.

Carbonate sedimentary textures are systematically distributed on a carbonate platform.   Assuming the products of diagenesis conform reasonably well to the depositional textures, predictions of petrophysical properties can be made based on predictions of the three-dimensional patterns of petrophysically significant depositional facies. Depositional patterns in carbonates are highly variable, and there is extensive literature available on the subject.

In Chapter 2 we grouped petrophysical data into rock fabrics and petrophysical classes, in Chapter 3 we discussed the vertical distribution of rock fabrics and petrophysical properties, and in this chapter we discussed the 3D distribution of rock-fabric facies. Next we will discuss the lateral variability of petrophysical properties and the rock-fabric approach to building a petrophysical model.

References

Ball M M 1967 Carbonate sand bodies of Florida and the Bahamas. J Sediment Petrol 37:556-591

Cook H E, Mullins HT 1983 Basin margin environment. In: Scholle P A, Bebout D, Moore H M (eds) Carbonate depositional environments. AAPG Mem 33:539-618

Deffeyes KS, Lucia FJ, Weyl PK 1965 Dolomitization of Recent and Plio-Pleistocene sediment by marine evaporate waters on Bonaire, Netherlands Antilles. In: Pray LC, Murray RC (eds) Dolomitization and limestone diagenesis—a symposium. SEPM Spec Publ 13:71-88

Dunham RJ 1962   Classification of carbonate rocks according to depositional texture.   In: Ham   W E, (ed) Classifications of carbonate rocks—a Symposium. AAPG Mem 1:108-121

Embry AF, Klovan FE 1971 A late Devonian reef tract of northeastern Banks Island, N.W.T.. Bull Can Pet Geol 19:730-781

Enos P 1983 Shelf environment. In: Scholle PA, Bebout D, Moore HM (eds) Carbonate depositional environments. AAPG Mem 33:267-296

Enos P, Moore CH 1983 Fore-reef slope environment. In: Scholle PA, Bebout D, Moore HM (eds).Carbonate depositional environments. AAPG Mem 33:507-538

Enos P, Sawatsky LH 1981 Pore networks in Holocene carbonate sediments. J Sediment Petrol 51, 3:961-985

Folk RL, Lynch RL 2001 Organic matter; putative nannobacteria and the formation of ooids and hardgrounds. Sedimentology, 48, p.215-229

Gebelein CD, Steinen RP, Garrett P, Hoffman EJ, Queen JM, Plummer LN 1980 Subsurface dolomitization beneath the tidal floats of central West Andros Island, Bahamas. In: Zenger DJ, Duhnam JB, Ethington RL (eds) Concepts and models of dolomitization. SEPM Spec Publ 28:31-49

Gerhard LC 1985 Porosity development in Mississippian pisolitic limestone of the Mission Canyon Formation, Glenburn Field, Williston Basin, North Dakota. In: Roehl PO, Choquette PW (eds) Carbonate petroleum reservoirs, Springer, Berlin Heidelberg New York, pp 193-205

Gischler E, Zingeler D 2002 The origin of carbonate mud in isolated carbonate platforms of Belize, Central America: International Journal of Earth Science, 91:1054-1070

Halley RB, Harris PM, Hine AC 1983 Bank Margin Environment. In: Scholle PA, Bebout D, Moore HM (eds) Carbonate depositional environments. AAPG Mem 33:463-506

Harris PM 1979 Facies anatomy and diagenesis of a Bahamian ooid shoal. University of Miami, Florida, Comparative Sedimentology Laboratory, Sedimenta 7, 163 pp

Inden RF, Moore CH 1983 Beach environment. In: Scholle PA, Bebout D, Moore HM (eds) Carbonate depositional environments. AAPG Mem 33:211-267

James NP 1983 Reef environment. In: Scholle PA, Bebout D, Moore HM (eds) Carbonate depositional environments. AAPG Mem 33:345-462

James NP 1984 Reefs. In: Walker RG, (ed) Facies models, 2nd edn. Geoscience Canada, Reprint Series 1, Geological Association of Canada, Ottawa, pp 229-244

Kerans C, Fitchen WM 1995 Sequence hierarchy and facies architecture of a carbonate-ramp system: San Andres Formation of Algerita Escarpment and western Guadalupe Mountains, West Texas and New Mexico. The University of Texas at Austin, Bureau of Economic Geology, Report of Investigations 235, 85 pp

Kerans C, Lucia FJ, Senger RK 1994 Integrated characterization of carbonate ramp reservoirs using outcrop analogs. AAPG Bull 78 2:181-216

Kerans C, Tinker SW 1997 Carbonate sequence stratigraphy and reservoir characterization: SEPM Short Course No. 40, 155 pp

Lloyd RM, Perkins RD, Kerr SD 1987 Beach and shoreface ooid deposition on shallow interior banks, Turks and Caicos islands, British West Indies, J Sediment Petrol 57, 6:976-982

Lucia FJ 1968 Recent sediments and diagenesis of south Bonaire, Netherlands Antilles. J Sediment Petrol 38, 3:845-858

Lucia FJ 1972 Recognition of evaporate-carbonate shoreline sedimentation. In: Rigby JK, Hamblin WK (eds) Recognition of ancient sedimentary environments. SEPM Spec Publ 16:160-191.

Milliman JD, Freile D, Steiner RP, Wilber RJ 1993 Great Bahama Bank aragonite mud: mostly inorganically precipitated, mostly exported. J Sediment Petrol 63, 4:589-695

Patterson RJ, Kinsman DJJ 1981 Hydrologic framework of a sabkha along Arabian Gulf. AAPG Bull 65. 8:1457-1475

Reed JF 1985 Carbonate platform facies models. AAPG Bull 69, 1:1-21

Schmoker JW, Halley RB 1982 Carbonate porosity versus depth: a predictable relation for south Florida. AAPG Bull 66, 12:2561-2570

Schmoker JW, Krystinic KB, Halley RB 1985 Selected characteristics of limestone and dolomite reservoirs in the United States. AAPG Bull 69, 5:733-741

Scholle PA, Arthus MA, Ekdale AA 1983 Pelagic environment. In: Scholle PA, Bebout D, Moore HM (eds) Carbonate depositional environments. AAPG Mem 33:619-692

Shinn EA 1983 Tidal flat environment: In: Scholle PA, Bebout D, Moore HM (eds) Carbonate depositional environments. AAPG Mem 33:172-210

Walker RG 1894 Facies models, 2nd edn. Geoscience Canada, Reprint Series 1, Geological Association of Canada, Ottawa, 317 pp

Walter LM 1985 Relative reactivity of skeletal carbonates during dissolution: implication for diagenesis. In: Schneidermann N, Harris, PM (eds) Carbonate cements. SEPM Spec Publ 36:3-16

Warren FK, Kendall CGSC 1985 Comparison of sequences formed in marine sabkha (subaerial) and salina (subaqueous) settings—modern and ancient. AAPG Bull 69, 6:1013-1023

Wilkinson BH 1979 Biomineralization, paleoecology and the evolution of calcareous marine organisms. Geology 7:524-527

Wilson JL, Jordan C 1983 Middle shelf environment: In: Scholle PA, Bebout D, Moore HM (eds) Carbonate depositional environments. AAPG Mem 33:267-344

Chapter 5 Reservoir Models for Input into Flow Simulators

5.1 Introduction

Reservoir characterization is defined as the construction of realistic three-dimensional images of petrophysical properties to be used to predict reservoir performance. In previous chapters we have discussed petrophysical properties and emphasized that permeability and saturation are a function of pore-size distribution and that pore size distribution is a function of particle size, sorting, interparticle porosity, separate-vug porosity, and touching-vug pore systems. We have discussed the use of core description and wireline logs for characterizing the one-dimensional distribution of the rock fabrics and associated petrophysical values. We have described the sequence stratigraphic approach to constructing a three-dimensional chronostratigraphic framework and the importance of defining rock-fabric facies within that framework for filling the 3D volume with porosity, permeability, and initial saturation values.

We now have the tools to construct a three-dimensional geological model suitable for petrophysical quantification and to calculate the basic petrophysical properties from well logs. We have yet to discuss methods of distributing petrophysical data in the interwell environment to build the reservoir model. In the past, petrophysical models have been prepared by several different methods including (1) the layered reservoir method, (2) the continuous pay method, and (3) the facies method (Fig. 1). A key aspect of these methods has been the correlation of similar gamma-ray responses and porosity profiles using the assumption that the layers are horizontal to some key structural marker. As pointed out in Chapter 4, the only surface that is known to be present in each well is a time surface, and the accuracy of any layers defined by the gamma-ray and porosity logs will depend upon how well they conform to chronostratigraphic surfaces defined by sequence stratigraphic considerations.
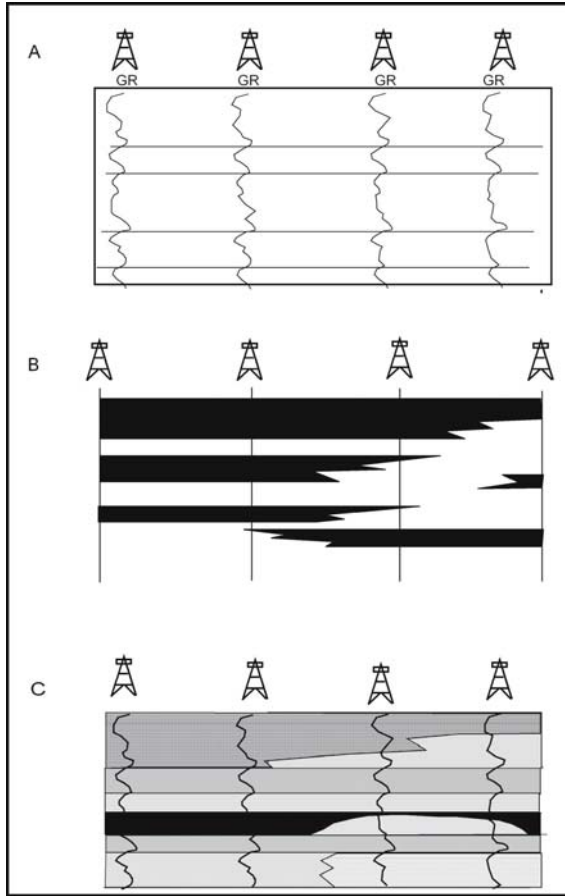
Fig. 5.1. Three methods of reservoir characterization. **A** The layered reservoir method, **B** The continuous pay method, **C** The facies method

In the layered reservoir method, the reservoir is divided into pay zones using correlations based on gamma-ray and porosity logs, and the net feet of porosity (net pay maps) or the porosity-times-oil-saturation (SoPhiH maps) isopached for each layer. The layers commonly lump several petrophysical rock fabrics, and the average petrophysical values tend to average out high and low permeability values. The result is a permeability model that is too uniform to adequately model fluid flow in the reservoir.

In the continuous pay method, the layers are defined as porous intervals and are assumed to correlate laterally parallel to structure. Porous intervals are extended horizontally between wells and the percentage of porous inter- vals that are continuous between any two wells calculated. The expected in- cremental recovery of an infill well is inversely related to the percent continu-

ity of the individual porous intervals (George and Stiles, 1978; Barber et al. 1983). This method is best applied in reservoirs with discrete reservoir and nonreservoir intervals.

In the facies method, the reservoir is layered using correlatable gamma-ray markers. Depositional facies are described from core material and mapped within the layers, and average petrophysical properties are assigned to each facies. Depositional facies are commonly defined by their fossil content and other depositional features for the purpose of predicting and mapping facies distribution. This is a useful method for delineating reservoir patterns and is most effective in exploration and initial field development. It is not effective in reservoir characterization because 1) the layers are not chronostratigraphic and 2) geological facies commonly lump several rock fabrics so that the average petrophysical properties even out high- and low-permeability layers. To be useful, the facies must be defined in terms of petrophysical rock fabrics, as described in Chapter 2.

In this chapter we will describe the rock-fabric method for building a reservoir model. Four basic steps in this method are (1) constructing the 3-D chronostratigraphic framework and mapping the sequences and high-frequency cycles (Chapter 4), (2) defining the vertical succession of rock fabrics and rock-fabric flow layers, (3) developing rock-fabric-specific transforms for estimating the one-dimensional distribution of permeability and initial fluid saturation at each well using core-log calibration methods (Chapters 2 and 3), and (4) filling the interwell environment with petrophysical properties. Steps 1 and 3 have been discussed in previous chapters. In this chapter we will discuss the difficult task of defining flow layers and filling the interwell environment with petrophysical properties before outlining a work flow for building the reservoir model.

Filling the interwell volume is an extremely important task because well data sample less than 1 percent of the reservoir volume. Therefore, it is necessary to use geostatistical methods to fill the interwell void. The statistics must be constrained by the stratigraphic framework, which is a deterministic interpretation based on the small amount of well data and guided by geologic principles and seismic data. It follows then that the petrophysical properties are distributed statistically within the framework and may be guided by seismic and production data. Statistical methods include linear interpolation among wells, geostatistical variography, and stochastic distribution of petrophysical objects. We have not discussed modern spatial statistical methods in the previous chapters; we will present a brief overview of variography before proceeding.

5.2 Geostatistical Methods

5.2.1 Variography

The problem is to estimate the distribution of porosity, permeability, and initial water saturation in interwell space based on detailed vertical profiles or these properties calculated from wireline logs. The approach is to statistically distribute these properties using a spatial geostatistical method called variography. Variography uses variograms to statistically characterize spatial variability of a property. In essence, the variogram is a tool that under certain circumstances can be used to quantify the spatial continuity that is either explicitly exhibited in the data or inferred from the data through geological interpretation.

The following is taken from Fogg and Lucia (1990). Modern geostatistics differs from classical population statistics in that geostatistics is designed to handle data that exhibit spatial correlation; that is, the data are not totally random, and neighboring values bear some relation to each other. Nearly all geology-related data exhibit spatial correlation. The likelihood that measurements of a spatially correlated variable are close or equal in value increases as distance between the points of measurement decreases. Another distinction between the two methods is that in classical statistics, the mean and variance are generally the fundamental measures of a distribution, whereas in geostatistics, the mean and covariance or variogram are the fundamental measures. The covariance and variogram are statistical functions used to describe spatial correlation.

In reservoir characterization, geostatistical methods are used to generate realistically complex interwell patterns of heterogeneity, which are critical for recovery efficiency. These methods are also used to estimate probabilities for various interwell permeability patterns and, in turn, to estimate error bars for simulated production and recovery efficiency. The geostatistical approach is essentially a quantitative geological mapping technique in which geological interpretation is included through the variogram. Geostatistics in no way lessens the need for valuable, subjective mapping by the geologist. On the contrary, properly applied geostatistics increases the need for geological input and helps define which geological data are most applicable to a particular problem. Thus the need exists for a stratigraphic framework and rock-fabric flow layers to constrain the application of variography.

To visualize how the variogram can be estimated from data, consider the data points along the line in Fig. 2. At each point, the variable of interest, Y (Y could equal permeability), is known. Each pair of numbers can be

grouped into a distance class, depending on the distance separating the pair. An experimental variogram value (γ) can then be calculated for each distance class from the mean of the squared differences between pairs of values (see equation in Fig. 2).
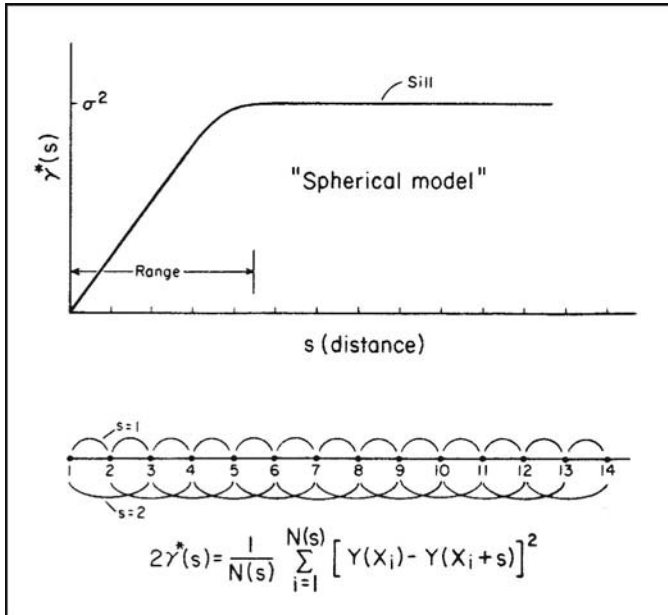

Fig. 5.2. Schematic example showing how the experimental variogram can be calculated in one dimension

When (γ) is calculated as a function of distance for data that are spatially correlated, the values commonly form a curve like the one in Fig. 2. The value of (γ) rises from near zero and then levels off into a segment known as the sill. When a horizontal sill exists, the value of (γ) at the sill is equal to the variance of Y. The curve in Fig. 2 indicates that the variability, or variance, of the data pairs increases with distance until the separation distance is too large for values to be correlated. The distance at which (γ) stops increasing significantly is known as the range. The initial value of (γ) may not be zero, but may be any value up to the value of (γ). This is known as the nugget effect, and the higher the initial value is, the poorer is the spatial correlation.

5.2.2 Conditional Simulation

Conditional simulation reproduces or simulates the true variability of a field such that the simulated values (1) vary stochastically between data points as a function of the variogram and data distribution and (2) honor the data points. The simulation produces the same degree of variability and spatial correlation as the variogram and honors all data points. Out of hundreds of realizations of a conditional simulation, one or more realizations would probably approximate the true distribution. Conditional simulation, however, is not used to estimate reality but to produce realizations that have the same degree of spatial variability and complexity as reality. Spatial distributions of permeability in two stochastic realizations illustrated in Fogg and Lucia (1990) are shown in Fig. 3. Realization (a) represents relatively high permeability and continuity, and (b) represents relatively low permeability and continuity.
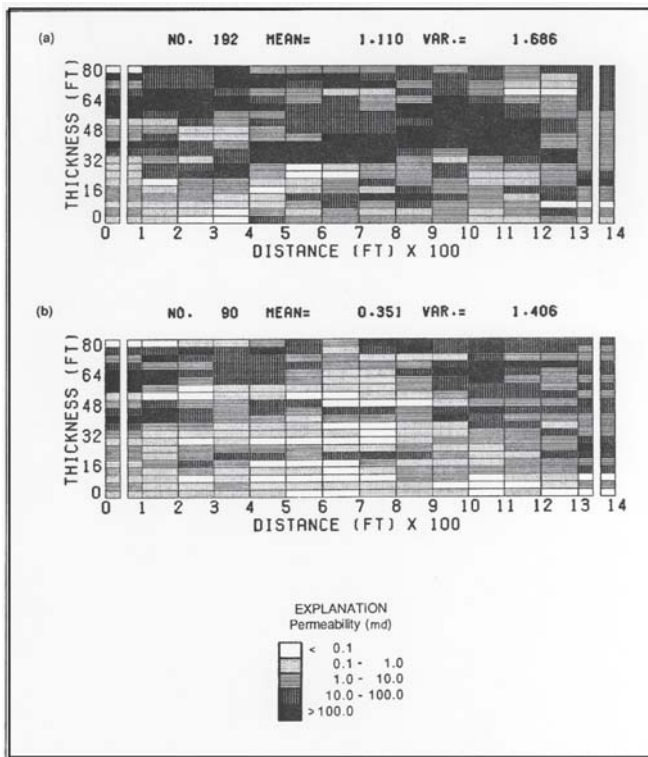
Fig. 5.3. Spatial distribution of permeability in two stochastic realizations. **a** Realization representing relatively high permeability and continuity. **b** Realization representing relatively low permeability and continuity

5.3 Scales of Variability and Average Properties

A characteristic of carbonate reservoirs is extreme scatter when porosity and permeability are graphed (Fig. 4A). We have identified some of the reasons
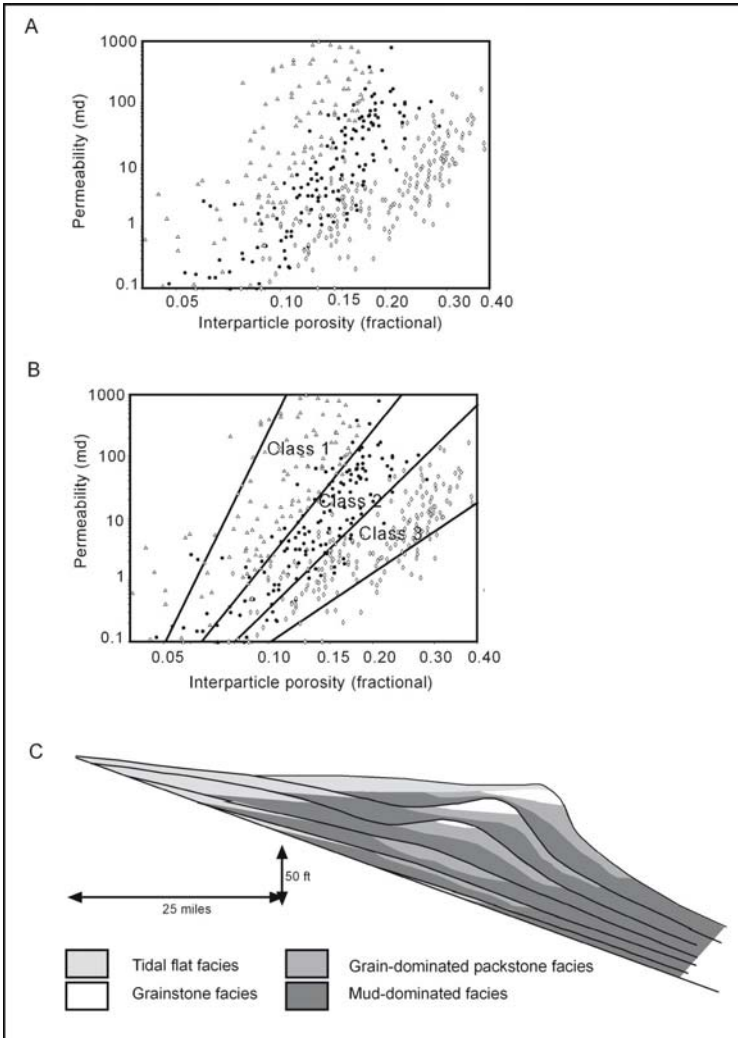
Fig. 5.4. Variability in porosity and permeability in carbonate rocks. **A** Porosity-permeability cross plot showing extreme scatter typical of carbonate reservoirs. **B** Systematic organization of variability into petrophysical classes based on rock fabrics and interparticle porosity. **C** Systematic spatial distribution of rock-fabric facies within a high-frequency sequence

for this scatter through our rock-fabric classification. In nonvuggy carbonates the scatter is reduced by grouping data into petrophysical classes using particle size and sorting (Fig. 4B). In Chapter 4 we showed that, in limestones, rock fabrics and petrophysical classes have a predictable pattern based on sedimentological processes and stratigraphic stacking (Fig. 4C). However, there is considerable variability in petrophysical properties within a rock-fabric or petrophysical class. To study the spatial distribution of these properties we will use core data for vertical variability and outcrop data for lateral variability.

Spatial distribution of permeability and porosity within a rock-fabric facies has been studied by making extensive permeability measurements on carbonate outcrops (Jennings et al. 2000). The San Andres outcrop found in Lawyer Canyon, Algerita Canyon, Guadalupe Mountains, New Mexico has perhaps the most permeability measurements of any carbonate outcrop in the world (Senger et al. 1993; Grant et al. 1994; Jennings et al. 2000; Jennings 2000). There are approximately 5,000 mechanical field permeameter (MFP) measurements and 1,200 plug samples with porosity and permeability. Permeability measurements were made on the scale of inches to feet in vertical transects, horizontal transects, and grids.

One set of data is concentrated in the dolograinstone facies of cycle 1. Analysis of the data shows that the scale of variability is a function of the sample spacing. Permeability was sampled every foot in vertical traverses spaced 50 to 150 ft along a 2600-ft lateral distance (Fig. 5a), every foot in vertical traverses spaced every 5 ft over a lateral distance of 40 ft (Fig. 5b), and every foot in a 20 x 15 ft grid pattern (Fig. 5c). Permeability isopach maps were made for each case, and a comparison of the three maps shows variability on the scale of several orders of magnitude, with the scale of variability related to the sampling density. Therefore, within a rock-fabric facies, permeability can vary several orders of magnitude on the scale of feet to inches. This result was also observed by Hinricks et al. (1986).

We are particularly interested in the data from horizontal transects because this data cannot be obtained from vertical wells. The MFP data from four horizontal transects are shown in Figure 6. The data come from grainstone facies in cycle 1 (described above), cycle 2, and cycle 9. The most striking observation is the high degree of variability; as much as three orders of magnitude. Much of the variability is concentrated at the foot scale, as suggested by the permeability maps in Figure 5. However, there are longer range features at the 100-ft scale. Thus, within a single rock fabric bed there appear to be two scales of variability, a short range and a longer range, both with several orders of variability.

Extensive geostatistical analyses have been made on this data (Senger et al. 1993; Grant et al. 1994, Jennings et al. 2000; Jennings 2000). The most
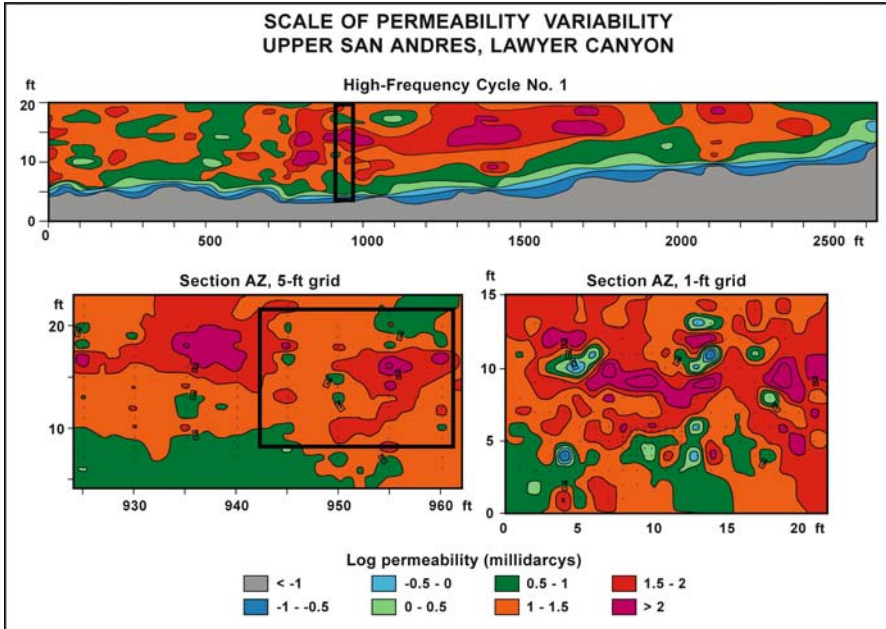
Fig. 5.5. Permeability distribution in cycle 1 grainstone rock-fabric facies at three different scales. **A** 20 by 2500 ft scale with 1ft data from vertical transects spaced 50 to 150 ft apart. **B** 17 by 35 ft scale with 1 ft from vertical transects spaced 5 ft apart. **C** 15 by 20 ft scale with 1 ft data from vertical transects spaced 1 ft apart

recent variogram analysis by Jennings is illustrated in Figure 7. The data are weakly correlated with a range of less than 20 ft. The longer range variability is expressed as three oscillations in the variogram with a periodicity of 140 ft. The cause of this periodicity is unknown but believed to be in part a function of porosity because of a relationship between porosity and permeability observed from the plug data of cycle 1. The short range data compose more than half and up to 87% of the variance. *Therefore, within a rock-fabric facies, permeability varies several orders of magnitude on the scale of feet to inches, and the poor spatial correlation suggests that the data can be legitimately averaged for modeling purposes.*

Simulation experiments were conducted on the grainstone facies to examine the effect of using various permeability distributions on simulation results (Senger et al. 1993). Comparisons between recovery efficiency using a spatially distributed permeability structure and a single average value show little difference. Flow simulations on cycle 1 by Jennings et al. (2000) have a similar result and showed that the addition of the longer range structure had little effect on recovery. However, an analysis of the permeability structure
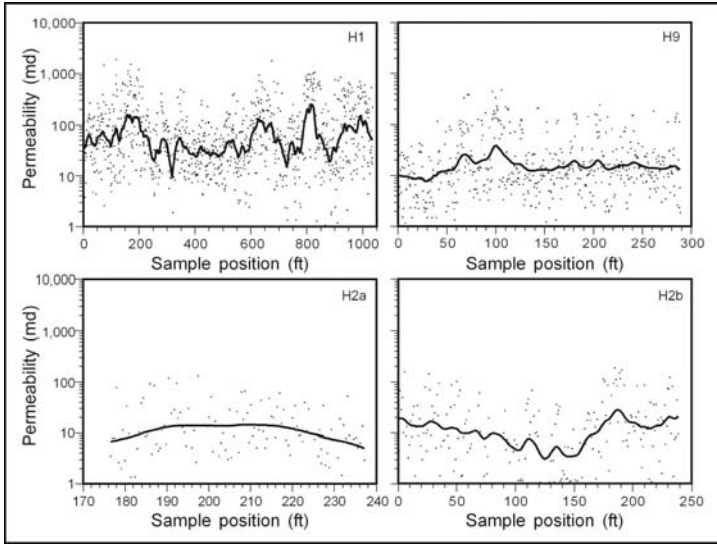
Fig. 5.6. Lawyer Canyon horizontal permeability transects showing raw data (points) and filtered data (curves). H1 is from cycle 1, H9 is from cycle 9 and H2a and H2b are from cycle 2. All transects are in grainstone beds
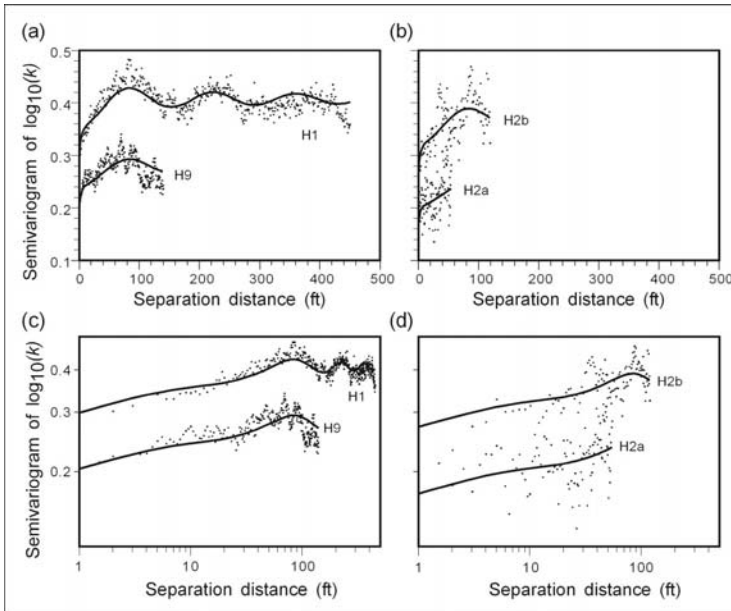
Fig. 5.7. Lawyer Canyon horizontal permeability semivariograms from cycle 1 (H1) and cycle 9 (H9), Cartesian coordinates (**a**, **b**) and logarithmic coordinates (**c**, **d**) showing data and models (curves)

in cycle 2 showed that permeability structure linked to bedding forms within a grainstone unit can result in faster water breakthrough and lower recovery (Fig. 8).
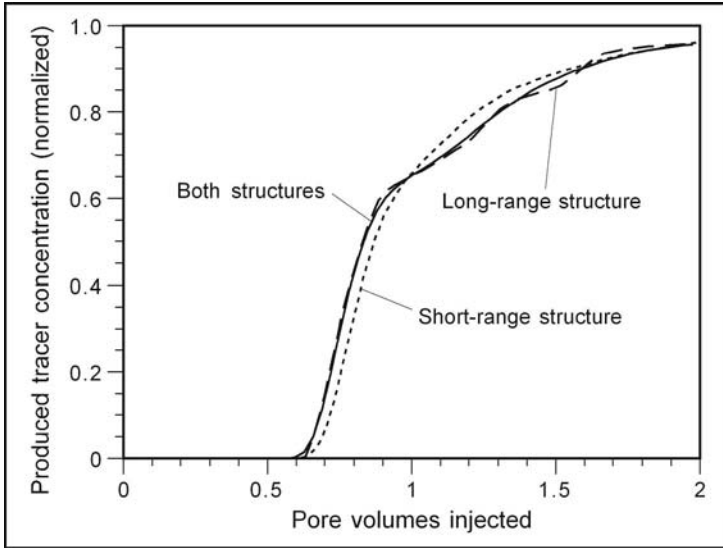
Fig. 5.8. Produced tracer concentrations for 2D aerial models for Lawyer Canyon cycle 1 showing little difference in recovery between models with only short-range variability and only long-range variability

Thirteen bed forms were mapped in a cycle 2 grainstone outcrop (Fig. 9) and permeability values from each bed form averaged. Two fluid-flow models were constructed, one that contained the small-scale variability only and one that contained the bed permeabilities as well as small-scale variability. The results show that, compared with a homogeneous permeability, the small-scale variability has a small effect on the flood front, whereas the bed permeability structure has a large effect on the flood front (Fig. 10).

The conclusion is that the small-scale variability, which makes up most of the scatter found on porosity-permeability cross plots, has little spatial correlation and has little effect on reservoir performance. The large-scale variability, which makes up perhaps only 20 % of the scatter in permeability data, can have a marked impact on reservoir performance. The problem is to be able to define the 20 % of the data within a rock fabric or petrophysical class that has meaningful spatial correlation.

Subsurface studies show high variability of porosity and permeability at the scale of inches and feet similar to that observed in the outcrop. A core from well 2505, Seminole San Andres Unit, Gaines County, Texas, was used
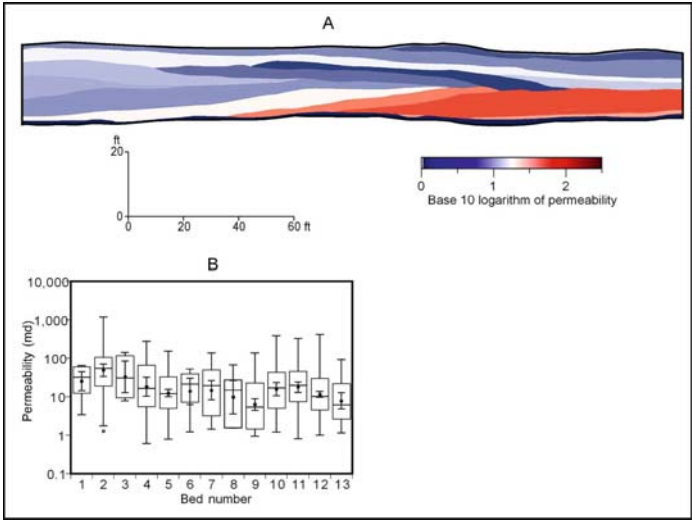
Fig. 5.9. Permeability models for the grainstone bed in Lawyer Canyon cycle 2.
A Bed forms showing large-scale permeability heterogeneity. **B** Permeability statistics by grainstone bed-form
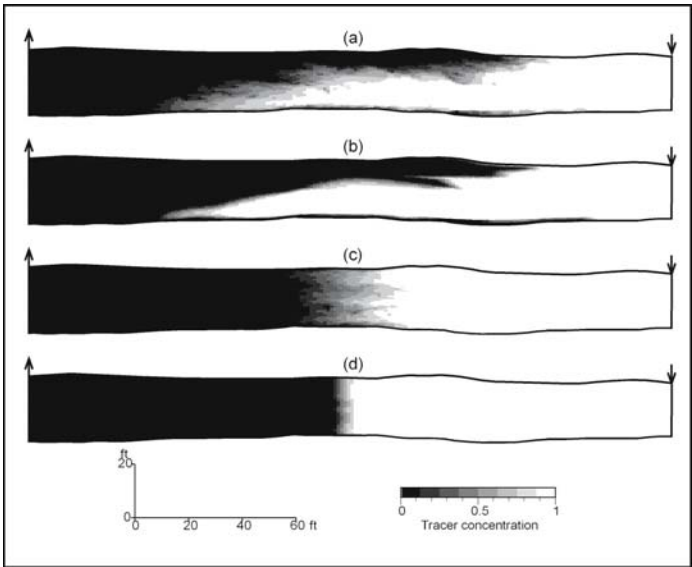
Fig. 5.10. Tracer simulations for Lawyer Canyon cycle 2 at one-half pore volume injection. **a** Small-scale and bed-form scale heterogeneity showing strong control by bed-form scale. **b** Bed-form heterogeneity only. **c** Small-scale heterogeneity only showing small effect of small-scale heterogeneity on flood front. **d** No heterogeneity

to study permeability variability. Twelve even-textured samples for which whole-core permeability values were available were selected. The samples include dolograinstone, mud-dominated dolopackstone, and dolowackestone. A 1-in. permeability grid of the 7- by 3.5-in. slab surface of the 12 samples was measured using a mechanical field permeameter (MFP; Fig. 11). Three 1-in. plugs were then drilled from the whole-core samples, analyzed for porosity and permeability, and the permeability of each end of the plug measured with an MFP.
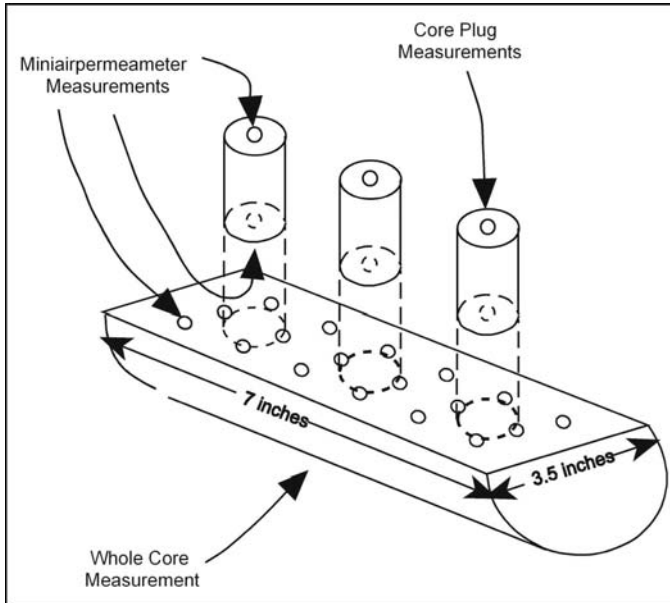
Fig. 5.11. Sampling method for detailed permeability study, Seminole San Andres Unit well 2505

The permeability values were compared with the whole core permeability, and examples of the results are presented in Figs. 12, 13, and 14. Permeability varies between 0.5 and 2 orders of magnitude on the scale of inches, that is, within each core sample (Fig. 15). Neither the geometric nor the arithmetic mean values match the whole-core permeability. Whole-core permeability is best characterized by the geometric mean in 50% of the samples and the arithmetic mean in 50% of the samples, suggesting that, at this scale, any average value between the geometric and arithmetic mean can be considered appropriate.

Contrary to the poor spatial correlations seen in horizontal variograms, vertical variograms base on subsurface porosity logs commonly show good spatial correlation (Fig. 16). In the example illustrated in Figure 16, the
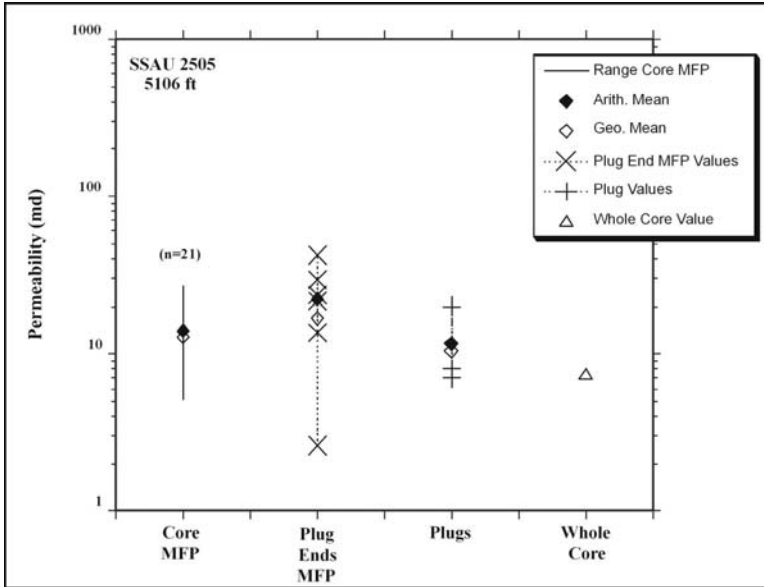
Fig. 5.12. Detailed permeability results from sample 5106 ft, Seminole San Andres Unit well 2505, showing variability factor of 10
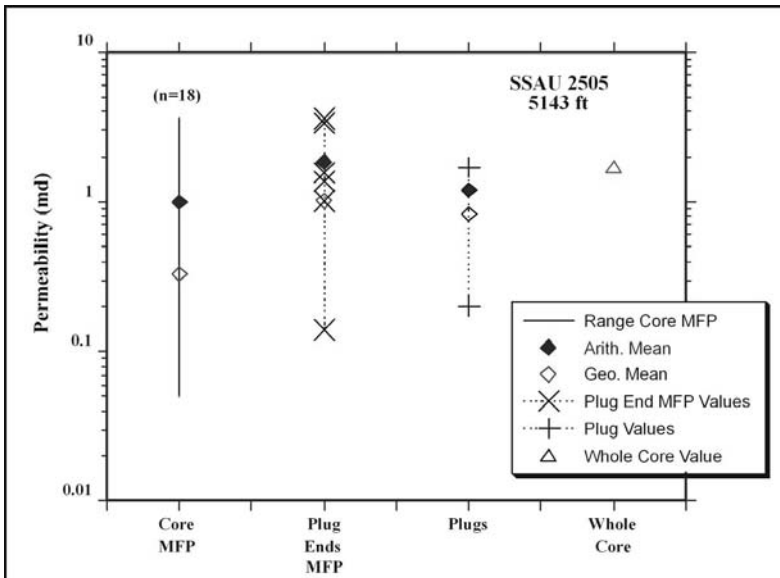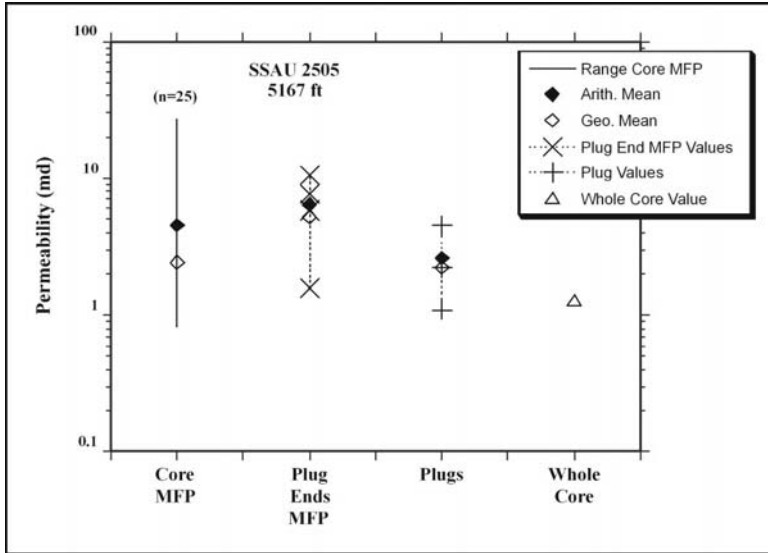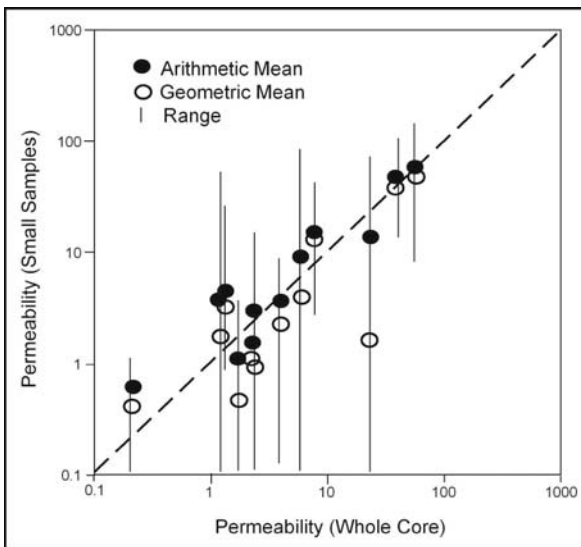

Fig. 5.13. Detailed permeability results from sample 5143 ft, Seminole San Andres Unit well 2505, showing variability factor of 100

Fig. 5.14. Detailed permeability results from sample 5167 ft, Seminole San Andres Unit well 2505 showing variability factor of 50

Fig. 5.15. Summary of results of detailed permeability study from 12 core samples, Seminole San Andres Unit well 2505. Variability within a core sample is on the order of 1 or 2 orders of magnitude (variability factor of 10 to 100). Assuming the whole-core value to be ground truth permeability, neither the geometric or arithmetic mean values consistently match the true average permeability
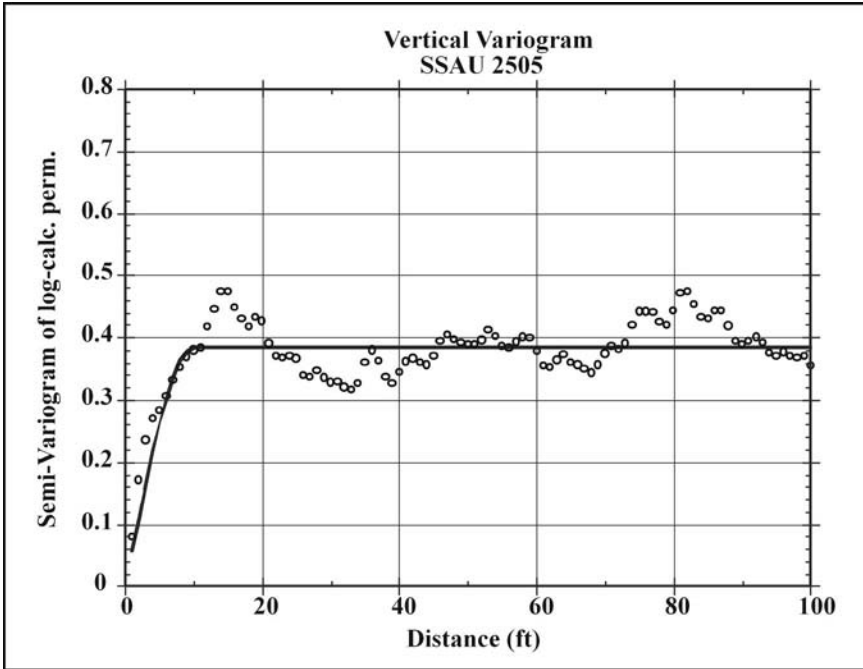
Fig. 5.16. Vertical variogram from well SSAU 2505 showing good spatial correlation up to a range of 10 ft

variogram has a very small nugget and a well-defined range of 10 ft. The correlation range is commonly similar to the general thickness of the rock-fabric facies described from cores. This supports the concept that rock-fabric facies are the basic petrophysical elements that should be mapped in a carbonate reservoir to ensure the construction of a realistic reservoir model.

The lack of spatial correlation of petrophysical properties within a rock-fabric bed makes correlations based on porosity logs suspect. The basic flaw in this approach is the assumption that petrophysical measurements have spatial information, which they do not. Only some geologic attributes can be correlated, and porosity cannot be used for correlation without a robust relationship between porosity and those attributes. This is illustrated by permeability profiles from vertical traverses taken from an outcrop of dolograinstone (Fig. 17A). The vertical variability in each profile is commonly assumed to be correlatable between the profiles, and correlation is accomplished by using pattern recognition and the "law of horizontality." The result is a layered permeability model (Fig. 17B). Because this is an outcrop, however, we can collect detailed permeability data from between the vertical profiles and find that the permeability is not layered but is characterized by "bull's eyes" or a patchy permeability pattern (Fig. 17B). Only the grain-

stone and wackestone facies can be correlated and not the permeability values.
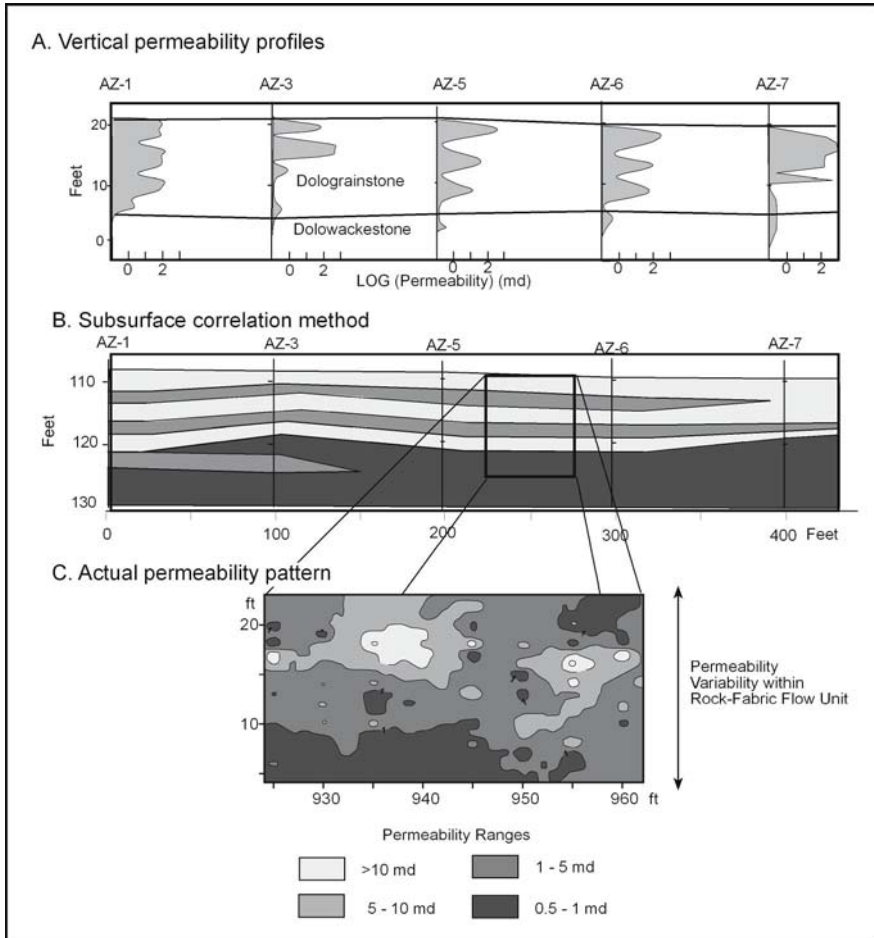
Fig. 5.17. Impact of high variability and lack of spatial correlation on correlation strategies. **A** Closely spaced vertical permeability profiles from outcrop measured sections and rock-fabric layering. **B** Correlation of permeability based on layered model compared with actual permeability structure showing that the high-permeability peaks are "bull's-eyes" rather than "layers"

5.4 Lawyer Canyon Reservoir Analog Study

5.4.1 Introduction

Reservoir models should be realistic images of the three-dimensional distribution of petrophysical properties, and it is generally agreed that the most important values to image properly are high and low permeability values. High-permeability layers control water breakthrough and patterns of bypassed oil, whereas low-permeability values tend to be baffles and inhibit cross flow. More realistic reservoir models can be constructed from outcrop data because detailed two- and three-dimensional geological and petrophysical data can be obtained as opposed to one-dimensional data from subsurface reservoirs. The outcrop study at Lawyer Canyon on the Algerita Escarpment, Guadalupe Mountains, New Mexico, provides an opportunity to construct a reservoir model of a carbonate ramp reservoir and investigate the impact of various geological elements on performance prediction.

5.4.2 Model Construction

The Lawyer Canyon reservoir window is a two-dimensional outcrop composed of nine upward-shallowing depositional cycles (Fig. 18). The cycles are typically upward-shallowing subtidal cycles composed of a vertical sequence of dolomudstone at the base, grading upward through dolowackestone and dolopackstone to cross-bedded dolograinstone at the top. Locally, the cycles are capped by a fenestral fabric interpreted to represent shoaling into the intertidal environment. The sequence is not always complete, but a vertical increase in grain size and sorting can typically be observed within any one cycle.
  Cycles 1 and 2 are dolograinstone-capped cycles. Cycle 1 has a continuous basal mudstone whereas cycle 2 has discontinuous thin dolomudstone beds at the base. Cycles 3-6 are primarily composed of grain-dominated dolopackstone in the southern area and dolowackestone in the northern area of the study window. Cycle 3 contains a small ooid dolograinstone body in the southern area, but cycles 4-6 are devoid of dolograinstone. Discontinuous fenestral beds are found capping some cycles, and discontinuous tight and dense dolomudstones are found at the base of the cycles. Cycle 7 is a dolograinstone-capped cycle. It is unique in that it contains large amounts of moldic pore space (separate vugs). Cycle 8 is a thin moldic grain-dominated dolopackstone or grainstone. Cycle 9 contains an upper dolograinstone unit
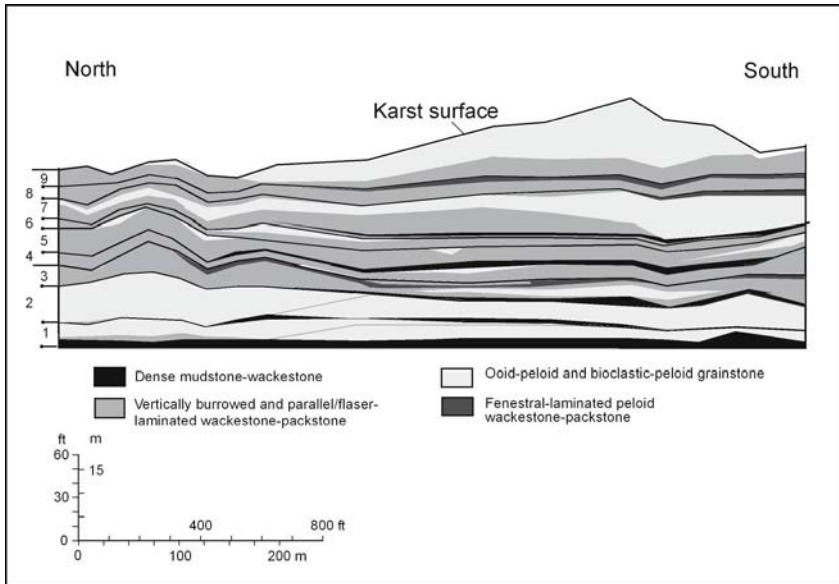
Fig. 5.18. High-frequency cycle framework, Lawyer Canyon, Algerita Escarpment (Kerans et al. 1994)

that varies in thickness from 0 to 10 ft in the north, to 40 ft in the south and terminates in the southern portion of the study area.

The interval has been completely dolomitized, probably from refluxing hypersaline marine water from a source in the overlying tidal-flat and evaporite beds. The mud-dominated dolostones are petrophysical class 3 fine crystalline dolostone and the grain-dominated dolopackstones and class 2 medium crystalline dolostones. Dolomitization occurred soon after deposition, and shallow compaction/cementation and resulted in a high conformance between depositional texture and rock fabric. The moldic porosity in cycle 7 is an example of selective dissolution associated with a local freshwater lens (Hovorka et al. 1993).

The high-frequency cycles are composed of five fundamental rock fabrics: (1) dolograinstone, (2) moldic dolograinstone, (3) medium crystalline grain-dominated dolopackstone, (4) fine crystalline mud-dominated dolopackstone/wackestones, and (5) dense, fine crystalline dolowackestone/mudstone. Core plugs taken from each of these rock fabrics were analyzed for porosity and permeability. The cross plot of interparticle-porosity and permeability exclusive of the moldic dolograinstone shows that the rock fabrics fall into the generic rock fabric/petrophysical fields (Fig. 19A). A cross plot of total-porosity and permeability for samples from the moldic grainstone facies shows a general grouping by moldic porosity (Fig. 19B).
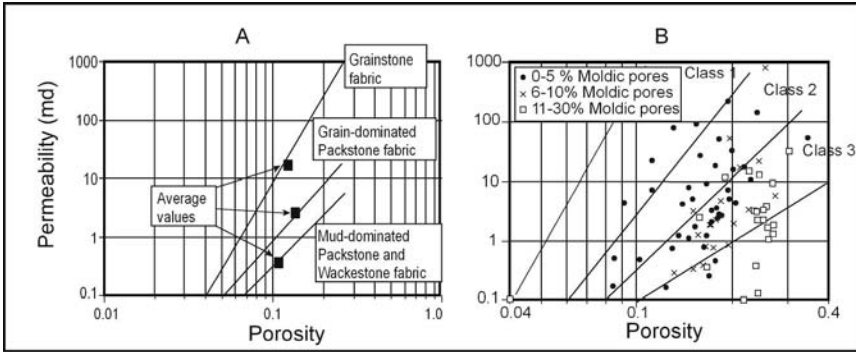
Fig. 5.19. Porosity/permeability relationship for **A** nonvuggy rock-fabric types and **B** separate-vug (moldic) pore types. The nonvuggy pore types have rock-fabric-specific transforms. The moldic grainstones do not have a transform but can be related to the grainstone transform by subtracting moldic porosity from total porosity

A flow model was constructed of the Lawyer Canyon window using the rock-fabric method. A generalized illustration of the rock-fabric reservoir model is shown in Fig. 20. The rock-fabric facies were mapped within the cycle framework, and porosity and permeability values from each rock-fabric facies were averaged using an arithmetic average for porosity and geometric average for permeability. Water saturation values were obtained from gneric rock-fabric-specific S_w, porosity, and reservoir-height relationships discussed in Chapter 2. Key elements are the high-permeability grainstones of cycles 1, 2, and 9, the low-permeability discontinuous mudstones at the base of most cycles, and the high-porosity low-permeability moldic grainstone of cycle 7.

5.4.3 Rock-Fabric Flow Units

The general vertical succession of rock fabrics within each cycle is from mud-dominated to grain-dominated, resulting in rock-fabric layers that may be continuous or discontinuous. These rock fabric layers provide the basic framework to the petrophysical model shown in Figure 20 and are referred to as rock-fabric flow layers or units. Cycle 1 is an example of this definition of a rock-fabric flow unit (Fig. 21). As discussed, permeability distribution within the capping grainstone layer is highly variable and has weak spatial correlation (Fig. 21). We have little permeability data from the underlying wackestone, but the data available suggest similar variability, and we would assume a similar lack of spatial correlation. This observation is represented in the cross plot illustrated in Figure 20. Statistics from the two rock fabrics show that they have significantly different average porosity and permeability
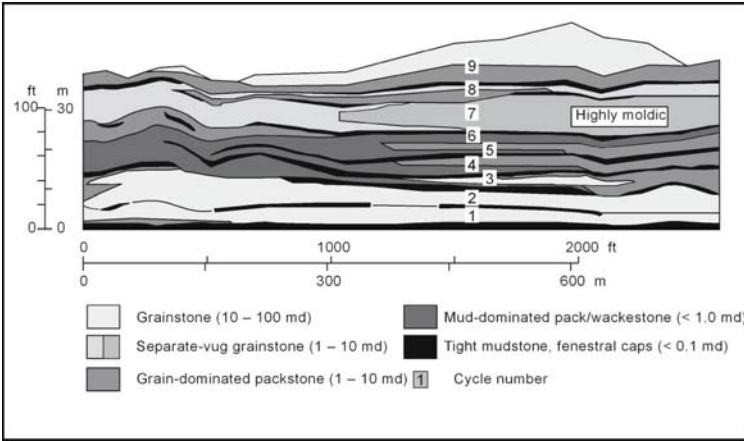
Fig. 5.20. Spatial distribution of average permeability in the Lawyer Canyon reservoir window. Permeability is averaged within rock-fabric flow layers/units (Lucia et al. 1992)
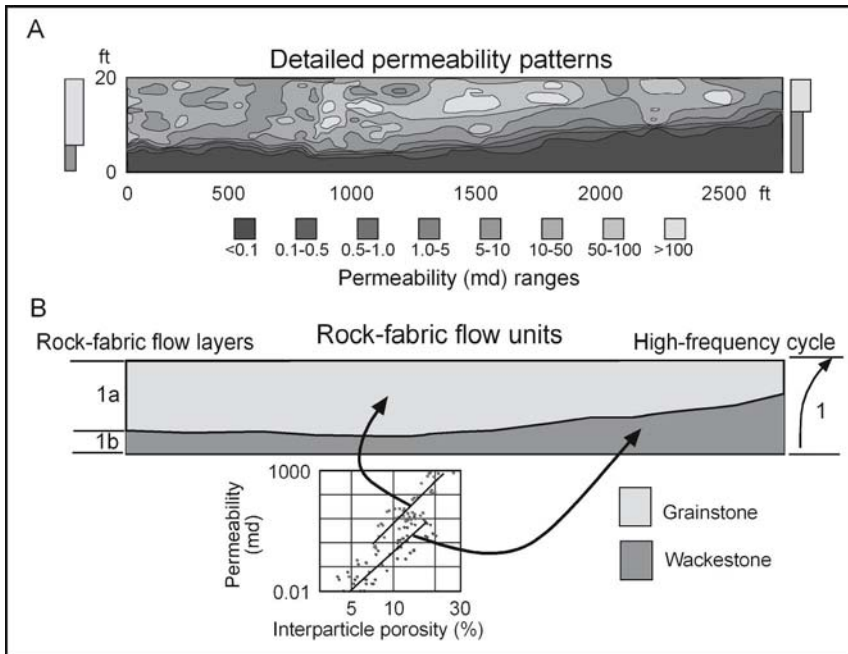
Fig. 5.21. Definition of a rock-fabric flow layer using cycle 1 as an example. **A** Cross section showing the highly variable and poorly correlated permeability distribution within the capping grainstone layer. **B** Cycle 1 divided into two rock-fabric flow layers and a cross plot showing typical petrophysical scatter but different statistics for each rock-fabric layer

values and should be treated has separate units. Therefore, *a rock-fabric flow unit is defined as a geologic unit that has a characteristic rock fabric, and within which the petrophysical properties are near randomly distributed* (Lucia et al. 1992). This definition amplifies the flow unit definition of Hearn et al. (1984). They define flow units as representing fairly distinctive rock types and have petrophysical characteristics significantly different from those of adjoining units.

5.4.4 Fluid Flow Experiments

Flow simulation experiments using the Lawyer Canyon reservoir model were conducted to test the sensitivity of performance prediction to certain geological and operational conditions. The results of these experiments are illustrated in Fig. 22. Two permeability models are shown, one based on outcrop data and one a simple layer model constructed by interpolation of geologic and petrophysical data between the two ends of the Lawyer Canyon window. The layered model has a recovery of almost 50% of the oil in place whereas the outcrop model has a much lower recovery of 35% (Fig. 23A). The effect of operational conditions was simulated by flooding the outcrop model from different directions. Oil recovery by flooding left to right is 44%, whereas flooding right to left recovers only 35% (Fig. 23B). This difference can be related to the distance between the producer and the termination of the high-permeability grainstone in cycle 9. As injecting from right to left progresses, cross flow occurs from cycle 9 into cycle 7 at the termination of the cycle 9 high-permeability grainstone at a distance of about 700 ft from the producing well (Fig. 22d). In the left-to-right flood the distance from the grainstone termination to the producer is about 100 ft, and no cross flow was observed (Fig. 22c).

Importantly, the remaining oil is concentrated in the moldic grainstone facies of cycle 7 and would be a target for horizontal wells. The grainstones all have the highest initial oil saturation, but the cycle 7 grainstone has very low permeability because most of the pore space is located within the grains as grain-molds rather than between the grains as interparticle pore space. The injected water flows at a faster rate through the high-permeability grainstone beds and at a lower rate in the low-permeability moldic grainstone bed, effectively bypassing much of the oil in cycle 7. This suggests that moldic grainstones are excellent targets for horizontal wells because they have high porosity, low permeability, and high initial oil saturation.

In all the flow models the kv/kh was set at 1. However, in the subsurface the kv/kv ratio often must be set at less than 1 (commonly 0.01 or less) for
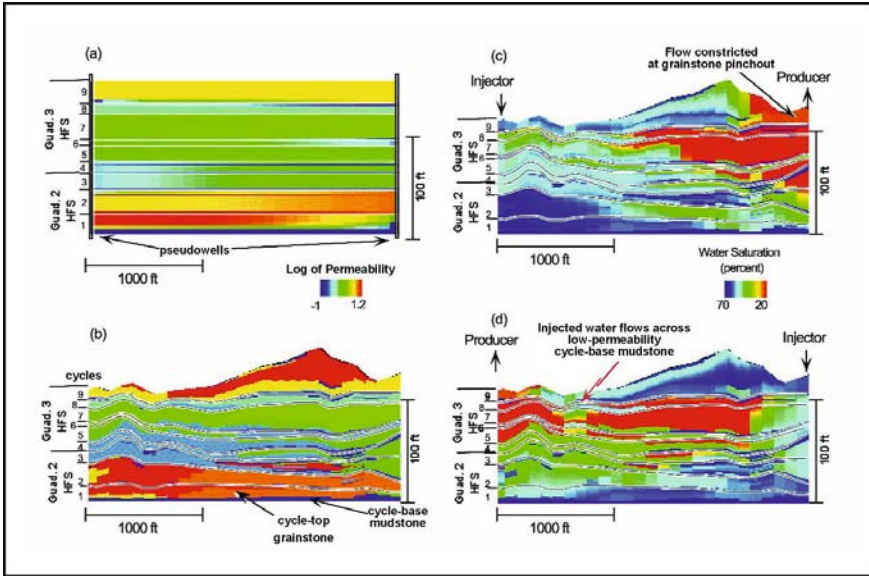
Fig. 5.22. Lawyer Canyon flow models. **a** A linear interpolation of permeability data taken from two pseudowells on each end of the Lawyer Canyon window. **b** The rock-fabric permeability model based on facies averaging of outcrop data. **c** Left-to-right injection experiment showing water saturation after 40 years of injection and crossflow point at downflow termination of high permeability in cycle 9. **d** Right-to-left injection experiment showing water saturation after 40 years of injection and crossflow point at downflow termination of high permeability in cycle 9

predicted and historical performance to match. The Lawyer Canyon model contains thin discontinuous dense mud layers that act as baffles to fluid flow, restricting gravity flow. Flow experiments were conducted with and without the mud layers and with various values of kv/kh (Fig. 24). The results showed that a kv/kh of 0.02 was necessary in the model without mud layers to match recovery from the model with mud layers and a kv/kh of 0.3. Therefore, the inclusion of thin dense layers in carbonate flow models is necessary to simulate realistic flow performance. However, in the subsurface we are limited by wireline logs that average the low porosity of these dense layers with the porosity of surrounding beds. Therefore, discontinuous thin dense layers must be inserted into the model based on core data.
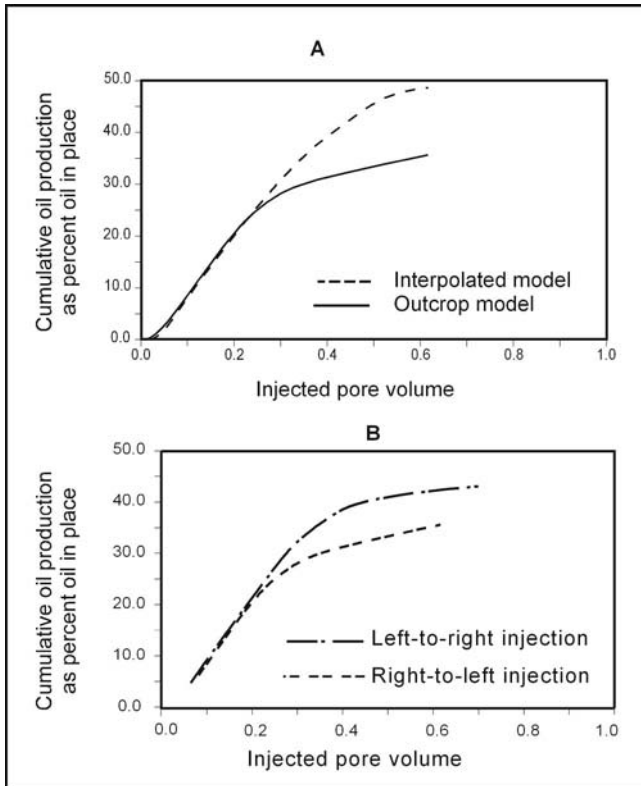
Fig. 5.23. Sweep efficiency plots comparing **A** linear interpolation model with outcrop model and **B** left-to-right with right-to-left injection experiment

5.5 Work Flow for Construction of the Reservoir Model

A work flow for constructing a carbonate reservoir mode is illustrated in Figures 25. 26. and 27. The construction of a reservoir model begins with core description, which provides the basic geologic data required to build a geological and petrophysical model (see Chapters 2 and 3). Core descriptions are the only source of data to describe the vertical facies successions that are paramount to defining sequences and HFC's; the stratigraphic elements key to building a petrophysical model. All cores from the reservoir that are of sufficient length should be described to provide a robust data set from which to define sequences and HFC's. Descriptions are normally made from core slabs augmented by thin sections to verify descriptions. Seismic data can be
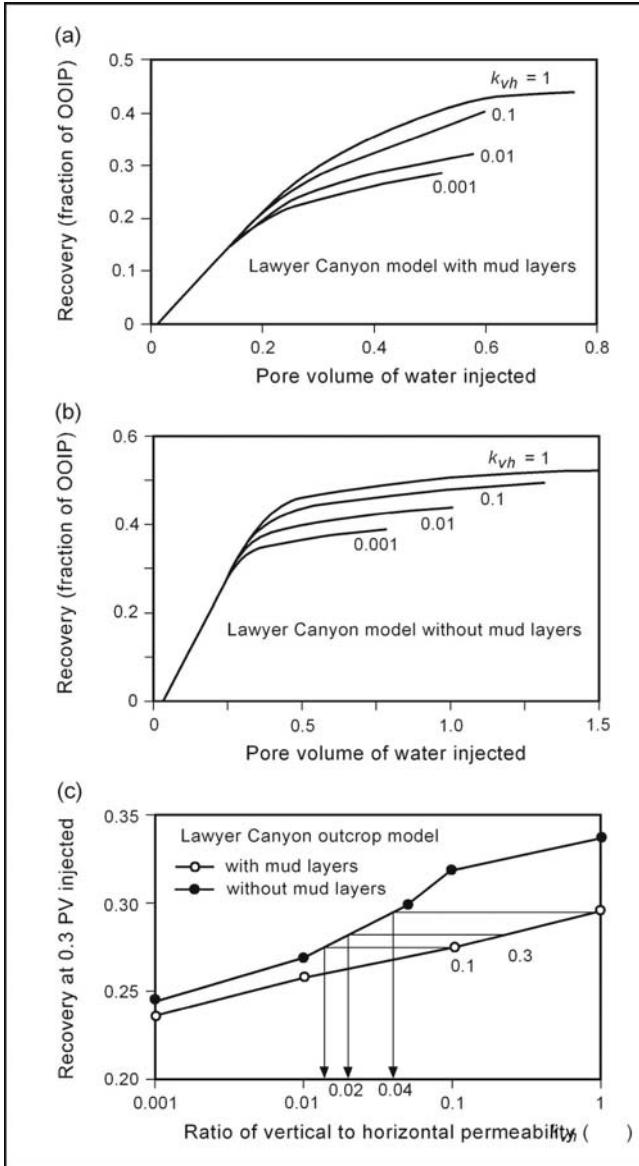
Fig. 5.24. Waterflood recovery as a function of pore volume injected for Kv/Kh ratios of 0.001, 0.01, 0.1 and 1 using Lawyer Canyon outcrop model. **a** Includes dense mudstone layers as baffles to gravity flow. **b** Dense mudstone layers are removed. **c** A comparison of recoveries from the two models at 0.3 pore volumes injected. A Kv/Kh ratio of 0.3 is realistic based on core data, and a ratio of 0.02 is required for recovery of the model without mud layers to match recovery of the model with mud layers

helpful in defining sequence boundaries and in selecting key correlation surfaces. Cycles and sequences are identified in each core (Fig. 25A), and only after all the cores have been described can the HFC and HFS be defined for mapping. The surfaces that can most easily be correlated between every core will define the HFC's and HFS's most suitable for mapping (Fig. 25B).

Rock fabric studies are also based on descriptions of core material (Fig. 26A). Rock-fabric descriptions must be made of the cores because most geologic core descriptions focus on interpreting depositional facies, use the Dunham classification, and do not quantify grain- vs. mud-dominated packstones, dolomite crystal size, or separate-vug porosity. A number of geologic facies may be the same rock-fabric facies. For example, a fusulinid wackestone and a peloid wackestone may have significance in determining water depth, but they are the same rock fabric, a class 3 mud-dominated fabric. In addition, geologic descriptions commonly use the Dunham classification, which does not distinguish between grain- and mud-dominated packstone. The more enlightened geologists, however, do make this distinction by using terminology such as mud-lean and mud-rich packstone or by restricting packstone to mud-dominated packstone. Also, the distinction between 10 μm and 30 μm dolomite crystals in a dolostone is critical, as is detailed information on the amount and type of vuggy pore space. Geologic descriptions do not commonly provide this information. Therefore, both a geologic and a petrophysical description of the cores must be made to have the information needed to build a reservoir model.

Rock fabrics can be described from core slabs if the describer is experienced, but the preferred method is to use thin sections made from core samples. It is important that the samples be collected from material used to measure the petrophysical properties, porosity, permeability, relative permeability, capillary pressure, etc. Samples from core plugs are best suited for this work because a thin section from the end of the plug is a cross section of the flow path used to measure permeability. However, thin sections are a very small sample of the core plug, and the use of high-resolution CT and NMR scans in conjunction is recommended. If whole-core analyses are done, the small-scale variability adds to the difficulty of relating the fabrics seen in thin section to the petrophysical measurements. In general, only the rock fabric can be assumed to be constant within a whole core sample, not interparticle or vuggy porosity or mineralogy.

Rock fabric flow units are defined by identifying every vertical change in basic rock fabrics observed in core descriptions (Fig. 26B). In general there will be a single vertical change from mud-dominated fabrics to grain-dominated fabrics defining two flow layers. If both a grainstone and grain-dominated packstone are present in the succession, a decision must be made as to whether to lump them together or keep them as separate layers. This is
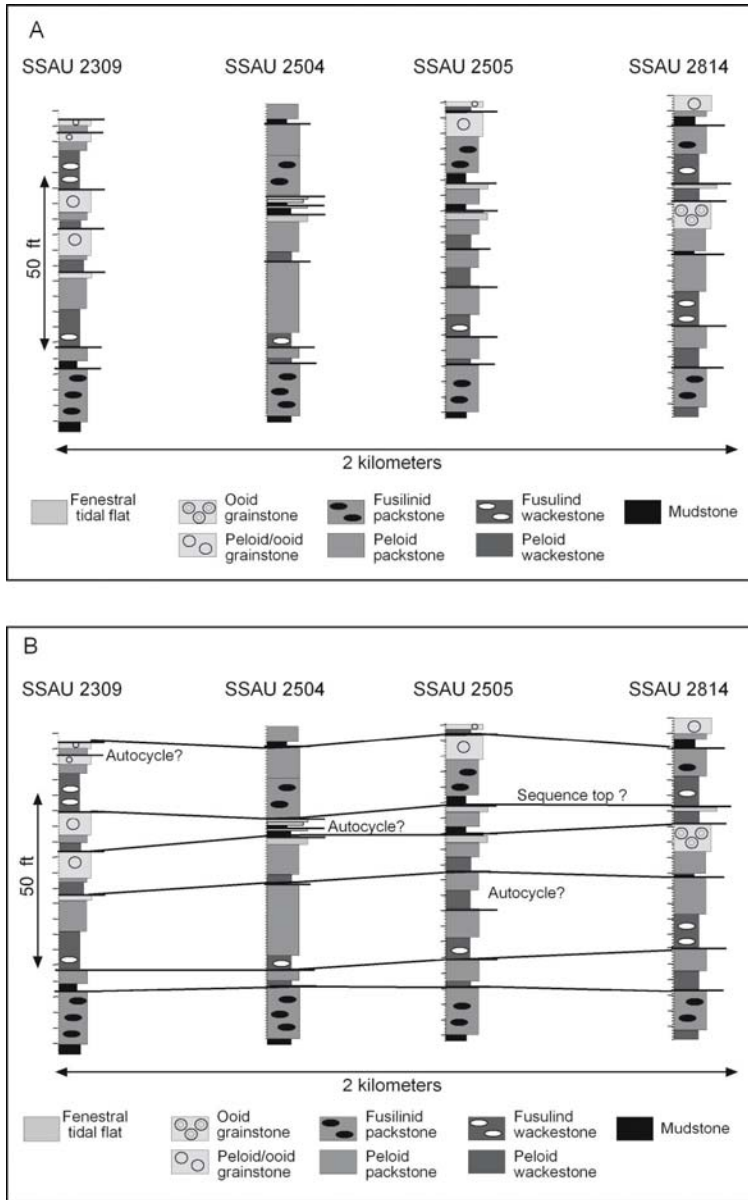
Fig. 5.25. Approach to constructing stratigraphic framework. **A** Describe facies successions for available core material and pick the top of every upward-shoaling cycle. Each core will not have the same number of cycles because of autocyclicity. **B** Define high-frequency cycles and sequences. Select the most continuous cycle tops to correlate and define as high-frequency cycles. Sequence boundary suggested by concentration of tidal-flat facies
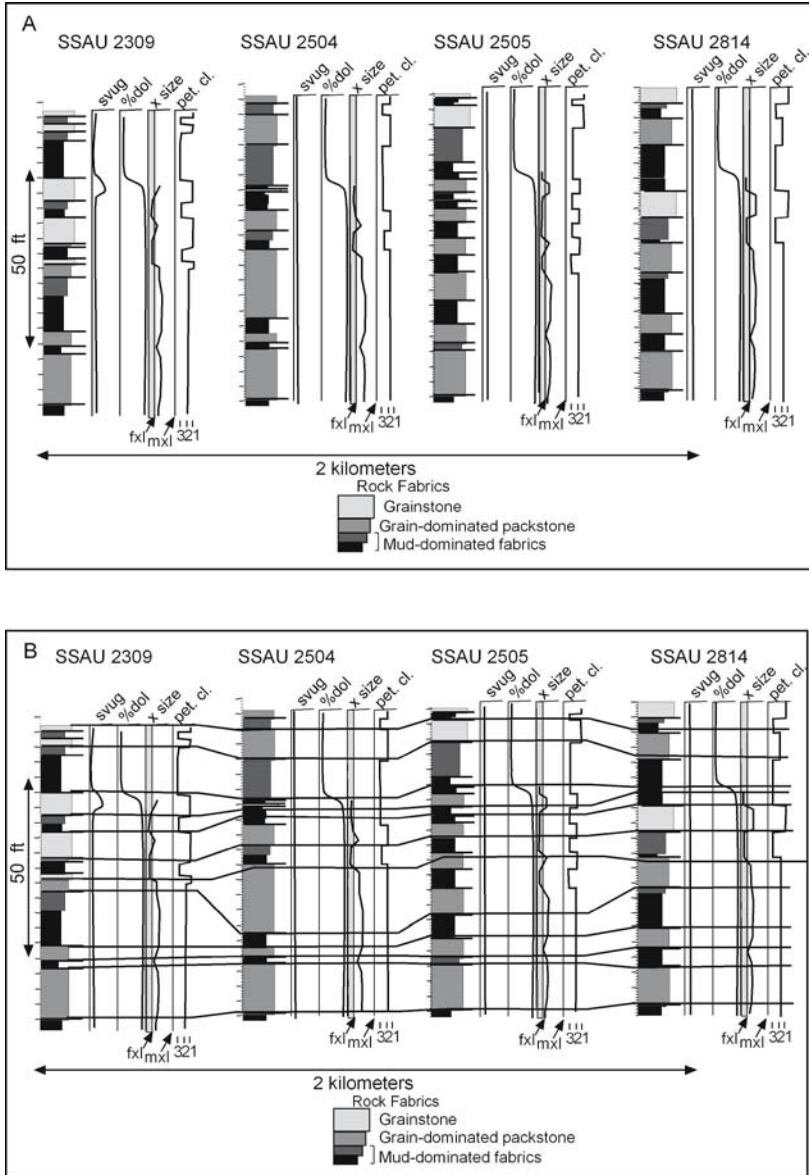
Fig. 5.26. Rock fabric approach to linking petrophysical properties to stratigraphic framework. **A** Describe rock-fabric facies, quantify lithology, separate-vug porosity, and dolomite crystal size, and determine petrophysical class of rock-fabric number. **B** Define rock-fabric flow layers by picking the top of change between mud-dominated fabrics, grain-dominated packstone, and grainstone and correlate the flow layers between cored wells. Each well will not have the same number of flow layers, and some judgment will have to be made as to which flow layer to pick as continuous

normally done on the preponderance of each fabric. If more than one mud-dominated layer is present in the succession, a similar decision must be made: group with adjacent fabrics or keep as a separate layer.

Once flow units have been defined they are correlated across all cores forming flow layers. There are two basic rules of correlation. 1) Flow layers cannot cross HFC boundaries and 2) flow layers must be continuous to accumulate the layering of reservoir simulation programs. Generally there will be at least 2 flow layers per HFC; a lower mud-dominated layer and an upper grain-dominated layer. In some cases the grain-dominated layer may be divided into a grainstone and a grain-dominated layer if there is a sufficient amount of each to warrant separation.

A layer may change laterally from one rock fabric to another, and one rock fabric interval may contain several flow layers if needed (Fig. 26B). In outcrop, rock-fabric flow layers and HFC's commonly have abrupt vertical boundaries, and rock-fabric boundaries should not cross HFC boundaries. Although the vertical contacts generally are abrupt, lateral boundaries are not sharp but are gradational. As can be seem in outcrops, facies tend to change laterally over distances of hundreds of feet, making it difficult to define a boundary in any usable sense. Therefore, petrophysical properties are expected to change abruptly in the vertical dimension and gradually in the lateral dimension. This suggests that petrophysical properties can be linearly interpolated between wells in reservoirs with closely spaced well control.

Rock fabric facies are defined by limestone textures, whereas petrophysical properties are defined by petrophysical classes. Petrophysical classes include the effects of diagenesis, whereas rock-fabric facies are defined by limestone textures. In limestone intervals the petrophysical classes are defined by the rock fabrics. When diagenetic products do not mimic limestone textures, petrophysical classes and rock fabrics will not conform. In the case of dolostones, fabrics with fine size dolomite crystals will mimic rock fabrics, whereas fabrics with medium and large size dolomite crystals will not, and the petrophysical class will be related to the dolomite crystal size and well as the rock fabric (Fig. 26A).

The rock fabrics are related to porosity, permeability, and capillary properties using the approach described in Chapter 2 (Fig. 27A, 1 and 2). The basic approach is to group rock fabrics into petrophysical classes, but in some instances it is useful to use a modified rock-fabric-number approach or even the apparent-rock-fabric-number approach. The end result is a series of rock-fabric-specific porosity-permeability transforms and porosity-saturation transforms that can be linked to the geologic model through maps of petrophysical class.
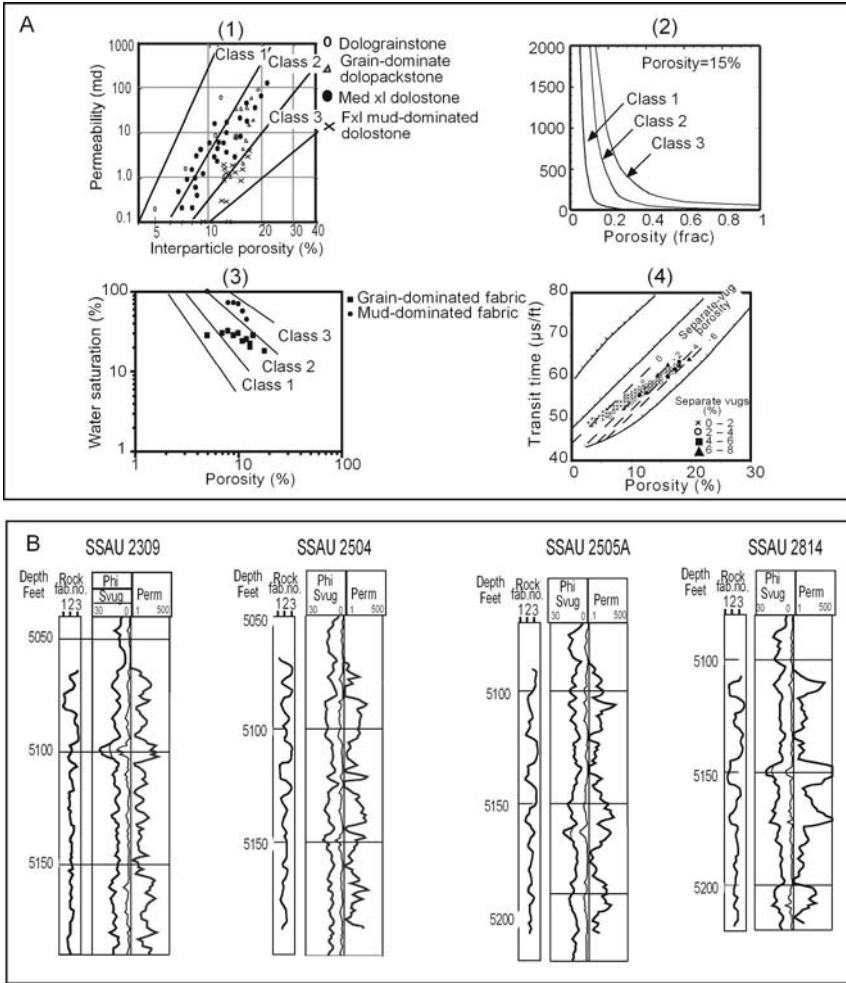
Fig. 5.27. Develop relationships between rock fabrics and petrophysical properties and wireline logs. **A** Develop transforms between rock-fabric petrophysical class, porosity, permeability, and initial water saturation. Develop transforms between rock-fabric petrophysical class, porosity, log-derived initial water saturation and between separate-vug porosity, log derived total porosity and acoustic travel time. **B** Use transforms to calculate vertical profiles of permeability and initial water saturation for each well in the field. Notice several locations where total porosity and interparticle porosity are different.

The next major activity is calibrating rock-fabric and petrophysical class or rock-fabric number to wireline logs (Fig. 27A, 1 and 2). The robustness of the calibration will depend upon the quality and types of wireline logs avail-

able. The basic logging suite composed of gamma-ray, neutron, density, sonic, PEF, various resistivity tools, and caliper provides the best chance for developing a robust calibration. However, useful calibrations have been made using reliable gamma-ray and neutron logs only. There are numerous methods available that can be used to accomplish this task, and in Chapter 3 we discussed some of the fundamentals. For correlation is it imperative that the vertical succession of rock fabrics be clearly identifiable. Generally, the number of facies needed to interpret the depositional history and to define sequences and HFS's are more than the four or five rock fabrics needed to correlate the cycle boundaries, define flow layers, and calculate permeability and initial water saturation. For estimating permeability and initial water saturation it is imperative that petrophysical class or rock-fabric number, interparticle porosity and separate-vug porosity be evident. These factors are used to calculate vertical profiles of permeability (Fig. 27B) and initial water saturation for each well with the appropriate log suite.

A critical subactivity is defining the zero capillary pressure level (zcpl), which is needed to model initial water saturation. This is a difficult task, but it is often accomplished by converting a capillary pressure curve into reservoir height and placing the top of the transition zone defined by a capillary pressure curve at the producing oil/water contact. The zcpl is located at zero reservoir height on the capillary pressure curve.

The vertical profiles of petrophysical properties are calculated for each well and the high-frequency sequences, high-frequency cycles, and flow layers are correlated without the reservoir (Fig. 28A). This provides the basic framework for the last step, which is to distribute porosity, permeability and initial water saturation within the rock-fabric flow layers. There are several methods for doing this task. The petrophysical properties at each well are averaged within rock-fabric layers and the average values are interpolated between wells within the rock-fabric layers. Petrophysical properties can be distributed within the rock-fabric layers between wells by variography conditioned on well data and by interpolation of well data between wells (Fig. 28B). The advantage of variography over simple interpolation is that the continuity of permeability within each rock-fabric layer can be adjusted by using various variograms to match production and injection rates. However, whereas vertical variograms can be readily calculated from well data, the critical horizontal variograms needed to distribute permeability between wells must be guessed at or estimated from outcrop data.
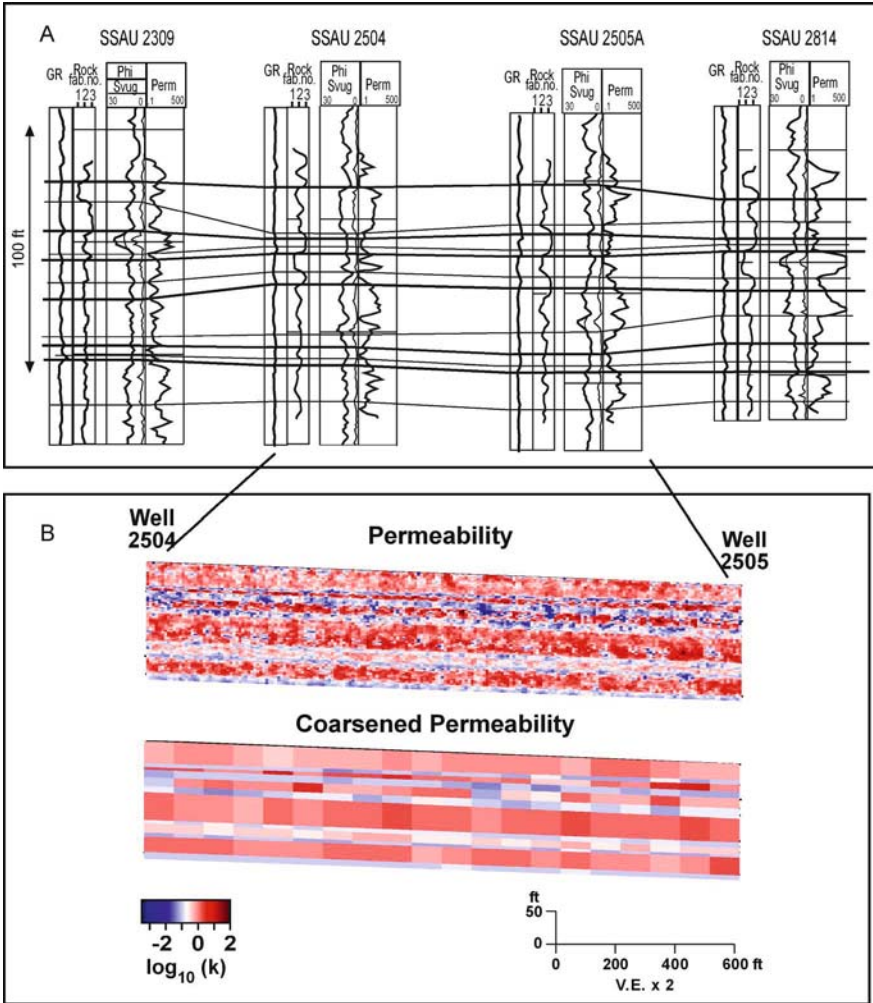
Fig. 5.28. Distribute petrophysical properties in the interwell volume. **A** Correlate high-frequency cycles and flow layers throughout the reservoir. **B** Distribute petrophysical properties within flow layers and conditioned to well data using various geostatistical methods. The resulting permeability structure can be coarsened up to the thickness of the flow layers (after Jennings, unpublished data)

Four types of models are illustrated in Fig. 29. The models are from the Seminole San Andres reservoir in West Texas. The first illustration is the rock-fabric model constructed using the approach described above. The second is a geocellular model with 1-ft permeability data linearly interpolated between wells parallel to the cycle boundaries. This approach is not realistic
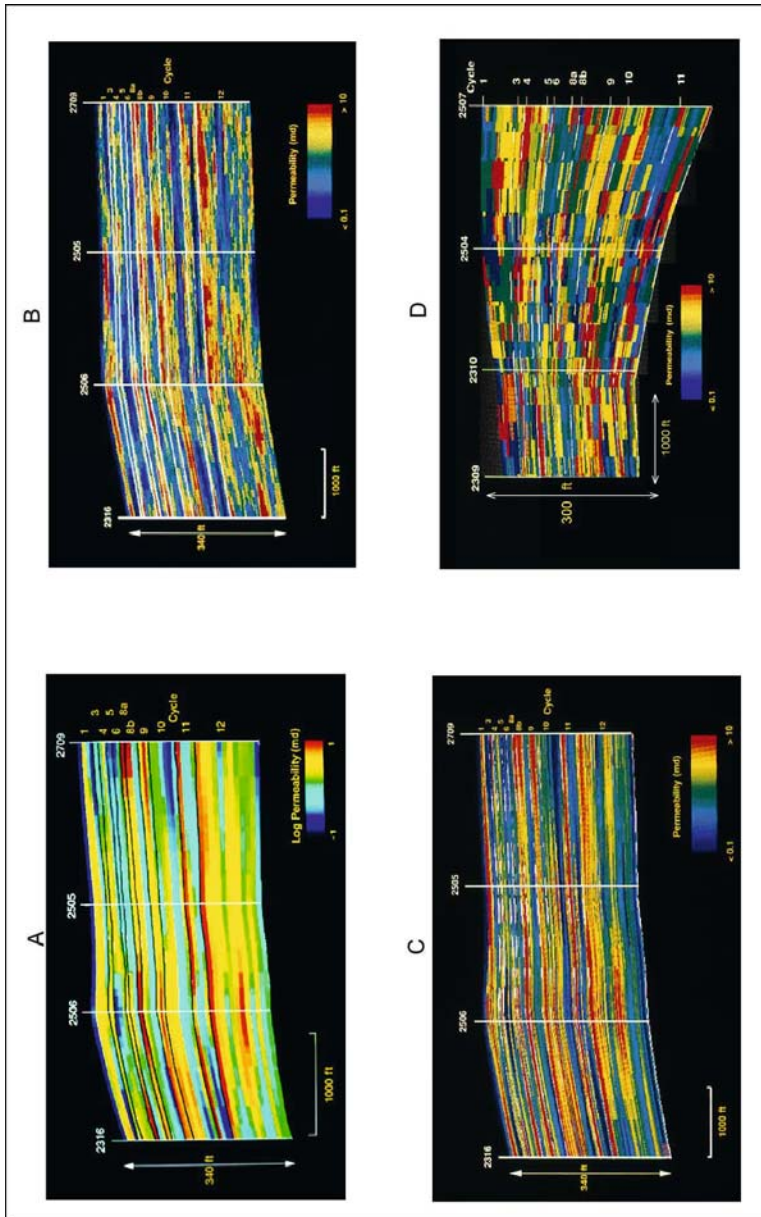
Fig. 5.29. Four methods of filling the reservoir volume between wells. **A** Linear interpolation of well data averaged within rock-fabric units and constrained by cycle boundaries. **B** Stochastic distribution of permeability based on variograms and constrained by rock-fabric units. **C** Linear interpolation of point well data constrained by cycle boundaries. **D** Stochastic distribution of permeability based on vertical and horizontal variograms but not constrained by cycle boundaries

because outcrop data show that permeability is near randomly distributed on the rock-fabric scale and not laterally correlatable on a 1-ft scale. The third model is the rock-fabric model with permeability distributed stochastically within the rock-fabric flow units, using vertical variograms from well data and estimated horizontal variograms. This image is perhaps the most realistic and results in higher production and injection rates than the linearly interpolated rock-fabric model. The last model is a stochastic model where permeability is distributed without regard to the high-frequency cycles. The permeability patterns show no resemblance to the cycle architecture of the geological model. An important test of any reservoir model is how well it reflects the geologic model and the geologic layering in particular.

5.6 Summary

In this chapter we described the rock-fabric method for building a reservoir model. Constructing the 3-D chronostratigraphic framework was discussed in Chapter 4, and linking petrophysical measurements to the geologic framework through rock fabrics was discussed in Chapter 2. The important step of calibrating wireline logs was the subject of Chapter 3. The methods described in these chapters provide the tools needed to calculate vertical profiles of petrophysical properties given an adequate suite of logs. In this chapter we focus on methods for distributing the properties in the interwell environment, which comprises 99% of the reservoir volume.

Perhaps the most important observation discussed in this chapter is the high variability of permeability, and presumably porosity, within a grainstone bed. Geostatistical analysis shows that this variability occurs on the scale of feet or inches, has little spatial correlation, and can be legitimately averaged for modeling purposes. However, there is a longer range variability with a periodicity of hundreds of feet. Flow simulation experiments demonstrate that the short-range data have little effect on the flood front, whereas the larger scale variability may control the rate of water breakthrough. Approximately 80% of the variance is in the small-scale, poorly correlated data that have little effect on flood response. Therefore, much of the scatter observed in cross plots of interparticle porosity and permeability constrained to one rock fabric has little spatial significance and can be considered as noise in the system. The problem is to sort out the 20 % that may have spatial importance.

We have shown that HFC's are the basic geologic element for building a reservoir model. For building the reservoir model, however, the basic geologic element is the rock-fabric flow layer. The Lawyer Canyon outcrop

study demonstrates that there can be significant differences in the petrophysical properties between the basic rock-fabric layers of grainstone, grain-dominated packstone, and mud-dominated fabrics as well as between the basic fabrics and moldic grainstones and dense mudstones. Within each of these rock fabric layers the petrophysical properties have poor spatial correlation. Therefore, each rock-fabric bed constitutes a flow layer and is the basic building block for distributing porosity, permeability, and initial water saturation within the interwell environment.

Petrophysical properties can be distributed within the flow layers using several different approaches. The well data can be linearly interpolated between wells using either the foot-by-foot data or data averaged over one flow layer. The interwell volume can be filled using conditional stochastic simulations based on well data and vertical and horizontal variograms. Whatever method is used, the result must clearly reflect the layering present in the geological and petrophysical models.

The work flow presented in this chapter is outlined below.

1) Describe the vertical succession of depositional facies in core slabs identifying depositional cycles.
2) Identify sequence boundaries and high-frequency cycles
3) Describe and quantify rock fabrics and important rock-fabric textures.
4) Link rock fabrics and textures to petrophysical properties and develop relationships among porosity, permeability, and initial water saturation.
5) Calibrate rock fabrics and petrophysical classes to wireline log response.
6) Calculate vertical profiles of permeability and initial water saturation using porosity and petrophysical class.
7) Correlate sequences, HFC, and flow layers over the field area.
8) Distribute petrophysical properties in the interwell volume constrained by well data and flow layers.

References

Barber AJ, George CJ, Stiles LH, Thompson BB 1983 Infill drilling to increase reserves - actual experience in nine fields in Texas, Oklahoma, and Illinois. J Pet Technol August 198:1530-1538

Fogg GE, Lucia FJ 1990 Reservoir modeling of restricted platform carbonates: geologic/geostatistical characterization of interwell-scale reservoir heterogeneity, Dune Field, Crane County, Texas. The University of Texas at Austin, Bureau of Economic Geology, Report of Investigations No 190, 66 pp

Galloway WE, Ewing TE, Garrett CE, Tyler N, Bebout DG 1983 Atlas of major Texas oil reservoirs. The University of Texas at Austin, Bureau of Economic Geology, 139 pp

George CJ, Stiles LH 1978 Improved techniques for evaluating carbonate water-floods in West Texas. J Pet Technol Nov 1978:1547-1554

Grant CW, Goggin DJ, Harris PM 1994 Outcrop analog for cyclic-shelf reservoirs, San Andres Formation of Permian Basin: stratigraphic framework, permeability distribution, geostatistics, and fluid-flow modeling. AAPG Bull 78 1:23-54

Hearn CJ, Ebanks WF Jr, Tye RS, Ranganathan V 1984 Geological factors influencing reservoir performance on the Hartzog Draw field, Wyoming. J Pet Technol Aug 1984:1335-1344

Hinricks PD, Lucia FJ, Mathis RL 1986 Permeability distribution and reservoir continuity in Permian San Andres Shelf Carbonates, Guadalupe Mountains, New Mexico. In: Moore GE, Wilde GL, (eds) Lower and Middle Guadalupian facies, stratigraphy, and reservoir geometries, San Andres/Grayburg formations, Guadalupe Mountains, New Mexico and Texas. Permian Basin Section, Society of Economic Paleontologists and Mineralogists Publication 86-26:37-47

Hovorka SD, Nance HS, Kerans C 1993 Parasequence geometry as a control on porosity evolution: examples from the San Andres and Grayburg formation in the Guadalupe Mountains, New Mexico. In: Loucks RG, Sarg JF, (eds) Carbonate sequence stratigraphy: recent developments and applications. AAPG Mem 57:493-514

Jennings JW 2000 Spatial statistics of permeability data from carbonate outcrops of West Texas and New Mexico: Implications for improved reservoir modeling. The University of Texas at Austin, Bureau of Economic Geology, Report of Investigations No. 258, 50 pp

Jennings JW, Ruppel SC, Ward WB 2000 Geostatistical analysis of permeability data and modeling of fluid-flow effects in carbonate outcrops. SPE Reservoir Eval & Eng 3, 4:292-303

Kerans C, Lucia FJ, Senger RK 1994 Integrated characterization of carbonate ramp reservoirs using Permian San Andres Formation outcrop analogs. AAPG Bull 78, 2:181-216

Kerans C, Lucia FJ, Senger RK, Fogg GE, Nance HS, Hovorka SD 1993 Characterization of facies and permeability patterns in carbonate reservoirs based on outcrop analogs. The University of Texas at Austin, Bureau of Economic Geology, final report prepared for the Assistant Secretary for Fossil Energy, US Department of Energy, under contract no DE-AC22-89BC14470, 160 pp

Lucia FJ 1983 Petrophysical parameters estimated from visual descriptions of carbonate rocks: A field classification of carbonate pore space. J Pet Technol 35, 3:629-637

Lucia FJ 1995 Rock-fabric/petrophysical classification of carbonate pore space for reservoir characterization. AAPG Bull 79, 9:1275-1300

Lucia RJ, Conti RD 1987 Rock fabric, permeability, and log relationships in an upward-shoaling, vuggy carbonate sequence. The University of Texas at Austin, Bureau of Economic Geology, Geological Circular 87-5, 22 pp

Lucia FJ, Major RP 1994 Porosity evolution through hypersaline reflux dolomitiza-
tion. In: Purser BH, Tucker ME, Zenger DH, (eds) Dolomites, a volume in
honor of Dolomieu. Int Assoc Sedimentol Spec Publ 21:325-341

Lucia FJ, Kerans C, Senger RK 1992 Defining flow units in dolomitized carbonate-
ramp reservoirs. Society of Petroleum Engineers, Paper No. SPE 24702, Wash-
ington D.C., pp. 399-406

Lucia FJ, Kerans C, Wang FP 1995 Fluid-flow characterization of dolomitized car-
bonate-ramp reservoirs: San Andres Formation (Permian) of Seminole field and
Algerita Escarpment, Permian Basin, Texas and New Mexico. In: Stoudt EL,
Harris PM (eds) Hydrocarbon reservoir characterization: geologic framework
and flow unit modeling. SEPM (Society for Sedimentary Geology), SEPM
Short Course 34:129-153

Senger RK, Lucia FJ, Kerans C, Ferris MA, Fogg GE 1993 Dominant control on res-
ervoir-flow behavior in carbonate reservoirs as determined from outcrop studies.
In: Linville B, Burchfield TE, Wesson TC, (eds) Reservoir characterization III.
Proc 3rd Int Reservoir Characterization Tech Conf, Tulsa, Nov 1991. PennWell
Books, Tulsa, Okla, pp 107-150

Wang FP, Lucia FJ 1993 Comparison of empirical models for calculating the vuggy
porosity and cementation exponent of carbonates from log responses. The Uni-
versity of Texas at Austin, Bureau of Economic Geology, Geological Circular
93-4, 27 pp

Wang FP, Lucia FJ, Kerans C 1994 Critical scales, upscaling, and modeling of shal-
low-water carbonate reservoirs. Society of Petroleum Engineers, Paper No. SPE
27715, Midland, Texas, pp. 765-773

Wang FP, Lucia FJ, Kerans C 1998 Integrated reservoir characterization study of a
carbonate ramp reservoir: Seminole San Andres Unit, Gaines County, Texas.
SPE Reservoir Evaluation & Engineering 1, 3:105-114

Chapter 6 Limestone Reservoirs

6.1 Introduction

The three-dimensional spatial distribution of petrophysical properties is controlled by the spatial distribution of geologic processes; processes that can be separated into depositional and diagenetic. In Chapter 4 we discussed depositional processes and focused on (1) the origin of depositional textures, (2) the relationship between porosity, permeability, and depositional texture, (3) the vertical and lateral distribution of depositional textures related to topography, current energy, biologic activity, and eustatically controlled cyclicity, and (4) the fundamentals of sequence stratigraphy. The importance of chronostratigraphic surfaces was emphasized as the fundamental element in constructing a geological framework within which petrophysically-significant depositional textures can be systematically distributed.

Whereas it is clear that the three-dimensional spatial distribution of petrophysical properties is initially controlled by patterns of depositional textures, it is also clear from reservoir studies that the petrophysical properties found in carbonate reservoirs are significantly different from those of modern carbonate sediments. Diagenesis typically reduces porosity, redistributes the pore space, and alters permeability and capillary characteristics. The porosity of modern sediments ranges from 40 to 70%, whereas the porosity of carbonate reservoirs in the USA ranges from 9 to 17% (Schmoker et al. 1985). The permeability of carbonate reservoirs is similarly reduced relative to that found in carbonate sediments. Therefore, an understanding of diagenetic processes and the patterns of their products is essential for carbonate reservoir description and reservoir model construction.

The basic diagenetic processes discussed here are (1) calcite carbonate cementation, (2) mechanical and chemical compaction, (3) selective dissolution, (4) dolomitization, (5) evaporite mineralization, and (6) massive dissolution, cavern collapse, and fracturing. Each of these

processes can be identified by specific fabrics. Occlusion of pore space by calcite can be identified by crystal geometry and position relative to grain fabrics. Compaction can be identified by grain interpenetration, grain breaking, grain deformation, grain spacing, and stylolitization. Selective dissolution refers to the formation of pore space by the removal of a specific rock-fabric element forming a fabric-selective vuggy pore type. Dolomitization is identified by the presence of the mineral dolomite, and evaporite mineralization is identified by the presence of evaporite minerals such as anhydrite, gypsum, and halite. Massive dissolution refers to the formation of relatively large pore space without regard to rock fabric, and the voids may be sufficiently large to collapse, forming collapse breccia and associated fracture patterns.

Whereas each of these diagenetic processes can be identified and studied independently, they overlap in time and place and therefore have an effect on each other.   A sedimentary deposit is formed only once, whereas it may be overprinted by any or all of the diagenetic processes listed above. Petrographic studies are useful for determining the sequence of diagenetic events: these studies often show a great deal of overlap in diagenetic timing, and they may show that processes recur.   Indeed, diagenesis is a continuing process, starting with the cessation of sedimentation and ending with the onset of metamorphism. Thus, the sequence of diagenetic events may be extremely complicated and the pattern of diagenetic products difficult to predict if they are not related to depositional patterns.

Distribution of diagenetic products is controlled by the nature of the precursor carbonate, and with increasing time the nature of the precursor carbonate becomes more and more unlike depositional textures. Compaction starts with burial and may end only with uplift and exposure. Cementation can be penecontemporaneous with deposition or may occur later during burial, and early cementation may inhibit later burial compaction. Dolomitization can occur immediately after sedimentation or millions of years after deposition; and the cementation, dissolution, and compaction that occurs before dolomitization will affect the pattern of dolostone.   Early dolomitization may produce stratiform dolostone, whereas late dolomitization may be controlled by fractures and collapse breccias and form discontinuous bodies of dolostone.

Therefore, to distribute petrophysical properties within a carbonate reservoir model, the process of diagenetic overprinting of depositional textures must be understood. A key question is the degree of conformance between diagenetic products and depositional patterns.   If transport of material in and out of the system is not an important factor in producing the diagenetic product, the product will generally conform to depositional

patterns. However, if transport of ions in and out of the system by fluid flow is required to produce the diagenetic product, then the diagenetic product may not conform to depositional patterns. In this case, knowledge of the geochemical-hydrological system may be required to map the diagenetic products, including knowing the source of the fluid and the direction of fluid flow.

In the following chapters we will group carbonate reservoirs based on diagenetic processes. The simplest reservoirs are limestone characterized by cementation, compaction, and selective dissolution. Dolostone reservoirs are more complicated, and evaporate mineralization commonly adds to the complexity. Reservoirs characterized by pore systems that are not linked to matrix pore systems are the most complicated because they involve a combination of fracturing, massive dissolution, collapse, and cementation.

The products of cementation, compaction, selective dissolution and neomorphism can normally be linked to depositional textures. Compaction and associated cementation is a diagenetic process that is a function of rock strength and the time-overburden history (Weyl 1959). It does not involve transport and is closely linked to depositional textures. Selective dissolution and recrystallization of unstable aragonite allochems and associated precipitation of calcite cement is normally linked to depositional environments and may not require fluid transport. Early cementation processes require fluid flow to import calcium and carbonate into the system, but the fluid flow is closely tied to the depositional environment. Late or burial cementation may occur by chemical compaction and thus may be linked to a depositional environment, or it may require regional transport of ions by ground water and may not be linked to a depositional environment.

Dolomitization requires fluid flow for the introduction of magnesium into the system. Therefore, fluid flow is an important element in the origin of dolomite fabrics, and dolomite patterns may not be linked to depositional patterns. The source and flow paths of dolomitizing water are best known for reflux dolomitization. The source is the tidal flat or saline lake, and the flow paths are generally downward and seaward. Gypsum and anhydrite are commonly associated with dolomitization and require the transport of sulfate into the system by hypersaline water. Studies have shown little linkage between depositional facies and patterns of diagenetic gypsum or anhydrite. Patterns of burial dolomitization are difficult to predict because predolomite diagenetic history may significantly alter the permeability structure and result in dolomitizing waters following diagenetic rather than depositional flow paths. However, faults are known to control flow paths of dolomitizing fluid, although the fluid source is not

well known. The hydrology of other dolomitization models is generally arguable.

Touching-vug reservoirs are the product of fracturing, dissolution, compaction, and collapse brecciation. They are the most difficult to model because they have little relationship to depositional patterns. Their products are controlled by precursor diagenetic events, including fracturing, and ground water flow. Pore space is totally reorganized through the removal of carbonate from some areas and reprecipitation in other areas through a complex geochemical-hydrological meteoric flow system.

This chapter will focus on limestone reservoirs characterized by cementation, compaction, and selective dissolution. Dolostone and touching-vug reservoirs will be addressed in the following chapters.

6.2 Cementation/Compaction/Selective Dissolution

The processes of cementation, compaction, and selective dissolution comprise a diagenetic environment characterized by shallow marine diagenesis, shallow meteoric diagenesis related to local subaerial exposure of shoals and tidal flats, and simple burial in sea water and ground water. Cementation and compaction reduce depositional porosity and systematically reduce pore size. Selective dissolution typically forms separate-vug porosity by selectively dissolving grains composed of unstable minerals. Dissolved carbonate may be precipitated in the form of calcite cement in adjacent pore space. The patterns of these diagenetic products are normally closely linked to depositional textures and can be predicted by mapping these textures.

6.2.1 Calcium Carbonate Cementation

Calcium carbonate cementation occludes pore space and reduces pore size. Studies have shown typical textures to be isopachous fibrous and bladed cements, equant or blocky sparry cements, syntaxial cements, pendulous cements, meniscus cements, and radiaxial cements (Harris et al. 1985; Hurley and Lohmann 1989; Fig. 1). Calcite cements are composed of calcite, high-magnesium calcite, or aragonite when they are formed. However, high-magnesium calcite and aragonite are unstable minerals and are replaced by the stable form, calcite, with time and burial.

Cementation starts soon after deposition. Indeed, clasts of cemented sediment, called intraclasts, are found redeposited in later sediment. Early
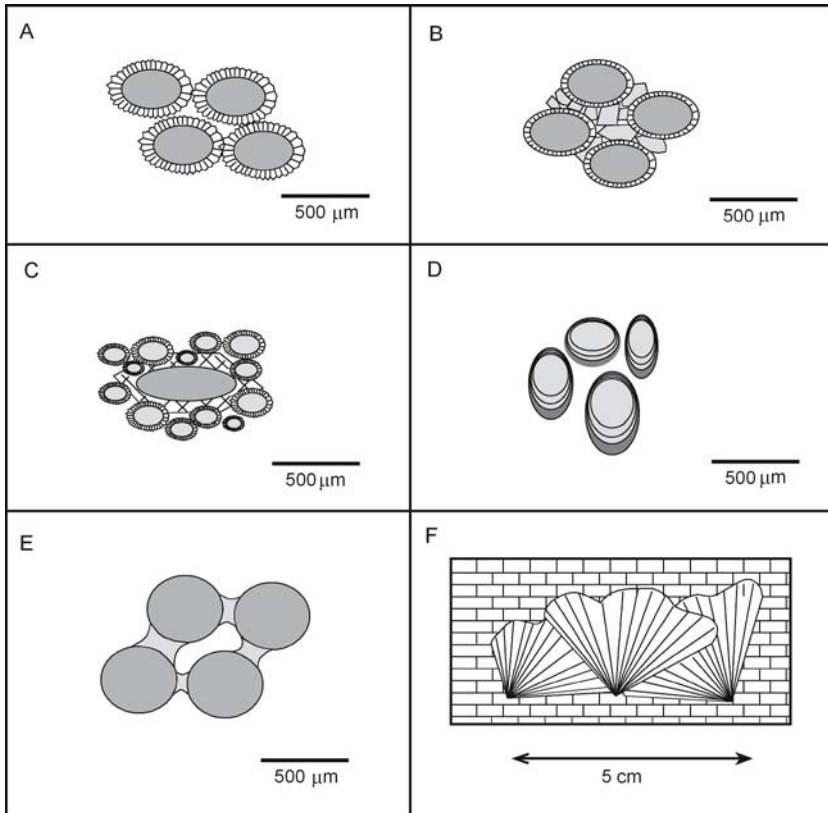
Fig. 6.1. Common calcite cement textures. **A** Fibrous or bladed isopachous cement: **B** Equant or blocky sparry cement, **C** Syntaxial or overgrowth cement: **D** Pendular or microstalactitic cement: **E** Meniscus cement: **F** Radiaxial or botryoidal cement

cementation of sediments in the shallow burial environment results from the circulation of large quantities of marine water through very permeable sediments such as grainstones and reef debris (Shinn 1969; James and Ginsburg 1979). The driving force is tidal and wave energy characteristic of high-energy environments occupied by reefs and grainstone sediments. Marine cement typically precipitates evenly around the grains as fibrous or bladed cement and is referred to as isopachous cement. Large voids commonly found in carbonate reefs are often filled with large botryoidal fans of radiaxial marine carbonate cement (Fig. 1).

Cementation by calcite continues as the sediment is buried (Heydari and Moore 1993). The process of burial cement is poorly understood. Budd et al. (1993) report no burial cementation in the Florida Aquifer. Instead, cementation is precompaction and related to the Oligocene

exposure surface or early mineralogical stabilization. Heydari and Moore (1989, 1993), however, describe burial cementation related to thermochemical sulfate reduction. Sources of the calcium and carbonate ions required for continued cementation are (1) grain dissolution associated with chemical compaction, (2) dissolution of unstable minerals such as aragonite, and (3) long-distance transport of ions by ground-water flow. Common burial cement fabrics are equant calcite spar and syntaxial overgrowths. Equant cements are often unevenly distributed throughout the rock, producing a small-scale heterogeneity that may explain some small-scale permeability variability. Syntaxial cements are overgrowths on grains that are composed of a single calcite crystal. Echinoderm fragments commonly have syntaxial overgrowths, and pore space in sediments composed predominantly of echinoderm particles is commonly totally occluded (Lucia 1962).

Several cement fabrics are unique to the vadose zone (zone of air saturation). Meniscus cement is unique because is retains the shape of the air/water interface (Fig. 1). It is confined to pore throats and reduces permeability more than would be expected from a similar volume of isopachous or equant cement. Pendulous or microstalactitic cements preferentially grow down from the bottom of grains, suggesting growth from waters percolating downward through partially air-filled pores.

A characteristic of all cements is that they propagate from pore walls into pore space and therefore reduce pore size as they grow. In the case of evenly distributed cement, pore size is reduced in proportion to the amount of cement precipitated (Fig. 2). The systematic reduction in pore size accounts for the observed systematic changes in permeability and capillary properties with changes in interparticle porosity. Therefore, pore-size distribution is a function of interparticle porosity, grain size, and sorting (Fig. 3).

Unevenly distributed calcite cement will produce small-scale heterogeneity. The total porosity of the sample will be reduced, but the porosity and pore size of the noncemented portions will remain unchanged. Because permeability and capillary properties are principally a function of pore size, they will be reduced less than they would be if the same volume of cement were evenly distributed. Therefore, patchy calcite cement reduces porosity but may not have a significant effect on permeability and capillary properties. Lonoy (2006) published data supporting this view.
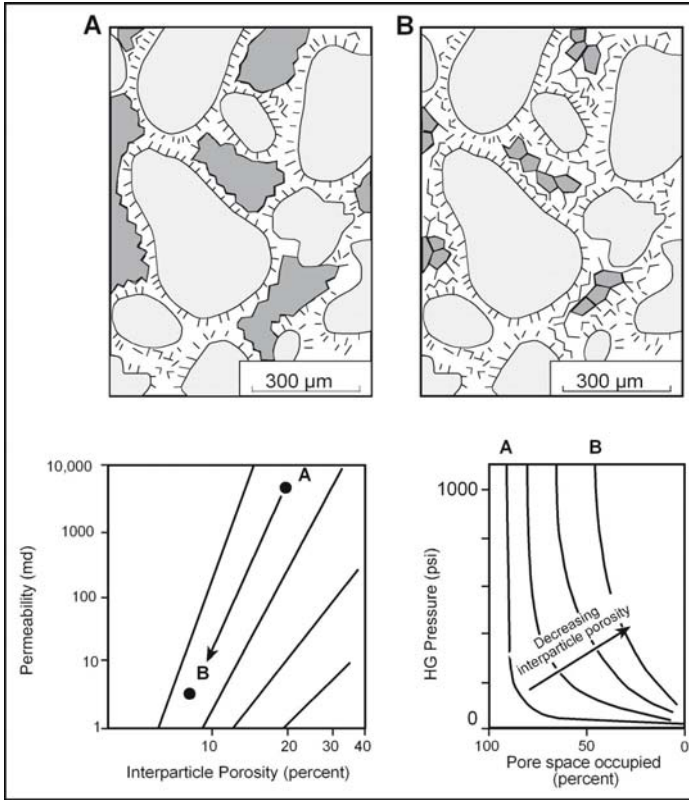
Fig. 6.2. The change in permeability and capillary properties with decreasing porosity resulting from occlusion of intergrain pore space. As 20% intergrain pore space in sample **A** is reduced by cementation to 7% in sample **B**, permeability is systematically reduced, and the shape of the capillary pressure curve is systematically changed to reflect smaller pore sizes

6.2.2 Compaction

Compaction effects are difficult to separate from cementation effects, but they both reduce pore-size and porosity. Budd (2002) has presented data suggesting that compaction and cementation reduce pore sizes differently, resulting to two slightly different porosity-permeability cross plots. For our purpose, however, we will lump the two processes together.

Compaction is both a physical and chemical process resulting from the increased overburden pressure due to burial. Textural effects include the
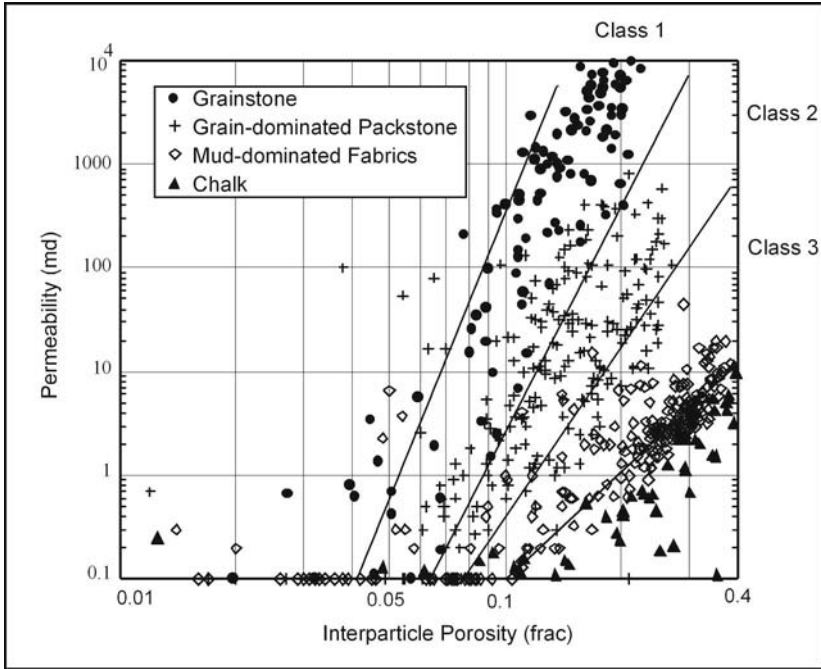
Fig. 6.3. Cross plot of log permeability and interparticle porosity for nonvuggy limestones showing rock-fabric fields. The scattering of data within a field is due to the variability of grain size, sorting, and cement distribution and size

loss of porosity, reduction of pore-size, grain penetration, grain deformation, grain breaking, and fracturing. Compaction does not require the addition of material from an outside source, and it is a function of texture only. In addition, compaction is a source of energy to move fluids out of the sediment and into adjacent sediments, usually flowing upward.

Experimental data have shown that simple mechanical compaction can reduce the porosity of lime muds from 70% to about 40% within the first 100 m (330 ft) of burial (Fig. 4) (Goldhammer 1997). Soft fecal pellets will be compacted, changing the texture from a pellet grain-dominated packstone to a pellet mud-dominated packstone, wackestone, or mudstone fabric. Hard pellets will retain their shape and intergrain pore space. In contrast, grain-supported sediments can retain the original porosity of 47% to a depth of about 700 m (2310 ft) before closer packing and grain breakage begin to significantly reduce pore space (Fig. 4).

In addition to porosity loss through mechanical compaction, chemical compaction in the form of pressure solution at grain contacts will also result in porosity reduction with burial and time. Pressure solution of carbonate grains provides calcium and carbonate ions that can be precipi-
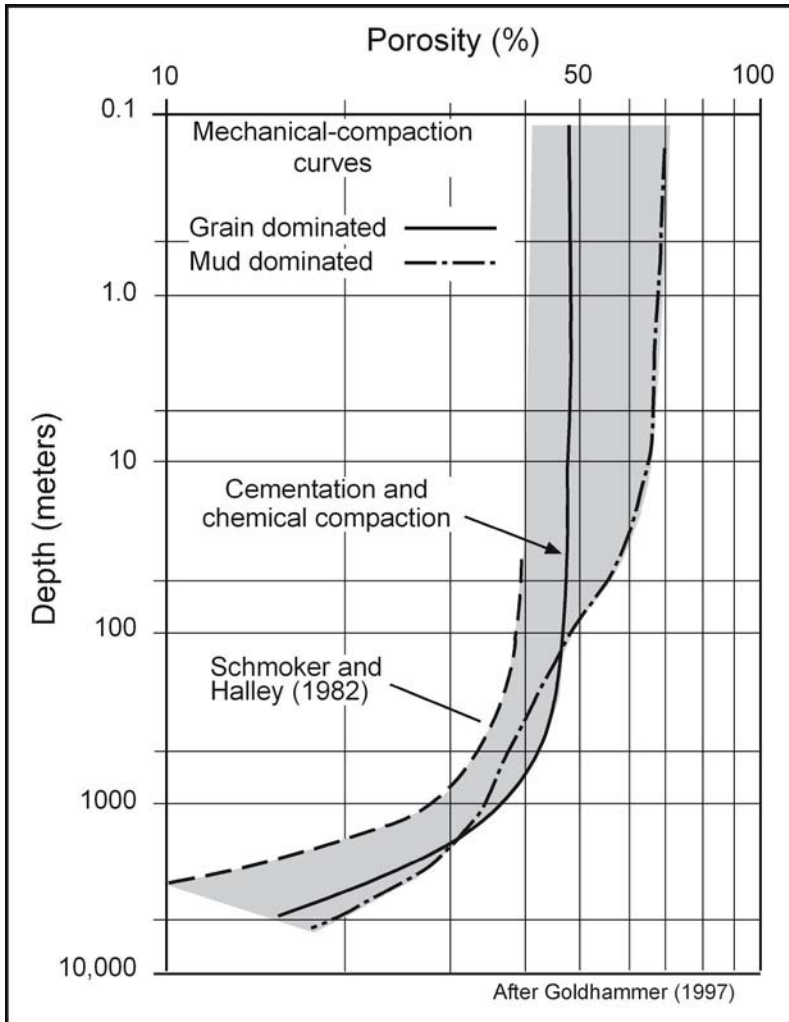
Fig. 6.4. The change in porosity of mechanically compacted mud and sand sediments with depth (Goldhammer 1997). The potential effect of chemical compaction and cementation is shown by the difference between mechanical compaction and subsurface porosity vs. depth data from South Florida (Schmoker and Halley 1982)

tated as cement in adjacent pore space. Schmoker and Halley (1982) present an example from South Florida of the combined effect of cementation and compaction with time and burial. The comparison of this curve with the mechanical compaction curve illustrates that cementation

and chemical compaction are important processes in the loss of porosity with burial (Fig. 4).

Compaction curves suggest that carbonate sediments lose their porosity slowly with burial. Porosity values between 30 and 40% should not be unusual at depths of 1000 m (3000 ft). This has been observed in the Neogene of the Bahama Platform, where core and log data demonstrate consistently high porosity values of 35 to 50% at depths of 700 m (2100 ft) (Anselmetti and Eberli 1993, Melim et al. 2001).

6.2.3 Selective Dissolution

Dissolution is the diagenetic process by which carbonate and evaporite minerals are dissolved and removed, thus creating and modifying pore space in reservoir rocks. The effect of this process on permeability depends upon the geometry and location of the resulting voids relative to the rock fabric. Dissolution can be fabric selective and can form moldic pores, a type of separate vug. In other cases, dissolution is not fabric selective and results in interconnected voids referred to here as touching vugs. This type of dissolution will be discussed later.

Selective dissolution occurs when one fabric element is selectively dissolved in preference to others. This usually results from the fact that carbonate sediments are composed of minerals with different solubility. Anhydrite and gypsum are more soluble than calcite or dolomite and are commonly dissolved selectively to form sulfate molds. Laboratory experiments have shown that solubility of calcium carbonate minerals increases from low-magnesium calcite (LMC) to aragonite to high-magnesium calcite (HMC, see Chapter 4). However, depositional particles originally composed of high-magnesium calcite are commonly replaced with low-magnesium calcite rather than dissolved. The common observation in the geological record is that aragonite grains tend to be dissolved in preference to LMC and HMC (Swirydezuk 1988; Melim et al. 2001).

Formation of vugs by selective dissolution commonly inverts pore-space fabrics in grainstones from intergrain porosity and solid grains to moldic porosity and occluded intergrain pore space. Comparative data suggest that porosity does not increase as a result of this process (Fig. 5). Modern ooid grainstones have 45% porosity, and ooid grainstones with moldic pore space rarely have more than 30% porosity. Core analyses of moldic grain/packstone samples taken from wells Unda and Clino, from below the upper karsted interval, all show porosity values between 40 and 50% (Melim et al. 2001), suggesting only a slight reduction in porosity
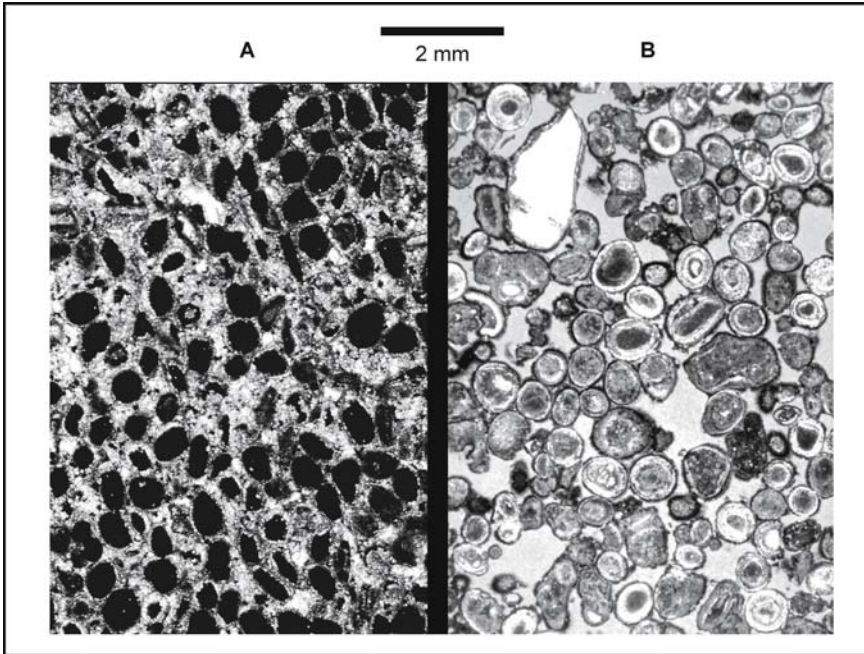
Fig. 6.5. Inverted texture. Both samples have between 20 and 25% porosity. **A** Photomicrograph of moldic porosity with occluded intergrain pore space. **B** Photomicrograph of intergrain porosity

from the time of deposition. Most likely, the porosity does not increase because the calcium and carbonate ions produced by dissolution of unstable aragonite are precipitated as calcite cement in the juxtaposed pore space. This can occur with burial in the presence of marine ground water (Dix and Mullins 1988) or in the shallow burial environment in the presence of a localized freshwater lens such as those found in grainstone shoals (Budd and Land 1990).

Moldic pore space is connected only through the interparticle pore network. As a result, moldic pore space contributes little to permeability. The presence of separate vugs in limestones and dolostones results in less permeability than would be anticipated if all the porosity were interparticle (Lucia 1983).

Enlargement of interparticle pore space is another type of selective dissolution. The resulting enlargement of interparticle pore space improves flow characteristics and capillary properties, the reverse of moldic pore space. For example, intergrain pore space in some Jurassic grainstone reservoirs in the Gulf Coast, USA, has been enlarged by dissolution in the presence of late subsurface brines containing high

concentrations of H_2S (Moore and Druckman 1981). In another example, intergrain lime mud in a crinoidal grain-dominated packstone has been dissolved by late subsurface brines creating a reservoir rock in the Andrews South Devonian Field, West Texas, USA (Lucia 1962).

6.2.4 Effects on Petrophysical Properties Distribution

The effect of shallow diagenesis and simple burial diagenesis on petrophysical properties can usually be related to depositional textures and burial depth or geologic time. Porosity in reefs appears to be substantially reduced by early marine cementation. The Capitan reef of Permian age in the Guadalupe Mountains, West Texas and New Mexico, contains up to 70% by volume early radiaxial marine cement, suggesting that most of the large construction voids formed with the reef were occluded soon after deposition. Early marine cement apparently occluded large pores in the early reef growth found at the base of Silurian pinnacle reefs in Michigan (Sears and Lucia 1980). Other textures appear to lose porosity gradually through time in a passive margin setting, although in a tectonic setting porosity is lost at a much higher rate.

To illustrate the gradual loss of porosity with time, porosity and fabric data from several limestone studies ranging in geologic time were plotted on a ternary diagram (Fig. 6). The 70% porosity found in modern mud-domina-
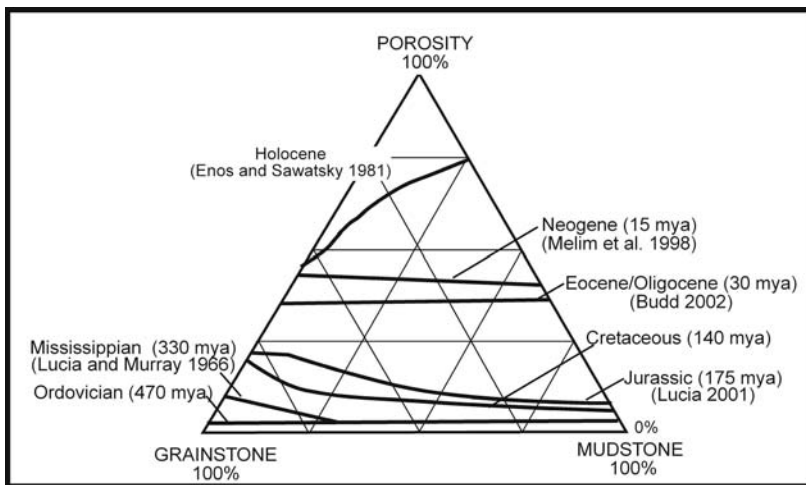
Fig. 6.6. The relationship between porosity, depositional texture, and geologic time. The loss of porosity with time and burial in a simple burial diagenetic environment is slow. The rate of loss in mud-dominated textures is faster than in grain-dominated textures

ted sediments is reduced after about 10-20 million years of compaction and cementation, but porosity values of between 30 and 40% are still common. After about 150 million years Jurassic grain-dominated limestones retain 25% porosity whereas the porosity of mud-dominated sediments is significantly reduced. In the upper Paleozoic, only grain-dominated fabrics retain sufficient porosity to be considered as reservoir quality, and lower Paleozoic limestones are normally dense.

In this diagenetic environment, the distribution of porosity and permeability after burial would be related to the distribution of depositional textures, as presented in Chapter 4. The rate of porosity reduction is greater in mud-dominated textures than in grain-dominated textures. Selective dissolution of aragonite grains will form moldic porosity, cementation of intergrain pore space, and a reduction in permeability (Fig. 7).
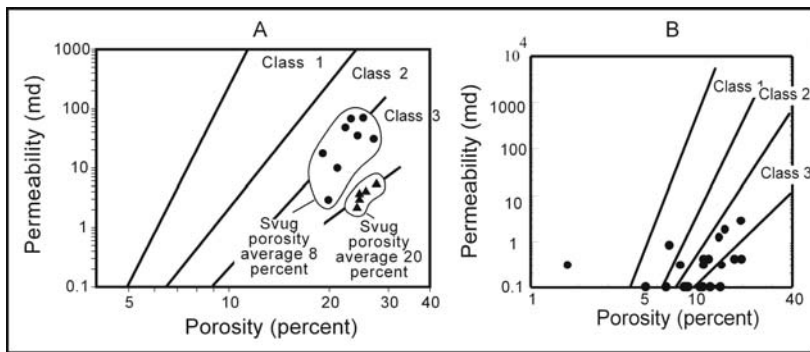
Fig. 6.7. The effect of separate vugs on permeability in carbonate rocks. **A** Oo-moldic porosity in a grainstone. **B** Intragrain microporosity in ooid grainstone

This dissolution may be in response to the development of local fresh-water lenses in association with upward-shoaling depositional sequences, or in response to the dissolution of unstable aragonite and precipitation of intergrain cement with burial. The formation of moldic porosity in grainstones does not alter the porosity as much as it significantly reduces the permeability.

These diagenetic effects will significantly enhance the control of grain-dominated fabrics on reservoir distribution. The permeability of the grain-dominated packstones would be significantly higher than that of the mud-dominated fabrics, and grainstones would have the highest permeability (Fig. 8). The geological age will dictate the porosity and permeability values. Assuming the Jurassic model of the Middle East, the grainstones will average
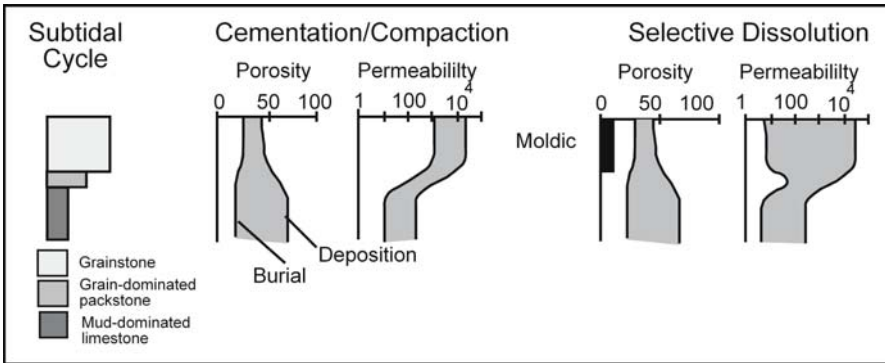
Fig. 6.8. The reduction in porosity and permeability with burial diagenesis for typical depositional cycles. The porosity and permeability profile of a typical upward-shoaling depositional cycle will be reduced by a time/depth-dependent factor. The burial curves are based on Jurassic Arab D data from Powers (1962). Selective dissolution will not alter the porosity profile but will significantly reduce the grainstone permeability

1000 md, grain-dominated packstones 100 md, and mud-dominated fabrics 1 md. The permeability of moldic grainstones will be between 1 and 10 md.

Permeable grain-dominated fabrics are typically found capping subtidal depositional cycles. They are concentrated in the shelf-margin, ramp-crest facies tract (Fig. 9). The close conformance of the diagenetic products to depositional texture allows the use of depositional models for predicting the distribution of petrophysical properties. The principal difference is the very low permeability of moldic grainstones.

6.3 Limestone Reservoir Examples

6.3.1 Mississippian Chester Field, Oklahoma, USA

The Mississippian Chester gas reservoir of northwestern Oklahoma is an example of a Paleozoic limestone reservoir in which the porosity is controlled by depositional facies and type of calcite cement (Lucia and Murray 1966). Although this is an old study, it is an excellent example of how depositional environments can be used to model reservoir properties when the diagenetic products are closely linked to depositional textures. The diagenetic history is relatively simple, being confined to compaction and cementation. The reservoir section is composed of two upward-shoal-
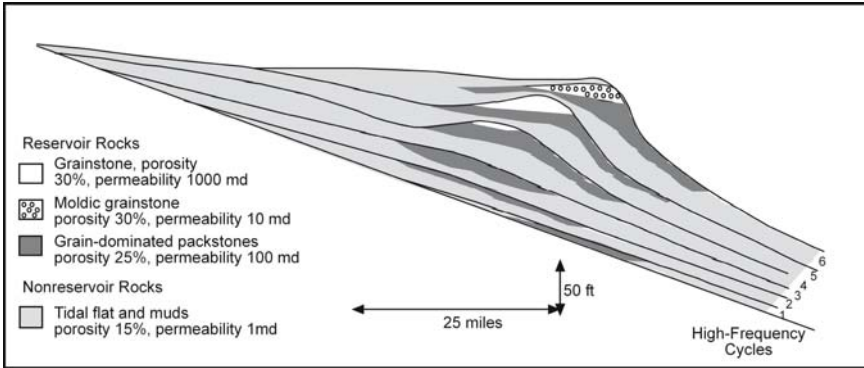
Fig. 6.9. Distribution of reservoir rocks in a high-frequency sequence framework overprinted by cementation, compaction, and selective dissolution

ing high-frequency cycles consisting of a lower crinoidal wackestone and an upper crinoidal grain-dominated packstone and grainstone facies. Each high-frequency cycle is divided into two rock-fabric flow layers (Fig. 10).
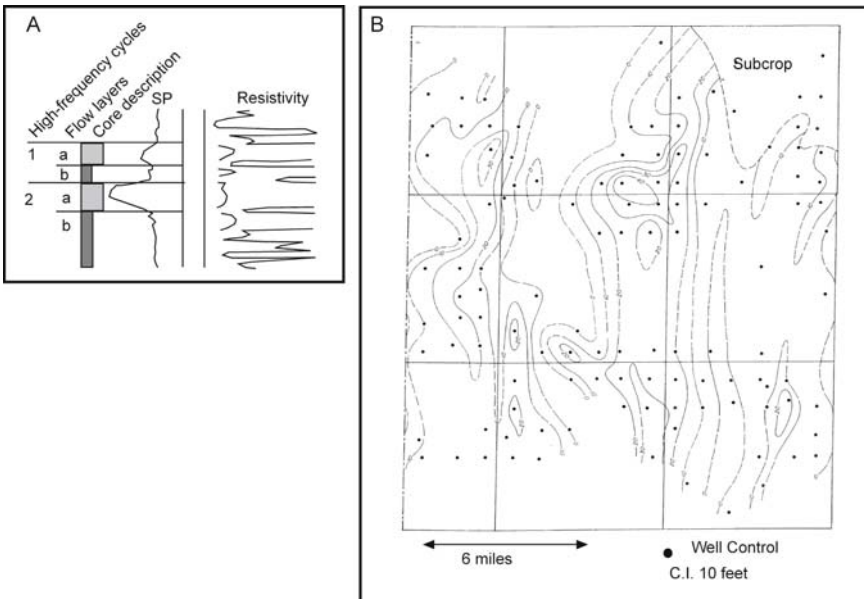
Fig. 6.10. Chester Mississippian field, Oklahoma, USA. **A** Reservoir is divided into two high-frequency cycles each with two flow layers based on core descriptions. **B** Isopach map of net bar facies thickness based on the SP curve showing linear trends predicted from modern oolitic grainstone shoal models. (Lucia and Murray 1966)

The rock fabrics are grainstone, grain-dominated packstone, and mud-dominated limestone. The only pore type visible is between the grains in some of the grainstones. Most of the pore space has been occluded by syntaxial and isopachous cement and compaction. The presence of the intergrain pore space is related to the nature of the calcite cement. Skeletal grains are mostly crinoid fragments. The cement that is commonly found on single-crystal crinoid fragments is a calcite overgrowth called "syntaxial cement" which normally fills intergrain pore space. When the crinoids are oolitically coated, however, isopachous cement develops instead of the syntaxial cement, and this isopachous cement does not fill intergrain pore spaces.   Petrographic studies show that all the productive rocks are grainstones in which 80% or more of the grains are oolitically coated (Fig. 11).
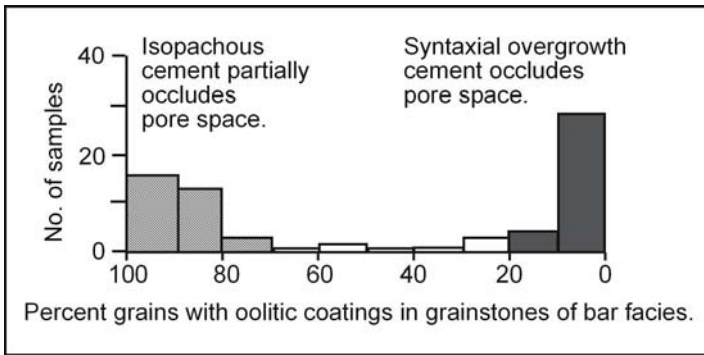
Fig. 6.11. Rock-fabric plot from the Chester Mississippian field showing nonproductive non-oolitic crinoidal grainstones with pore space occluded by syntaxial overgrowth cement, and productive ooid crinoidal grainstones with pore space partially occluded by isopachous cement. Oolitic coatings inhibit the growth of single crystal syntaxial cement and promote the growth of multicrystal isopachous cements. (Data from Lucia and Murray 1966)

Depositional patterns can be used to predict the distribution of petrophysical properties because of the close conformance between porosity and ooid grainstones.   Ooid grainstones are deposited in high-energy environments, commonly in a bar-and-channel pattern. The Mississippian Chester rocks were divided into two facies: the bar facies, which contains ooid grainstone, and the interbar facies, which is characterized primarily by the abundance of less fragmented, non-ooid skeletal debris, the presence of laminated and intermixed lime mud, and numerous shale laminations.

The Spontaneous Potential (SP) curve is used to identify bar and interbar facies from wireline logs. Although some gamma ray logs were available,

the SP was more responsive to the geologic facies. The SP shows high displacement opposite the bar facies and suppressed SP adjacent to the interbar facies. Microlog separation within the bar facies indicates the presence of grainstones with more than 80% ooids. These empirical relationships between facies and log response were used to correlate the high-frequency cycles and flow layers over a wide area. Isopachs of the bar facies (Fig.10) and porosity-feet were mapped using a grainstone bar and channel depositional model.

6.3.2 Tubarao (Cretaceous) Field, Offshore Brazil

The Cretaceous (Albian) Tubarao oil reservoir in the Santos Basin, offshore Brazil, studied by Cruz (1997), is an example of a reservoir where diagenetic products can be linked to depositional fabrics for mapping but the diagenetic history has altered the pore structure and petrophysical properties. The diagenetic history is somewhat more complicated than that of the Mississippian example in that, in addition to simple cementation compaction, microporosity is located within the grains (a type of separate-vug porosity) and has a large effect on petrophysical properties. Rock fabrics range from mud-dominated limestones to grainstone, and pore types from intergrain to separate vug. The rock fabrics and petrophysical properties can be linked to depositional texture, and depositional models can be used in construction of the reservoir model.

Core description (Fig. 12) shows a vertical succession of upward-shallowing subtidal cycles composed of mud-dominated packstone to either oncoid grain-dominated packstone or ooid grainstone. These high-frequency cycles are packaged into two high-frequency sequences defined by a wackestone interval suggesting a major flooding event. Each sequence is composed of six high-frequency cycles. The lower sequence (BIC) is characterized by oncoid grains, whereas the upper sequence (BIB) is characterized by ooid grains.

Rock-fabric studies show the presence of petrophysical class 1 grainstones, petrophysical class 2 grain-dominated packstones, and class 3 mud-dominated packstones and wackestones. The vertical succession of rock fabrics from mud-dominated to grain-dominated packstone in the lower sequence and from mud-dominated to grainstone in the upper sequence define two flow layers in each high-frequency cycle (Fig. 12).

A porosity-permeability cross plot of the ooid grainstones shows that the data plot in the class 3 field and below (Fig. 13A). The reason is that, although there is some intergrain pore space, most of the porosity is contained within the grains as intergrain microporosity, a type of separate
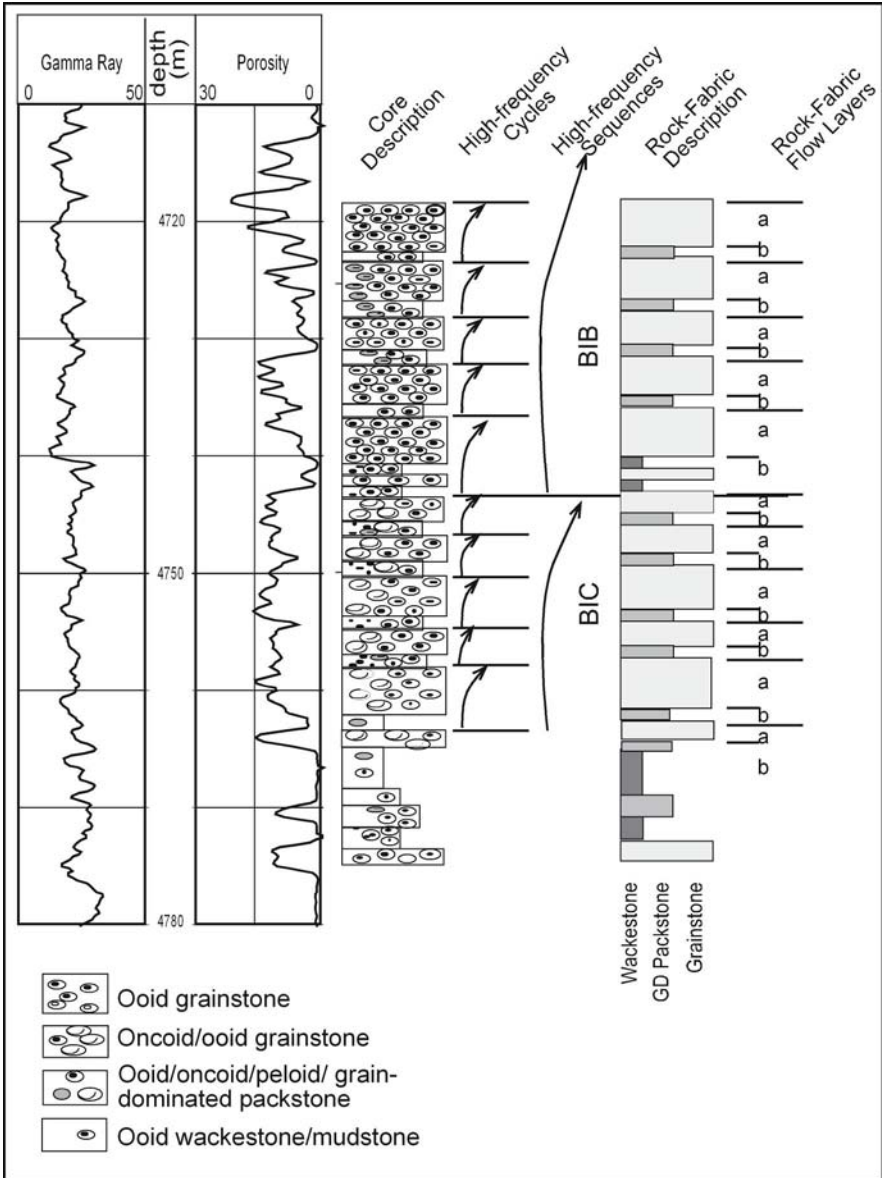
Fig. 6.12. Vertical stacking patterns from core descriptions of the Cretaceous of the Santos Basin, offshore Brazil (Cruz 1997). Core description reveals the presence of grainstone-capped subtidal high-frequency cycles that can be grouped into high-frequency sequences based on cycle thickness and the distribution of mud-dominated fabrics. The four geologic facies are grouped into the three basic rock fabrics, and each HFC is divided into an upper grain-dominated layer and a lower mud-dominated layer. (Cruz 1997)
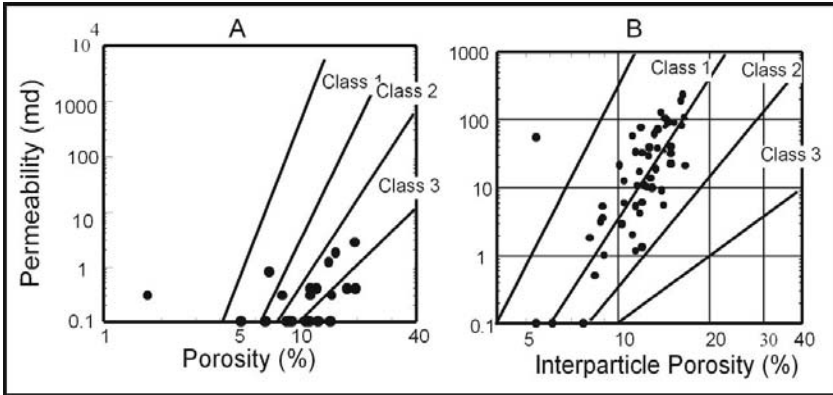
Fig. 6.13. Porosity-permeability-rock fabric plot from the Tubarao field, Santos Basin. The permeability is confined to petrophysical class 2 oncoid grain-dominated packstones (GDP). Mud-dominated fabrics have low permeability values. **A** Ooid grainstone with intragrain microporosity has porosity values similar to oncoid GDP (B) but has less than 1 md permeability. **B** The GDPs straddle the boundary between class 1 and 2 because the oncoids are very large in size. (Data from Cruz 1997)

vug. As discussed in Chapter 2, pore space within grains in grain-dominated fabrics adds little to the permeability. There is considerable scatter in the data, but a rock-fabric number of 3 might give reasonable permeability values. A porosity-permeability cross plot of the oncoid grain-dominated packstone shows that the data plot along the border between class 1 and 2 (Fig. 13B). The oncoids are quite large being more than 1 mm in diameter, which results in larger pores than normally observed in grain-dominated packstones. As a result, the data plot on either side of the class 1-2 boundary, and a rock-fabric number of 1.5 would predict permeability. Mud-dominated packstones and wackestones have an average of 2% porosity and <0.1 md. The few samples that have more than 0.1md permeability fall within the class 3 field, as predicted.

Capillary pressure curves are used to estimate initial water saturation. Curves from the ooid grainstone are bimodal, showing a low entry pressure into the small amount of intergrain pore space and a higher entry pressure into the small pores of the intragrain microporosity, which makes up most of the porosity (Fig. 14a). Curves from the oncoid grain-dominated packstones are slightly bimodal, showing low entry pressure into the inter-oncoid pores and higher entry pressure into the smaller pores found in the intergrain lime mud and perhaps in the oncoid grains themselves (Fig. 14b). These relationships indicate that the grain-dominated packstone will have the lowest initial water saturation and the
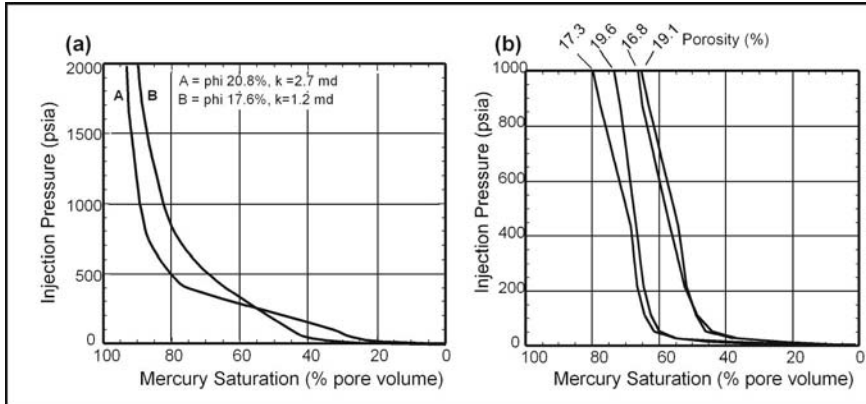
Fig. 6.14. Capillary pressure curves from the Tubarao field, Santos Basin. **a** Examples of curves from the oncoid grain-dominated packstone showing low entry pressures typical of large intergrain pore space and relatively high water saturation (1-mercury saturation) typical of small pore space in intergrain mud and intragrain microporosity. **b** Examples of curves from porous ooid grainstone showing bimodal curves typical of grainstones with most of the pore space located within the ooids

grainstone the highest water saturation for the same reservoir height and porosity. Thus, most of the oil will reside in the oncoid grain-dominated packstone.

This difference in capillary properties can be used to distinguish between the ooid grainstone (rfn = 3) and the oncoid grain-dominated packstone (rfn = 1.5) using resistivity logs. A cross plot of Archie initial water saturation vs. log porosity shows that the ooid facies has a higher water saturation than the oncoid facies for the same porosity (Fig. 15). The mud-dominated fabrics (rfn = 3) can be distinguished by their characteristic low porosity.

Vertical permeability profiles are calculated using the global permeability transform. Porosity was read from the porosity log and rock fabric number from the porosity-saturation cross plot.

A 2D reservoir model was constructed using the rock-fabric approach. The cycles and sequences are mapped within the field area and form a chronostratigraphic framework for the construction of a petrophysical model (Fig. 16). Each cycle was divided into two rock-fabric flow layers based on vertical successions of mud- to grain-dominated fabrics. Vertical permeability profiles are calculated using the global permeability transform. Porosity was read from the porosity log and rock-fabric number determined from porosity-saturation cross plots. Initial water saturation was based on Archie log calculations. Permeability and initial
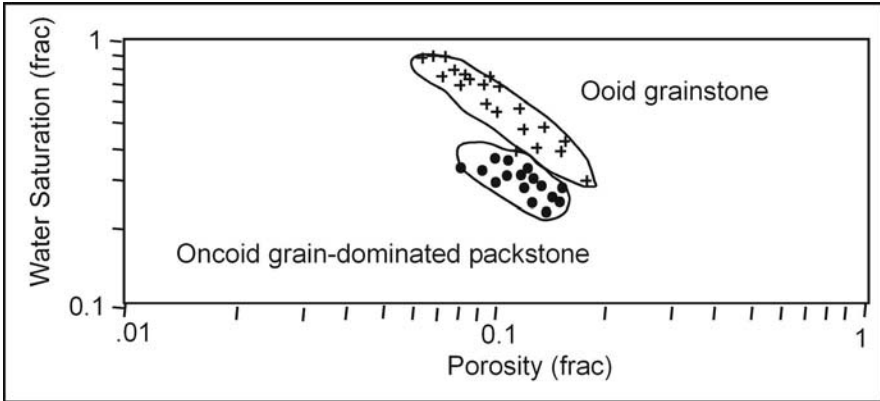
Fig. 6.15. Porosity-saturation cross plot showing a distinction between ooid facies, in which pore space is dominated by intragrain microporosity, and oncoid facies, in which pore space is dominated by large intergrain pore space

water saturation values are averaged within each flow layer. Permeability distribution is illustrated in Fig. 16. Although both grain-dominated fabrics
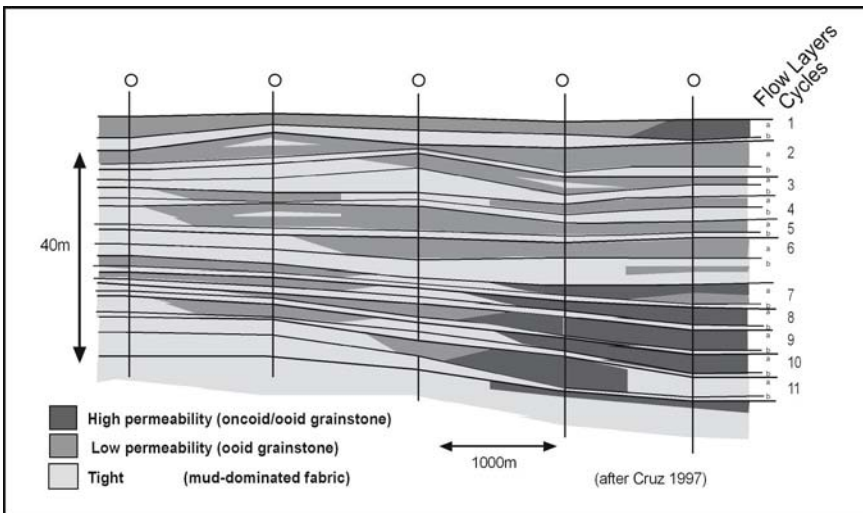
Fig. 6.16. A reservoir model illustrating the 2-D distribution of reservoir-quality oncoid facies and poor-reservoir-quality ooid facies. (Cruz 1997)

have high porosity, the model indicates extreme lateral and vertical variability in permeability due to the differences in rock fabrics. A significant error in reservoir performance would result if a single permeability transform or saturation model were used.

6.3.3 Moldic Grainstone, Permian, Guadalupe Mountains, USA

The results of a study on a body of moldic grainstone are included here as an example of the effect of selective dissolution on the distribution of petrophysical properties. In Chapter 4 the Algerita Escarpment outcrop study was used to illustrate the concentration of grainstones in the progradation, HST. Although the section is completely dolomitized, the fabrics closely mimic depositional textures. Data collected from the outcrop show that the grainstones have average permeability values of 100 md, grain-dominated packstones 10 md, and wackestones 1 md, whereas all three fabrics have porosity values close to 13%.

The exception to this is the grainstone in cycle 7, where selective grain dissolution has inverted the pore structure, resulting in areas of high porosity (average 20%) but low permeability (average 2.5 md) within the cross-bedded grainstone (Hovorka et al. 1993; Fig. 17). The formation of the moldic porosity is interpreted as resulting from a local fresh-water lens that formed in response to either the overlying tidal flat deposits or the overlying high-frequency sequence boundary. Therefore, the pattern of the moldic grainstone is linked not only to the depositional pattern of the grainstone, but also to local paleogroundwater movements.

6.3.4 Idd el Shargi Cretaceous Reservoir, Qatar, Middle East

In the previously discussed limestone reservoirs, the productive fabric is grainstone or grain-dominated packstone, and the mud-dominated fabrics have little permeability. The Cretaceous Shuaiba formation in the Middle East is an example where much of the production is from highly porous class 3 wackestones and mudstones. The Idd el Shargi field, located off the eastern coast of Qatar, is an example of this type of reservoir. The field is located on a structural closure thought to be related to a deeper salt structure. It is highly faulted and high production rates are attributed to fractures associated with faulting.

The Shuaiba can be divided into four units, D through A, with production concentrated in A (Fig. 18). Unit D, the lowest unit, as about 60 ft thick and represents transgression. Units C through A are each about 100 ft thick and represent the filling of a subsiding basin. The only shallow-water facies are found at the top of the Shuaiba underlying the Nahr Umr Shale. The nature of the contact between the Shuaiba and the Nahr Umr has been debated and often interpreted as a subaerial exposure, and the porous mud-dominated
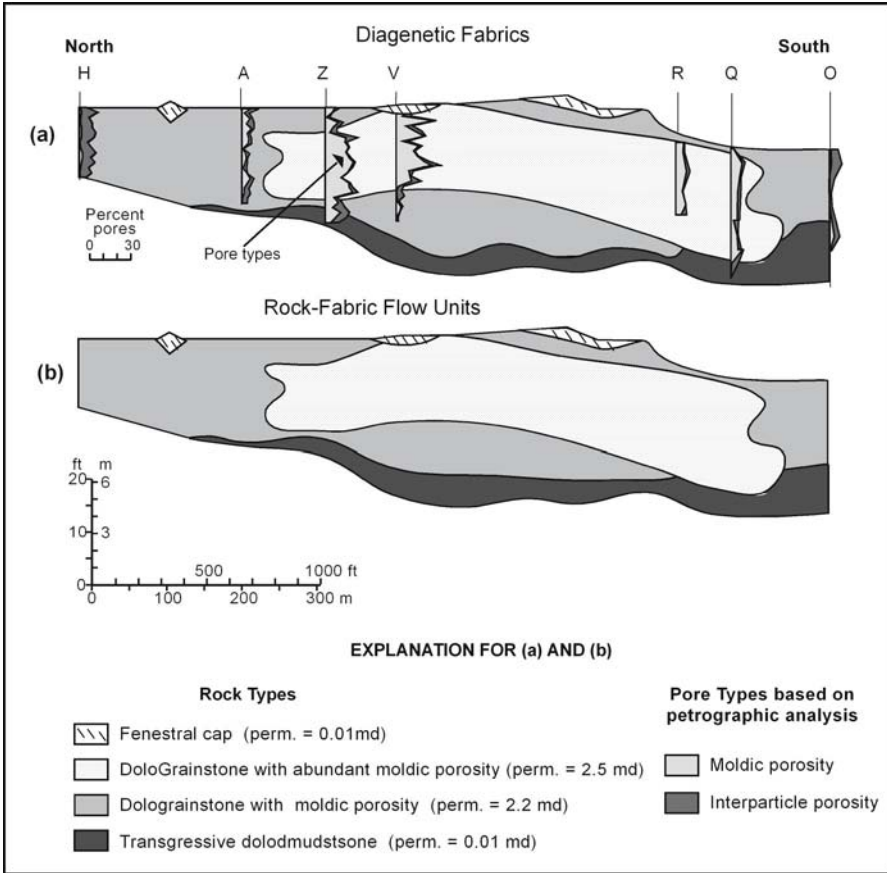
Fig. 6.17. Cross section of cycle 7, Lawyer Canyon, Algerita Escarpment, show-ing the 2D geometry of a moldic grainstone body. Selective dissolution of grains in the grainstone has resulted in significantly lower permeability than would be expected. (After Kerans et al. 1994)

limestones are often interpreted as produced by meteoric leaching in a freshwater lens. However, no evidence of exposure was found in this study of the Idd el Shargi field.

The A and B units are divided into cycles based on upward-shallowing cycles (Fig. 19). Ten facies have been defined keyed to water depth, and all but two are mud-dominated limestones. There are three cycles in unit B and six in unit C. The water depths are based more on faunal content than on rock fabrics.   Because all but the upper two cycles are composed of deep water facies, the cyclicity is probably not related to eustasy.

Facies variability is restricted to units A1 and A2 (Fig. 20). The facies pattern is interpreted to reflect the eventual shoaling of the structure into fair-
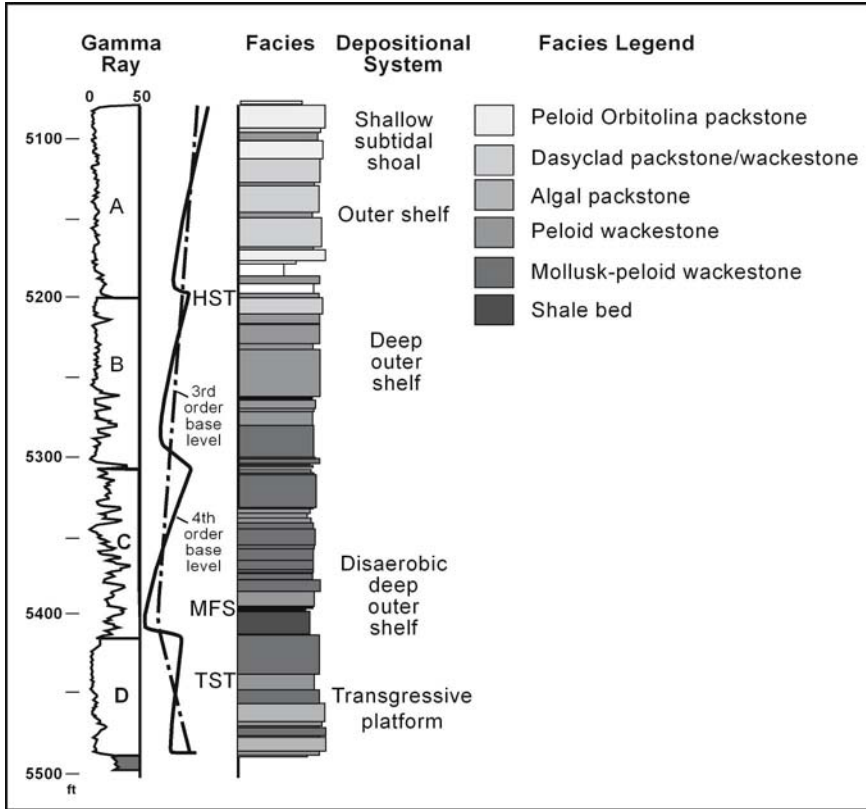
Fig. 6.18. Vertical facies profile and sequence stratigraphic interpretation of the Shuaiba Formation in the Idd el Shargi field (from Kerans)

weather wave base, thereby setting up a windward-leeward asymmetry driven by northwesterly prevailing winds. The windward side is characterized by *Orbitolina* fine-peloid grain-dominated packstone and occasional coral bafflestones. Behind this belt is a dasyclad-algal/*Orbitolina* mud-dominated packstone protected lagoon. Low-energy *Orbitolina* wackestones are found on the leeward flank.

All the facies are classified as mud-dominated fabrics, mudstone, wackestones and mud-dominated packstone, and all the data from the field plot in the class 3 field (Fig. 21). However, there are significant differences in permeability between rock fabrics. Wackestones define the lower limit of class 3 with porosity typically around 30% and a permeability of about 3 md. This fabric is referred to as rock-fabric type C. As the lime mud becomes more pelleted and pore space between 80 micron peloids becomes visible, the permeability increases to about 10 microns, although the porosity remains
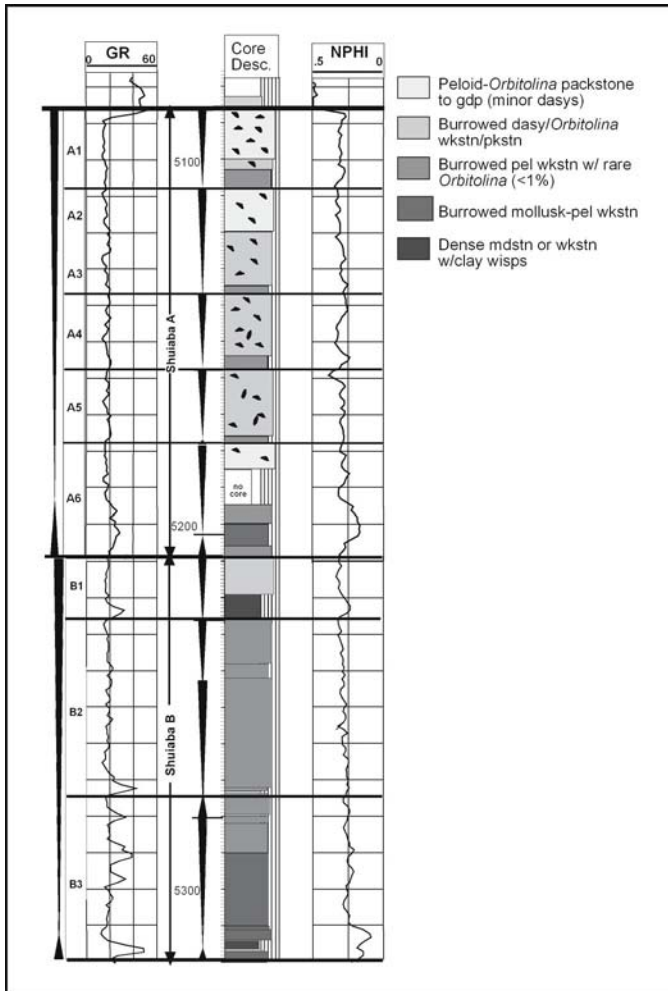
Fig. 6.19. Vertical facies succession in the A and B units. The A unit is composed of six upward-shoaling successions interpreted to be high-frequency cycles. The B unit is composed of three symmetrical cycles that show little evidence of shoaling (from Kerans)

common permeability fabric is a moldic dasyclad mud-dominated packstone where compaction has compressed the grain molds producing microfractures. The microfractures have the effect of connecting the grain molds and producing a micro-touching-vug pore geometry. Typical permeability is about 10 – 20, md, and porosity is similar to that of the other two fabrics. This fabric is referred to as rock-fabric type A.
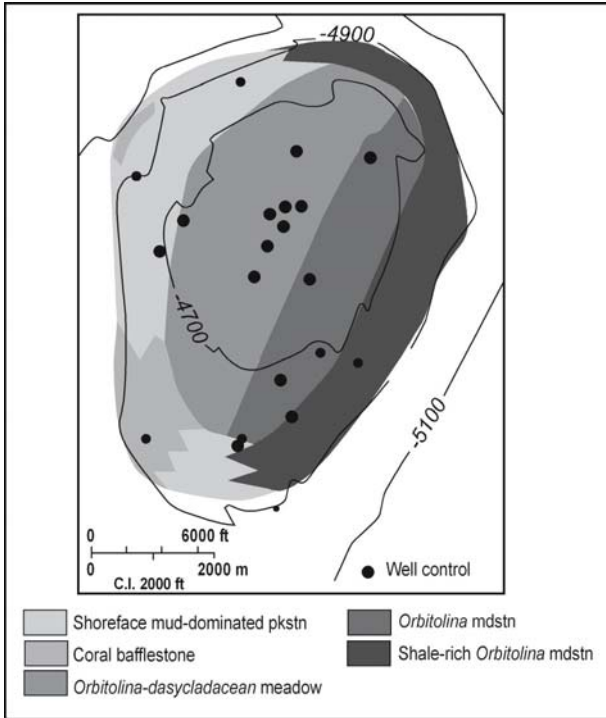
Fig. 6.20. Facies map of uppermost two cycles in Unit A, A1 and A2, showing a distinct northwest-southeast asymmetry to the facies patterns (from Kerans)

Porosity-permeability transforms for each rock-fabric type were developed and are presented below.

Rock-fabric type A: $k = 5286 \times \phi^{4.306}$

Rock-fabric type B: $k = 1096 \times \phi^{3.86}$

Rock-fabric type C: $k = 270 \times \phi^{3.86}$

Permeability profiles are calculated using these transforms. The three rock types can be identified by cross-plots of initial water saturation vs. porosity (Fig. 22a). Initial water saturation was calculated from wireline logs using the Archie equation. For a given porosity, rock-favric type C has the highest saturation and type A the lowest. The lack of capillary pressure data from types A and B precludes the development of a numerical equation to calculate the vertical profiles of the three rock-fabric types from water saturation and porosity. Instead, the types were identified for each well using individual cross plots, and permeability was calculated using the rock-fabric-specific transforms and wireline log porosity. An example is illustrated in Fig. 22b. Most of the well is rock type C, but the upper intervals are rock
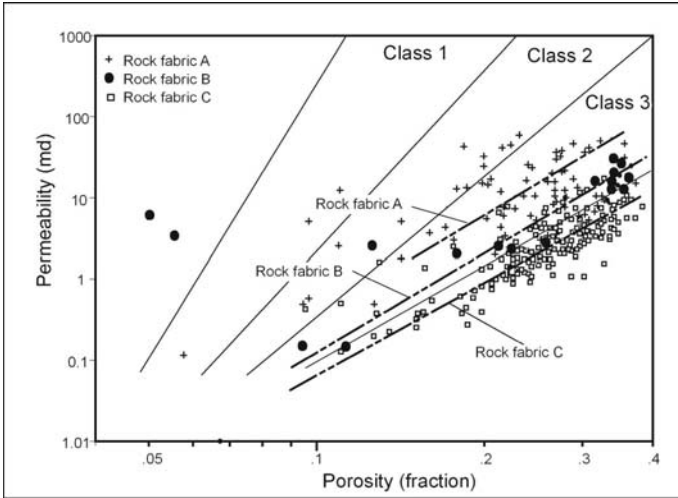
Fig. 6.21. Porosity-permeability cross plot showing rock-fabric permeability transforms for the three rock fabrics that characterize this reservoir. Notice that almost all of the data plot within the class 3 field. It is necessary to define three different rock fabrics within the class 3 field in order to characterize this reservoir
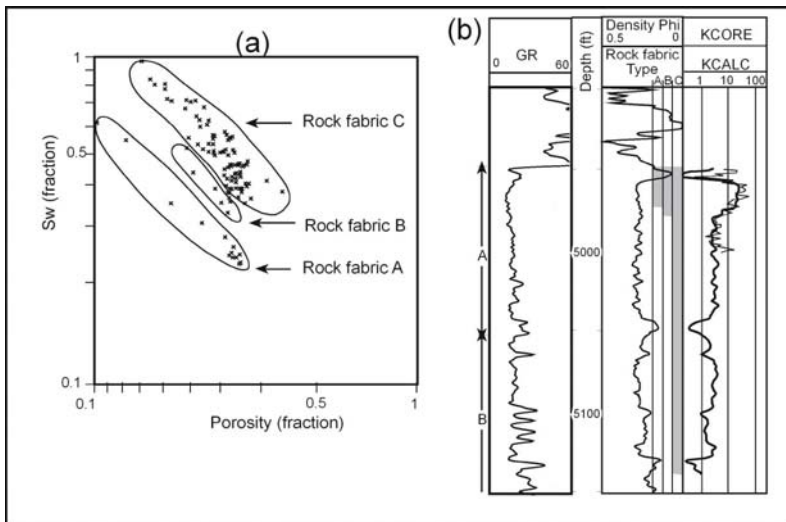
Fig. 6.22. An illustration of the calibration between rock fabrics and wireline logs and calculated permeability vs. core permeability. **a** Cross plot of log porosity and Archie water-saturation showing a distinct difference between the three rock fabrics. **b** Vertical profile of permeability calculated using the rock-fabric-specific permeability transforms and log porosity. Note good agreement between calculated and core permeability values

types A and B and have the highest permeability. The calculated permeability agrees with core permeability measurements.

A two-dimensional reservoir model was constructed by (1) integrating the rock-fabric facies with the sequence stratigraphic framework, (2) constructing rock-fabric flow layers that conform to rock-fabric facies and cycle boundaries, and (3) distributing the rock-fabric specific petrophysical parameters between wells conforming to the rock-fabric flow layers. The first step in this method is the integration of the rock-fabric facies and the sequence stratigraphic framework. Figure 23a illustrates this step for a portion of the reservoir model. The rock-fabric facies determined from porosity/water-saturation cross plots are integrated with the sequence stratigraphic framework with little modification required because of the close tie between the petrophysical rock-fabrics, facies descriptions, and stratigraphy. Rock-fabric types A, B, and C, and thin stylolitic beds are distributed within the 10 high-frequency cycles. Low porosity layers (dense layers) within rock-fabric type C are located at the base of cycles A6, B1, and B3.

The second step in this method is the construction of rock-fabric flow layers, layers that form the basic building blocks of the reservoir model. Each vertical change in rock-fabric is a boundary between rock-fabric layers. The boundaries must be continuous across the model for simulation constraints and conform to the HFC boundaries for geological constraints. To comply with this rule it may be necessary for some rock-fabric intervals to contain more than one rock-fabric layer. Thin beds that represent barriers to vertical flow, such as the stylolitic beds in this study, are captured at boundaries between rock-fabric flow layers.

As illustrated in Fig. 23b, 17 rock-fabric flow layers are required to capture the distribution of rock fabrics, dense layers, and thin stylolitic beds. Cycles A1 and A2 contain two layers each. Cycles A3, A4, and A5 have one layer each, although the boundary between A5 and A4 contains a discontinuous stylolitic bed. Four layers are required for cycle A6, two to distinguish between fabric types 2 and 3, and two to define the basal dense bed and the stylolitic bed within it. In the B interval, cycle B1 has a basal dense bed layer and an upper fabric type C layer. Cycle B2 is split in two layers to define a discontinuous stylolitic bed within the cycle.   The boundary between cycles B2 and B3 defines a continuous stylolitic bed. Cycle B3 contains only 1 layer because the basal dense layer is not included in the model.

The third step in this method is to distribute the rock-fabric-specific petrophysical parameters between wells and conforming to the rock-fabric flow layers. There are several basic methods of accomplishing this step. The method employed in this study is data interpolation between wells
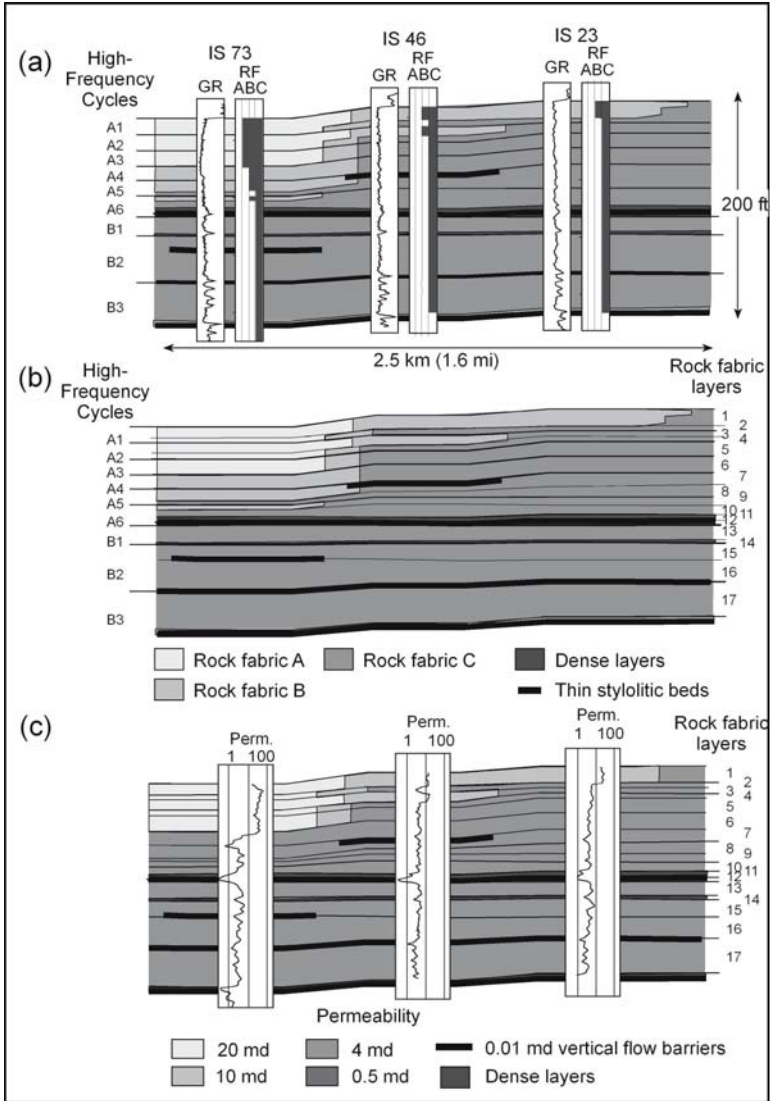
Fig. 6.23. Methodology for constructing the reservoir model. **a** Integration of high-frequency cycles and rock-fabric petrophysical types. **b** Construction of rock-fabric flow layers. Each vertical change in rock fabric defines a flow boundary. It is necessary that some rock-fabric intervals contain more than one layer in order for the layers to be continuous. Layers 12 and 16 are required to capture thin stylolitic units. **c** Quantification of model with permeability for simulation input. Notice the uniform permeability values in all layers except the upper layers 1-5

within the rock-fabric layers. This step is illustrated in Fig. 23c. Vertical permeability profiles calculated from density porosity and rock-fabric-specific permeability transforms are presented for each well Previous studies have shown that each rock-fabric layer can be considered to be a flow unit within which porosity, permeability, and saturation values can be legitimately averaged. Therefore, the permeability data are averaged within each rock-fabric flow unit layer and interpolated between the wells (Fig. 23c).

The stylolitic beds are considered to be flow barriers but are too thin to be input into most flow simulators. However, their location is noted and vertical flow across the flow-unit boundary is limited at their location within the attributes of the flow simulator.

6.3.5 Upper Devonian Reef Buildups, Alberta, Canada

The examples of limestone reservoirs presented above are all located on carbonate ramps. Major limestone reservoirs also occur in steep-sided, rimmed carbonate platforms, both attached and isolated. Highly productive Upper Devonian reef buildups are found in the Alberta Basin, Alberta, Canada. These buildups are isolated platforms with several hundreds of feet in relief and up to 150 square miles in area, and are excellent examples of rimmed platforms. In the past, the buildups have been referred to as "reefs". However, they are more correctly called "buildups" restricting the term "reef" to bindstone facies. The margins have relatively steep slopes into the basin and contain bindstone reef facies characteristic of rimmed platforms. Many have been completely dolomitized. The Redwater and Swanhills buildups are limestone, and production is controlled by the distribution of depositional facies.

The Redwater buildup is the largest, covering about 150 square miles (Fig. 24A). Production is located on the structurally high northeastern margin on the buildup. Klovan (1964) presents a detailed description of this area. The key facies is the organic reef (bindstone: Fig. 24), which is composed of stromatoporoids that overgrow each other to form a bound fabric. Tabulate corals are also present and brachiopods are abundant. The reef is located at the shelf margin. A stromatoporoid detritus facies (rudstone) is also found at the shelf margin (Fig. 24A) and is interpreted to be a reef broken up by strong wave action. Fore-reef deposits are wacke-stones with scattered stromatoporoid and coral fragments. The back reef is composed of seven facies. A peritidal facies (laminite) composed of ir-regular laminations and fenestral fabric is located on the paleotopographic
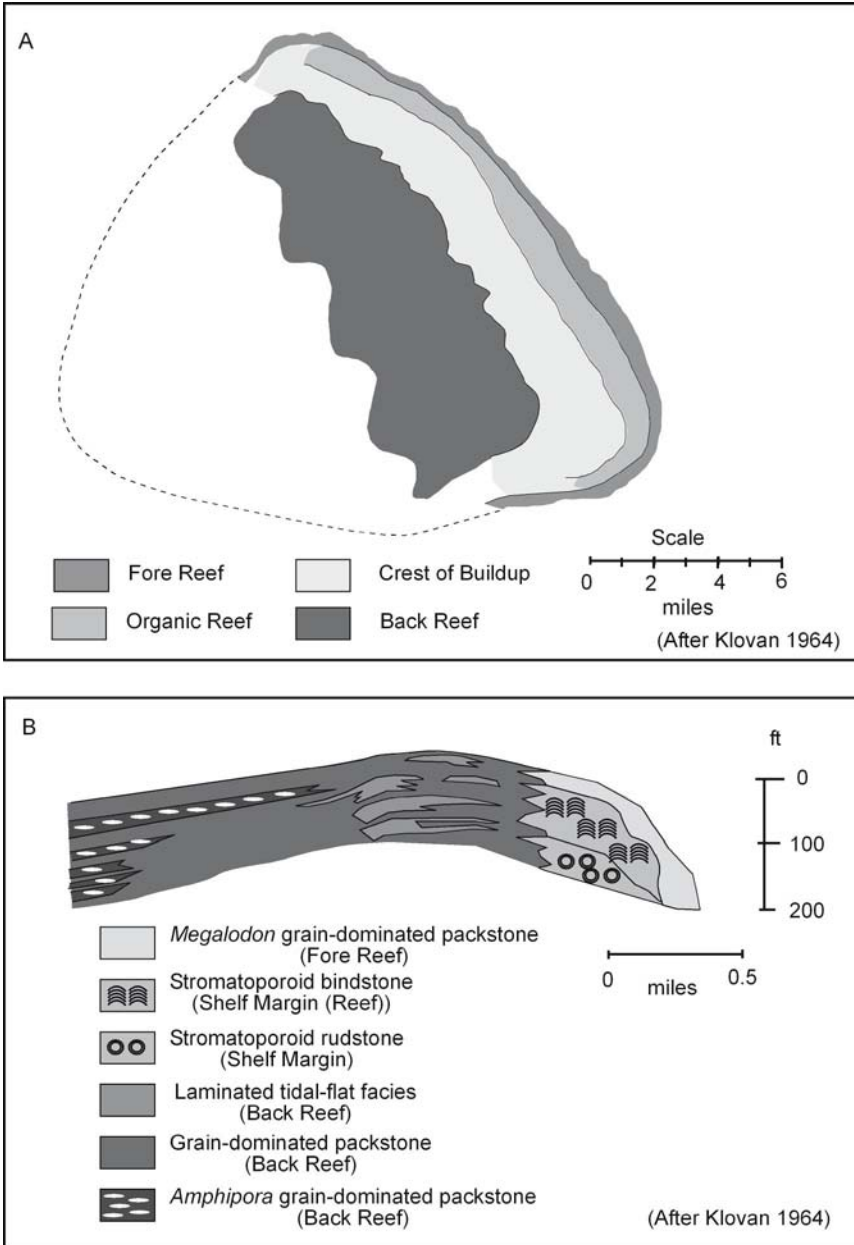
Fig. 6.24. Facies distribution in the Upper Devonian Redwater buildup (Klovan 1964). **A** Map showing buildup outline and general depositional facies patterns. **B** Cross section through the northeastern margin of the buildup showing general facies patterns

high of the buildup, and an *Amphipora* facies composed of wackestones and grain-dominated packstones is located in the interior of the buildup.

The Swanhills buildup is in an area of numerous Upper Devonian buildups. The facies progression is similar to Redwater, but the buildup is smaller, covering about 40 square miles (Fig. 25). A stromatoporoid
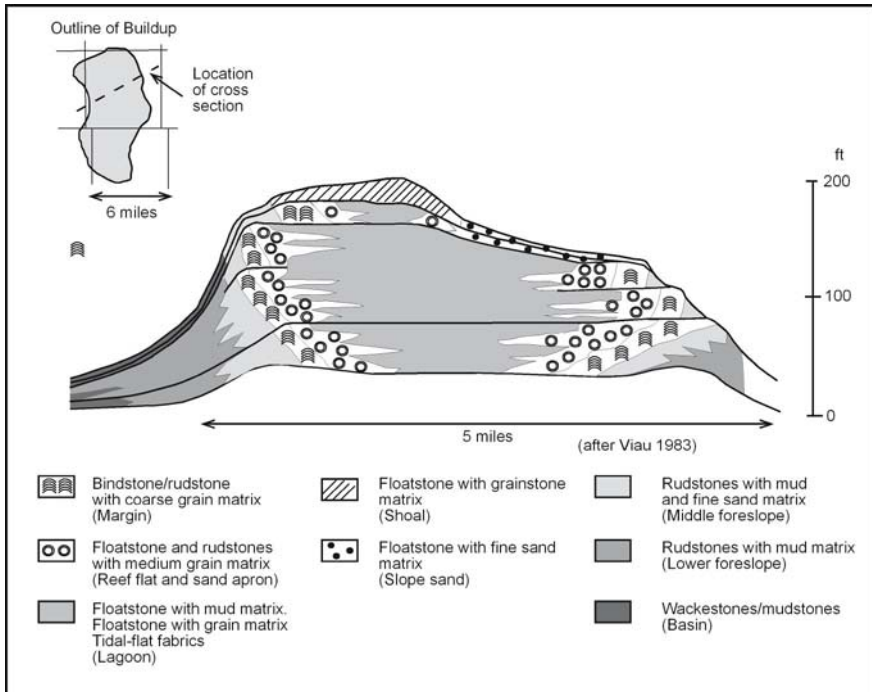
Fig. 6.25. Facies distribution in the Upper Devonian Swanhills buildup (Viau 1983). The most common large fossils are stromatoporoids and *Amphipora*

bindstone/rudstone with a matrix of coarse-grained skeletal grainstones and packstones is located at the margin of the buildup, and reef debris mixed with skeletal grains and mud are found in the fore slope facies (Fig. 25). The volume of mud increases downslope, and the basin facies is composed of wackestones and mudstones. Immediately behind the reef are stromatoporoid floatstones and rudstones with a matrix of grainstone and packstone. The interior of the buildup is composed of *Amphipora* floatstones with a matrix varying from mud-dominated to grain-dominated fabrics (Fig. 25). The buildup is divided into six growth stages, and the interior of the upper stage is composed of stromatoporoid floatstone with a grainstone matrix and flanking beds of floatstone with a fine sand matrix.

Intergrain and intragrain pore types are the most common in both of these buildups. Moldic porosity is present in the form of dissolved aragonite grains, and fenestral porosity is present in back-reef tidal flat facies. No massive dissolution fabrics have been described, although exposure surfaces are present, and only minor dolomite is reported. Therefore, compaction, cementation, and selective dissolution are the dominant diagenetic processes, and the distribution of petrophysical properties should conform to patterns of depositional textures.

Geological descriptions of rimmed platforms are dominated by detailed descriptions of fossil material because the organisms are the key indicators of depositional environment. The facies patterns and depositional environments in these two buildups are described on the basis of buildup topography and various types of stromatoporoids, *Amphipora*, and corals. Typically, little attention has been paid to the grain size that controls the pore size. The fossils occur as large particles, giving rise to the terms "rudstone" and "floatstone". However, the description of the sediment between the large fossil fragments is of principal interest when characterizing the petrophysical properties for reservoir characterization.

Descriptions of both buildups suggest the presence of grain-dominated fabrics in the vicinity of the bindstone reef and mud-dominated fabrics in the interior and fore slope facies. The facies are typically composed of large fossil fragments with a matrix of grains and mud, and the particle size, sorting, and interparticle porosity of the matrix control the pore-size distribution. In the vicinity of the bindstone (reef) facies, the volume between large particles is normally filled with sand-sized particles, and the sand size controls the pore size. Occasionally the volume between large particles is pore space and the pore size is controlled by the size of the large particles. In the interior (lagoon) and down the flanks, the volume between the large particles is normally filled with mud, but beds are occasionally present where the matrix is grain-dominated packstone.

The highest production rates are typically from wells that penetrate the margin of the buildup where intergrain porosity in the grain-dominated matrix of rudstones is concentrated. Production from the interior is from discontinuous beds of grain-dominated fabrics.

References

Anselmetti FS, Eberli GP 1993 Controls on sonic velocity in carbonates. Pageoph. 141, 2/3/4:287-323

Budd DA, Land LS 1990 Geochemical imprint of meteoric diagenesis in Holocene ooid sand, Schooner Cays, Bahamas: correlation of calcite cement geochemistry with extant groundwaters. J Sediment Petrol 60, 3:361-378

Budd DA, Hammes U, Vacher HL 1993 Calcite cementation in the upper Floridian aquifer: a modern example for confined-aquifer cementation models?. Geology 21, 1:33-37

Budd DA 2002 The relative roles of compaction and early cementation in the destruction of permeability in carbonate grainstones: a case study of the Paleogene of west-central Florida, U.S.A. J Sediment Research 72, 1:116-128

Cruz WM 1997 Study of Albian carbonate analogs: Cedar Park Quarry, Texas, USA, and Santos Basin reservoir, southeast offshore Brazil. Unpubl PhD thesis, The University of Texas at Austin, Austin, Texas

Dix GR, Mullins HT 1988 Rapid burial diagenesis of deep-water carbonates: Exuma Sound, Bahamas. Geology 16, 8:680-683

Enos P, Sawatsky LJ 1981 Pore networks in Holocene carbonate sediments. J. Sediment Petrol 51, 3:961-985

Goldhammer RK 1997 Compaction and decompaction algorithms for sedimentary carbonates. J Sediment Res 67, 1:26-56

Harris PM, Kendall CGSTC, Lerche I 1985 Carbonate cementation: a brief review. In: Schneidermann JS, Harris PM, (eds) Carbonate cements. SEPM Spec Publ 36:79-95

Heydari E, Moore CH 1989 Burial diagenesis and thermochemical sulfate reduction, Smackover Formation, southeastern Mississippi salt basin. Geology 17, 12:1080-1084

Heydari E, Moore CH 1993 Zonation and geochemical patterns of burial calcite cements: Upper Smackover Formation, Clarke County, Mississippi. J Sediment Petrol 63, 1:44-60

Hovorka SD, Nance HS, Kerans C 1993 Parasequence geometry as a control on porosity evolution: examples from the San Andres and Grayburg Formation in the Guadalupe Mountains, New Mexico. In: Loucks RG, Sarg JF, (eds) Carbonate sequence stratigraphy: recent developments and applications. AAPG Mem 57:493-514

Hurley NF, Lohmann KC 1989 Diagenesis of Devonian reefal carbonates in the Oscar Range, Canning Basin, Western Australia. J Sediment Petrol 59, 1:127-146

James NP, Ginsburg RN 1979 The seaward marginal Belize barrier and atoll reefs. Int Assoc Sedimentol Spec Publ 3, 191 pp

Kerans C., Lucia FJ, Senger RK 1994 Integrated characterization of carbonate ramp reservoirs using outcrop analogs. AAPG Bull 78, 2:181-216

Klovan FE 1964 Facies analysis of the Redwater Reef Complex, Alberta, Canada. Bull Can Pet Geol 12, 1:1-100

Lonoy, A 2006 Making sense of carbonate pore systems. AAPG Bull 90, 9:1381-1405

Lucia FJ 1962 Diagenesis of a crinoidal sediment: J Sediment Petrol 32, 4:848-865

Lucia FJ 1983 Petrophysical parameters estimated from visual description of carbonate rocks: a field classification of carbonate pore space. J Pet Technol March:626-637

Lucia FJ 1995 Rock/fabric petrophysical classification of carbonate pore space for reservoir characterization. AAPG Bull 79, 9:270-300

Lucia FJ, Murray RC 1966 Origin and distribution of porosity in crinoidal rocks. Proc 7th World Petroleum Congress, Mexico City, Mexico, 1966, pp 409-423

Melim, LA, Anselmetti, FS, Eberli, GP 2001 The importance of pore type on permeability of Neogene carbonates, Great Bahama Bank, In Ginsburg, RN (ed) Subsurface geology of a prograding carbonate platform margin, Great Bahama Bank: Results of the Bahamas drilling project. SEPM Spec Publ 70:217-240

Mitchell FJ, Lehman PJ, Contrell DL, Al-Jallal IA, Al-Thagafy MAR 1988 Lithofacies, diagenesis, and depositional sequence; Arab-D member, Ghawar field, Saudi Arabia. In: Lomando AJ, Harris PM, (eds) Giant oil and gas fields: A core workshop. SEPM Core Workshop 12, 2:459-514

Moore CH, Druckman Y 1981 Burial diagenesis and porosity evolution, upper Jurassic Smackover, Arkansas and Louisiana. AAPG Bull 65, 4:597-628

Munn D, Jubralla AF 1987 Reservoir geological modeling of the Arab D reservoir in the Bul Hanine Field, offshore Qatar: approach and results. SPE Middle East Oil Show, Bahrain, SPE Paper 15699, pp 109-120

Powers RW 1962 Arabian Upper Jurassic carbonate reservoir rocks, in Classification of Carbonate Rocks: A Symposium. AAPG Mem 1:122-192

Schmoker JW, Halley RB 1982 Carbonate porosity versus depth: a predictable relation for south Florida. AAPG Bull 66, 12:2561-2570

Schmoker FW, Krystinic KB, Halley RB 1985 Selected characteristics of limestone and dolomite reservoirs in the United States. AAPG Bull 69, 5:733-741

Sears SO, Lucia FJ 1980 Dolomitization of northern Michigan Niagaran reefs by brine refluxion and freshwater/seawater mixing. In: Zenger DH, Dunham JB, Ethington RL, (eds) Concepts and models of dolomitization. SEPM Spec Publ 28:215-236

Shinn EA 1969 Submarine lithification of Holocene carbonate sediments in the Persian Gulf. Sedimentology 12:109-144

Swirydezuk K 1988 Mineralogical control on porosity type in upper Jurassic Smackover ooid grainstones, southern Arkansas and northern Louisiana. J Sediment Petrol 58, 2:339-347

Viau C 1983 Depositional sequences, facies and evolution of the Upper Devonian Swan Hills reef buildup, Central Alberta, Canada. In: Harris PM, (ed) Carbonate Buildups—A Core Workshop. SEPM Core Workshop 4:112-143

Weyl PK 1959 Pressure solution and the force of crystallization—a phenomenological theory. J Geophys Res 63, 11:2001-2025

Chapter 7 Dolostone Reservoirs

7.1 Introduction

The three-dimensional spatial distribution of petrophysical properties is controlled by the spatial distribution of two geological processes, depositional and diagenetic. Although it is clear that the three-dimensional spatial distribution of petrophysical properties is initially controlled by the spatial distribution of depositional textures, it is also clear from numerous reservoir studies that the petrophysical properties found in carbonate reservoirs are significantly different from those of modern carbonate sediment. Diagenesis typically reduces porosity, redistributes the pore space, and alters permeability and capillary characteristics.

The basic diagenetic processes discussed here are (1) calcite cementation, (2) mechanical and chemical compaction, (3) selective dissolution, (4) dolomitization, (5) evaporite mineralization, and (6) massive dissolution, collapse, and fracturing. The processes of cementation, compaction, and selective dissolution were discussed in Chapter 6 under the title of Limestone Reservoirs. In this chapter we will discuss dolostone reservoirs.

A key question in mapping diagenetic effects is the degree of conformance between diagenetic products and depositional patterns. If the transport of material in and out of the system is not a major factor in producing the diagenetic product, the product will generally conform to depositional patterns. However, if the transport of ions in and out of the system by fluid flow is required to produce the diagenetic product, then the diagenetic product may not conform to depositional patterns. In this case, knowledge of the hydrological system may be required to map the diagenetic products, including the source of the fluid, the direction of fluid flow, and the geochemical changes that occur along the flow path.

As discussed in Chapter 6, the products of cementation, compaction, and selective dissolution can normally be linked to depositional textures. The transport of material is not a major consideration for compaction, selective dissolution of unstable aragonite allochems, and associated precipi-

tation of calcite cement, although the local introduction of meteoric water may enhance the dissolution process. Early cementation processes require fluid flow to import calcium and carbonate into the system, but the fluid flow is closely tied to the depositional environment. Late or burial cementation may be formed by chemical compaction and thus may be related to a depositional environment, or it may require regional transport of ions by ground water, in which case it need not be related to a depositional environment. As a result, the permeability structure of simple limestone reservoirs is closely linked to the basic rock fabrics of grainstone, grain-dominated packstone, mud-dominated limestones, and intragrain porosity.

In this chapter, we will focus on dolomitization and associated evaporite mineralization. Dolomitization requires fluid flow for the introduction of magnesium into the system. Therefore, fluid flow is an important factor in the origin of dolomite fabrics, and the dolomite pattern may or may not conform to depositional patterns. The key is to locate the source and flow path of the dolomitizing fluids. Early dolomitizing fluids are most likely hypersaline fluids sourced from peritidal environments and flow paths most likely controlled by depositional fabrics and early diagenetic events. The predolomite diagenetic history may significantly alter the permeability structure and result in late dolomitizing waters following diagenetic rather than depositional flow paths. Diagenetic gypsum and anhydrite are commonly associated with dolomitization and require the transport of sulfate into the system by high-sulfate, hypersaline water. Studies have shown little linkage between depositional facies patterns and patterns of diagenetic gypsum or anhydrite. Bedded anhydrite/gypsum, of course, is a sedimentary deposit and its spatial geometry can be predicted by depositional models.

7.2 Dolomitization

7.2.1 Hydrologic Models

Modified sea water is thought to be the only adequate source of magnesium for the volume of dolomite observed in nature. However, a mechanism for driving large volumes of modified sea water through carbonate strata is required to convert a limestone into a dolostones. Several hydrologic models have been proposed to circulate large volumes of sea water through a stack of carbonate (1) hypersaline reflux flow, (2) mixing zone, and (3) thermal (Kohout) convection (Fig. 1). The *mixing zone* is focused
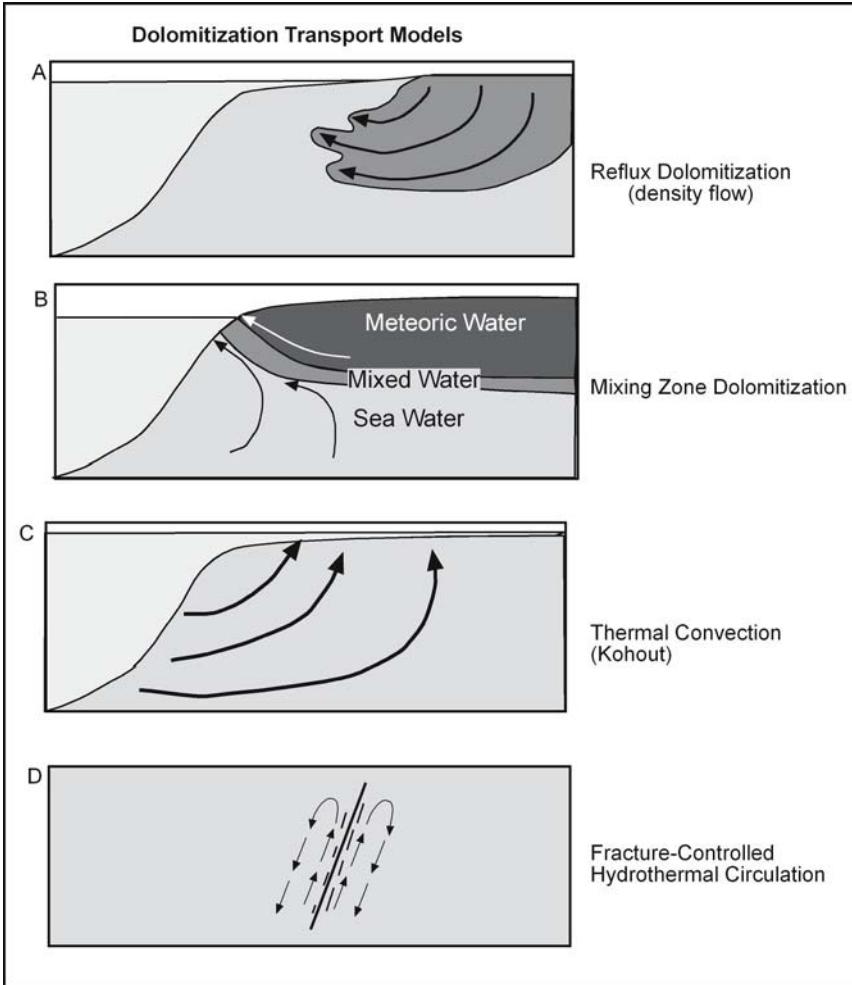
Fig. 7.1. Hydrologic models of dolomitization showing source and flow patterns of dolomitizing fluids. (A) Reflux dolomitization with source-area being tidal-flat environments and downward flow directions. (B) Mixing-zone dolomitization with source located at the intersection of meteoric water and phreatic seawater and no specific flow direction implied. (C) Thermal convection dolomitization with seawater source at the platform slope and flow direction inward and upward. (D) Thermal convection of dolomitizing fluids localized by fracture zones with source unknown and flow direction upward and outward into permeable beds

on the mixing of meteoric and marine phreatic waters along the margins of platforms and under islands. Dolomitization is thought to occur because mixing of two fluids saturation with calcite can result in a fluid undersaturated with calcite (Ward and Halley 1985) and can produce a chemical en-

vironment suitable for calcite to dissolve and dolomite to precipitate; this process is known as dolomitization. *Thermal (Kohout) convection* relies on temperature gradients to move sea water through a carbonate platform (Whitaker et al. 2004). Sea water has been shown to be oversaturated with dolomite and capable of dolomitizing limestones if sufficient volumes of sea water move through the platform. Several studies of carbonate atolls have attributed the dolomitization to this model (Saller 1984). However, attempts to model this process numerically have failed to produce large amounts of dolomite (Whitaker et al. 2004). *Thermobaric (hydrothermal)* is a burial model, and the source of the hydrothermal solutions is arguable. The circulation results from the heating of connate waters, which increases their buoyancy and causes them to rise along fractures and other zones of relatively higher permeability. Fault-controlled dolomitization is well known, especially associated with mineral deposits (Davies and Langhorne 2006). Whether the volumes are sufficient to produce large volumes of dolostones is in doubt at the present time. We will focus on the hypersaline reflux model because it has been applied to many large reservoirs, and its relationship to peritidal environments provides a robust basis for identifying source areas and overall flow paths.

The *hypersaline reflux* model is characterized by refluxing hypersaline evaporated sea water from the surface down into underlying strata replacing sea water and interacting with ground water (Fig. 2). Hypersaline tidal-flat environments and associated hypersaline ponds, lakes, and lagoons are common sources for hypersaline water. The high density of the saline water and the elevation of the tidal flats produce the hydrodynamic potential needed for saline water to flow down and seaward through the underlying sediment, replacing calcium carbonate with dolomite and precipitating gypsum and anhydrite. This robust model is the most predictable dolomite model available to us. The hypersaline model has been modeled effectively by Jones and Xiao (2005).

7.2.2 Dolomitization and Petrophysical Properties

Dolomitization is a diagenetic process that converts limestones to dolostones through a microchemical process of calcium carbonate dissolution and dolomite precipitation. Two equations for dolomite formation are
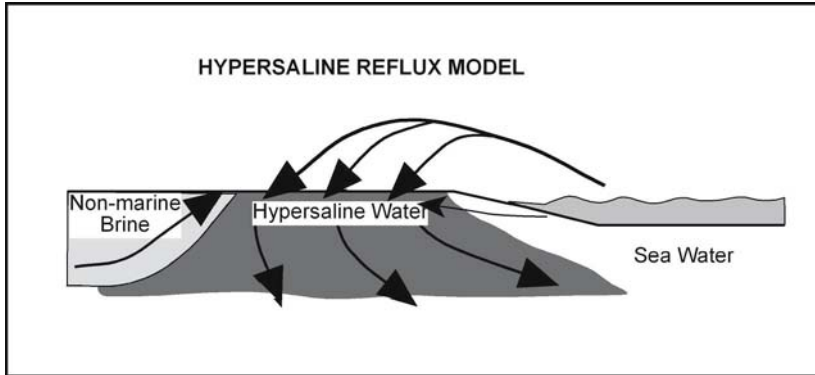
Fig. 7.2. Hypersaline reflux model based on modern data from the Trucial Coast and Qatar, Middle East. Seawater transported onto an arid tidal flat evaporates and flows downward through the underlying tidal-flat and subtidal sediments, converting the calcium carbonate sediment to dolomite. Hypersaline seawater mixes with the regional groundwater landward, forming a mixed seawater/meteoric water hypersaline fluid

shown below. They form end members of a continuous series of possible reactions.

$$2CaCO_3 + Mg^{++} = CaMg(CO_3)^2 + Ca^{++} \text{ (mole-for-mole replacement)},$$

$$Mg^{++} + Ca^{++} + 2CO_3^{=} = CaMg(CO_3)^2 \text{ (cementation)}.$$

The replacement equation is a mole-for-mole reaction and suggests that the Mg/Ca ratio in the water is a controlling factor in the reaction. Analysis of waters associated with both ancient and modern dolomite indicates that a Mg/Ca ratio of higher than 1 is required for dolomitization of limestones (Folk and Land 1975) (Fig. 3). Normal marine water, however, has a Mg/Ca ratio of 7 without forming significant quantities of dolomite, demonstrating the impact of kinetics on dolomitization. Marine dolomite is commonly found associated with evaporated marine water with Mg/Ca ratios of between 10 and 50. These increased ratios result from loss of calcium through precipitation of gypsum, anhydrite, and calcium carbonate minerals in response to evaporation of sea water (Fig. 4).

In a closed system, the replacement of calcite or aragonite by dolomite will reduce mineral volume because dolomite has a smaller molar volume than either calcite or aragonite. For calcite, the decrease in molar volume is 12.5%, which is the basis for the much-heralded origin of porosity through dolomitization (Beaumont 1876). However, dolomitization involves the
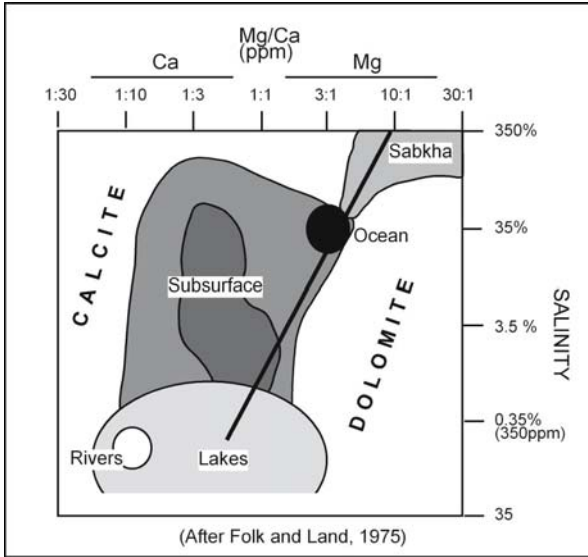
Fig. 7.3. Relationship of dolomite and calcite stability fields to Mg/Ca ratios and salinity (Folk and Land 1975). Dolomitizing water is found in a variety of environments including sabkha (tidal flat), groundwater, and saline lakes
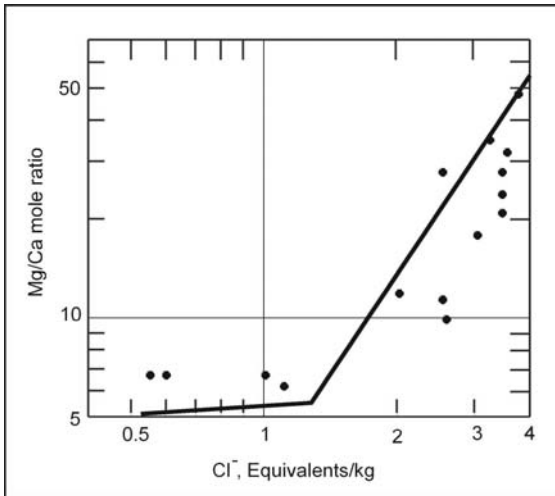
Fig. 7.4. The increase in Mg/Ca molar ratio during evaporation of seawater due to the precipitation of CaSO$_4$ (gypsum or anhydrite). Data are from Bonaire, N.A., and the curve is computed from gypsum and aragonite precipitation curves. (Deffeyes et al. 1965)

flow of large quantities of water through the rock, which requires an open system. Thus, not only magnesium but also carbonate can be added to the system, resulting in the formation of both replacement and pore-filling dolomite during the replacement process. Therefore, the dolomitization process includes both replacement of calcite or aragonite by dolomite and cementation of pore space by dolomite cement. This process is known as volume-for-volume replacement and can be expressed by the following equation (Morrow 1990).

$$(2-x)CaCO_3 + Mg^{+2} + xCO_3^{-2} = CaMg(CO_3)_2 + (1-x)Ca^{+2},$$
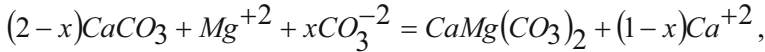
where x = moles of carbonate added from the dolomitizing fluid.

The origin of porosity in dolostones is much more complicated than the simple mole-for-mole reaction would suggest. A study of young limestones and associated dolostones suggests that much of the porosity in the dolostones is inherited from the precursor limestone and occluded by overdolomitization (Lucia 2004). Modern dolomitic sediments show little change in pore volume with increased amounts of dolomite (Fig. 5).
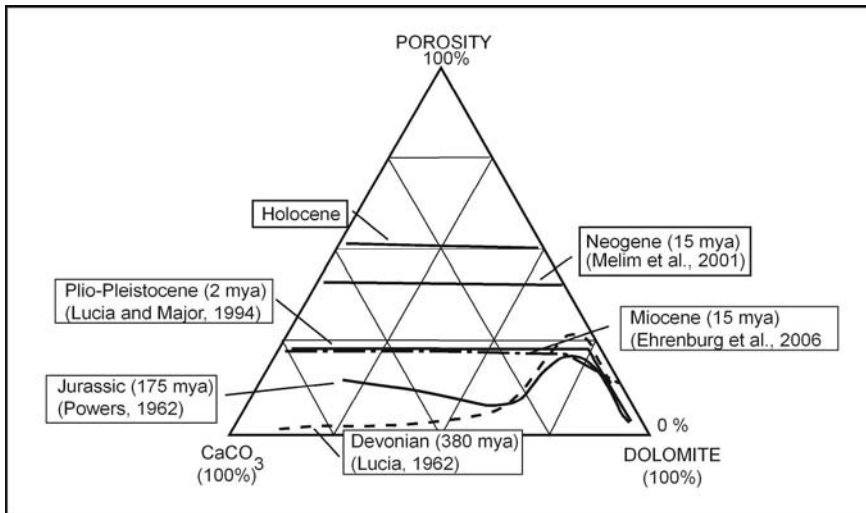
Fig. 7.5. Relationship among porosity, dolomitization, and time. Limestone is more porous in young carbonates than dolomites and less porous in older carbonates. The loss of porosity in limestones relative to dolomites with time and burial is probably due to differential compaction

Neogene limestone and dolostone on the Bahama Platform have similar porosity values (Melim et al. 2001), suggesting that the amount of porosity in the dolostones is basically inherited from the associated limestone. The same is true for Miocene limestones and dolostones found in the Miocene of the Great Barrier Reef (Ehrenburg et al. 2006). Plio-Pleistocene dolstones, however, are commonly less porous than their limestone counterparts. A dolomitization study of Plio-Pleistocene carbonate on the island of Bonaire in the Netherlands Antilles demonstrated that the limestone has an average porosity of 25% whereas the dolomite has an average porosity of 11%, suggesting a loss of porosity with dolomitization by overdolomitization (Lucia and Major 1994). If dolomitization occurred in a closed system and only magnesium were substituted for calcium in the carbonate lattice, the resulting dolomite would have an average porosity of 35% (Fig. 6).
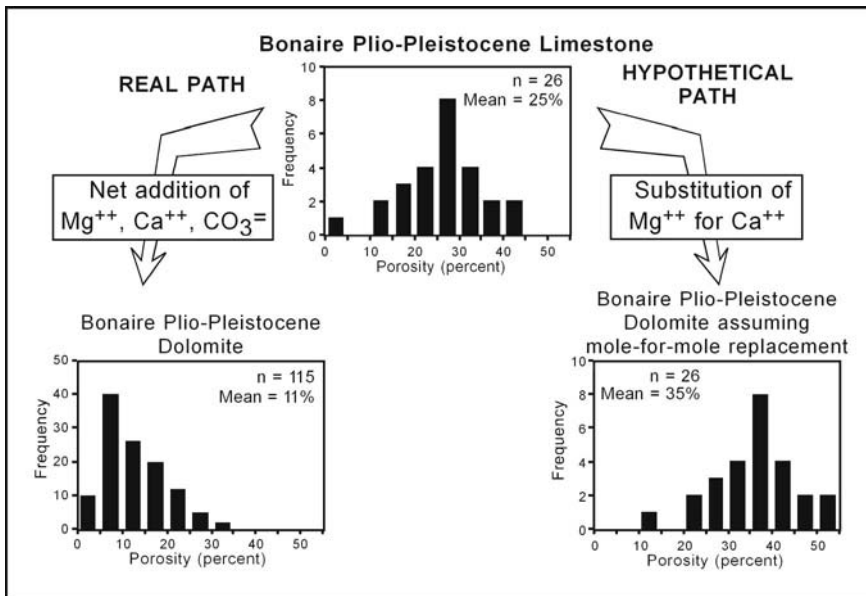
Fig. 7.6. Porosity frequency plots for dolomite, the precursor limestone, and for a hypothetical dolomite calculated from the limestone frequency plot assuming mole-for-mole replacement. (Lucia and Major 1994)

Paleozoic dolostones are often more porous than their associated limestones, an observation that is often used to "prove" that dolomitization creates 12.5% porosity. The alternative explanation is the limestones are more compactable than dolostones and lose porosity faster than dolostones. This relationship is seen in the depth plot of porosity from South Florida, where

dolostones are less porous than limestones at shallow depths and more po-
rous than the limestones at depth (Fig. 7; Schmoker and Halley 1982).
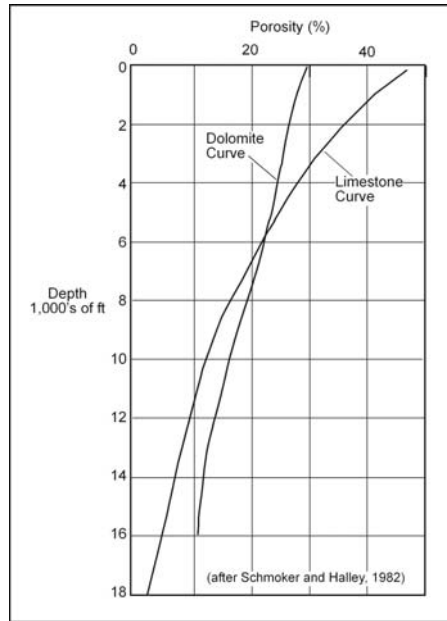
Fig. 7.7. Relationship of porosity to depth and lithology in South Florida. The
shallowest data are from Quaternary carbonates and the deepest data are from the
Cretaceous. Dolomite becomes more porous than limestone at a depth of 6000 ft,
which approximates the Tertiary-Cretaceous boundary. (Schmoker and Halley
1982)

It is also seen in data from the Ghawar field (Powers 1962, Lucia et al.
2001), where the grainstones and the dolostones have similar porosity
ranges and the mud-dominated fabrics have been compacted to lower po-
rosities. There is more dolomite in the mud-dominated fabrics, and a plot
of % dolomite and porosity shows decreasing porosity as the % dolomite
and lime mud increase and a sharp increase in porosity when all the car-
bonates have been replaced (Fig. 8). The effects of overdolomitization are
apparent in the 0 to 30% range of porosity found in the dolostones.

From these observations it is hypothesized that the porosity in dolos-
tones is a function of (1) the porosity of the precursor limestone, (2) the
amount of overdolomitization, and (3) compaction. Further cementation by
a later dolomitizing fluid is a fourth possible porosity-occluding event.

The timing of dolomitization is important for understanding the origin
of porosity in any specific dolostone body. To flow large quantities of
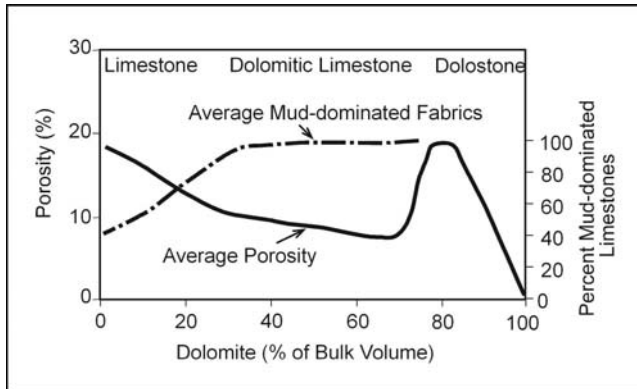
Fig. 7.8. Relationship among percent bulk volume dolomite, porosity, and percent mud-dominated facies showing that the porosities of grainstones and dolostones are similar but that porosity of mud-dominated facies is much less, probably due to differential compaction of these Jurassic sediments (Lucia et al. 2001)

water through a carbonate, the body of carbonate must be porous and permeable. This means that the precursor limestone must be porous. Dolostones attributed to hypersaline reflux dolomitization are most likely formed early in the diagenetic history and when the precursor limestones are relatively porous. Dolostones related to burial process most likely form late in the diagenetic history, and the precursor limestones are more likely to be less porous due to compaction and burial cementation. Both the timing of late dolomitization and the porosity of the precursor limestone are difficult to determine. Timing is normally based on textural relationships with other diagenetic events, such as fractures, collapse brecciation, cementation, etc. A unique approach is described by Davies and Langhorne (2006) where dolomitization temperatures obtained from fluid-inclusion analysis are compared with burial-history curves to determine the age of late dolomitization. The precursor limestone porosity is often obtained from porosity vs. depth curves, such as the one published by Schmoker and Halley (1982). However, generalized depth plots do not adequately account for the wide spread of porosities at various depths in carbonates and are of little use in studies of specific dolostone bodies (Fig. 9).

Dolomitization can change the rock fabric significantly (Fig. 10). In mud-dominated fabrics the dolomite crystals may be the same size as the mud-sized particles, or the dolomite crystals may be much larger than the mud-sized particles they replace. Dolomite crystals commonly range in size from several to 200 µm, whereas the crystals in calcium carbonate mud are usually l to 10 µm in size. Thus, dolomitization of a carbonate mud can result in an increase in crystal size from less than 20 µm to more
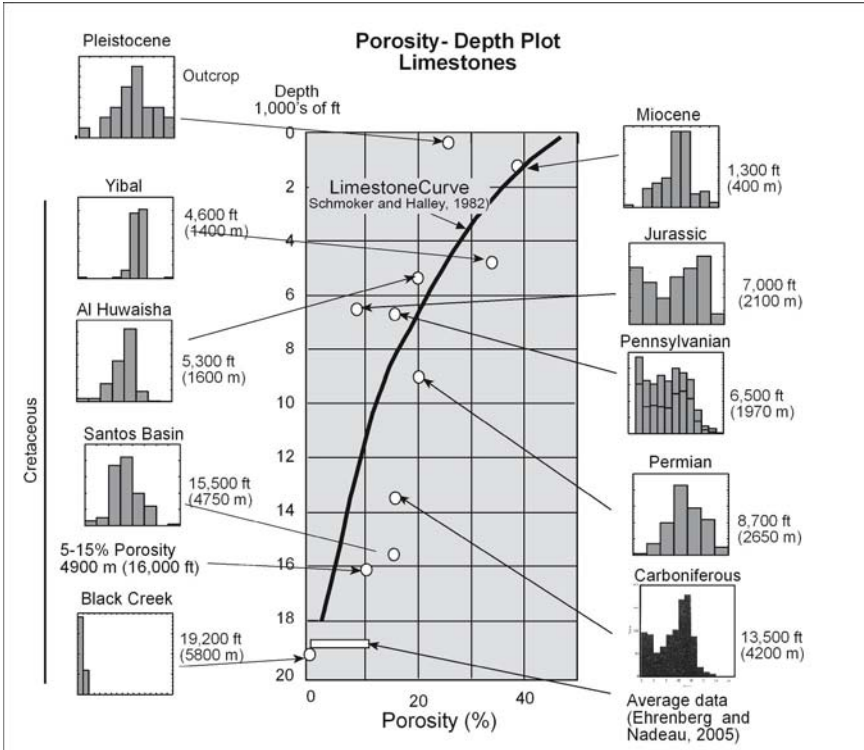
Fig. 7.9. Depth plot showing porosity ranges from various limestone fields compared with the depth plot from Schmoker and Halley (1982)

than 200 µm, with a corresponding increase in pore size. The increase in particle size caused by dolomitization of mud-dominated fabrics will greatly increase the flow characteristics of the rock and improve the capillary properties because of the corresponding increase in pore size. The pore size increase resulting from a larger particle size is offset by the addition of dolomite resulting from the importation of magnesium and carbonate with dolomitizing waters. The net addition of material results in an overall loss of porosity and a corresponding decrease in pore size.

The increase in pore size results from the reorganization of pore space during dolomitization. For example, 200-µm dolomite crystals will occupy space once occupied not only by the less than 20-µm calcite or aragonite crystals, but also by the micro pore space between those crystals. Thus, the 200-µm dolomite crystals are both replacing the calcite crystals and occluding the micro pore space between the crystals. Because the dolomite crystal occupies more space than preexisting calcite crystals, calcium, magnesium, and carbonate must be transported to the site of the growing

dolomite crystal. There are two basic sources for the calcium, magnesium, and carbonate ions (1) dissolution of nearby carbonate crystals and (2) regional ground water. These sources are referred to by Murray (1960) as local and distant sources. The dissolution of nearby carbonate produces intercrystal porosity, whereas precipitation of dolomite from regional ground water produces dolomite cement (Fig. 10).
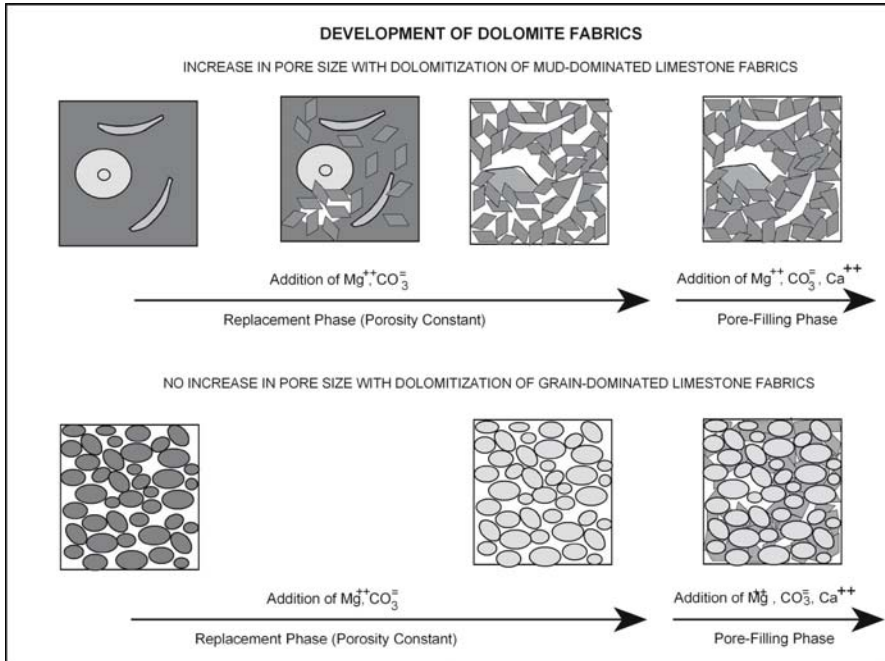
Fig. 7.10. Change in pore structure during dolomitization of **A** mud-dominated limestone and **B** grain-dominated limestone. The conversion of mud-dominated limestone to medium or large crystalline dolomite increases pore size, whereas the dolomitization of a grain-dominated fabric has little effect on pore size

Vuggy porosity is created similarly during dolomitization. Once dolomite crystals form, they become preferred sites for dolomite precipitation. Therefore, carbonate dissolved from one location will be transported to an existing growing dolomite crystal. Skeletal fragments are usually the last to be dissolved during dolomitization because of their size, and when the carbonate is transported to an existing growing dolomite crystal, a dissolved skeletal fragment is left as a fossil mold, a type of separate vug (Fig. 10). However, the creation of grain molds by dissolution is compensated for by the loss of intercrystal pore space by pore-filling dolomite and may have little effect on total porosity.

Grainstones are usually composed of grains much larger than the dolomite crystal size (Fig. 10), so that dolomitization does not have a significant effect on their pore-size characteristics. Grain-dominated packstones are also typically composed of large grains, so replacement by dolomite crystals much smaller than the grain size will not significantly affect their pore size. However, replacement grain-dominated packstones with larger than 100-μm dolomite crystals will significantly improve their petrophysical properties.

Dolomite crystal size is an important factor in the petrophysical properties of dolostones. Two factors that affect dolomite crystal size are (1) the saturation with respect to dolomite, as reflected by Mg/Ca ratios and (2) the surface area of the precursor fabric. In the evaporative reflux model, hypersaline water supersaturated with dolomite enters the system from the tidal-flat surface and flows down and out to the sea. The saturation with dolomite will decrease along the down-and-out flow path, and the dolomite crystal size should increase along the flow path. Modern dolomites found in evaporite tidal flats have a crystal size of around 5 μm, as do dolomitized tidal-flat sediments in the geological record. In the San Andres and Grayburg dolomite reservoirs of West Texas and New Mexico, the dolomite crystal size can often be correlated with distance below peritidal facies. In the Permian-age Seminole San Andres reservoir, West Texas, dolomite crystal size increases in size with depth (Fig. 11). The reservoir is capped by a peritidal facies tract, and the increase in dolomite crystal size is interpreted as reflecting a decrease in dolomite saturation as the dolomitizing water flows from the peritidal facies downward.

Dolomite crystal size is also correlated with precursor texture. Dolomitized grains are commonly coarser crystals than dolomitized mud. The most extreme case is pseudomorphic replacement of echinoderm fragments, producing millimeter-size dolomite crystals in a matrix of 200-μm crystals (Lucia 1962). Surface area can be correlated with the amount of carbonate mud in the rock and perhaps is a key parameter in control of dolomite crystal size. The effect of grain content on dolomite crystal size can be seen the Seminole depth plot (Fig. 11) in that the grain-dominated fabrics have larger dolomite crystals than the mud-dominated fabrics, even though the average crystal size increases with depth. The effect of surface area may also partially explain the observation that late-formed dolomites are always medium to large size. Predolomite burial cementation and compaction reduces porosity and surface area, establishing the conditions required for the formation of larger dolomite crystals.
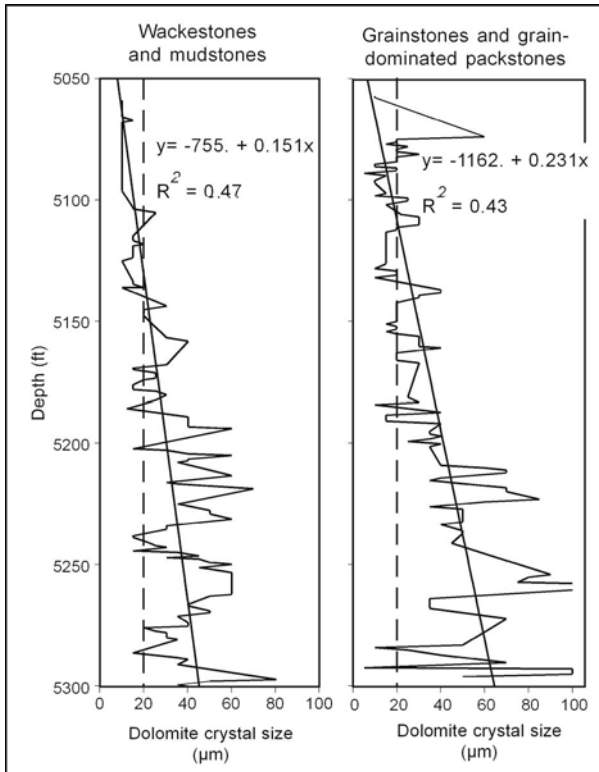
Fig. 7.11. Cross plot of depth versus dolomite crystal size for mud-dominated and grain-dominated dolostones in the Seminole San Andres reservoir, West Texas, showing overall increase in crystal size with depth

In summary, dolomitization affects the flow characteristics of carbonate reservoir rocks by (1) increasing particle size, (2) decreasing pore volume due to a net addition of dolomite, (3) developing moldic pores, and (4) increasing resistance to compaction.

The petrophysical class of a dolostone may not conform to the depositional texture because dolostone class is determined by dolomite crystal size as well as by depositional texture (modified Dunham categories, Lucia 1995). Dolograinstone, grain-dominated dolopackstone with crystal size less than 100 μm, and mud-dominated dolostone with crystal size less than 20 μm will plot in the class 1, 2 and 3 fields, respectively. Dolostones with less than 20-μm dolomite crystals are concentrated in tidal-flat and adjacent facies. Within these strata, the petrophysical classes will conform to

the depositional textures, and depositional patterns can be used to map the spatial distribution of petrophysical properties (Fig. 12). The dolomite
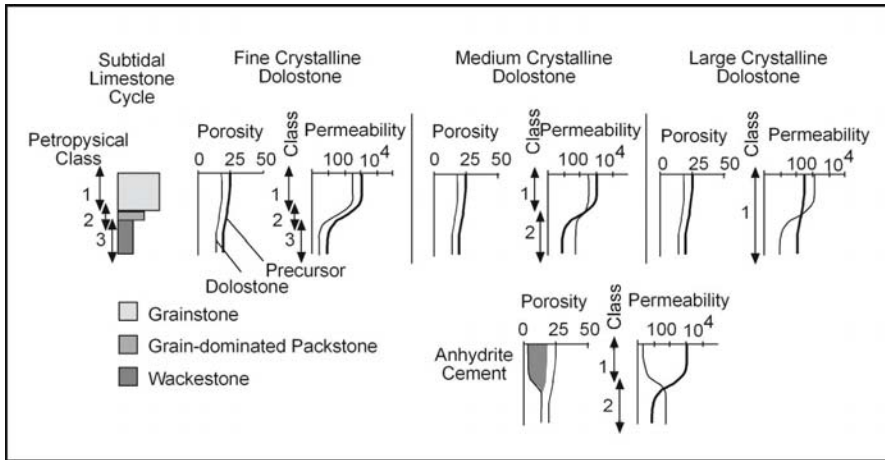
Fig. 7.12. Illustration of the effects of hypersaline dolomitization on porosity and permeability profiles in a single subtidal upward-shallowing cycle. Precursor limestone curves are based on Jurassic Arab D data from Powers (1962). Porosity of the precursor will be reduced during dolomitization by an amount related to the volume throughput of dolomitizing water. The permeability profile will change dependent upon (1) the change in porosity and (2) the resulting dolomite crystal size in the mud-dominated fabrics. Vertical stacking of petrophysical classes will change with the change in dolomite crystal size

crystal sizes of mud-dominated dolostones located farther from tidal-flat facies are typically larger than 20 μm but less than 100 μm. Within these strata, mud-dominated dolostones will be class 2, not class 3 like the precursor mud-dominated limestone (Fig. 12). Mud-dominated dolostones and grain-dominated dolopackstones will be class 2. Only dolograinstones will be class 1, and only one transform will be required except where grainstones are present. If the dolomite crystal size is larger than 100 μm, all the dolostones will plot in the class 1 field regardless of the depositional environment. Only one transform will be required, and depositional environments are not needed to determine the petrophysical class.

7.2.3 Distribution of Dolostone

The pattern of dolomitization will be controlled by the source, volume, and flow path of the dolomitizing water. For the hypersaline reflux model, the source of the dolomitizing water is the supratidal environment, the volume

of dolomitizing water will be related to the history of the peritidal environment, and the flow path will be controlled by the permeability structure of the underlying limestones. If a small volume of hypersaline water is formed, only the tidal-flat facies will be dolomitized. If large volumes of dolomitizing water are produced, hundreds of meters of underlying subtidal sediment can be dolomitized. For other dolomitization models the source and volume of the dolomitizing fluids is more difficult to define. Large bodies of late dolostones are not uncommon, however, and sources of large volumes of dolomitizing water, perhaps not directly linked to sea water, must exist. Permeability controls for late dolostones are commonly a combination of fractures, faults, karst, karst breccia, etc., and residual matrix permeability. We will explore some of these ideas when discussing specific field examples.

Dolomitization increases the reservoir potential of a carbonate platform (Fig. 13). In a limestone sequence, compaction normally reduces
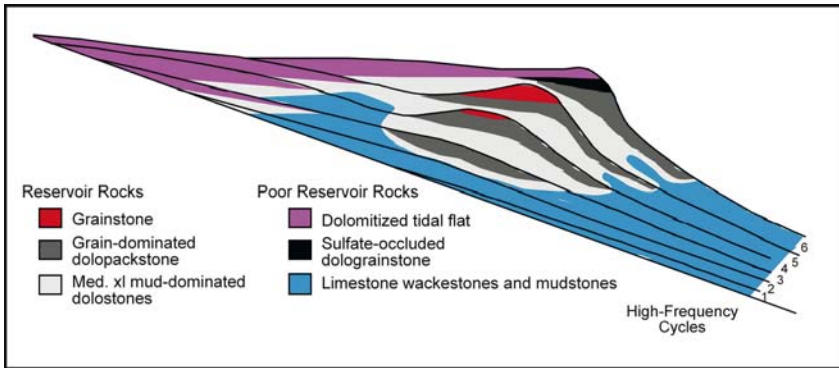
Fig. 7.13. Generalized distribution of reservoir rocks in a high-frequency sequence resulting from cementation-compaction followed by hypersaline reflux dolomitization and evaporite mineralization. The increase in particle size in mud-dominated dolostone increases the potentially productive volume

porosity in the mud-dominated facies to the point that permeability is too low to be considered reservoir. Dolomitization can convert these mud-dominated limestones to medium crystalline mud-dominated dolostones that both preserves the porosity from compaction effects and increases the pore size. As a result, dolostone reservoirs have the potential of having larger reservoir volumes than limestone reservoirs.

7.2.4 Calcitization of Dolomite

The dolomite replacement process is reversible, resulting in calcification of dolomite in the presence of high-calcium waters. Ground water with a Mg/Ca ratio of less than 1 is capable of dissolving dolomite and precipitating calcite. Models for the formation of low Mg/Ca ratio waters capable of calcitizing dolomite are highly varied, but all involve meteoric or deep ground waters. The dissolution of $CaSO_4$ by meteoric ground water creates a low-Mg/Ca water that is capable of calcitization (Lucia 1972; Back et al. 1983). Calcium-rich water that originates from deep saline deposits and migrates upward along faults is also capable of calcitizing dolomite (Land and Prezbindowski 1981).

Calcitized dolomite crystals commonly display calcite centers and dolomite rims. Hollow dolomite rhombs (often referred to as skeletal dolomite) have been observed in many dolostone bodies, suggesting that centers of dolomite crystals are more soluble than dolomite rims. Dissolution of dolomite crystals normally results in a separate-vug pore type. In some studies petrographic observations suggest that the calcite is occluding hollow dolomite rhombs, and in other studies the calcite appears to be replacing the dolomite (Evamy 1967).

7.3 Evaporite Mineralization

Anhydrite ($CaSO_4$) and gypsum ($CaSO_4 \cdot 2H_2O$) are evaporite minerals commonly found in dolomite reservoirs. Halite (NaCl) is uncommon but may be found occluding pore space adjacent to salt beds. Gypsum is the common evaporite mineral found in modern sediments and at shallow depths, but modern anhydrite nodules and layers are found in the Trucial Coast sabkha (Butler 1969) Evaporitic tidal-flat environments are a source of sulfate as well as magnesium-rich waters. Poikilotopic and nodular forms have little effect on reservoir properties. Bedded evaporites are commonly found in tidal-flat facies tracts and form reservoir seals and barriers. Pore-filling anhydrite is commonly found in grainstone bodies associated with thick tidal-flat facies and can be mapped according to depositional patterns.

The change from gypsum to anhydrite is controlled by temperature and the activity of water (Fig. 14). Recent anhydrite is found in Persian Gulf
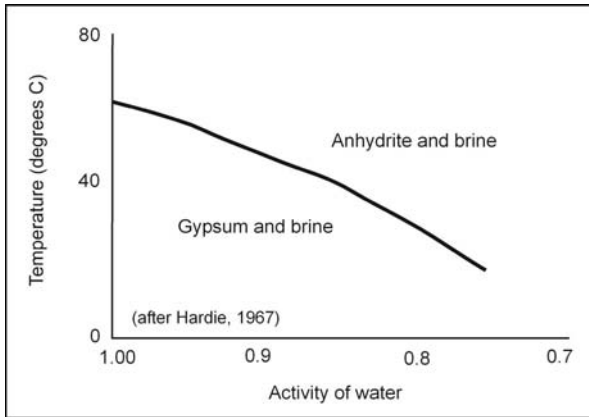
Fig. 7.14. Temperature and activity-of-water relationships of brines coexisting with gypsum and anhydrite. (Hardie 1967)

tidal-flat sediments, where the surface temperatures are very high and the interstitial waters very saline. The increase in temperature with depth results in near-surface gypsum converting to anhydrite. In the Permian Basin of West Texas, gypsum is found down to depths of 4000 ft (Murray 1964; Kasprzyk 1995).

Four types of anhydrite are commonly found in dolomite reservoirs (Fig. 15). Poikilotopic anhydrite is found as large crystals of anhydrite with inclusions of dolomite and is often distributed randomly throughout the rock. Crystals form by a combination of replacement and pore-filling mechanisms, and porosity is reduced in proportion to the amount of pore-filling. Poikilotopic anhydrite is typically scattered and unevenly distributed. Therefore, between the crystals the matrix maintains its original pore-size distribution. Permeability and capillary properties are related more to pore size than to porosity and are only slightly modified by the formation of poikilotopic anhydrite.

Nodular anhydrite is found in dolostone in the form of microcrystalline masses of anhydrite, and it commonly forms within the sediment by displacement as either anhydrite or gypsum. Therefore, it is a diagenetic texture and should not be used to interpret characteristics of the depositional environment. The nodules commonly make up a small percentage of the bulk volume and have little effect on porosity or permeability.

Pore-filling anhydrite is typically pervasive and reduces both porosity and pore-size distribution of carbonate reservoir rocks because it occludes intergrain, intercrystal, and vuggy pore space.

Bedded anhydrite is found in laterally continuous beds a few inches to hundreds of feet thick, and is deposited out of a hypersaline body of water
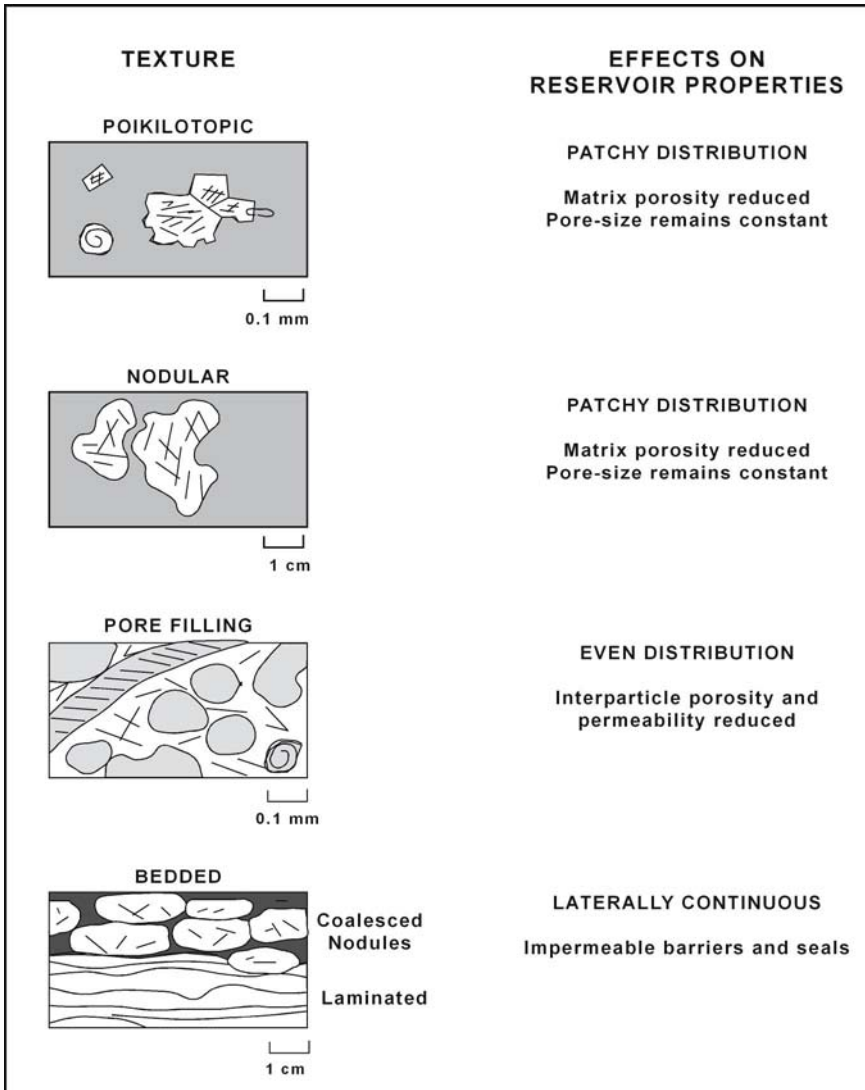
Fig. 7.15. Diagram showing basic anhydrite and gypsum textures found in carbonate rocks and their effect on reservoir properties

as gypsum and later converted to anhydrite. It can be either laminated or composed of coalesced nodules. Laminated anhydrite is interpreted to be a sediment of gypsum crystals that precipitated out of hypersaline water (Lucia 1968). Beds of coalesced nodules are interpreted to have formed as large gypsum crystals growing on the bottom of a hypersaline lake or la-

goon (Schreiber et al. 1976). Bedded anhydrite commonly acts as an excellent reservoir barrier or seal.

Halite is also found as a pore-filling evaporite mineral in carbonate reservoirs associated with bedded halite. Halite is very soluble and is easily dissolved out of subsurface samples during sample preparation. It is isotropic and clear under petrographic examination, making it difficult to identify in thin section. Impregnating the sample with blue plastic is very helpful in distinguishing halite from pore space.

Anhydrite has long been thought to occlude pore space in dolostones, producing a tight, nonproductive carbonate. Although this is true of bedded anhydrite and pore-filling anhydrite, our study of Permian dolostone reservoirs of West Texas demonstrates that it is not true for poikilotopic anhydrite (Lucia et al. 2004). Poikilotopic anhydrite is the most common form of anhydrite in Permian dolostone reservoirs of West Texas. It occurs in patches, commonly with dolomite inclusions, several millimeters to centimeters across, and it both fills interparticle porosity and replaces the host carbonate. Cross plots of interparticle-porosity and permeability measurements from medium crystalline mud-dominated dolostones and grain-dominated dolopackstones that have considerable amounts of poikilotopic anhydrite tend to plot in the petrophysical class 1 field rather than in the class 2 field as predicted by Lucia (1995) (Fig. 16). Also, capillary pressure data from these samples show anomalously large pore throats for a class 2 fabric.

These observations suggest that poikilotopic anhydrite reduces porosity but does not reduce pore-throat size. Permeability is fundamentally controlled by pore-throat size and remains near constant, whereas the pore-filling aspect of patchy anhydrite reduces porosity. This effect causes the data points to shift to the left, from the class 2 to the class 1 field. This effect has been verified by initial results from detailed flow simulations that compare the permeability of a dolostone with and without patches of anhydrite. Therefore, we suggest that poikilotopic anhydrite, and also anhydrite nodules, do not form dense, nonproductive dolomite but actually enhance petrophysical properties.

7.3.1 Calcitization of Anhydrite/Gypsum

Anhydrite or gypsum may be replaced by calcite and occasionally by native sulfur and authigenic silica (Lucia 1972). Outcrops of Permian-age ramp and shelf strata in the Guadalupe Mountains, Texas and New Mexico, contain calcite pseudomorphs of nodular, and poikilotopic anhydrite suggesting that anhydrite commonly found in subsurface equivalents has
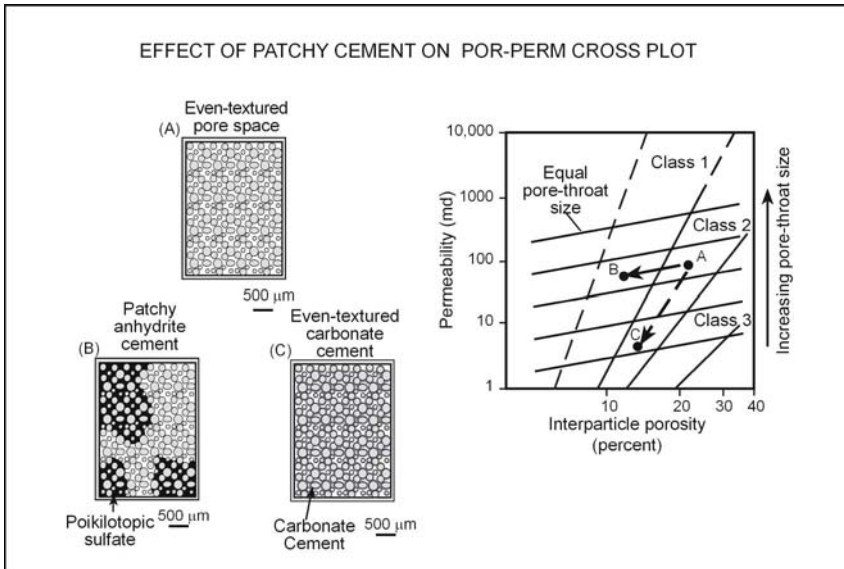
Fig. 7.16. Cartoon showing the effect of patchy anhydrite on porosity-permeability relationships. The evenly distributed addition of cement (C) reduces pore-throat size, porosity, and permeability within the petrophysical class fields (A to C). The addition of patchy cement (anhydrite in this case) reduces porosity but does not materially alter pore-throat size and reduces permeability slightly moving the fabric from class 2 to class 1 (A to B)

been replaced by calcite during uplift in the presence of shallow meteoric waters (Lucia 1961; Scholle et al. 1992). Unusually light carbonate iso-topic values found in some calcites suggest replacement by organic carbon, probably associated with hydrocarbons. Native sulfur is occasionally found, associated with calcite replacement of anhydrite nodules in the sub-surface equivalents, suggesting the presence of sulfate-reducing bacteria.

7.4 Field Examples – Dolostone/Limestone Reservoirs

Approaches to predicting the distribution of petrophysical properties in dolos-tones reservoirs vary, depending upon the association of dolostones with limestone. Where dolostones are interbedded with limestone, predicting the distribution of dolostones is a paramount issue. Where the reservoir is all dolostone, predicting the distribution of petrophysical classes within the dolostone is the key issue. We will discuss three dolostone/limestone reser-voirs, focusing on predicting dolostone distribution, and three dolostone res-ervoirs, focusing on predicting and modeling petrophysical class distribution.

The importance of realistic reservoir models for flow simulation and performance prediction will be emphasized in the studies of dolostones reservoirs.

7.4.1 Red River Reservoirs, Montana and North Dakota

The Red River reservoirs are examples of dolostone reservoirs with geometries linked to tidal-flat facies. They are upper Ordovician in age and are located in subtidal and supratidal sediments deposited on a very broad shallow carbonate shelf (Clement 1985). The dolostones show a good conformance to supratidal and peritidal facies and are widespread. However, there is little conformance between dolostones in subtidal facies. Instead, porous subtidal dolostones change laterally to dense limestone with no regard to facies patterns.

   There are three tidal-flat capped cycles in the Red River formation (Fig. 17). The supratidal facies in the lower cycle (C Zone) is a thick anhydritic
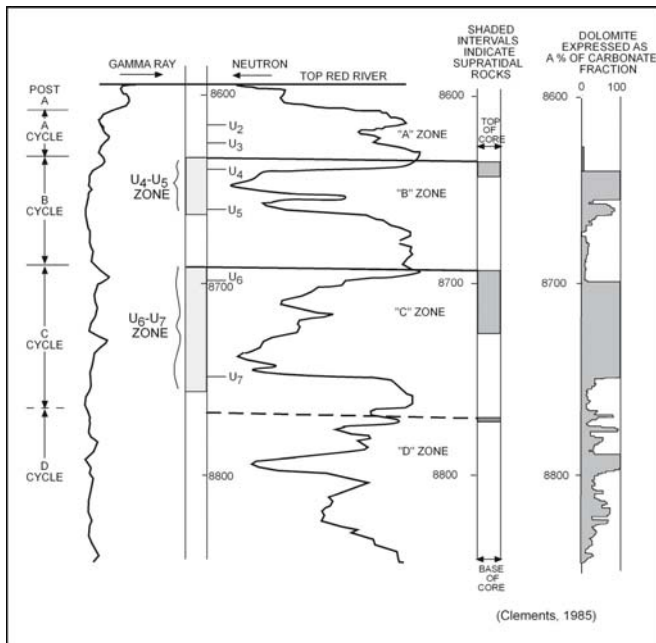
Fig. 7.17. Gamma-ray/neutron log showing depositional cycles and the principal upper Red River production zones related to dolomite and supratidal rocks. Limestone is dense and dolomite porous, and the dolomite conforms to the supratidal rocks and the underlying subtidal. (Clements 1985)

dolostone with beds of bedded and nodular anhydrite and is normally fine crystalline with low permeability. Dolomite extends varying distances beneath this facies into the subtidal facies, probably depending on the flux of hypersaline water formed by evaporation of sea water in the supratidal environment (Fig. 18). The subtidal dolostone is more coarsely crystalline than
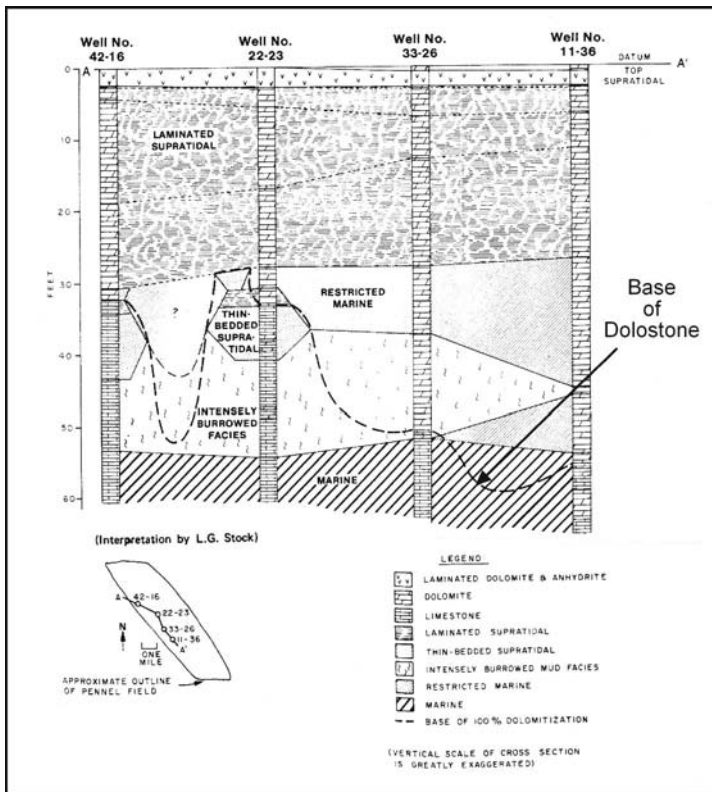
Fig. 7.18. Relationship of lithology to depositional facies U6-U7 zone, Red River Formation. The dolomite-limestone contact does not conform to subtidal facies because it is a function of the flow paths of dolomitization water and not patterns of sedimentation. (Clements 1985)

the supratidal dolostone and is typically porous and permeable. Thus, the thickness of productive dolostone is a function of the thickness of subtidal dolostone. It has been proposed that the geometry of the subtidal dolostone bodies are related to reflux of hypersaline fluids down regional permeable zones related to fracture patterns.

The middle cycle (B Zone) is the main producing horizon on the Cedar Creek Anticline of North Dakota, USA. The supratidal facies is thin and is

capped by bedded and coalesced nodular anhydrite. The supratidal is dolomitized and dolomitization extends varying distances into the underlying subtidal sediments. The cycle is divided into three porous and productive dolomite facies: supratidal, intertidal and subtidal. These facies can be recognized on porosity and resistivity logs because of their different particle and pore-size characteristics. The supratidal and intertidal facies are fine crystalline and have less permeability than the coarser crystalline subtidal dolostones. The supratidal and intertidal facies tend to be laterally continuous, whereas the subtidal dolomite zone is discontinuous.

These reservoirs are an excellent example of a situation where limestone is always dense and dolostones grade from dense to porous. Based on the hypothesis outlined above, the limestone is dense due to compaction, whereas the dolostone has resisted compaction. When dolomitization ceased, presumably soon after shallow burial, the subtidal dolostones had porosities similar to the adjacent limestones. During more than 500 m.y. of burial history the limestones lost their porosity to compaction, whereas the dolostones were more resistant to compaction and retained a measure of their porosity.

The vertical change from dense to porous is an example of overdolomitization related to the thickness of the peritidal facies. The thick peritidal sediments of zone C have little porosity and, based on the overdolomitization hypothesis, were somewhat overdolomitized during dolomitization because of the potential for a large volume of dolomitizing water circulating through these sediments. In contrast, the thin peritidal sediments of zone B are porous and permeable, which suggests a much smaller volume of dolomitizing fluid and less overdolomitization. Therefore, the porosity of the dolostones can be related to the thickness of the peritidal intervals.

7.4.2 Andrews South Devonian Field, West Texas

In some dolostone reservoirs dolomitization has selected the mud-dominated facies, and dolostone distribution can be predicted by a knowledge of mud-dominated depositional environments. The Andrews South Devonian field is an example where dolomitization has selected mud-dominated facies and dolostones can be predicted by knowledge of mud-dominated depositional environments.

Andrews South Devonian field is located in Andrews County, West Texas (Lucia 1962). It produces from carbonates deposited near the shelf margin during Devonian times. The sequence is upward-shoaling from mud-dominated to grain-dominated and is overlain by a regional unconformity. The productive facies are porous limestones and dolostones. The sequence is divided into a lower peloid grain-dominated packstone unit and an upper cri-

noidal grainstone unit. The units were calibrated with the gamma-ray log. The lower unit was deposited in a low-energy environment and has an irregular pattern of porosity related to the amount of mud in the sediment.

The upper unit is divided into three facies. The grainstone facies is dominated by crinoid fragments and cemented tight with syntaxial calcite cement. The grain-dominated packstone facies is a grain-supported sediment with some intergrain lime mud and is porous and permeable due to dissolution of the intergrain lime mud. The dolomite facies is a large crystalline dolowackestone and is the most permeable facies in the reservoir. The facies are calibrated with porosity (Fig. 19). The dolomitizing water was probably
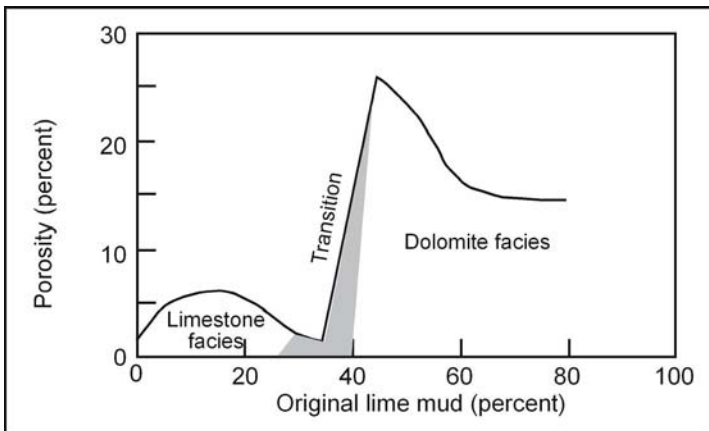
Fig. 7.19. Generalized relationship among percent of lime mud, porosity, limestone, and dolomite. In the Andrews South Devonian field, West Texas, porosity logs can be used to map rock-fabric facies. (Lucia 1962)

formed in an overlying supratidal environment and flowed down into these sediments. The crinoidal grainstones were cemented by that time and impermeable. The wackestones were still porous and permeable because they were not buried very deep. Therefore, the dolomitizing water preferentially flowed through the wackestones, converting them to dolomite.

The fabric-selective nature of the dolomitizing process allows depositional models to be used directly to map reservoir characteristics and predict other occurrences (Fig. 20). Rapid lateral changes from low or nonproductive limestones to highly productive dolostones can be expected. This same pattern of selective dolomitization in a crinoidal sediment has been described from the outcrop and subsurface Turner Valley (Mississippian) formation in Alberta, Canada (Fig. 21; Murray and Lucia 1967;Lucia and Murray 1966). In the outcrop dolostones layers can be seen to change vertically and laterally from dolowackestone to dolomitic crinoidal grain-dominated packstones to
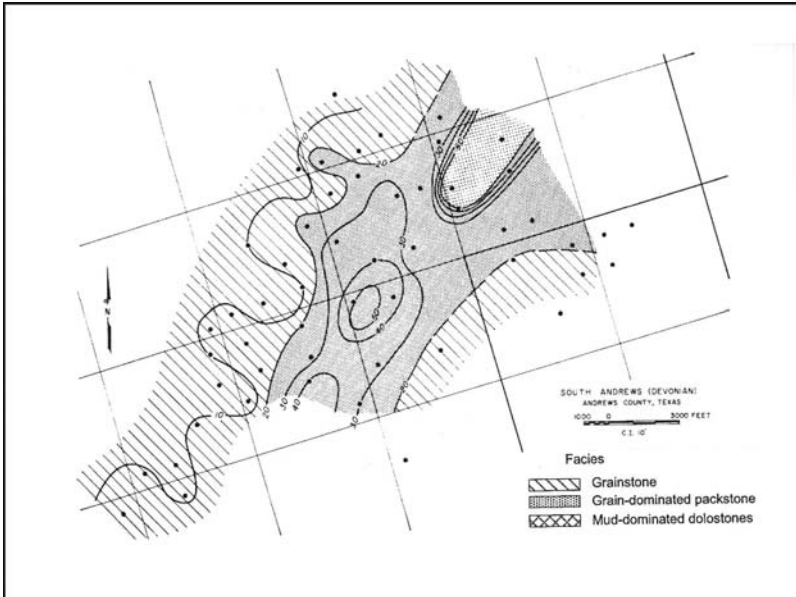
Fig. 7.20. Net pay isopach map of the Andrews South Devonian field showing highest net pay in the dolomitized mud-dominated facies, some net pay in the limestone grain-dominated packstone (inner bar) facies, and little net pay in the grainstone (bar) facies. (Lucia and Murray 1966)
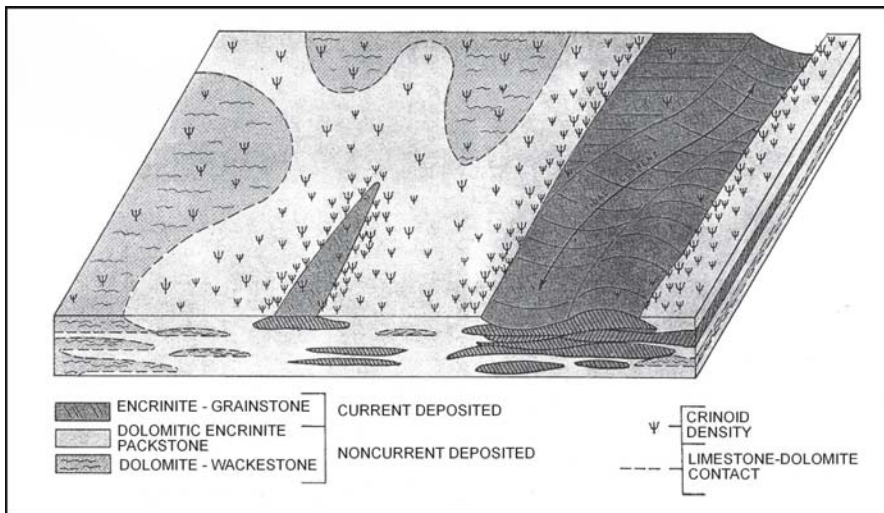
Fig. 7.21. Reconstructed depositional environment from the Turner Valley Formation as exposed at Moose Mountain, Alberta, Canada, showing facies control of medium crystalline dolowackestone (Murray and Lucia, 1967)

crinoidal grainstones. The resulting dolostone pattern is closely linked to depositional environments.

7.4.3 Haradh Section of Ghawar Field

The dolostone in the Ghawar field, Jurassic of Saudi Arabia, is an example where most of the dolostone cannot be linked to evaporitic tidal-flat facies and where predicting dolostone distribution is difficult. A thin bed of fine crystalline dolostone found directly under the overlying anhydrite formation is the only dolostone that can be directly linked to evaporite deposition and was probably formed from refluxing hypersaline water early in the diagenetic history. Most of the dolostone bodies, however, are large crystalline dolostones that are not directly linked to tidal-flat facies or to a specific depositional fabric. They appear to have formed later in the diagenetic history. Geochemical studies (Swart et al. 2005) suggest that the dolomitizing water was modified sea water, but the source and flow path of the fluid cannot be established. This makes predicting the distribution of dolostones difficult. Based on a map of the dolomite thickness in the Ghawar field, Cantrell et al. (2004) suggested that the dolomitizing fluid originated from the overlying anhydrite beds and flowed vertically down along fractures and laterally into permeability beds. This is arguably the best hydrologic model available, but the scale of the dolomite bodies is unknown.

Vertical succession of depositional textures

The Ghawar field can be divided into an upper unit characterized by grainstones and grain-dominated packstones and a lower unit characterized by mud-dominated fabrics (Fig. 22). Vertical successions of depositional facies from core descriptions suggest that the successions can be used to correlate high-frequency cycles and define chronostratigraphic surfaces for the construction of a sequence stratigraphic framework. However, this is possible only in limestone intervals. Replacement of limestone by dolomite complicates the analysis of vertical facies successions because the large dolomite crystals typical of the dolostone mask the depositional texture of the precursor limestone.

Rock Fabric Description and Petrophysical Properties

This reservoir contains all the basic limestone rock fabrics as well as fine-crystalline and large crystalline dolostones (Lucia et al. 2001). The grainstones contain well-sorted, coated grains (200–400 μm), isopachous calcite

cement on multicrystalline grains, and syntaxial-overgrowth cement on single-crystal echinoderm fragments. The grain-dominated packstones show a wide variety of fabrics. In the more even-textured samples, inter-
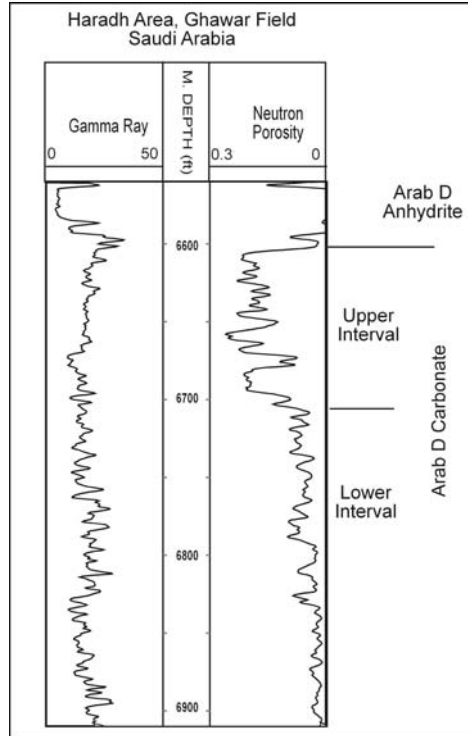
Fig. 7.22. Type log of Ghawar reservoir in the Haradh area

grain lime mud ranges from a few % to 40 to 50% of the bulk volume. Mud-dominated fabrics are (1) mud-dominated packstones having grains as a supporting fabric but the intergrain space filled with micrite, wackestone having micrite clearly as the supporting fabric, and mudstone having few observable grains. With the exception of the thin fine crystalline dolostone found at the contact with the overlying anhydrite, dolostone samples are characterized by dolomite crystals ranging from 100 to 500 µm in size.

Most of the large crystalline dolostones are permeable and plot in the class 1 field (Fig. 23). The grainstones also plot in the class 1 field. Grain-dominated packstones cluster in the class 2 field and mud-dominated fabrics in the class 3 field.

Calibration of wireline logs

Gamma-ray and porosity logs have been used in other studies to identify depositional facies. However, this is not a robust method in this field. A Zee plot of initial water saturation, porosity, and rock fabric (Fig. 24) tends to group rock fabrics into fields similar to the petrophysical class fields (Lucia et al. 2001; Jennings and Lucia 2003). Class 1 large crystalline dolostones and grainstones form a field characterized by low water saturation, and the coarser dolostones tend to have the lowest water saturations. The lower limit of this field is assigned a rock-fabric number of 0.5 and the upper-limit a rock-fabric number of 1.5 to conform to the rock-fabric values assigned to the global transform. Class 2 grain-dominated packstones comprise most of the data points that form a prominent high-porosity trend on the cross plot. This trend characterizes the limestones in the upper interval. The upper boundary of this trend is assigned a rock-fabric number of 2.5. Class 3 mud-dominated fabrics form a trend above the class 2 fabrics. This trend characterizes the limestone of the lower interval. The upper limit of mud-dominated fabrics is spaced above the class 3 group and labeled rock-fabric number 4.

A relationship between rock-fabric petrophysical class, water saturation, and porosity was developed by multilinear regression and using the equations for the class boundaries. In this study, porosity and interparticle porosity are similar because of the small volume of vuggy pore space. Therefore, total porosity was used in this equation. The relationship is

$$\log (\text{rfn}) = (A + B\log (\phi) + \log(Sw))/(C + D\log(\phi)),$$

where
  rfn = rock-fabric number ranging from 0.5 to 4,
  A = 3.1107,
  B = 1.8834,
  C = 3.0634, and
  D = 1.4045.

A comparison between calculated rock-fabric number and observed petrophysical class for the two calibration wells is illustrated in Figure 25. In general, the upper interval is dominated by class 1 and 2, grain-dominated fabrics and large crystalline dolostone, whereas the lower interval contains more class 3 mud-dominated fabrics. The calculated rock-fabric numbers form a continuum, whereas the petrophysical-class values obtained from core description are constrained to three numbers. However,
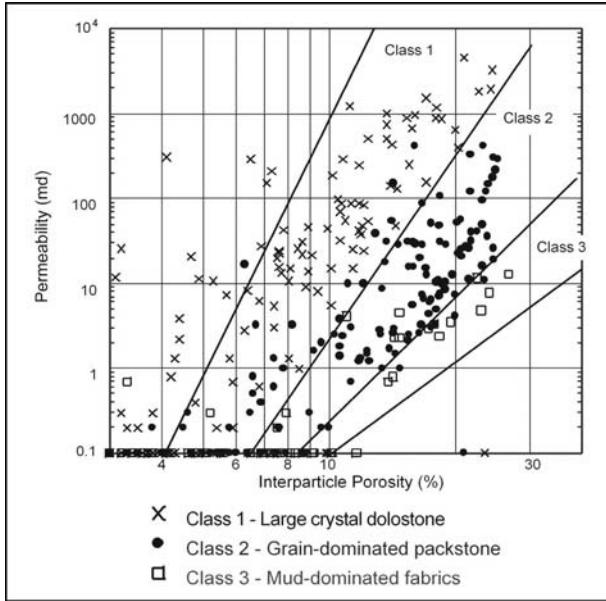
Fig. 7.23. Porosity-permeability cross plot for the Haradh sector of the Ghawar field showing rock fabrics and petrophysical classes. Most of the class 3 mud-dominated fabrics have <0.1 md permeability
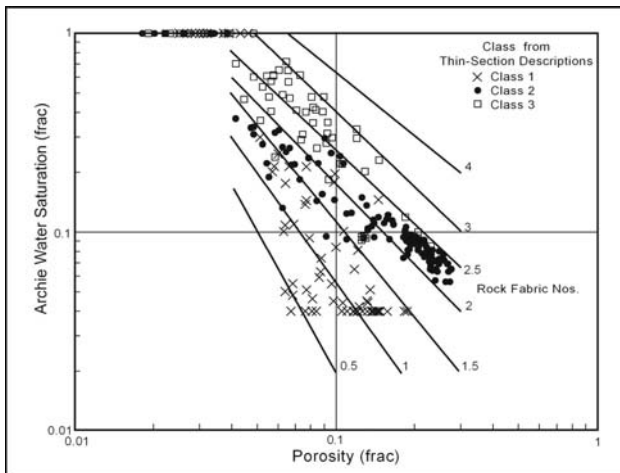
Fig. 7.24. Cross plot of porosity and water saturation for Haradh (Lucia 1995). The class 1 field is dominated by large crystalline dolostone. Grain-dominated packstones form the basis for the class 2 field. Data that overlap into the class 1 field may be responding to large-grain fabrics. Low porosity mud-dominated fabrics define the class 3 field. The class 4 boundary was spaced above the class 3 samples

the calculated rfn's plot generally within the range of the three classes from thin-section descriptions.

The rfn's can be equated to the basic rock-fabric facies within the limestone successions but not in the dolostone because the precursor depositional fabric is not known. Figure 25 shows that most of the limestones
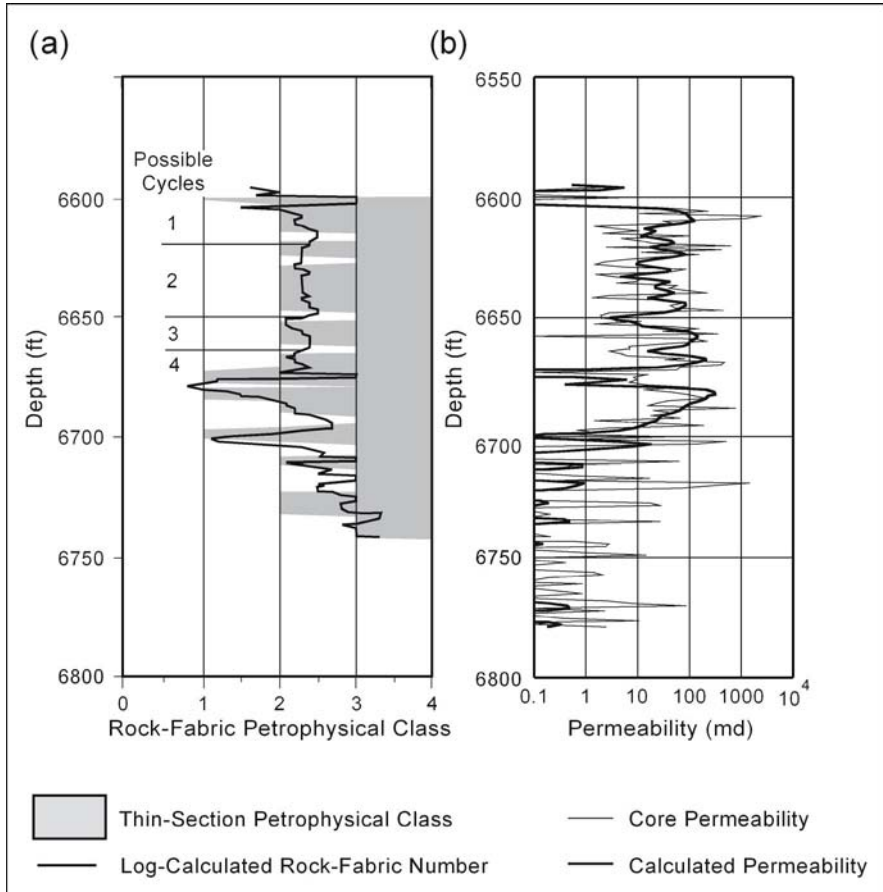
Fig. 7.25. Comparison of **(a)** rock-fabric number calculated using the saturation equation and **(b)** permeability calculated using the global transform with core petrophysical class and permeability. In the upper interval the permeability comparison is good, although there is much more small-scale variability in the core data than in the log data. In the lower interval, thin beds of high permeability are too thin to be captured in the log data. Four possible upward-coarsening high-frequency cycles are defined based on decreasing rock-fabric number

in the upper unit are class 2 grain-dominated packstones with a few thin beds of wackestones. Wackestones mark the base of four possible high-frequency cycles. Most of the limestones in the lower unit are class 3 mud-dominated fabrics with thin beds of large grain grain-dominated packstone. High-frequency cycles in the lower unit are more difficult to define.

Calculation of vertical profiles of petrophysical properties

Permeability was calculated from wireline logs by substituting rock-fabric number and interparticle porosity into the global permeability transform. Total porosity is used because of the small volume of separate-vug poros-ity in the Haradh area. Permeability estimates calculated by using this method compare well with core-plug permeability in the upper interval (Fig. 25). Core-plug values show more variability than calculated values because wireline logs average out small-scale variability. Scattered, high, core-plug permeability values are present in the lower interval, and they are not matched by log calculations. The high permeability is from large-grain, grain-dominated packstones, which are found in thin beds within an overall mud-dominated interval, and the resistivity logs do not resolve these beds. The porosity values are reasonable, but the petrophysical class tends to be overstated, resulting in permeability values that are much too low.

Reservoir Model construction

The four cycles can be correlated between wells with little dolostone. Cor-relating the dolostones between represents a more difficult problem. Whereas the tops of high-frequency cycles are chronostratigraphic sur-faces, there is no time associated with the dolostones. The dolostone pat-terns illustrated in Figure 26 are purely schematic and are not based on any hydrological process model. It has been suggested that the dolostones are selectively replacing a specific texture, but there is no convincing petro-graphic evidence for that assertion. Petrographic and geochemical studies (Swart et al. 2005) suggest that these dolostones are not directly linked to peritidal facies, although the source of the dolomitizing water may be from the overly anhydrite unit. If so, the water passed through or around a thick section of limestone before dolomitizing. Without knowledge of the source and the fluid-flow pattern, the geometry of the dolostones cannot be pre-dicted in any meaningful way.
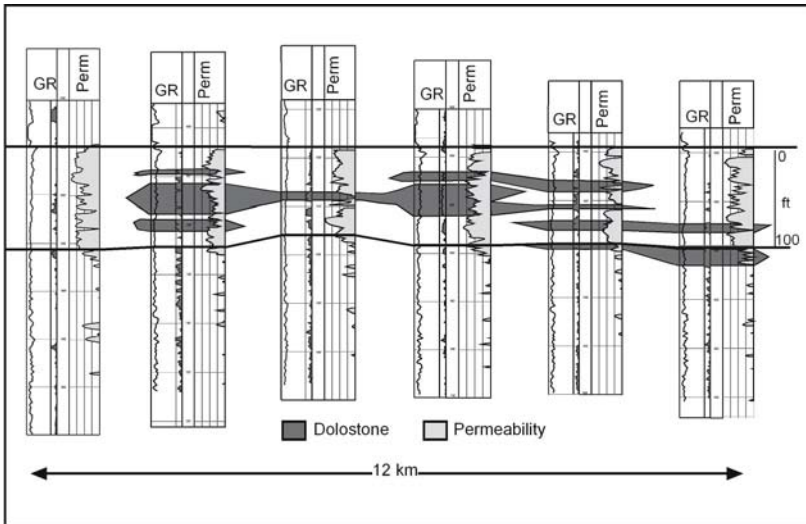
Fig. 7.26. Dolomite distribution illustrated in a cross section of four wells. Correlations are arbitrary because the hydrology of the dolomitization process is poorly understood

7.5 Field Examples - Dolostone Reservoirs

The rock-fabric method of model construction consists of (1) describing the vertical succession of depositional textures, (2) describing vertical successions of rock fabric and relating petrophysical properties to rock fabrics, (3) calibrating depositional facies and rock fabrics to wireline logs, (4) calculating vertical profiles of porosity, permeability, and initial water saturation (Sw_i), (5) constructing a high-frequency-cycle framework from core descriptions and wireline log correlations, (6) constructing rock-fabric flow layers, and (7) distributing petrophysical properties within the rock-fabric layers using various geostatistical methods. The reservoir model is upscaled for input into a flow simulator to predict reservoir performance.

We will describe how this method has been used to construct reservoir models in three dolostones reservoirs from West Texas, USA. There are many similarities between these three reservoirs in that they are all of Permian age from the Permian Basin in West Texas and are all located in a middle-ramp location. However, the relationship between depositional facies and petrophysical class and the determination of how petrophysical class and depositional facies are defined from wireline logs differ in all three examples. In the Seminole field example, three transforms are needed

to calculate permeability and Sw$_i$ from porosity and the gamma-ray log, porosity log, and Sw$_i$ /porosity relationship are used to identify depositional facies and flow layers. In the South Wasson Clear Fork field example, only one transform is needed and porosity logs are used as a surrogate for depositional facies. In the Fullerton Clear Fork field example, three transforms are needed, petrophysical class is linked to stratigraphy, and porosity logs are the principal link to depositional facies and flow layers.

7.5.1 Seminole San Andres Unit, Gaines County, Texas

The Seminole San Andres study is an example of the use of multiple transforms to calculate rock-fabric facies, permeability and Sw$_i$ from porosity logs. The Seminole reservoir is located within the Permian Basin on the northern Central Basin Platform (Fig. 27). The reservoir produces from the
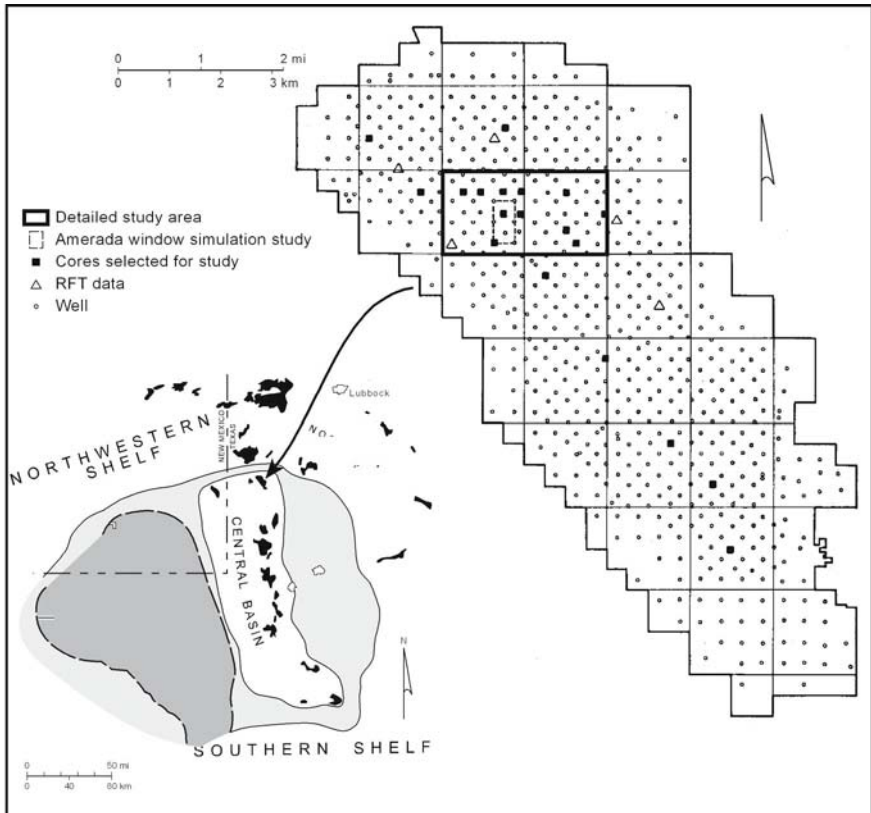
Fig. 7.27. Location of the Seminole San Andres Unit

San Andres Formation of Guadalupian age. The field covers approximately 23 square miles and contains over 600 wells. Discovered in 1936, the reservoir is a solution-gas drive type with a small initial gas cap. Original oil in place is estimated to be 1100 MSTB (Galloway et al. 1983). Waterflooding was initiated in 1970 using alternating rows of 160-acre inverted nine-spot patterns. Infill drilling occurred in 1976, converting the pattern to a mixed 80- and 160-acre inverted nine spot. A second infill program took place in 1984-1985, converting the pattern to an 80-acre inverted nine spot. CO_2 flooding began in 1985.

Vertical Succession of Depositional Textures

Descriptions of the vertical succession of depositional textures for constructing the sequence stratigraphic framework are based on descriptions of core slabs. The most common depositional cycle in the reservoir is the subtidal, upward-coarsening cycle composed of a lower mud-dominated unit overlain by a grain-dominated unit. Most subtidal cycles are capped by a mud- or grain-dominated packstone, but a few cycles have grainstone caps. A few cycles found toward the top of the reservoir are capped by thin tidal-flat units.

The vertical facies successions from 11 cores were described in detail and form the basis for constructing a chronostratigraphic sequence stratigraphic framework for the Seminole field. Through an interactive process of core description and correlation, 12 high-frequency cycles (HFC) were confidently identified in cores and correlated with wireline logs (Fig. 28, Kerans et al. 1993). Two high-frequency sequences are suggested by the vertical facies succession and lateral continuity of facies. The lower three HFC's (cycles 10, 11, and 12) are part of the outer-ramp facies tract, and are fusulinid-rich 40- to 50-ft-thick units containing low-porosity fusulinid-peloid mud-dominated dolostones coarsening upward into more porous crinoid-fusulinid-peloid grain-dominated dolopackstones (Fig. 28) and appear to comprise a transgressive facies tract. The upper nine HFC (cycles 1-9) contain fewer fusulinids and record progradation of ramp-crest and inner ramp facies. HFCs are typical upward-shallowing cycles with basal mudstones and wackestones grading upward into grain-dominated packstones and grainstones (Fig. 28). Cycles 9-5 appear to be progradational facies with a sequence boundary at the top of cycle 5 marked by the occurrence of tidal-flat facies. Cycle 4 marks a deepening event because it contains abundant fusulinids, a well-established key indicator of water depth. Cycle 1 is capped by a thick interval of grain-dominated sediment, which is in turn overlain by the upper 300 ft of peritidal deposits. This major facies offset probably marks a second sequence boundary.
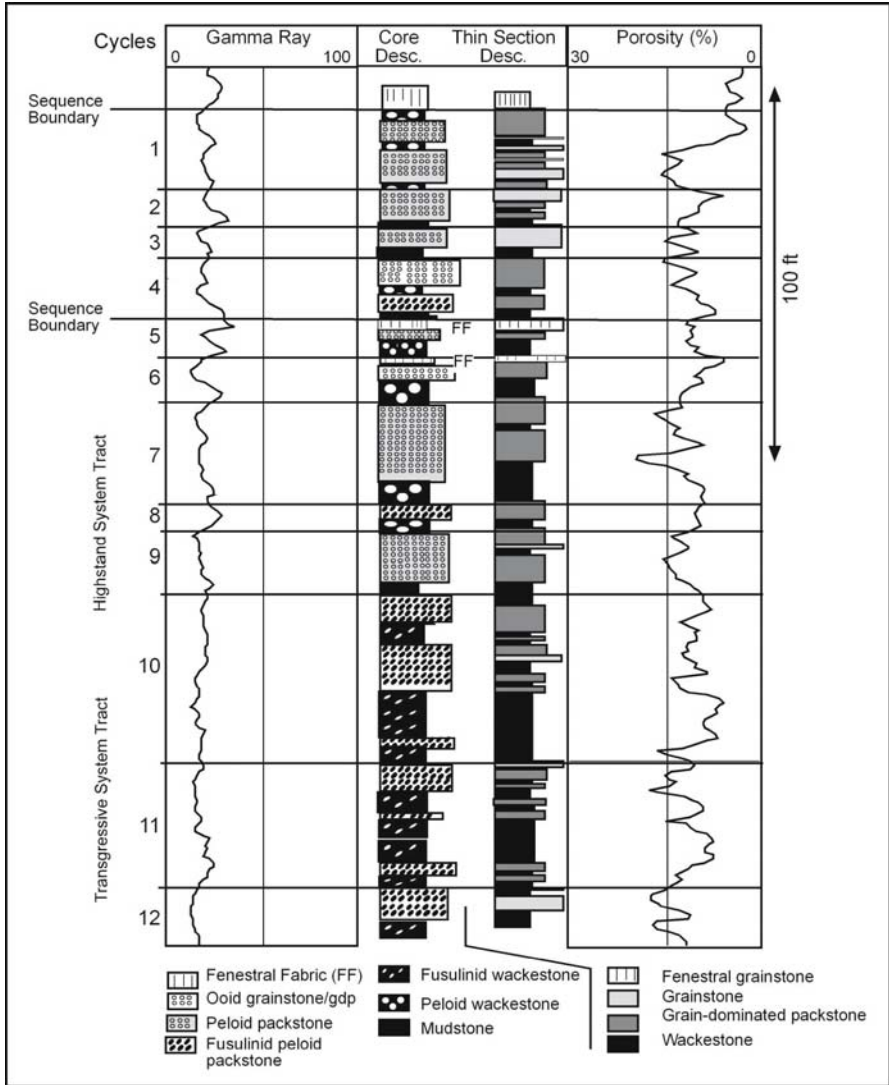
Fig. 7.28. Vertical facies succession, sequences, and cycles at Seminole

Rock-Fabric Descriptions and Petrophysical Properties

Descriptions of the vertical succession of rock fabrics for petrophysical quantification and depositional textures for sequence stratigraphic analysis are closely linked and are best done in concert. However, rock-fabric descriptions differ from descriptions of depositional textures in that they in-

clude effects of diagenesis and are focused on present-day fabrics rather than depositional textures. It is common to use core slab descriptions for sequence stratigraphic analysis, but thin sections are commonly needed to make the fine distinctions among (1) grainstone, grain-dominated packstone, and mud-dominated fabrics, (2) inter- and intraparticle pore space, and (3) fine, medium, and large dolomite crystal sizes. This difference in scale of observation commonly results in some differences in fabric descriptions, which must be resolved as part of the process of integrating geological descriptions and petrophysical data (Fig. 28).

The Seminole San Andres reservoir produces from anhydritic dolostone and contains five principal rock fabrics: (1) dolograinstone (class 1), (2) fine to medium crystalline dolomitized grain-dominated packstone (class 2), (3) fine crystalline mud-dominated dolostone (class 3), (4) medium crystalline mud-dominated dolostone (class 2), and (5) separate-vug (moldic and intrafossil) dolostones (Fig. 29).

Class 1 dolograinstone is the least common fabric in the two-section study area. Although grainstones have the potential for having the highest permeability and lowest initial water saturation, in this reservoir they are often cemented tight with anhydrite. Class 2 grain-dominated dolopackstones are very common in the Seminole reservoir. They are often misidentified as grainstones because they are grain supported and may have very little intergrain mud. Peloids and fusulinids are the most common grain type. Class 2 medium crystalline mud-dominated dolostones are very common in the lower portions of the reservoir. The medium dolomite crystal size elevates mud-dominated fabrics from class 3 to petrophysical class 2 because the intercrystal pore size is larger than interparticle pore size in micrite. Class 3 fine crystalline mud-dominated-packstones, wackestones, and mudstones are common in the upper portions of the reservoir. Common grain types are peloids, mollusk fragments, and fusulinids. These fabrics have the lowest flow potential and the highest initial water saturations.

Core analysis data available for this study included whole-core porosity and permeability measurements, and a limited number of capillary pressure curves and relative permeability curves. An error was suspected in the core porosity values, and to check the accuracy of the core analysis, 3 core plugs were drilled from each of 12 whole-core samples. The average porosity of the new samples was 2 porosity units higher than the original values, probably related to improper cleaning of the original whole-core samples (see Chapter 3).

The interparticle porosity, permeability, rock-fabric cross plot using data from the new plugs is in agreement with the generic cross plot (Fig. 30B). The recleaned samples are dolograinstone (class 1), grain-dominated dolopackstone (class 2), and mud-dominated dolostone with 20 to 25 μm
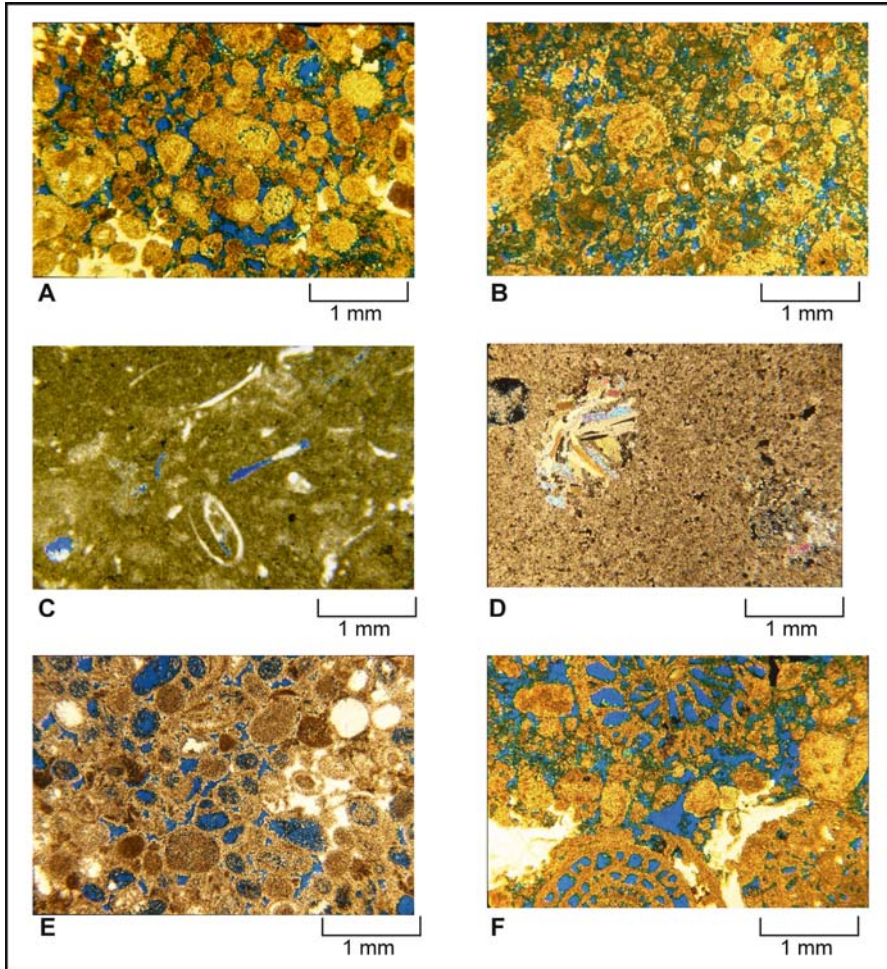
Fig. 7.29. Photomicrographs of thin sections impregnated with blue dye illustrating rock fabrics (*white areas* are anhydrite). **(A)** Dolograinstone with intergrain pore space; **(B)** grain-dominated dolopackstone with intergrain pore space and intergrain dolomitized micrite; **(C)** fine crystalline dolowackestone; **(D)** medium crystalline dolowackestone (cross polarizers); **(E)** separate-vug (moldic) porosity in ooid dolograinstone; and **(F)** separate-vug (intrafusulinid) porosity in grain-dominated dolopackstone

dolomite crystals (class 2.5 because it falls on the line between classes 2 and 3). None of the recleaned samples are class 3. Based on this data it is assumed that the generic cross plot is representative of the relationship between rock fabric, interparticle porosity, and permeability, and the global permeability transform I s assumed to apply. In the original study rock-
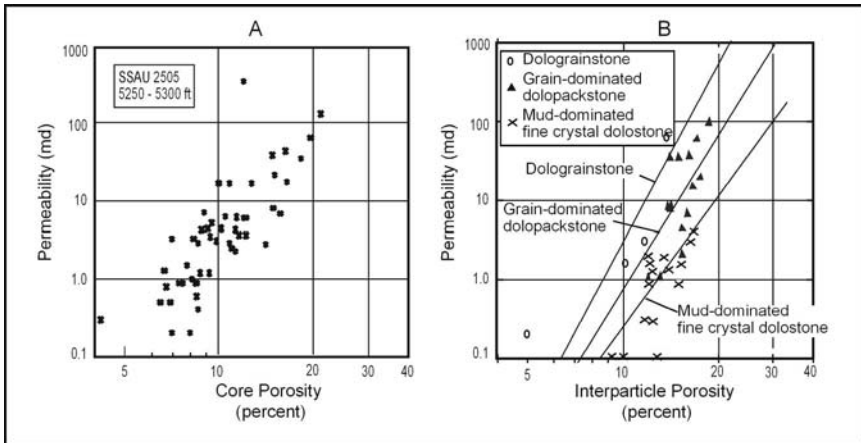
Fig. 7.30. Porosity, permeability, rock-fabric transforms from core plugs, well 2505. **A** Cross plot of porosity versus permeability for grain-dominated dolopack-stone and medium crystalline mud-dominated dolostones in the lower portion of the reservoir. The distribution conforms to petrophysical class 2. **B** Cross plot of interparticle porosity versus permeability using data from recleaned core plugs showing higher permeability for grain-dominated dolopackstones than mud-dominated dolostones. The transforms conform to the generic petrophysical class fields of Lucia (1995)

fabric-specific transforms were developed using core permeability and wireline log porosity, a procedure that is flawed because of the problems of scale and depth matching.

Grain molds and intrafossil pores are the principal separate-vug types and consist of (1) dissolved ooids, mollusk fragments, and fusulinids, and (2) intrafusulinid pores. An interval containing separate-vug porosity in SSAU 2309 well was sampled to investigate the effect of separate vugs on permeability. As is expected from generic relationships, the presence of this pore type reduces permeability over what would be expected if all the porosity were interparticle (Fig. 31).

Dolomite crystal size increases with depth from 10-20 μm to 50-100 μm (Fig. 11). Dolomite crystals in grain-dominated fabrics are larger than in mud-dominated fabrics. Mud-dominated fabrics in the upper portion of the reservoir are characterized by fine crystalline dolostones, and the dolomite fabrics mimic the precursor limestone fabrics. These fabrics are petrophysical class 3. In the lower portion of the reservoir, the dolomite crystal size of mud-dominated dolostone is typically between 20 and 100 μm (class 2), and the petrophysical characteristics of the mud-dominated dolostone no longer mimic the precursor limestone. The increase in parti-
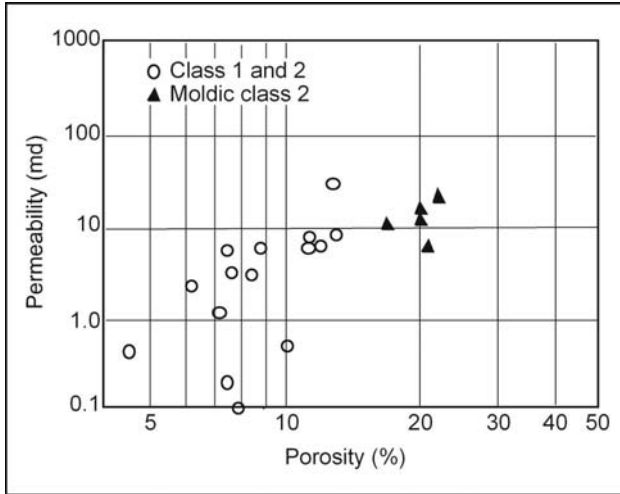
Fig. 7.31. Cross plot of total porosity and permeability showing moldic grain-dominated packstones with lower permeability than expected for class 2 grain-dominated dolopackstones with high porosity

cle size from fine to medium results in an increase in pore size and improvement in the petrophysical properties (Fig. 30A).

Calibration of wireline logs

Wireline logs are the basic information used to build reservoir models. However, the logs must be calibrated with core data to be useful for extracting facies and rock-fabric information. The most useful logs are gamma-ray for correlating, neutron and density for calculating porosity, and acoustic and resistivity logs for estimating interparticle porosity and petrophysical class/rock-fabric number.

The gamma-ray log was useful in this reservoir for correlating high-frequency cycles. Mud-dominated facies tended to have higher gamma-ray values than grain-dominated facies (Fig. 32). Porosity logs were also useful in that the mud-dominated facies tend to have lower porosity values than grain-dominated (see Chapter 3). Mud-dominated sediments compact more than grain-dominated sediments, resulting in cycles characterized by an upward increase in porosity and permeability. A distinction between petrophysical class 3 and combined class 1 and 2 can be made using these calibrations.

In order to distinguish between petrophysical class 1 and 2, a relationship between porosity, initial saturation, petrophysical class, and reservoir height was developed. Using data from cycles 1-9, initial water saturations
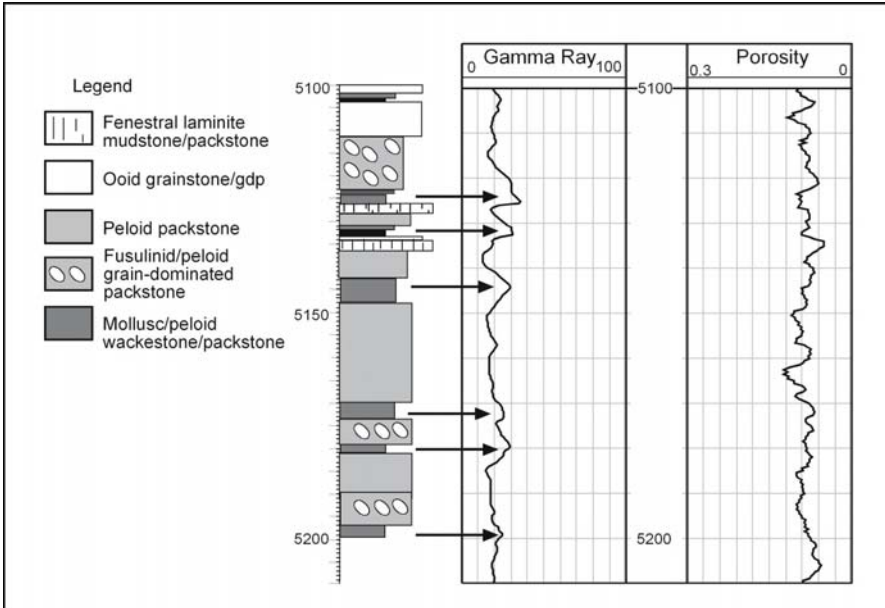
Fig. 7.32. An illustration of using the gamma-ray log to correlate grain- and mud-dominated facies in the Seminole field. There are more facies described in the core description than can be defined by the gamma-ray log

and porosity from log calculations were compared with rock fabrics described from thin sections (Fig. 33). A cross plot of porosity and initial water saturation shows that class 1 fine crystalline mud-dominated dolostones can be separated from class 2 grain-dominated dolopackstones and class 2 medium crystalline mud-dominated dolostones. Too few grainstone fabrics are found in this test sample set, but, if present, should plot below the class 2 field. In the original study equations for each boundary were used to estimate the petrophysical class from Swi/porosity values. Later, however, the Swi-Phi-rfn equation presented in Chapter 3 was developed during a study of the Ghawar field (Lucia et al. 2001) that closely approximates these petrophysical-class fields (Fig. 34).

The limitations of using water saturation to determine petrophysical class are listed below.

1. The method does not work in water-saturated intervals. The Seminole logs used to construct the model are all within the oil column.

2. The height above the zero-capillary-pressure elevation (herein called reservoir height) must be accounted for. Only intervals above the transition zone were used in this study.

3. The method will not work in zones that have been waterflooded. In the Seminole field, wells that were completed water free are considered to have original water saturation values and original water resistivity.
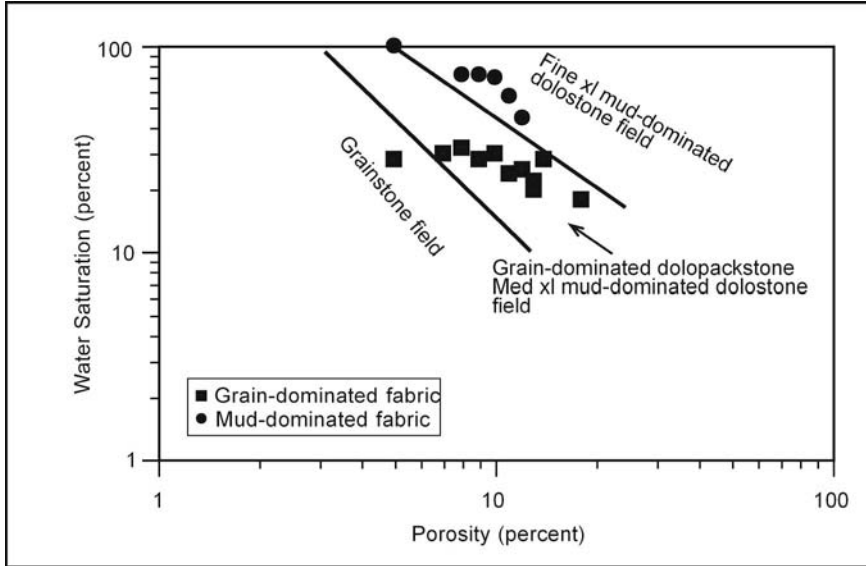
Fig. 7.33. Relationship among water saturation, porosity, and rock-fabric/petrophysical class. The porosity and saturation values have been averaged within rock-fabric units in cycles 1-9

Interparticle porosity was estimated by subtracting separate-vug porosity from total porosity. Lucia and Conti (1987) developed a method for estimating separate-vug porosity in limestones by relating separate-vug porosity measured from thin sections to deviations from the Wyllie Time Average equation. In a similar manner, an empirical equation relating separate-vug porosity to total porosity and Δt has been established for the Seminole field (see equation below; Fig. 35). The equation is similar to Lucia and Conti's, but it is shifted due to the difference in velocity of limestone and anhydritic dolomite.

$$\phi_{sv} = 10^{4.4419 - 0.1526[\Delta t - 145\phi]}$$

With this equation, total porosity can be divided into interparticle porosity and separate-vug porosity by subtracting total porosity from separate-vug porosity.
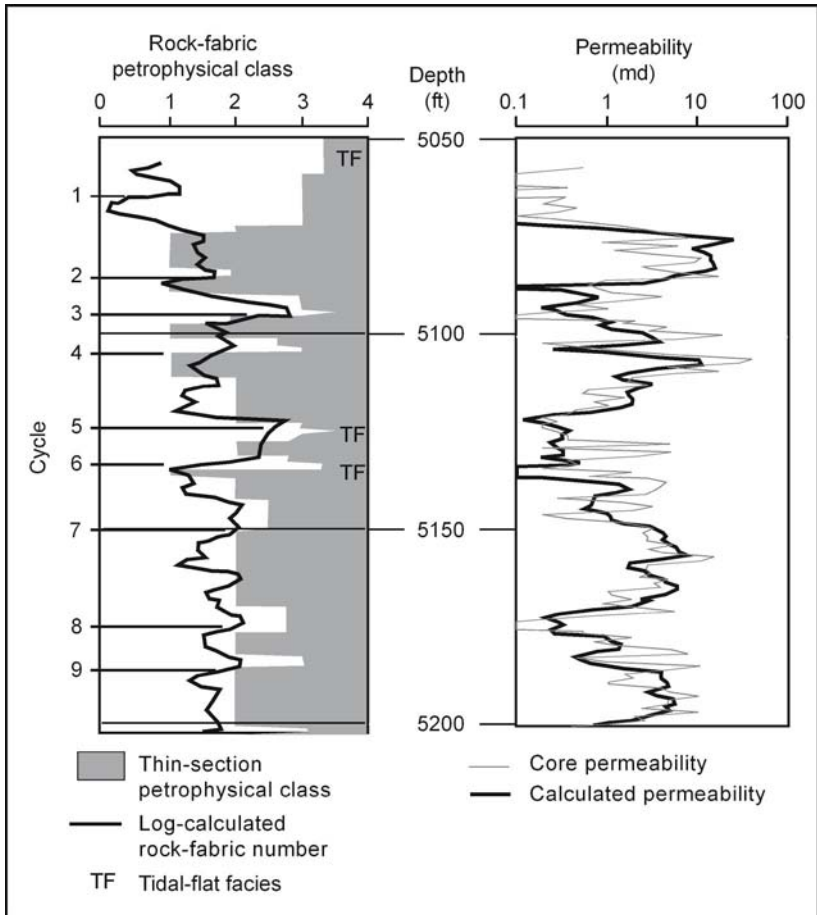
Fig. 7.34. Comparison of rock-fabric number calculated using the saturation equation and permeability calculated using the global transform with core petrophysical class and permeability for Seminole field

Calculating vertical profiles of petrophysical properties

Vertical profiles of porosity were based on neutron, density, and sonic logs. Interparticle porosity was computed using the above equation. In wells completed free of water, Archie water saturations were calculated and permeability was calculated using interparticle porosity and rock-fabric numbers from the Swi-phi algorithm. For wells completed producing water, stratigraphic correlations were used to estimate the petrophysical class values to be used in the global transform and in the generic capil-
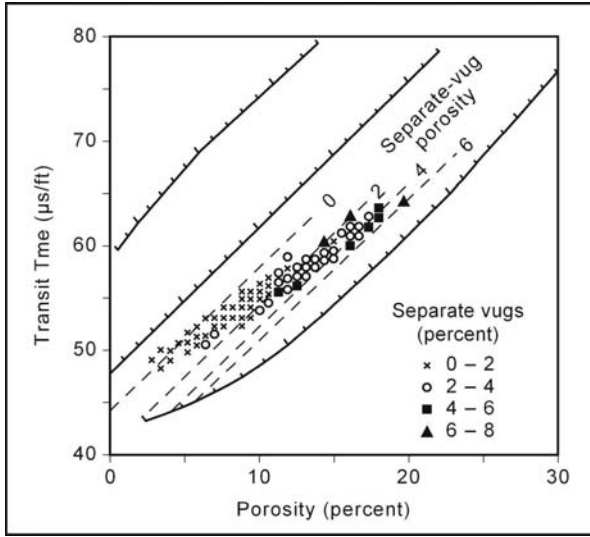
Fig. 7.35. Relationship among transit time, total porosity, and separate-vug porosity in the Seminole field
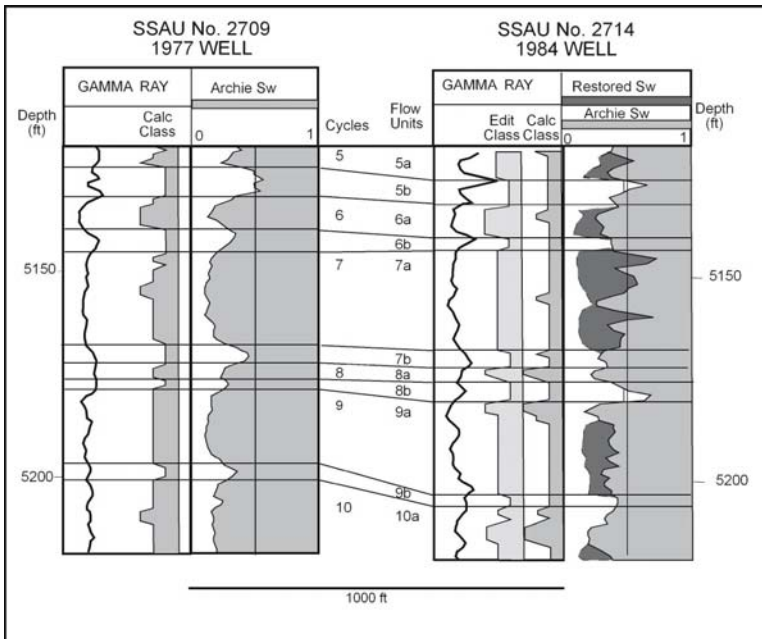
Fig. 7.36. Example of locating flooded intervals using petrophysical class from stratigraphic correlations to calculate initial water saturations from capillary pressure models in the Seminole field

lary pressure models developed in Chapter 3 (Fig. 36). An example of calculated vs. core permeability and thin section descriptions of petrophysical class is shown in Figure 34.

Reservoir Model Construction

There are five steps in the construction of a rock-fabric layered model: (1) construction of the HFC framework, (2) identification of petrophysically significant rock-fabric facies within each well, (3) construction of rock-fabric flow layers, and (4) calculation of average petrophysical properties within rock-fabric facies, and (5) distribution of properties in the interwell environment. The HFC framework is built by correlating the 12 defining surfaces throughout the study area (Fig. 37).
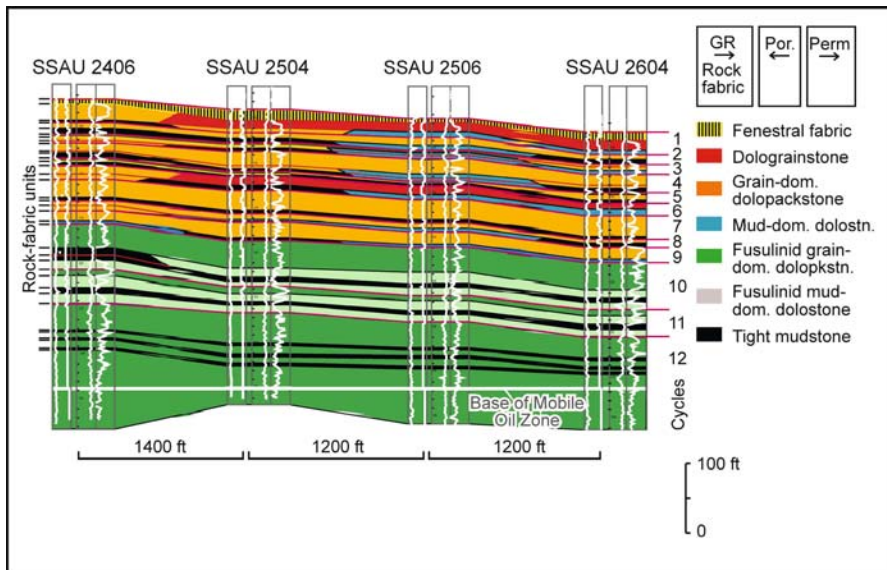
Fig. 7.37. Cross section illustrating the distribution of rock-fabric facies and rock-fabric flow layers within the high-frequency cycle framework for a portion of the Seminole San Andres Unit

Flow units, herein called rock-fabric flow layers, are the basic stratigraphic element in a reservoir model. The term "flow units" has been used in many different ways. As discussed in Chapter 5, flow units, or flow layers, are defined as a rock-fabric facies in which the petrophysical properties are near randomly distributed. Therefore, it is not sufficient to map the tops of high-frequency cycles. To properly distribute petrophysical properties rock-fabric flow layers must also be mapped. In the Seminole field,

mud-dominated and grain-dominated fabrics can be defined using gamma-ray and porosity logs and correlated throughout the study area.

Rock-fabric facies can be defined by the Swi-phi method in dolostone reservoirs only when the mud-dominated fabrics are composed of fine crystalline dolomite. This is found only in the upper half of the reservoir, and rock-fabric numbers conform to depositional textures and can be used to define flow layers. In the lower half of the reservoir, the mud-dominated fabrics are composed of medium crystalline dolomite and fall in the petrophysical class 2 field along with grain-dominated packstone, and the rock-fabric numbers cannot be used to define rock-fabric flow layers.

As shown in Fig. 38, cycle 11 contains 4 rock fabric layers defined by
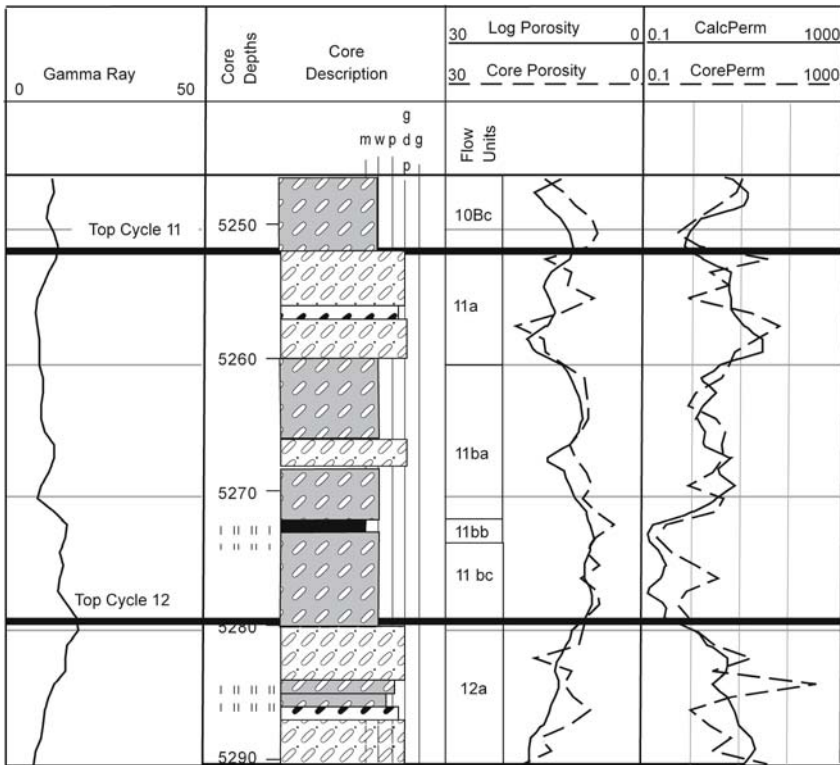
Fig. 7.38. Cycle 11 core description, rock-fabric flow units, core and log-calculated porosity and permeability, and gamma-ray log. Rock-fabric flow unit 11a is distinguished by higher porosity values, and rock-fabric flow unit 11bb is based in a tight mudstone layer from the core description. Permeability calculations are based on a single class 2 porosity-permeability transform

(1) an upper class 2 medium crystalline grain-dominated dolopackstone, (2) a lower class 2 medium crystalline dolowackestone, and (3) a dense dolomudstone. A 2-ft bed of grain-dominated dolopackstone has been averaged into the class 3 flow layer because it is thinner than wireline logs can resolve. Using the class 2 porosity-permeability transform for all four flow layers results in an excellent match between core and calculated permeability values.

Above cycle 10, the dolomite crystal size tends to mimic the precursor limestone texture, and petrophysical rock-fabric classes 1, 2, and 3 conform to depositional textures grainstone, grain-dominated packstone, and mud-dominated fabrics. As shown in Fig. 39, cycles 4, 3, and 2 are upward
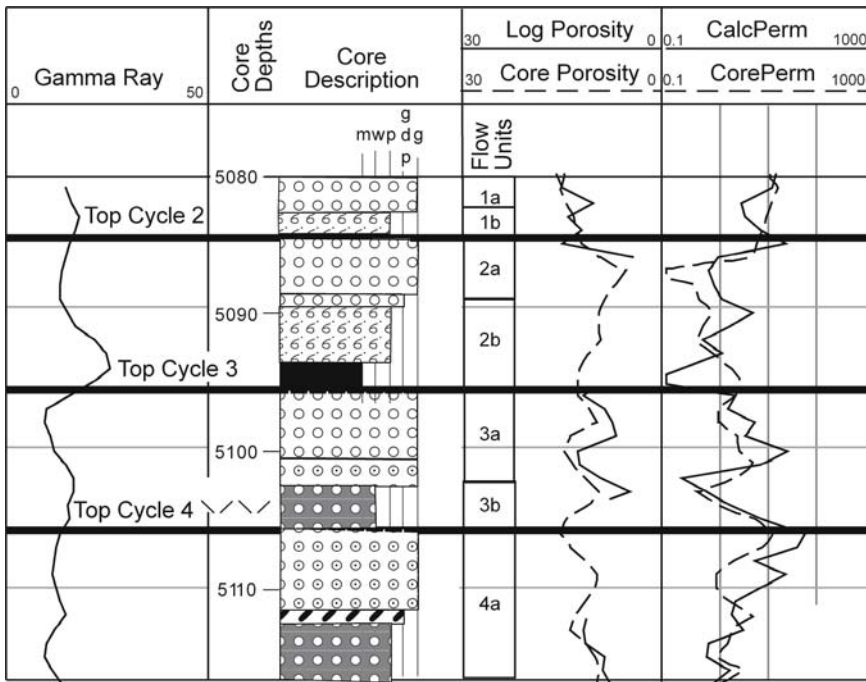
Fig. 7.39. Cycles 2-4 core description, rock-fabric flow units, core and log-calculated porosity and permeability, and gamma-ray log. Rock-fabric flow units are based on petrophysical classes from wireline log calculations and conform well to rock-fabric facies from core descriptions. Permeability is calculated using three rock-fabric porosity-permeability transforms

-shallowing cycles, and each contains two rock-fabric flow units: a lower class 3, fine crystalline mud-dominated unit, and an upper class 2 or 1, grain-dominated dolostone unit. Three rock-fabric-specific porosity-

permeability transforms were used, and the results are in excellent agreement with core permeability. The Swi/petrophysical-class/porosity relationship is used to define the three classes because there is little relationship to porosity and, although the gamma- ray log can be used to pick cycle tops, it cannot distinguish between class 1 and class 2 rock fabrics.

Rock-fabric flow units are defined from wireline log calculations in each well. In cycles 12-10 they are based on porosity differences within each cycle, and in cycles 9-1 they are based on the Swi/petrophysical-class/porosity relationship. Dense thin mud layers are superimposed on these flow units to complete the definition of flow units. The flow units are correlated between wells to form the rock-fabric flow layers. Because most reservoir simulation programs do not allow for discontinuous layers, all flow layer boundaries must be continuous within the model. This can result in one flow layer containing more than one rock-fabric facies, and one rock-fabric facies containing more than one flow layer. This fact is not a problem in this reservoir because the 20-acre well spacing is arguably smaller than facies heterogeneity.

The resulting reservoir model consists of 41 rock-fabric layers (Fig. 37). Rock-fabric facies change laterally within the rock-fabric layers. There is little lateral rock-fabric variability in the transgressive system tracts (cycles 12-10), whereas more lateral variability is found in the prograding systems tracts (cycles 9-5, 3-1). No sharp lateral boundaries are placed between the facies because no sharp boundaries have been found in analog outcrops on the scale of 1000 ft.

Flow Simulation Model

For each well, the petrophysical data within each rock-fabric facies are averaged, assigned to a rock-fabric layer, and interpolated between wells. The layers and average petrophysical data are input into a fluid flow simulator, and the resulting simulation model is shown in Fig. 40. The simulation model contains 41 rock-fabric flow layers within the 12 high-frequency cycles. Petrophysical properties vary laterally on the scale of 1000 ft and vertically on the scale of feet or tens of feet. This model was used in flow simulations to determine the location of remaining oil (Wang et al. 1998).

The rock-fabric method described herein results in a 3-D image of petrophysical properties that is comparable with outcrop descriptions. It preserves not only the cycle-based geological framework but also the architecture of petrophysically based rock-fabric facies. The problem of scale averaging is minimized by averaging petrophysical data within rock-fabric facies and using rock-fabric layers for constructing the simulation
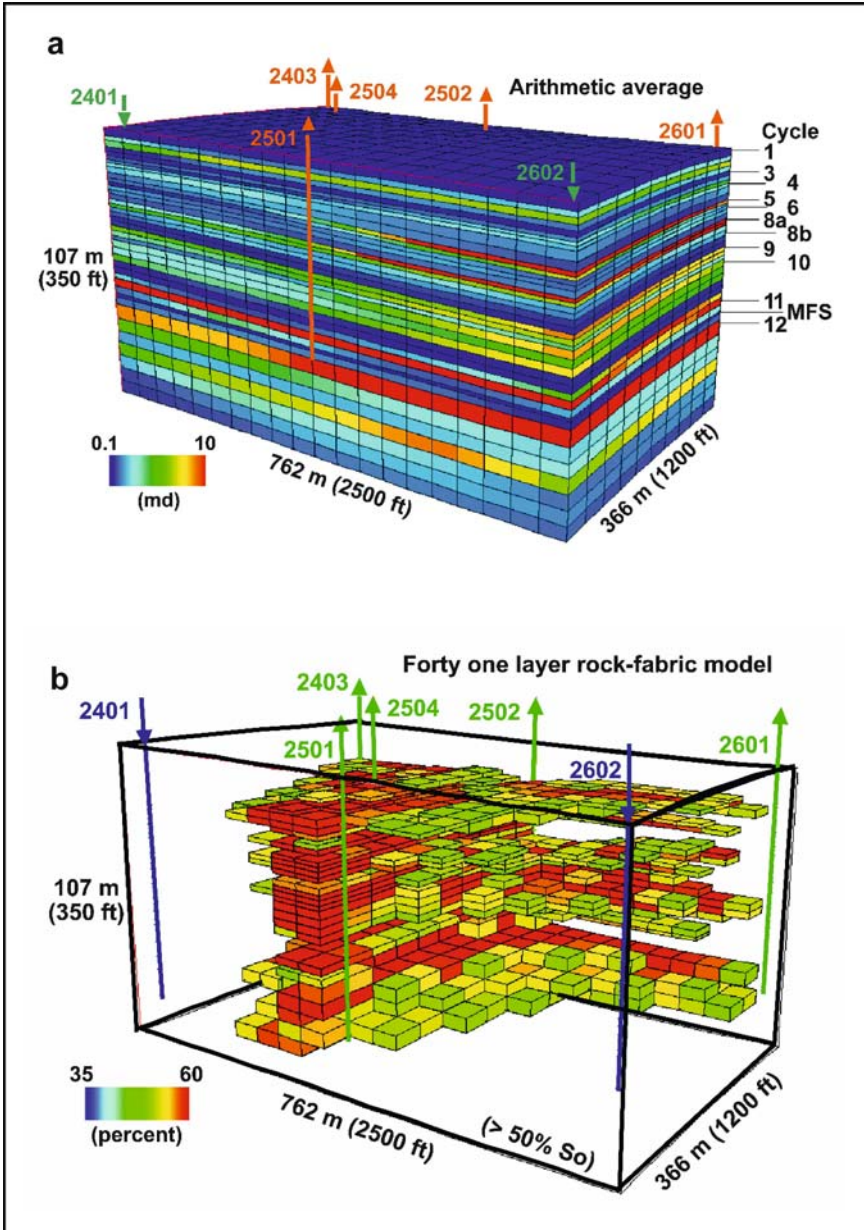
Fig. 7.40. a Permeability distribution in rock-fabric 80-acre simulation model. The model contains 41 rock-fabric layers. **b** Simulation results showing distribution of greater than 50% oil saturation after 17 years of waterflooding

model. The use of rock-fabric-specific permeability transforms preserves high and low values better than the commonly used single transform, and calculation of separate-vug porosity eliminates overestimation of permeability in zones of high separate-vug porosity. In addition, rock-fabric simulation models allow for easy inclusion of rock-fabric specific relative permeability curves in the model (Wang et al. 1994).

The 41-layer simulation model was used to simulate production from an 80-acre area within the two-section study area. The resulting image of the remaining oil saturation (Fig. 40) shows layers of bypassed oil. Recovery efficiency from this type of reservoir is typically 35% of the original oil in place from primary production and conventional waterflooding, and the simulation results shows the remaining 65% to be located in bypassed low-permeability layers. This is a realistic image and will provide more accurate performance predictions of proposed recovery programs than traditional simulation models (Wang et al. 1994; Lucia et al. 1995).

7.5.2 South Wasson Clear Fork

The South Wasson Clear Fork Field is an example of using the porosity log as a surrogate for rock-fabric facies and using one transform for permeability and initial water saturation. The full report of this study can be found at the Department of Energy web site (Lucia 2002). The field is one of several fields developed in the Clear Fork along the eastern margin of the northern shelf in the Permian Basin of West Texas. Structurally, the field is part of a northeast-striking, southeast-dipping monocline that extends from Russell field to the southwest to Prentice field to the northeast (Fig. 41). A small dome within the field provides local closure in the middle of the field. The updip seal is formed by evaporite-rich carbonates; the top seal for the lower Clear Fork is created by the Tubb sandstone, and the seal for the middle Clear Fork is a tight-and-dense dolostone (Fig. 42).

Cumulative production from the South Wasson field totals more than 138 million barrels, the majority coming from the upper and lower Clear Fork. Most of the production comes from the middle part of the upper Clear Fork and the lower Clear Fork. Minor production comes from the underlying Wichita/Albany or Abo Formation. Like that in most Leonardian platform carbonates, recovery efficiency from these rocks is low.

Vertical Succession of Depositional Textures

Cycles defined in the Clear Fork at South Wasson field are based on vertical facies stacking patterns observed in cores. In the lower Clear Fork,
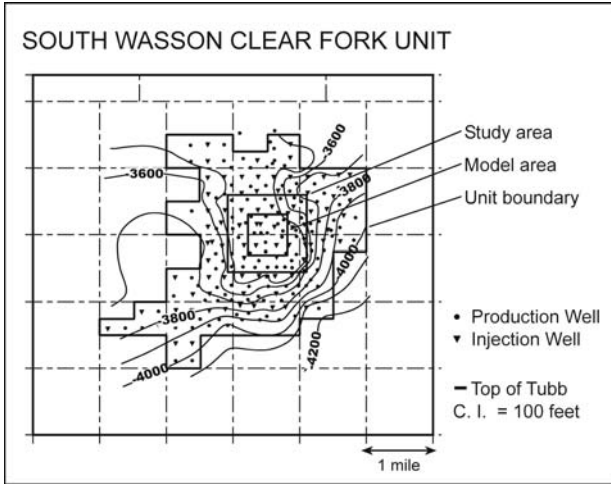
Fig. 7.41. Field map of South Wasson Clear Fork field showing structure
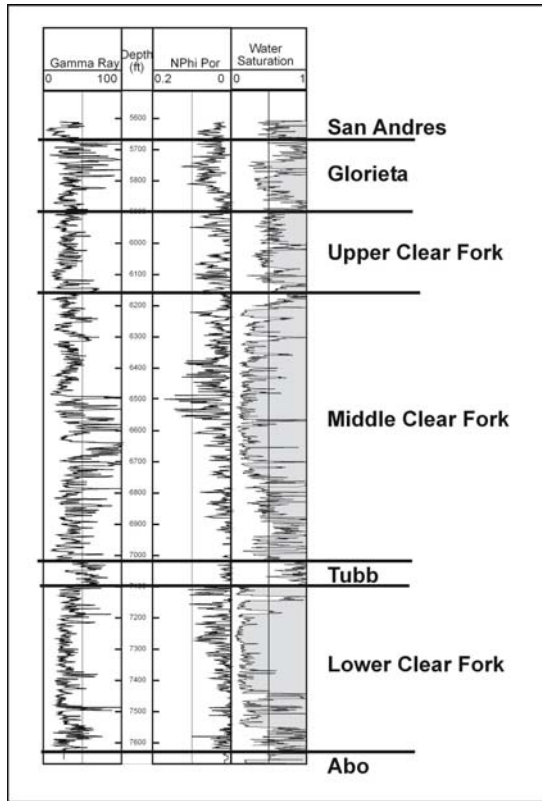
Fig. 7.42. Type log from the South Wasson Clear Fork field

high-frequency cycles range from 2 to 15 ft in thickness and average about 6 ft. Subtidal cycles are dominantly two types: outer platform (deeper water) cycles are composed of fusulinid wackestone-packstone bases and peloid packstone tops; shallow platform cycles contain peloid-skeletal wackestone bases and peloid grain-dominated packstone tops.

High-frequency cycles in the middle Clear Fork are similar in thickness facies stacking patterns to those in the lower Clear Fork, ranging from 2 to 15 ft in thickness and averaging about 7 ft (Fig. 43). Component facies
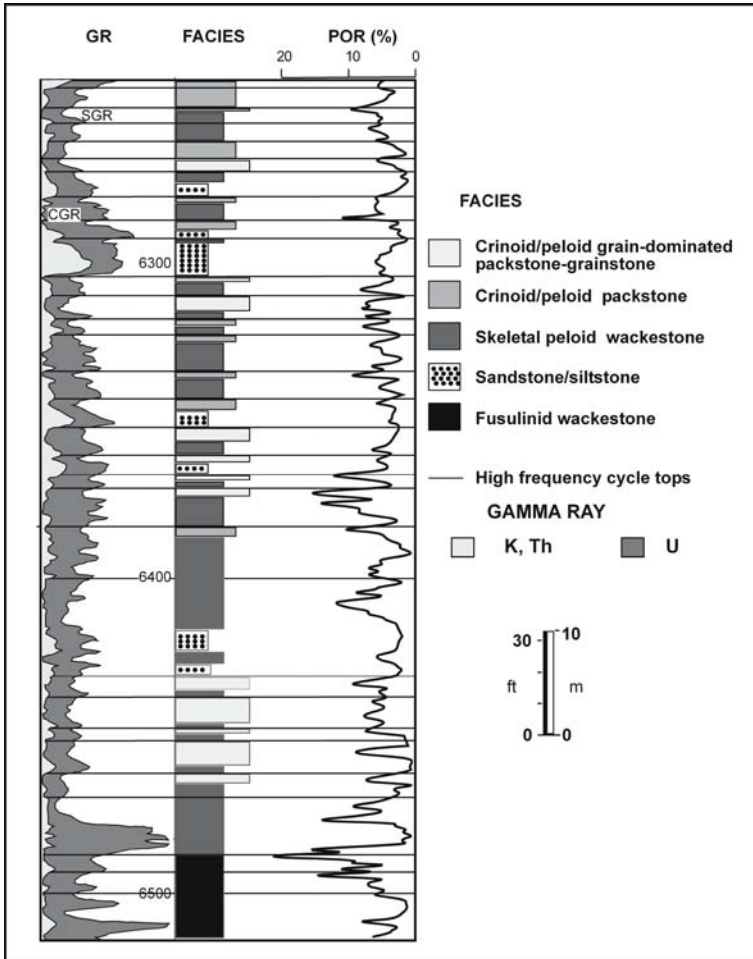
Fig. 7.43. South Wasson Clear Fork core description showing high-frequency cycles and cycle sets in the middle Clear Fork reservoir. Note the large amount of uranium as indicated by the gamma-ray log

in cycles vary from skeletal wackestone bases and peloid packstone tops to peloid wackestone bases and peloid grain-dominated packstone-packstone tops. Siltstone and silty wackestone facies are common in the bases of the upper cycles.

Rock-Fabric Descriptions and Petrophysical Properties

The vertical succession of rock fabrics was described from core slabs and thin sections. The rock-fabric descriptions are different from facies descriptions in that the Dunham term "packstone" is replaced with either mud-dominated or grain-dominated packstone, and dolomite crystal size and the amount of anhydrite is measured.

The rock fabrics described from the South Wasson Clear Fork field include class 1 large crystalline dolostones, dolograinstones, and large-grain grain-dominated dolopackstones. Included in class 2 are grain-dominated dolopackstones and medium crystalline mud-dominated dolopackstones and dolowackestones. Only a few class 3 fine crystalline mud-dominated dolopackstones and dolowackestones have been described from the SWCF field. Separate-vug porosity is rare because most of the intrafossil and moldic pore space has been filled with anhydrite. Some touching-vug porosity is present in the form of microfractures, but most of the fractures have been filled with anhydrite. Sandstones are composed of silt-sized quartz and rare feldspar grains mixed with dolomite, usually fine crystalline. The sandstones have less than 0.1 md permeability and form flow barriers in this reservoir.

Anhydrite is a major component of these dolostones and is present as pore-filling, poikilotopic, and nodular anhydrite. Nodular anhydrite is scattered throughout the reservoir but occupies an insignificant volume. The average amount of pore-filling and poikilotopic anhydrite in the thin sections is 20 % and ranges from 0 to 60% of the thin section. The large volume of anhydrite has a major effect on relationships among rock fabric, porosity, permeability, and capillary properties.

Porosity-permeability cross-plots show a relatively good grouping of data greater than 1 md (Fig. 44a). Below 1 md the data are more scattered because of the presence of numerous samples that have low porosity and measurable permeability. It is judged that these data are biased owing to measurement error, poor sample preparation, and flow through stylolites or induced fractures. Careful measurements made by Westport Laboratory in Houston as part of this study on 41 new core plugs show a good grouping of data, including the samples having less than 1 md of permeability (Fig. 44b). This grouping supports the contention that the scatter below 1 md in
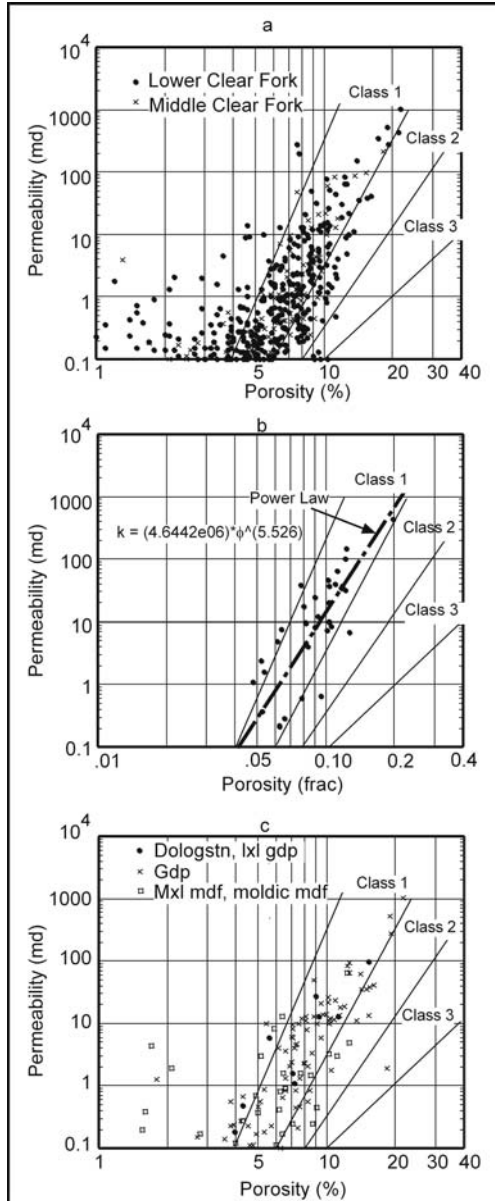
Fig. 7.44. Porosity-permeability cross plots of **(a)** old data, **(b)** new data showing power law transform, and **(c)** new and old data with rock-fabric descriptions thin sections. Note that 1) the new data have no scatteriang of points in the low porosity area and 2) class 2 grain-dominated dolopackstone and class 2 medium crystalline mud-dominated fabrics plot in the class 1 field

the routine core data is biased and should not be considered when developing a porosity-permeability transform.

Porosity-permeability cross plots for samples having thin sections are similar to plots of all the data, indicating that the thin sections are a good sampling of the reservoir (Fig. 44c). Rock fabrics, as described from thin sections, include class 1 dolograinstone, large grained grain-dominated dolopackstones and large grained grain-dominated dolopackstones and mud-dominated dolostones and class 2 medium crystalline grain-dominated dolopackstones and mud-dominated dolostones However, class 2 fabrics plot in the class 1 field (Fig. 44c), which is not predicted by Lucia (1995).

An explanation for this unpredicted behavior can be developed by exploring pore-size distribution. When developing rock-fabric-specific porosity-permeability transforms the basic assumption is that pore sizes are evenly distributed throughout the sample. However, there is a large volume of anhydrite in these samples, ranging from 0 to 60 % and averaging 20 %. The anhydrite patches have no porosity and create a nonuniform patchwork of porous and dense rock. Conceptually, adding the patches of anhydrite reduces porosity but does not affect the pore sizes. The pore-size distribution is changed radically but not the actual pore sizes and the pore sizes control permeability.

Pittman (1992) and Kolodizie (1980) have described the Winland R35 method of determining the effective pore-throat size for relating porosity and permeability (see Chapters 1, 2). Lines of equal pore-throat size cut across rock-fabric petrophysical-class fields because pore-throat size (or pore-size distribution) changes with changes in interparticle porosity within a rock-fabric class (Fig. 16). If it is assumed that a large volume of anhydrite is added in patches to a carbonate having a relatively uniform pore-throat size, the porosity will be reduced but the pore-throat size will remain constant. The result will be that as porosity is reduced, the sample will shift along the line of equal pore-throat size rather than along the rock-fabric transform. As the porosity is reduced, the sample will shift from a higher petrophysical class into a lower class. This model explains why the petrophysical class 2 samples containing large volumes of anhydrite have shifted from the class 2 field into the class 1 field.

As a result of the lateral shift into the class 1 field, a single porosity-permeability transform characterizes the middle and lower Clear Fork reservoirs in the study area. The transform given below has a correlation coefficient of 0.95 and is based on recent data from Westport Laboratory in Houston (Fig. 44b).

$$k = (4.6442*10^6) * \phi^{5.526} \ r = 0.95,$$

where k = permeability in millidarcys and ϕ = porosity in fractions.

The class 1 porosity-permeability transform for SWCF is unique for Permian reservoirs. A porosity cutoff of 4 % is indicated for this reservoir whereas San Andres and Grayburg reservoirs typically have cutoff porosities of 6 to 8 %. The transform's step slope means that small changes in porosity result in large changes in permeability. The transform calculates a permeability of 2 md at 7 % porosity, 14 md at 10 % porosity, and 60 md at 13 % porosity. Therefore, although the average porosity of the SWCF reservoir is lower than that of typical San Andres and Grayburg reservoirs, the average permeability is similar because of the large amounts and patchy distribution of anhydrite in the permeable intervals.

A capillary pressure model for initial water saturation was constructed from 19 capillary pressure curves. The data was divided into five porosity bins and average curves calculated. A saturation model that relates water saturation to porosity and capillary pressure was developed from these five average capillary pressure curves using multivariate analysis methods. The resulting model is presented below.

$$Sw = [1 - A*\ln(B/Pc)]^{\wedge}(-\lambda/A),$$
where,
   Pc = Capillary pressure, and
   $\lambda = C*(D + \ln\phi)$.

Constants are given as
   $A = 0.98$'
   $B = 22.7$'
   $C = 0.91$'
   $D = 4.2$.

Calibration of wireline logs

Depositional and rock-fabric facies could not be identified using the gamma-ray log because of the large amount of diagenetic uranium in the Clear Fork (Fig. 43), and cross plots of porosity and water saturation are of little use because the fabrics group into one petrophysical class. Sandstone facies could be easily identified by the acoustic-porosity cross plots (Fig. 45). Examination of rock fabric and porosity data, however, suggests that
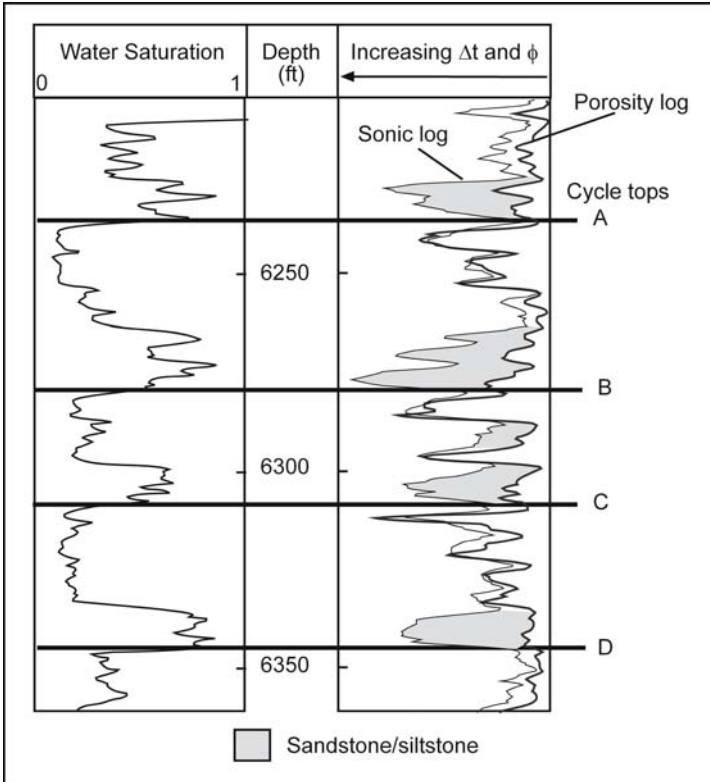
Fig. 7.45. Depth plot of the upper part of the middle Clear Fork showing silty beds defined by overlying conic and porosity logs and by high water saturation values

grain-dominated packstones tend to have higher porosity than do mud-dominated fabrics.

This observation was tested by using thin-section descriptions and core porosity data from both the lower and middle Clear Fork. In the middle Clear Fork, dolowackestones have an average porosity of 4.5% and make up 70% of the samples having <5% porosity. Mud-dominated dolopack-stones have an average porosity of 7%, and grain-dominated dolopack-stones an average porosity of 9%. Together, dolopackstones make up 70% of the samples having >5% porosity, and grain-dominated dolopackstones make up 70% of the samples having >10% porosity. A similar result was found in the lower Clear Fork, where the average porosity of the mud-dominated dolostones is 3%, and the grain-dominated dolopackstone 7%. Here, only 60% of the samples having <5% porosity are mud-dominated fabrics, whereas 80% of the samples having >5% porosity are grain-dominated packstone.

Therefore, in the middle Clear Fork, an interval having >10% porosity is most likely to be grain-dominated packstone. An interval having <5% porosity is most likely to be composed of mud-dominated fabrics. In the lower Clear Fork, an interval having >5% porosity can reasonably be concluded to be grain-dominated packstone, but lower porosity intervals can be either mud- or grain-dominated fabrics.

Figure 46 illustrates the result of using the porosity log to distinguish
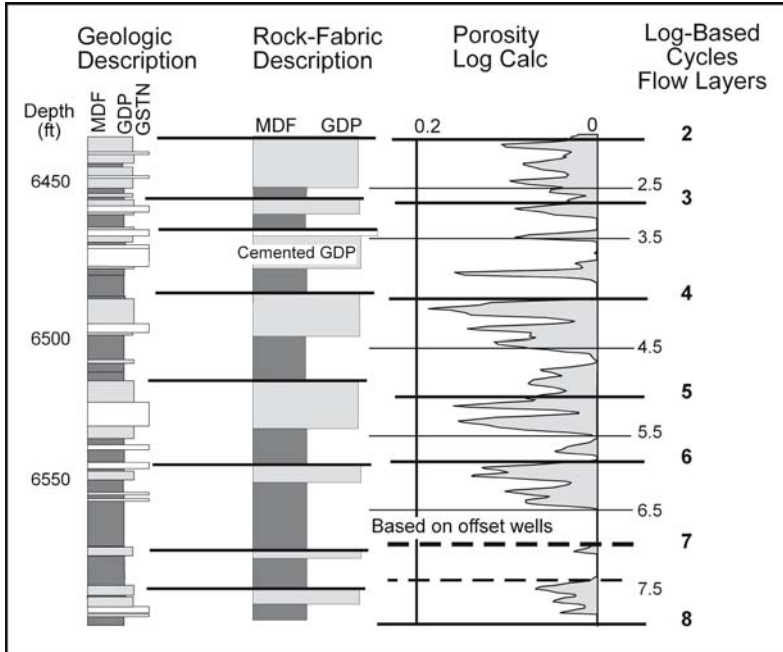
Fig. 7.46. Comparison of middle Clear Fork high-frequency cycles based on core and rock-fabric description with cycles based on the porosity log. The cycles are divided into two flow layers based on high and low porosity

between low-porosity mud-dominated fabrics and high-porosity grain-dominated fabric. Cycles 6, 5, 4, and 2 from the middle Clear Fork clearly show upward-increasing porosity and correlate with cycle tops identified by core descriptions. Cycle 3 top is highly interpretive. Cycle 7 does not have a well-defined high-porosity top in this well but does in offsetting wells. A cycle top labeled 4a identified in core descriptions is not clearly defined by the porosity log because thin sections show that anhydrite and dolomite cement fill the pore space in the capping grain-dominated dolo-packstone. Therefore, this approach clearly identified five out of seven tops using the porosity log. Cycle 3 and 7 tops are carried in from offset-

ting wells, and their exact location in this well is not critical to the flow model because, in this well, the cycles are dense. Therefore, seven tops are properly located in this example, including tops carried through dense intervals based on offsetting wells. Cycle 4a, however, was missed entirely and is combined with cycle 3.

Calculating vertical profiles of petrophysical properties

Vertical profiles of porosity were based on sidewall neutron, neutron-density cross plots, and sonic logs. Interparticle porosity is equal to total porosity because very little vuggy porosity was observed in the core material. Permeability and initial water saturation were calculated from porosity and the transforms described above. A separate transform for the sandstone layers was not required because their low porosity values result in < 0.1 md permeability and 100% water saturation using the above transforms. Archie water saturations were not used because resistivity logs tend to be inaccurate at low porosity values and Archie water saturations are overstated. A comparison of core and calculated permeability is presented in Fig. 47.
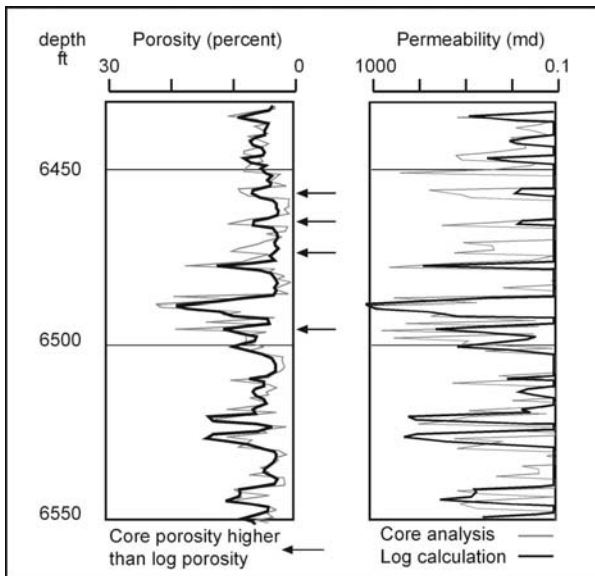
Fig. 7.47. Comparison of core and log-based porosity and permeability values for the middle Clear Fork reservoir. There is reasonably good agreement between core and log-calculated permeability values when core and log-based porosity values are in agreement

Reservoir Model Construction.

High-frequency cycles were picked in 48 wells within the study area using porosity as a surrogate for rock fabric. A segmented of the resulting cycle stratigraphy in the middle upper Clear Fork is shown in Fig. 48. In order
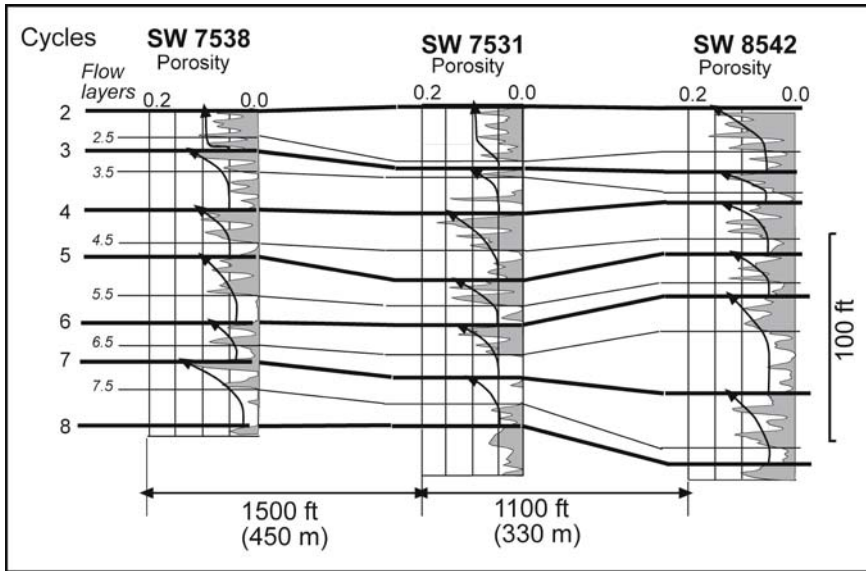
Fig. 7.48. Cross section from a portion of the middle Clear Fork reservoir showing correlation of high-frequency cycles and flow layers based on porosity logs

to maintain the high- and low-permeability intervals, each high-frequency cycle is divided into two rock-fabric flow layers, sandstone and mud-dominated dolostones at the base and grain-dominated dolostones at the top. The middle upper Clear Fork reservoir is divided into 21 high-frequency cycles and 42 flow layers, and the lower Clear Fork is also divided into 42 flow layers. The high-frequency cycles are the basic geological elements, and the flow layers are the basic petrophysical elements for constructing the reservoir model.

The high-frequency cycles and flow layers were correlated over the study area, forming the basis for the reservoir model. A cross section of the middle upper Clear Fork reservoir showing cycles and flow layers is illustrated in Fig. 49. No cycles are described in the lower measures because it is not part of the reservoir due to high water saturations typical of the transition zone. For illustrative purposes, petrophysical properties were distrib-
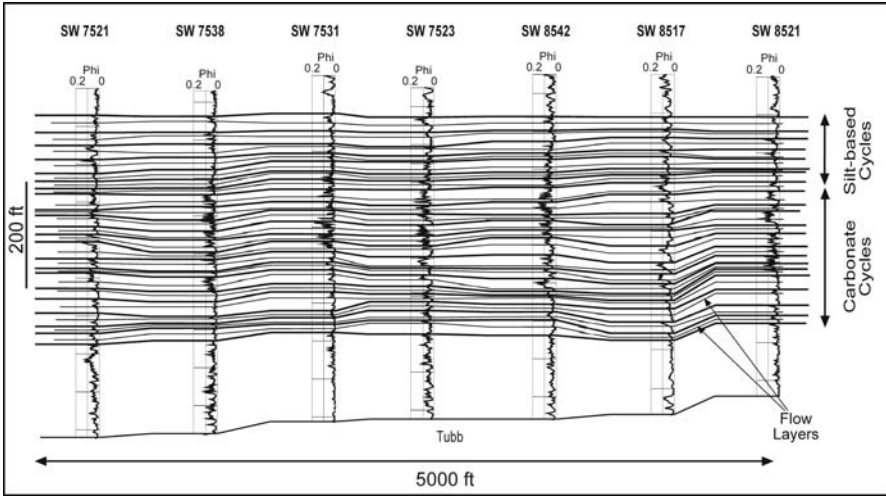
Fig. 7.49. Cross section illustrating the layer model for the middle Clear Fork reservoir showing 7 silt-based cycles labeled A-G, 14 carbonate cycles, and 21 rock-fabric flow layers
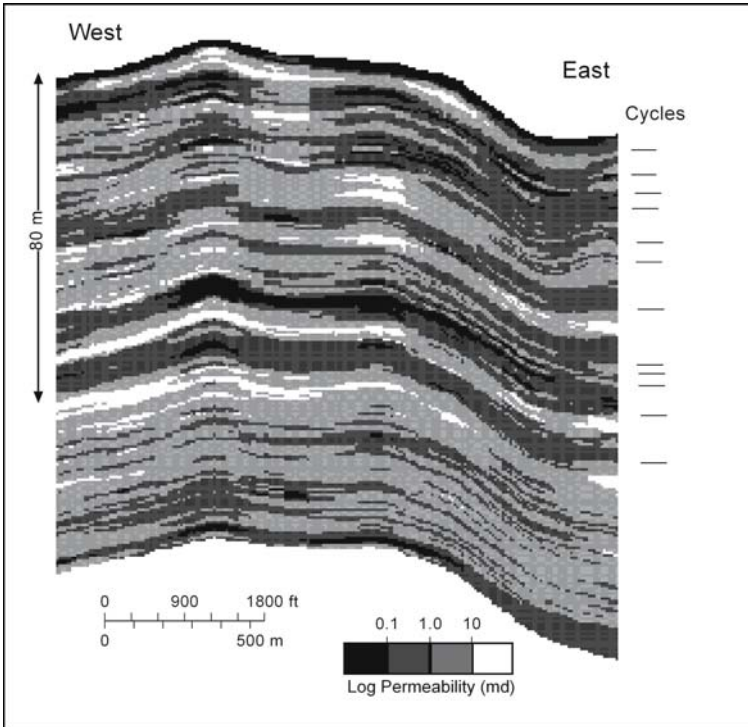
Fig. 7.50. North-to-south Stratamodel cross section of the middle Clear Fork reservoir showing permeability distribution

uted within the flow layers using simple linear interpolation methods (Fig. 50).

Flow Simulation Model

A 3-D reservoir flow simulation model of the study area was constructed (Fig. 51) using a method that links high-resolution sequence-stratigraphic frameworks, porosity-permeability relationships from core data, outcrop-derived models of small-scale spatial statistics, and a practical approach to porosity-permeability scaleup (Jennings et al. in press). Identification and
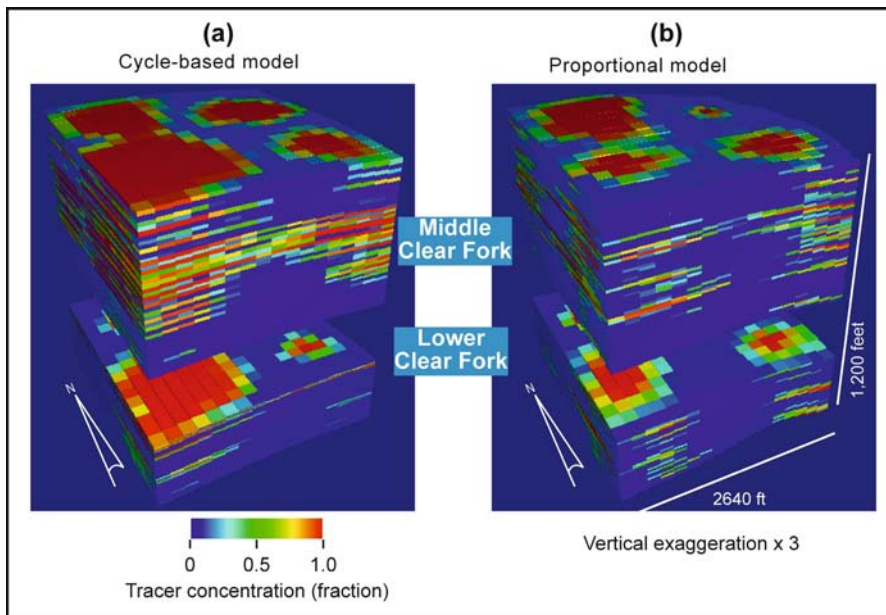
Fig. 7.51. Tracer simulation results. **a** Tracer sweep pattern in the improved model at one pore volume injection. **b** Tracer sweep pattern in the traditional model at one pore volume injection

modeling of petrophysical layering are critical for waterflood performance prediction. In this study the layering is based on high-frequency cycles and rock-fabric flow layers. The large-scale component of petrophysical variability is spatially organized into rock-fabric flow units with abrupt vertical contrasts at flow-unit boundaries and gradual lateral transitions. The flow-unit-scale petrophysical layering is laterally persistent at interwell scales, leading to highly stratified reservoir behavior with rapid waterflood sweep in the higher permeability layers, bypassing of the lower permeabil-

ity layers, minimal cross-flow between layers, and early water break-through.

Fluid-flow simulation was conducted to assess the benefits to reservoir performance prediction provided by the improved model described here compared with an existing model. The existing model was constructed without a high-resolution sequence-stratigraphic framework, and layering was assigned by proportioning layers between traditional stratigraphic markers. This model will be referred to as the "traditional model." The model developed in this study using layers defined by rock fabrics and high-frequency cycles will be referred to as the "improved model." The areal grid of the improved model was chosen to coincide exactly with that of the traditional model, and the same set of well-log data was used for the construction of both models. The same simplified set of well controls was used in both models.

Injectivity and sweep were the aspects of reservoir performance addressed in this study. Meaningful comparison of the injectivity and sweep predictions of the two models was achieved by conducting single-phase tracer injection simulations, avoiding the additional complications of waterflood modeling. Thus, no initial saturation, residual saturation, or relative permeability modeling was required. The single-phase fluid was modeled as an incompressible liquid having a constant viscosity.

Detailed waterflood matching of the traditional model to historical SWCF performance was conducted in a previous study. A good history match was obtained by applying a k_v/k_h multiplier of 0.0002 to reduce cross-flow between the layers and by increasing the horizontal permeabilities by a factor of 2 to match reservoir pressure behavior. In this study the improved model was matched to the traditional model, with both models running the same simplified incompressible tracer displacement case, by adjusting the same two parameters.

The k_v/k_h multiplier in the improved model was adjusted to obtain the same sweep at one pore volume injection. However, the k_v/k_h multiplier required to achieve this match was 0.02, two orders of magnitude larger than the 0.0002 required in the traditional model and much closer to the moderate flow-unit scale k_v/k_h ratio expected from typical whole-core data in carbonates. This improvement in performance modeling was produced by the improved representation of petrophysical layering in the model.

The tracer sweep patterns at one pore volume injection in the improved model are stratigraphically organized into alternating high- and low-permeability flow units in the middle Clear Fork, and thin higher permeability flow units near the top of the lower Clear Fork (Fig. 51a). These sweep patterns were produced by the stratigraphically organized petrophysical layering. The corresponding sweep patterns in the traditional

model are more random (Fig. 51b). The improved model also predicts more injection in the southern portion of the model, relative to the injection predicted by the traditional model, because of the subtle north-to-south porosity increase detected by the trend modeling portion of this study. Careful comparison with reservoir performance data, outside of the scope of this study, would be required to demonstrate that these sweep patterns in the improved model constitute a superior representation of reservoir behavior. Nevertheless, the sweep patterns are consistent with the SWCF geological interpretation and are thus more satisfying.

7.5.3 Fullerton Clear Fork Reservoir

The Fullerton Clear Fork study is an example of using stratigraphy to obtain petrophysical class numbers where only gamma-ray/neutron logs are available and multiple values are required because of the diversity of rock fabrics. The Fullerton Clear Fork field in Andrews County, Texas (Fig. 52) was discovered in 1942, and the Fullerton Clear Fork Unit formed in 1953. The unit has produced 289 million barrels of oil from 1,250 wells and covers an area of about 30,000 acres, or 47 square miles. Original oil in place (OOIP) is estimated at between 1.6 and 1.9 billion stock-tank barrels (BSTB), for a recovery efficiency of about 17%. The field produces from permeability zones scattered over 500 ft of Permian-age Wichita and Lower Clear Fork limestones and dolostones. The full report of this study can be found at the Department of Energy Web site (Ruppel 2004).

Vertical Succession of Depositional Textures

Twelve facies can be identified in the Fullerton reservoir succession on the basis of grain type, grain size and sorting, fabric, depositional texture, and lithology (Ruppel et al. 2004):

1. Peritidal Mudstone–Wackestone: generally dolomitized and most abundant in the Wichita and locally in the Lower Clear Fork associated with tidal-flat facies.
2. Clay-rich Carbonate Mudstone: generally thin and locally found associated with peritidal mudstone-wackestone facies.
3. Exposed Tidal Flat: defined by fenestra, pisolites, mudcracks, microbial laminations, and marked sea-level changes in the Wichita and Lower Clear Fork.
4. Peloid Wackestone: a burrowed mud-dominated fabric deposited in a low-energy subtidal setting.
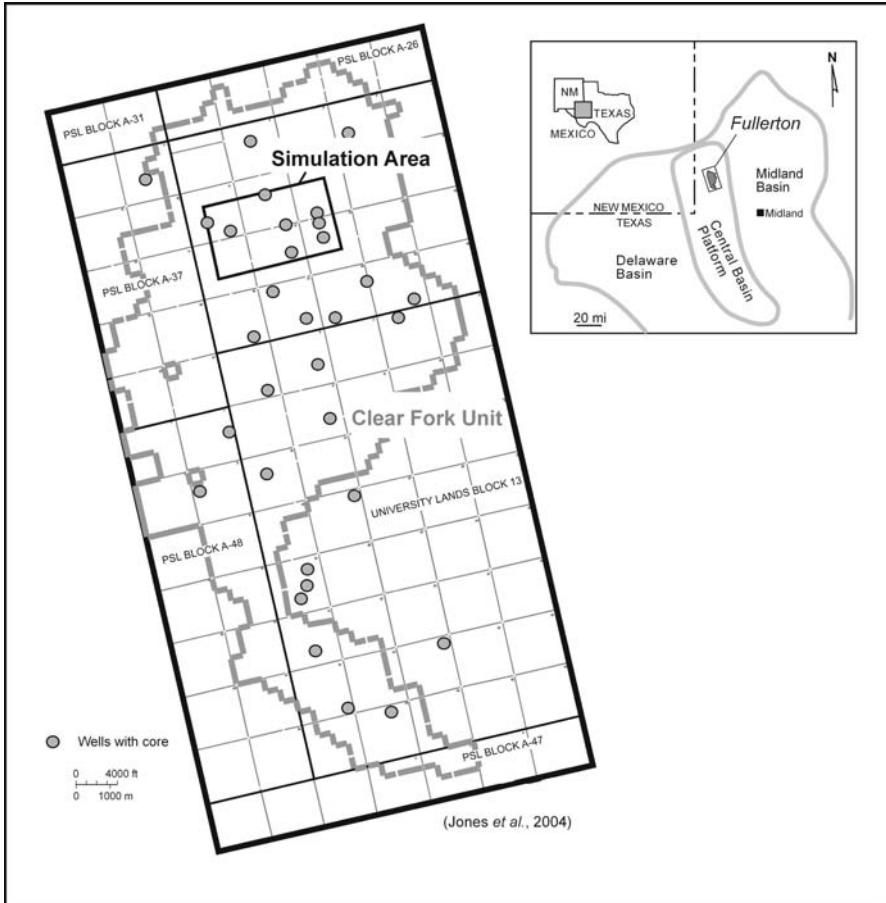
Fig. 7.52. Location of Fullerton Clear Fork field

5. Peloid Packstone: a burrowed mud-dominated fabric with abundant peloids (probably fecal pellets) deposited in a low-energy subtidal setting.
6. Peloid Grain-dominated Packstone: moderately well sorted peloids in intergrain pore space deposited in a subtidal setting having moderate energy levels.
7. Ooid-Peloid Grain-dominated Packstone-Grainstone: contains ooids and skeletal grains, in addition to peloids, and is moderate (grain-dominated packstone) to well (grainstone) sorted, suggesting moderate to high energy levels.
8. Fusulinid Wackestone-Packstone: most abundant in the Lower Clear Fork, found in sites suggesting water depths of 30 m of more, the deepest water facies at Fullerton.

9. Skeletal Wackestone-Packstone: found mainly in the Lower Clear Fork, containing mollusks and crinoids, suggesting a low-energy inner platform setting.

10.Oncoid Wackestone-Packstone: abundant at the base of the Lower Clear Fork through the entire field associated with fusulinids and other faunas, suggesting an open-marine environment during flooding of the platform.

11.Siltstone-Sandstone: restricted to the Tubb Formation that overlies the Lower Clear Fork, but traces can often be found in peritidal and tidal-flat facies.

12.Lithoclastic Wackestone: thin beds of tidal-flat fabrics overlying tidal-flat facies.

The producing interval of the Fullerton field is divided into sequences and cycles based on vertical successions of depositional facies from core description. Two sequences are defined: Leonardian 1 (L 1) and Leonardian 2 (L 2). Most of the reservoir is found in the L 2 sequence, which is divided into four high-frequency sequences (HFS): Leonardian 2.0 (HFS L 2.0), Leonardian 2.1 (HFS L 2.1), Leonardian 2.2 (HFS L 2.2), and Leonardian 2.3 (HFS L 2.3) (Fig. 53).

The Wichita consists of a diverse assemblage of peritidal and tidal-flat facies that group into the highstand leg of sequence L 1 and the transgressive leg of sequence L 2 (Fig. 54). The highstand leg of L 1 represents the landward tidal-flat equivalent of the basinward outer platform facies of the Abo Formation, and the transgressive leg of L 2 represents the landward tidal-flat equivalent of the basal Lower Clear Fork subtidal facies. Evidence of karst is found in a few cores below the L 1 – L 2 boundary in the middle Wichita (Fig. 54). Intervals of polymict breccia of at least 25 ft to as much as 60 ft in thickness are present in one core. Their discontinuous nature and association with other features indicative of karst processes suggest that they originated as cave-fill deposits.

Sequence L 2 is subdivided into four high-frequency sequences (L 2.0, L 2.1, L 2.2, L 2.3) (Fig. 54). HFS L 2.0 documents the initial flooding of the platform following exposure at the end of L 1 time. In the field area it consists of peritidal and tidal-flat facies of the upper Wichita. HFS L 2.1 forms the base of the Lower Clear Fork and consists of a basal section of transgressive subtidal platform facies and an upper section of highstand tidal-flat facies. It represents the sharp change from peritidal deposition of the Wichita to subtidal deposition of the basal Lower Clear Fork. HFS L 2.2 is similar to HFS L 2.1 in consisting of a basal transgressive leg composed of backstepping tidal-flat facies, a middle leg composed dominantly of subtidal facies, and an uppermost highstand leg composed of tidal-flat
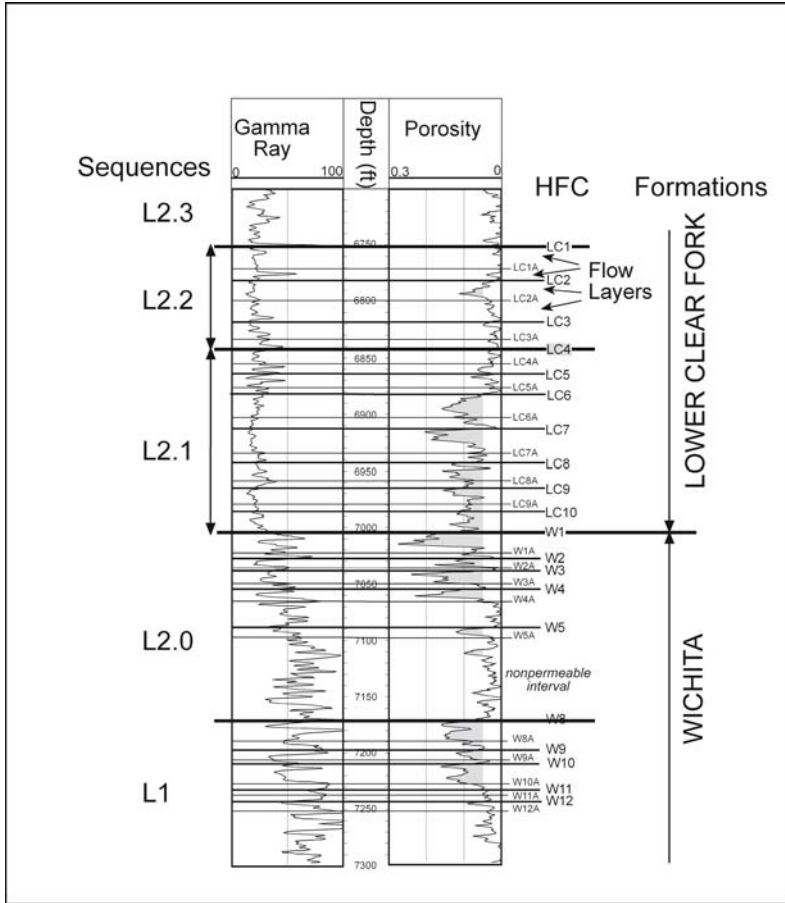
Fig. 7.53. Fullerton field type log showing formations, sequences, high-frequency cycles, and flow layers (Ruppel 2004)

facies. HFS L 2.3 is composed of tidal-flat-capped restricted subtidal cycles in the field area and is capped by the siliciclastic Tubb Formation.

The fundamental goal of cycle stratigraphy is to develop a correlation framework based on time-equivalent surfaces. These surfaces form the basic correlations for constructing the reservoir model and define high-frequency cycles (HFC's). Because the Wichita is composed of peritidal and tidal-flat facies, cycles are difficult to define and correlate. Only one bed of good subtidal facies was found. Most of the correlations were based on porosity and limestone-dolostone layering, the porous intervals being dolostone and the dense intervals being mostly limestone and occasionally dense dolostone. It is assumed that each dolostone bed was formed by hypersaline reflux flowing down from a tidal-flat into peritidal facies.
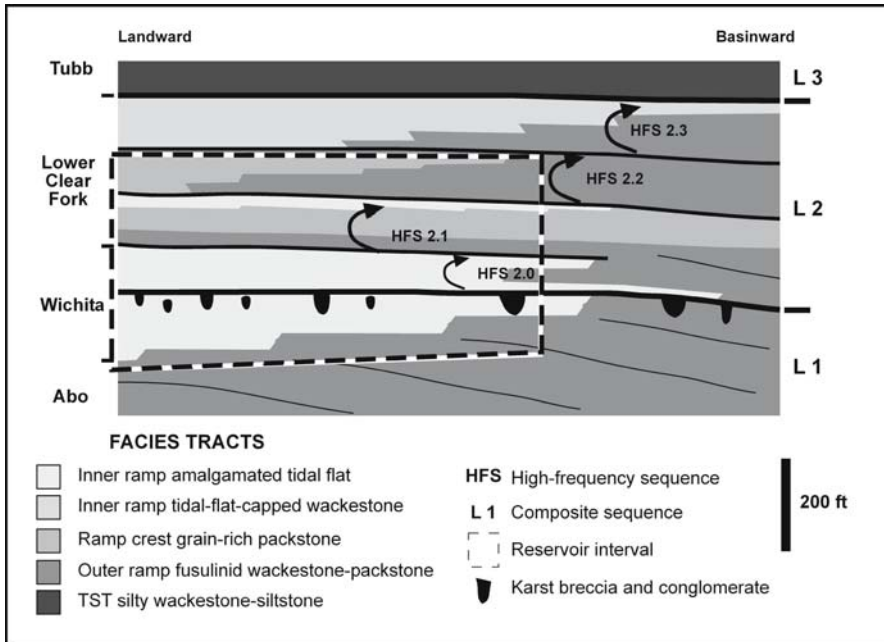
Fig. 7.54. Schematic cross section of Fullerton field showing formations, sequences, and general facies distribution (Ruppel, 2004)

Therefore, the dolostone beds mark the tops of the HFC's (Fig. 55). Using this approach, we divided the Wichita into 10 HFS's labeled W1 – W5 and W8 – W12. The interval between W5 and W8 has little porosity and was not subdivided.

HFS L 2.1 is divided into seven high-frequency cycles (Fig. 53). These cycles are labeled LC4 – LC10. The lower cycles are transgressive and typically grade upward from fusulinid and oncoid mud-dominated facies to better sorted peloid-rich and tidal-flat caps. The upper cycles are highstand and are typically composed of peloidal facies at their bases and grain-rich peloid- or ooid-bearing facies at their tops. The top two cycles are composed of peritidal and tidal-flat facies.

Cycle definition was difficult in the dolostones of HFS L.2.2 because of low porosity. However, three HFC's were proposed on the basis of a rare limestone core that consisted of three upward-shoaling successions. These successions are labeled LC 1 – LC 3. The three cycles were subdivided into eight autocycles for the purposes of full field mapping, but these subdivisions were not used in the simulation model.

High-frequency cyclicity is most readily definable in HFS L.2.3. These rocks, which are characterized by a tidal-flat-capped subtidal cycle, are
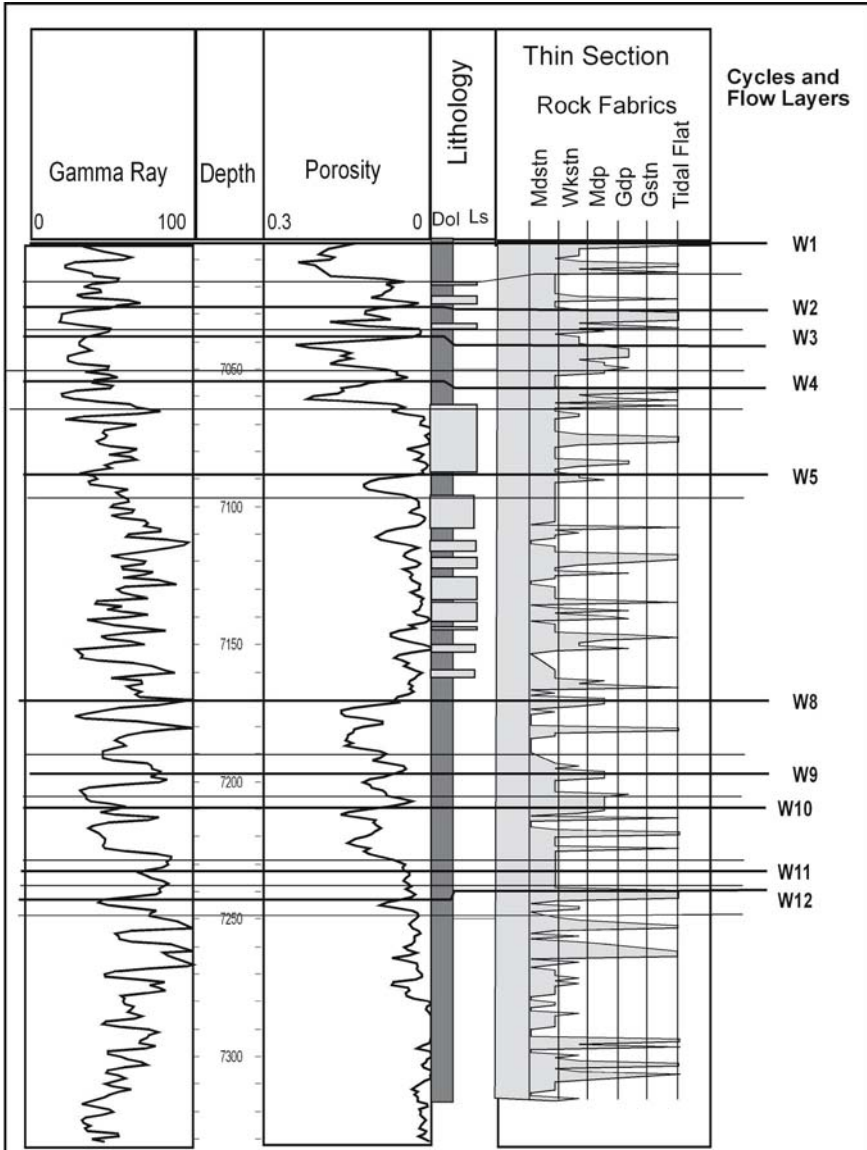
Fig. 7.55. Well log of Wichita formation showing high-frequency cycles and flow layers based primarily on porosity and lithology

more easily correlated than HFC's in L 2.1 or L 2.2. However, this HFS is not considered to be part of the reservoir and is not included in the reservoir model.

Rock Fabric Descriptions and Petrophysical Properties

In the Fullerton study rock-fabric-specific porosity-permeability trans-
forms and capillary pressure models are used to estimate permeability and
Sw_i (Lucia 1995, 1999). A large number of both limestone and dolostone
rock fabrics are present. The limestone rock fabrics are class 1 oomoldic
grainstone, class 2 grain-dominated packstone, and class 3 wackestones.
The dolostones fabrics are class 2 medium-to-fine crystalline grain-
dominated packstone, class 2 medium crystalline mud-dominated dolos-
tones, and class 3 fine crystalline mud-dominated dolostones. If permeabil-
ity were plotted against interparticle porosity for these rock fabrics, the
data would group into petrophysical class 1, 2, and 3 fields as predicted.
However, interparticle porosity cannot be calculated because almost all of
the wells in this field have only gamma-ray and neutron logs available.

Therefore, rock fabric cross plots using total porosity are used to gen-
erate permeability transforms (Jones and Lucia 2004). The fine crystalline
dolostones have little vuggy porosity and group in the class 3 field, as ex-
pected, and a class 3 transform characterizes this group (Fig. 56a). Class 3
mud-dominated limestones have low porosity values and less than 0.1 md
permeability. Class 2 medium crystalline mud-dominated dolostones,
grain-dominated dolopackstones, and grain-dominated packstones plot in
the class 2 field, as expected, and a class 2 transform characterizes this
group (Fig. 56b). Class 1 oomoldic grainstones plot in the class 2 and 3
fields because oomoldic porosity does not contribute significantly to per-
meability. Therefore, the oomoldic grainstone are grouped with the class 2
fabrics. The only fabric to plot in the class 1 field is a medium crystalline
dolostone with more than 10% poikilotopic anhydrite (Fig. 56c). The rea-
son for this is the fact that the anhydrite patches have reduced porosity to
zero without altering the pore size in the surround matrix. Therefore, is ap-
pears that the rock fabrics can be reasonably grouped into petrophysical
class 1, 2, and 3. Permeability can be calculated from total porosity and
petrophysical class using the global transform.

Estimates of Sw_i were made using capillary pressure models that relate
petrophysical-class- specific Sw_i to porosity and reservoir height. Six new
class 1 capillary pressure curves were obtained as part of this study, and
they compared well with the generic class 1 model. Eleven new class 2
capillary pressure curves were obtained, and they indicated somewhat
lower Sw_i values than the generic model. Eleven new capillary pressure
curves were also obtained from class 3 rocks, and they indicated signifi-
cantly lower Sw_i values than the generic model. Four curves were obtained
from oomoldic grainstones, and the curves are similar to the class 3 curves.
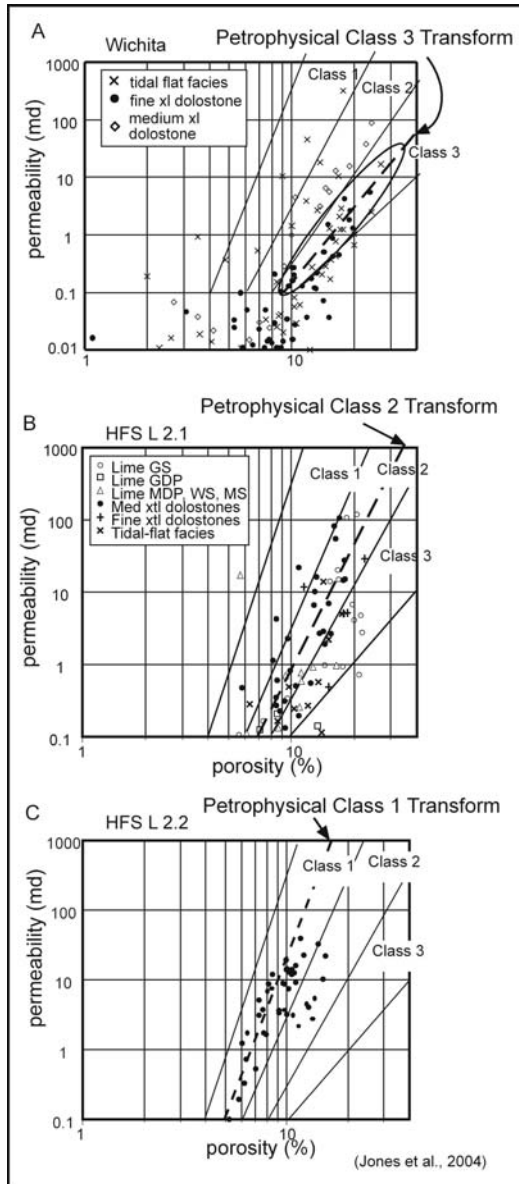
Fig. 7.56. Porosity-permeability cross plots of three stratigraphic units showing characteristic transforms. **A** Wichita formation showing petrophysical class 3 as characteristic of fine crystalline mud-dominated dolostone found in peritidal facies. **B** High-frequency sequence L 2.1 showing petrophysical class 2 as characteristic of the multiple fabrics found in the subtidal cycles. **C** High-frequency sequence L 2.2 showing petrophysical class 1 as characteristic of class 2 subtidal dolostones with abundant poikilotopic anhydrite

New models for class 2 and 3 fabrics were developed using the Thomeer (1960) method for characterizing capillary pressure curves. The Thomeer method estimates the irreducible water saturation, entry pressure, and shape of the capillary pressure curve (the G factor) from a cross plot of percent bulk-volume of mercury occupied and entry pressure corrected for surface effects. Relational studies indicated that extrapolated entry pressure correlated quite well with porosity, although the correlations were different in each case. There was no correlation between porosity and G factor, however, each petrophysical class having a unique G factor.

The models used are given below:

Class 1 $Sw_i = 0.02219 \ X \ H^{-0316} \times \tilde{\phi}^{-1.745}$

Class 2 $Sw_i = 1-[2.71828^{\wedge}(-0.2/(\log(15.5064*H/(Phi^{\wedge}-2.8394))))]$

Class 3 $Sw_i = 1-[2.71828^{\wedge}(-0.1/(\log(0.3827*H/(Phi^{\wedge}-1.9717))))]$

Calibration of rock fabrics and depositional textures to wireline logs

Most of the wells in the Fullerton field have only porosity and gamma-ray logs. The high uranium content of the Clear Fork and Wichita makes the gamma-ray log next to useless for fabric or facies calibration. The porosity logs provided a general method for correlation high-frequency cycles. In the lower Clear Fork HFS's L 2.1 and 2.2 the lower mud-dominated fabrics have lower porosity than the upper grain-dominated fabrics (Fig. 57). An analysis of rock fabrics and porosity shows that grain-dominated dolopackstones average 11.5% porosity, mud-dominated dolopackstones average 9.4% porosity, and dolowackestones and dolomudstones average 4.9% porosity. Lime grainstones average 14.9%, grain-dominated packstones 8.2%, and mud-dominated fabrics 7.3%. A simple porosity cutoff could not be used because there is considerable overlap in porosity values between these two fabrics. Therefore, high-frequency cycles are characterized by upward increases in porosity and porosity profiles are used to map cycles in the lower Clear Fork.

In the Wichita there is no clear relationship between fabric and porosity because the cycles are typically composed of mud-dominated limestones or fine crystalline mud-dominated dolostones. HFC's in the Wichita are thought to be tidal-flat-capped cycles with dolostone overlying limestone. The dolostones are typically porous, and limestones have less than 3% porosity. Therefore, the porosity profile reflects changes from low-
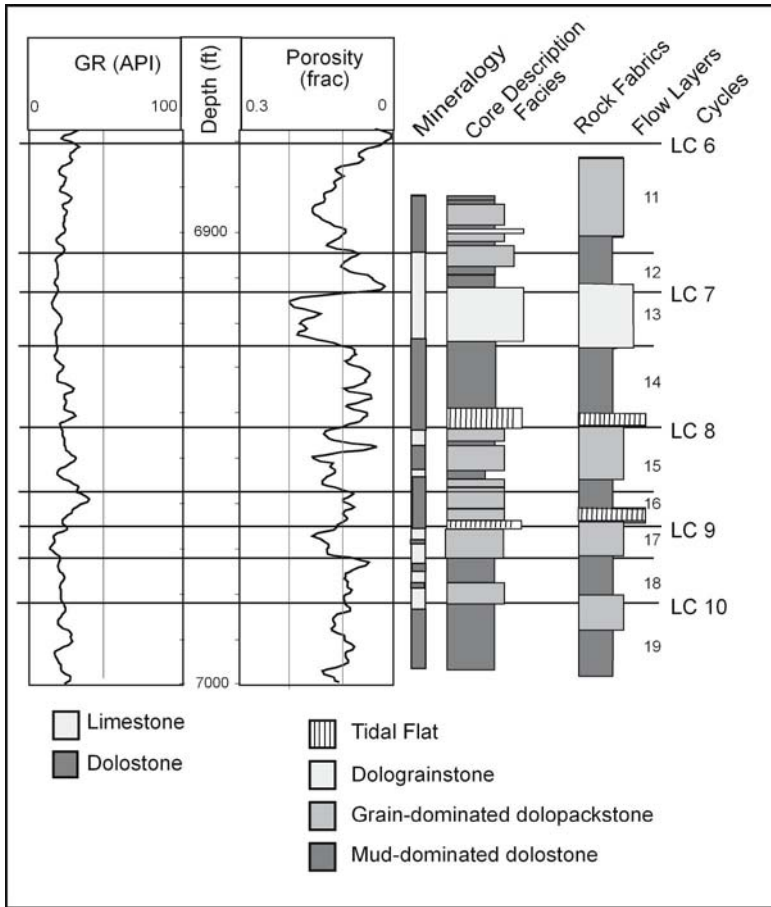
Fig. 7.57. Well log of lower Clear Fork L 2.1 sequence showing high-frequency cycles and flow layers based on vertical increases in porosity divided into a lower low-porosity flow layer and an upper higher porosity flow layer

porosity peritidal limestone to high-porosity tidal-flat peritidal facies (Fig. 55). In several HFC's the low-porosity as well as the high-porosity is dolostone, and it is assumed that a tidal-flat facies occurs at the top of the high-porosity zone. Therefore, vertical increases in porosity define tidal-flat capped high-frequency cycles and are used to map cycles in the Wichita.

The vertical succession of mud-dominated to grain-dominated cannot be used to estimate petrophysical class needed for petrophysical calculations because mud-dominated dolostones can be either class 1, 2, or 3 depending on crystal size, and grain-dominated fabrics can be class 1 or 2 and have varying volumes of separate-vug porosity. This problem was re-

solved using a unique approach. Instead of calibrating fabrics to wireline logs, the fabrics were calibrated to stratigraphy. The Wichita consists mainly of class 3 fine crystalline mud-dominated dolostone. Some tidal-flat fabrics have higher permeability due to fenestral porosity, and some class 2 grain-dominated dolopackstones and medium crystalline mud-dominated dolostones are present but appear to be few in number and locally developed. Therefore, a class 3 transform and capillary pressure model, together with total porosity, were used to calculate permeability and Sw_i in the Wichita.

The Lower Clear Fork HFS L 2.1 is composed of a variety of rock fabrics. Most mud-dominated fabrics have been dolomitized to a class 2 medium crystalline dolostones. Grain-dominated packstones are class 2 fabrics whether they are limestone or dolostone. Oomoldic grainstones plot in the class 2 and 3 field and are characterized as class 2, although permeability will be overestimated in some cases. Accordingly, the subtidal cycles of HFS L 2.1 were characterized as class 2. Mud-dominated limestone fabrics are also present in HFS L 2.1 and are a class 3 fabric. However, they have little porosity and less than 0.1 md permeability and a calculated permeability of less than 0.1 md using a class 2 transform. Therefore, it was not necessary to add a class 3 transform to calculate permeability or Sw_i.

The upper two cycles of HFS L 2.1, however, are composed of peritidal and tidal-flat facies. The rock fabrics are class 3 fine crystalline mud-dominated dolostones. Therefore, whereas the lower five high-frequency cycles of HFS L 2.1 are characterized by petrophysical class 2, the upper two are characterized by class 3.

The Lower Clear Fork HFS L 2.2 is composed of dolostone with a few small patches of limestone in the northern part of the field and interbedded limestone and dolostone in the southern part of the field. The dolostone fabrics include grain-dominated dolopackstones and medium crystalline mud-dominated dolostone, both class 2 fabrics. However, many samples plot in the class 1 field and not in the class 2 field and contain more than 10% poikilotopic anhydrite. The shift from the class 2 field to the class 1 field can be explained by the loss of porosity in the anhydrite patches without a change in pore size in the remainder of the rock (Lucia et al., 2004). Therefore, in the northern part of the field HFS L 2.2 was characterized as petrophysical class 1.

Limestone is interbedded with dolostone in HFS's L 2.1 and 2.2 over most of the southern part of the Fullerton field. Here the fabrics are low-porosity medium crystalline mud-dominated dolostones and high-porosity grain-dominated moldic limestones. Both of these fabrics tend to plot in the class 2 field when plotted against total porosity. Therefore, this southern area was characterized as petrophysical class 2.

Lower Clear Fork high-frequency sequence L 2.3 consists of peritidal and tidal-flat facies composed of fine crystalline mud-dominated dolostone fabric. Petrophysical class 3 best characterizes this sequence. This sequence is not considered part of the reservoir interval.

Calculating vertical profiles of petrophysical properties

Permeability and Sw_i were calculated using petrophysical class values from stratigraphic relations as discussed previously, total porosity for wireline logs, and transforms for specific petrophysical classes. The accuracy of calculated values is highly dependent upon the accuracy of porosity values obtained from wireline logs. The Fullerton has 1,206 wells with logs that spanned six decades of technology. Because of difficulties in calibrating older (pre-1960) wells, only 733 wells had porosity logs that could be calibrated for use in this study. These logs were digitized, and considerable effort was spent verifying the digital logs and headers against paper logs. After the logs were verified the porosity curves were normalized and compared with core data (Kane and Jennings 2005).

Permeability was calculated from wireline logs using the global transform. Interparticle porosity is normally used in the global transform equation because the petrophysical classes and rock-fabric numbers are based on interparticle porosity. However, in this study petrophysical class is based on total porosity and petrophysical class from stratigraphic relationships and total porosity from wireline logs is used in the global transform equation.

The method was tested on six cored wells with good results (Fig. 58). The Wichita is characterized by petrophysical class 3, and calculated permeability compares well with permeabilities in the upper Wichita (sequence L 2). The Lower Clear Fork is characterized by a variety of petrophysical classes. The Lower five high-frequency cycles of HFS L 2.1 are characterized as petrophysical class 2 and the upper two high-frequency cycles as class 3. The match between calculated and core permeability is quite good. HFS 2.2 is characterized as petrophysical class 1, and calculated and core permeability values also compare well.

Estimates of Sw_i were made using the capillary pressure models described above, assuming a zero capillary pressure level of -4,100 ft subsea. Archie saturations could be calculated from a few wells, and a comparison of saturation profiles from Archie calculations and capillary models is presented in Fig. 59. Archie saturation is higher than model saturation in zones that have been flooded.
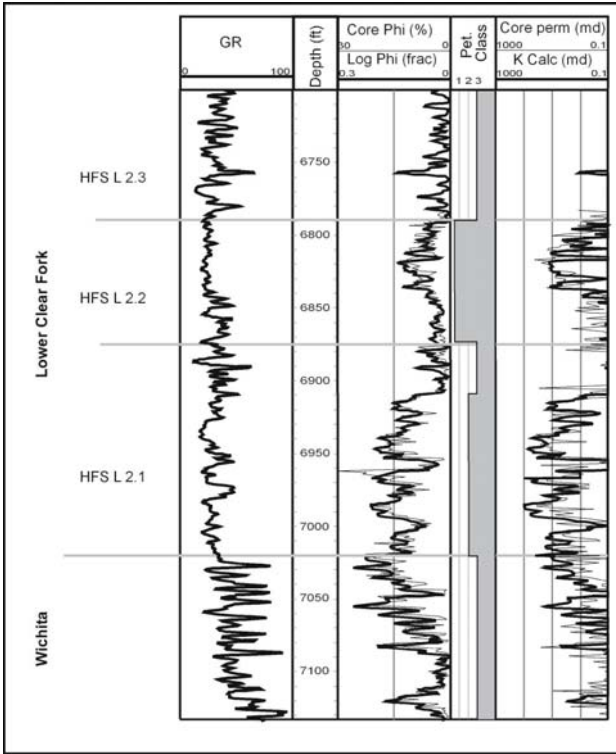
Fig. 7.58. Illustration of calculating permeability from log porosity and petrophysical class values from stratigraphy using the global transform. Calculated values are compared with core values
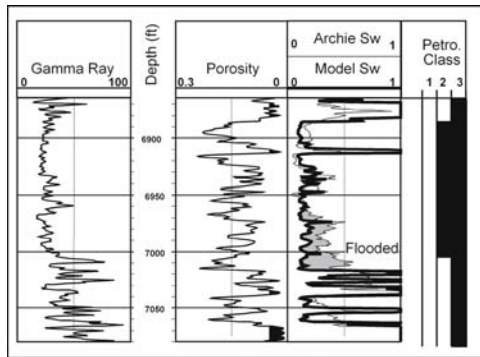
Fig. 7.59. Illustration of calculating initial water saturation from log porosity and petrophysical class values from stratigraphy using rock-fabric capillary pressure models. Calculated values are compared with Archie water saturations showing a flooded interval where the two values diverge

Full Field Model Construction

The high-frequency cycles were correlated throughout the study area using porosity logs aided by the gamma-ray log. Three-dimensional models of porosity, permeability, and initial water saturation were prepared using Gocad modeling software. Maps of petrophysical properties show that the distribution of properties varies considerably laterally and between sequences (Fig. 60). Porosity in the north area is generally higher than in the
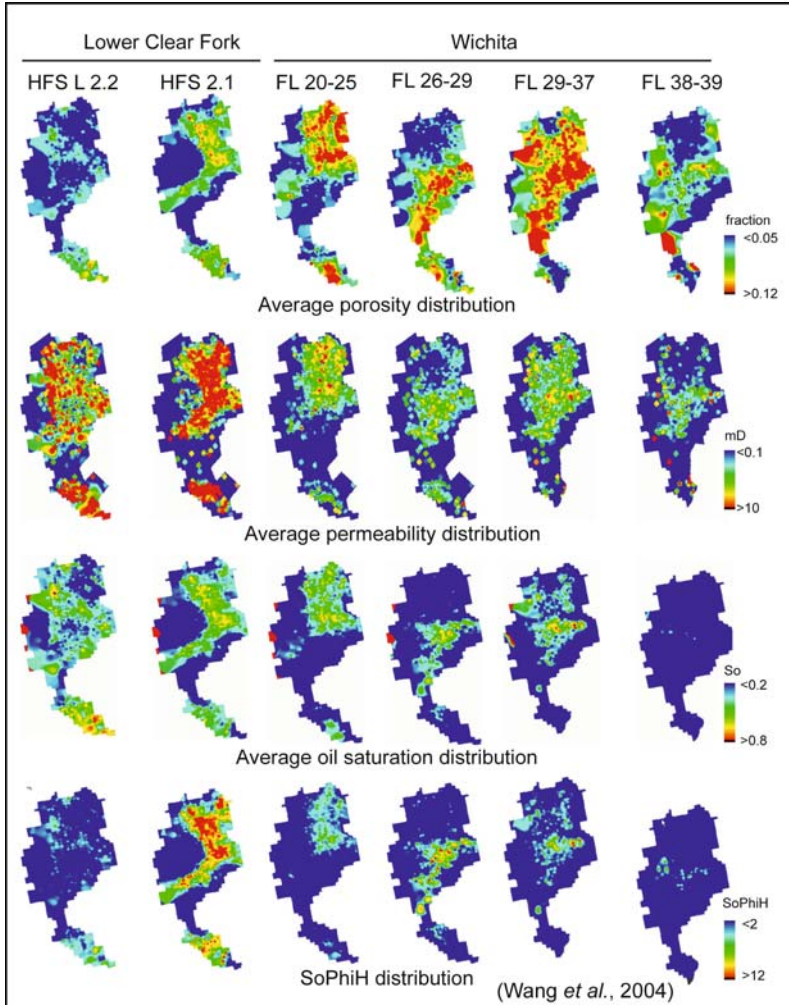
Fig. 7.60. Distribution of petrophysical properties for HFS's L 2.2 and 2.1 and for the Wichita by groups of flow layers

south area, and porosity in the Wichita is generally higher than in the lower Clear Fork. Porosity in the lower Clear Fork is best developed in HFS L 2.1. The maps show an arcuate porosity pattern in the north dome with porosity in the northeast and south and little porosity in the northwest. Porosity in the Wichita is best developed in the upper and lower zones. Porosity in the HFC W1 and W2 is confined to the northeast portion of the north dome and shifts to the southern portion in HFC W5. HFS's W8–W12 have scattered but good porosity development throughout the field.

Permeability distribution mimics the porosity distribution and reflects the impact of rock-fabric petrophysical class. The lower Clear Fork, which is dominated by class 1 and 2 fabrics, has much higher permeability than the Wichita, which is dominated by class 3 fabrics, even though Wichita porosity is generally higher. However, the permeability in HFS's W8–W12 may have higher permeability because of karsting effects. Although HFS L 2.2 has lower porosity than HFS L 2.1, it has good permeability because it contains class 1 fabrics.

Initial water saturation shows the effects of height above the zero capillary pressure, as well as rock-fabric petrophysical class. The lowest Wichita zones have high Sw_i even though they have high porosity values because of proximity to the zero capillary pressure level. HFS L 2.2 has water saturations similar to those of HFS L 2.1, although it has lower porosity because it is class 1, whereas HFS L 2.1 is class 2. The porosity difference is evident when hydrocarbon volumes are compared. As a result, almost 60% of the hydrocarbon volume resides in the lower Clear Fork (40% in HFS L 2.1), and almost 30% resides in the upper Wichita, the lower zones being porous but having high water saturation.

Flow Simulation Model

A 2,000-acre area containing the highest density of cores and best suites of wireline logs was selected for flow simulation (Fig. 52). For the construction of the simulation model, the HFC's were divided into two rock-fabric flow layers, a lower mud-dominated layer characterized by low porosity and an upper grain-dominated layer characterized by high-porosity. The resulting model has 39 rock-fabric flow layers (Fig. 61).

A fine-scale petrophysical model of the Fullerton Clear Fork Field was constructed containing 3.165 million 105 × 103-ft cells contained in 254 layers (Wang and Lucia 2004). This model was upscaled to flow-unit thickness for reservoir simulation. The simulation model contains 136,656 cells, 39 flow layers, and 200 × 200-ft cells. Porosity was averaged arithmetically, and permeability and Sw_i were calculated using correlations to rock-fabric petrophysical class and porosity, as described previously. Be-

cause permeability in the simulation model was calculated from k-phi relationships that underestimate cell permeability, permeability values were generally increased by a factor of 5 to match production history. Permeability in flow layers W9–W11 was increased by a factor of 30 to match
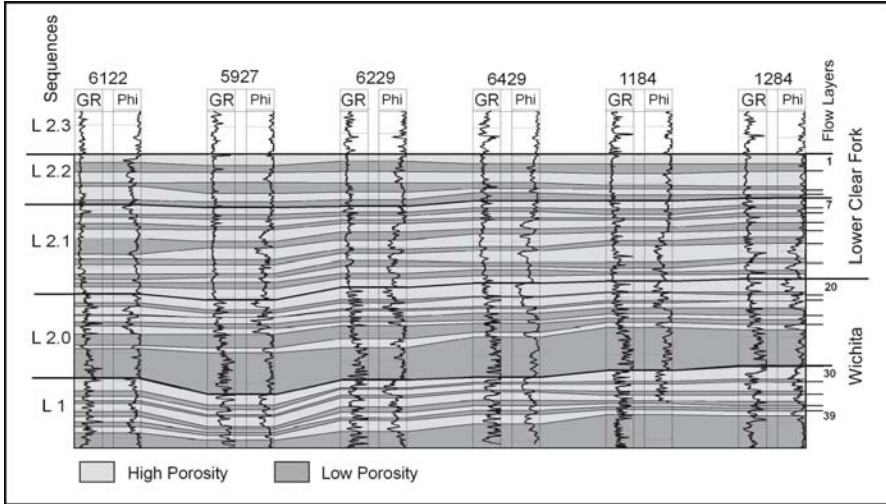
Fig. 7.61. Lower Clear Fork and Wichita flow layers in cored wells of simulation area illustrating the use of porosity to build a flow model

water production from karst-related fractures observed below the L 1-L 2 boundary.

A principal reason for detailed flow simulation in old carbonate fields is to locate remaining oil that has been bypassed by waterflooding operations. This is accomplished by reconstructing field history and simulating production history, and testing against known production history. The Fullerton simulation model was history matched from discovery to the year 2002. Simulated oil-saturation distribution in 2002 shows poor sweep efficiency in HFS L 2.2 because the low porosity restricts continuity between injector and producer. HFS L 2.1 has the best reservoir qualities in the field, but simulated oil-saturation distributions indicate that many areas have not been swept by water because of lateral permeability heterogeneities (Fig. 62). In the simulation model porosity and reservoir continuity are best developed in the Wichita HFC's W1 to W3. Simulated oil-saturation distributions in 2002 in flow layers 20 and 22 show they have been fully swept, except for areas where the wells are not completed in these layers (Fig. 62). Thus, bypassed oil is related to continuity between producer and injection, which can vary significantly between HFC's and flow layers.
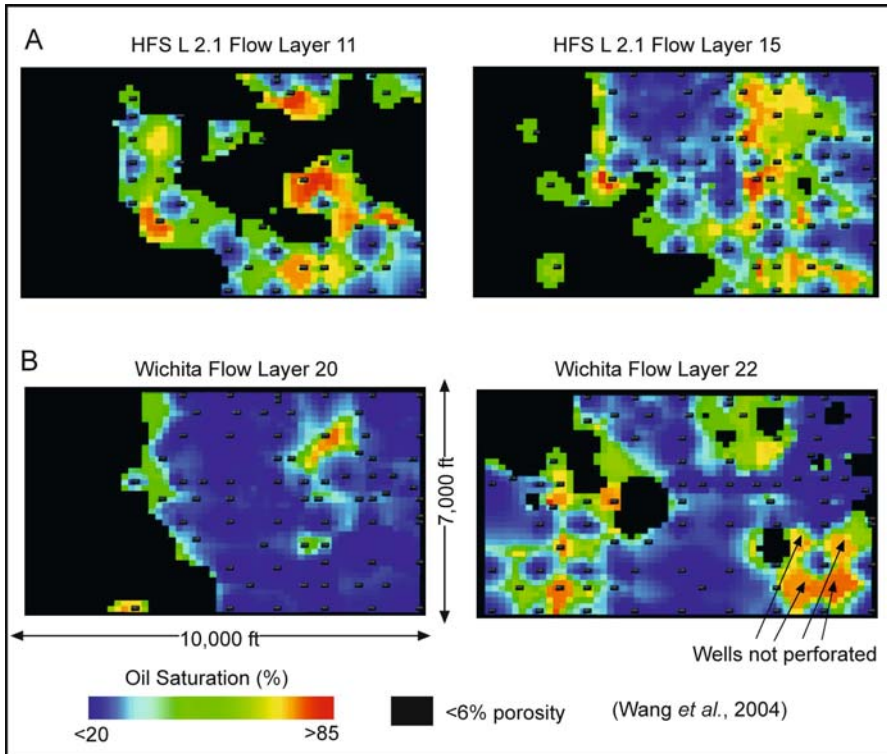
Fig. 7.62. Simulated oil saturation in 2002 showing remaining oil saturation after 60 years of waterflooding in **A** two Lower Clear Fork flow layers and **B** two Wichita flow layers (Wang et al. 2004)

References

Back W, Hanshaw BB, Plummer LN, Rahn PH, Rightmire CT, Rubin M 1983 Process and rate of dedolomitization: mass transfer and 14C dating in a regional carbonate aquifer. GSA Bull 94, 12:1415–1429

Beaumont E. De 1837 Application de calcul a l'hypothese de la formation par epigenie des anhydrites, des gypses et des dolomies.: Soc. Geol. France Bull. 8:174–177

Butler GP 1969 Modern evaporite deposition and geochemistry of co-existing brines, the sabkha, Trucial Coast, Arabian Gulf, Journal of Sed. Petrology 39:70–89

Cantrell D, Swart P, Handford RC, Kendall, CG, Westphal H 2004 Geologic and production significance of dolomite trends, Arab-D reservoir, Ghawar Field, Saudi Arabia. Geo-Arabia 6:45–60

Clement JH 1985 Depositional sequences and characteristics of Ordovician Red River Reservoirs, Pennel Field, Williston Basin, Montana. In: Roehl RO, Choquette PW, (eds) Carbonate petroleum reservoirs. Springer, Berlin Heidelberg New York, pp 85–106

Davies GR, Langhorne BS 2006 Structurally controlled hydrothermal dolomite reservoir facies: An overview. AAPG Bulletin, 90, 11:1641–1690

Deffeyes KS, Lucia FJ, Weyl PK 1965 Dolomitization of Recent and Plio-Pleistocene sediments by marine evaporite waters on Bonaire, Netherlands Antilles. In: Pray LC, Murray RC, (eds) Dolomitization and limestone diagenesis — a symposium. SEPM Spec Publ 13, pp71–88

Ehrenberg SN, Eberli GP, Baechle B 2006 Porosity-permeability relationships in Miocene carbonate platforms and slopes seaward of the Great Barrier Reef, Australia (ODP Leg 194, Marion Plateau). Sedimentology 53, 6:1–30

Ehrenberg SN, Nadeau PH 2005 Sandstone vs. carbonate petroleum reservoirs: a global perspective on porosity-depth and porosity permeability relationships.AAPG Bull, 89, 4:435–446

Evamy BD 1967 Dedolomitization and the development of rhombohedral pores in limestones. J Sediment Pet 37:1204–1215

Folk RL, Land LS 1975 Mg/Ca ratio and salinity: two controls over crystallization of dolomite. AAPG Bull 59, 1:60–68

Galloway WE, Ewing TE, Garrett CE, Tyler N, Bebout DG 1983 Atlas of major Texas oil reservoirs. The University of Texas at Austin, Bureau of Economic Geology, 139 pp

Hardie LA 1967 The gypsum-anhydrite equilibrium at one atmosphere pressure. Am. Mineral. 52:171–200

Jennings JW, Jr., Lucia FJ 2003 Predicting permeability from well logs in carbonates with a link to geology for interwell permeability mapping: Society of Petroleum Engineers Reservoir Evaluation & Engineering 6, 4:215–225

Jennings JW, Jr., Lucia FJ, Ruppel SC 2007 3D modeling of stratigraphically controlled petrophysical variability in the South Wasson Clear Fork Reservoir, In Press

Jones GD, Xiao Y 2005 Dolomitization, anhydrite, cementation, and porosity evolution in a reflux system: Insights from reactive transport models. AAPG Bull 89, 5:577–601

Jones, RH, Lucia, FJ 2004 Integration of rock fabric, petrophysical class, and stratigraphy for petrophysical quantification of sequence-stratigraphic framework, Fullerton Clear Fork field, Texas. In: Ruppel, SC (ed) Multidisciplinary imaging of rock properties in carbonate reservoirs for flow-unit targeting: Univ. Texas Austin Bureau of Economic Geology, final technical report prepared for U.S. Department of Energy under contract no. DE-FC26-01BC15351, p. 121–162

Kane, JA, Jennings JW Jr. 2005 A method to normalize log data by calibration to large-scale data trends. Society of Petroleum Engineers, Paper No. SPE 96081, 12 p

Kasprzyk A 1995 Gypsum-to-anhydrite transition in the Miocene of southern Poland. J Sedimentary Research, A65, 2:348–357

Kolodizie S Jr 1980 Analysis of pore throat size and use of the Waxman-Smits equation to determine OOIP in Spindle Field, Colorado. SPE paper 9382 presented at the 1980 SPE Annual Technical Conference and Exhibition, Dallas, Texas

Land LS, Prezbindowski DR 1981 The origin and evolution of saline formation water, lower Cretaceous carbonates, South-Central Texas, USA. J Hydrol 54:51–74

Lucia FJ 1995 Rock-fabric/petrophysical classification of carbonate pore space for reservoir characterization. AAPG Bull 79, 9:1275–1300

Lucia FJ 1961 Dedolomitization in the Tansill (Permian) Formation. Geol Soc Am Bull 72:1107–1110

Lucia FJ 1962 Diagenesis of a crinoidal sediment. J Sediment Petrol 32, 4:848–865

Lucia FJ 1972 Recognition of evaporite-carbonate shoreline sedimentation. In: Rigby JK, Hamblin WK, (eds) Recognition of ancient sedimentary environments. SEPM Spec Publ 16:160–191

Lucia FJ, Kerans C, Wang FP 1995 Fluid-flow characterization of dolomitized carbonate-ramp reservoirs: San Andres Formation (Permian) of Seminole field and Algerita Escarpment, Permian Basin, Texas and New Mexico. In: Stoudt EL, Harris PM (eds) Hydrocarbon reservoir characterization: geologic framework and flow unit modeling. SEPM (Society for Sedimentary Geology), SEPM Short Course 34:129–153

Lucia FJ, Major RP 1994 Porosity evolution through hypersaline reflux dolomitization. In: Purser BH, Tucker ME, Zenger DH, (eds) Dolomites, a volume in honor of Dolomieu. Int Assoc Sedimentol Spec Publ 21:325–341

Lucia FJ, Murray RC 1966, Origin and distribution of porosity in crinoidal rock. Proc World Petroleum Congr, Mexico City, Mexico, 1966, pp 406–423

Lucia FJ, Conti RD 1987 Rock fabric, permeability, and log relationships in an upward-shoaling, vuggy carbonate sequence. The University of Texas at Austin, Bureau of Economic Geology, Geological Circular 87-5, 22 pp

Lucia, FJ, Kane JA 2004 Calculations of permeability and initial water saturations from wireline logs. In: Ruppel SC (ed) Multidisciplinary imaging of rock properties in carbonate reservoirs for flow-unit targeting: Univ. Texas Austin Bureau of Economic Geology, final technical report prepared for U.S. Department of Energy under contract no. DE-FC26-01BC15351, p. 189–218

Lucia, FJ, Jennings JW Jr, Rahnis MA, Meyer FO 2001, Permeability and rock fabric from wireline logs, Arab-D reservoir, Ghawar field, Saudi Arabia. GeoArabia 6, 4:619–646

Lucia FJ 2002 Integrated outcrop and subsurface studies of the interwell environment of carbonate reservoirs: Clear Fork (Leonardian-age) reservoirs, West Texas and New Mexico, www.osti.gov/servlets/purl/811895-4EHgbz/native/

Lucia FJ, Jones RH, Jennings JW 2004 Poikilotopic anhydrite enhances reservoir quality (abs.): AAPG Annual Convention Abstracts Volume, v. 13, p. A88

Lucia FJ 2004 Origin and petrophysics of dolostone pore space, In: Braithwaite CJR, Rizzi G, Darke G, (eds), The geometry and petrogenesis of dolomite hydrocarbon reservoirs, London, Geological Society, Special Publications 235, pp 141–155

Lucia FJ 1968 Recent sediments and diagenesis of South Bonaire, Netherlands Antilles, J. Sediment Petrol 38:XX

Melim LA, Anselmitte FS, Eberli GP 2001 The importance of pore type on permeability of Neogene carbonates, Great Bahama Bank. In: Ginsburg RN (ed) Subsurface geology of a prograding carbonate platform margin, Great Bahama Bank: Results of the Bahamas drilling project. Society for Sedimentary Geology Special Publication 70, pp 217–241

Morrow DW 1990 Dolomite-part 1: the chemistry of dolomitization and dolomite precipitation. In: McIlreath, IA, Morrow, DW (eds) Diagenesis. Geoscience Canada, Reprint Series 4, pp 113–123

Murray RC 1960 Origin of porosity in carbonate rocks. J Sediment Petrol 30:59–84

Murray RC 1964 Origin and diagenesis of gypsum and anhydrite. J Sediment Petrol 34:512–523

Murray RC, Lucia FJ 1967 Cause and control of dolomite distribution by rock selectivity, Geological Soc. of America Bulletin, 78:21-36

Pittman, ED 1992 Relationship of porosity and permeability to various parameters derived from mercury injection—capillary pressure curves for sandstone. AAPG Bull72:191–198.

Powers RW 1962 Arabian Upper Jurassic carbonate reservoir rocks. In: Ham WE, (ed) Classification of carbonate rocks, AAPG Mem 1:122–192.

Ruppel SC, Jones, RH 2004 Facies, sequence stratigraphy and porosity development in the Fullerton Clear Fork reservoir. In: Ruppel, SC (ed) Multidisciplinary imaging of rock properties in carbonate reservoirs for flow-unit targeting: Univ. Texas Austin Bureau of Economic Geology, final technical report prepared for U.S. Department of Energy under contract no. DE-FC26-01BC15351, p. 1–120

Ruppel, SC., ed. 2004, Multidisciplinary imaging of rock properties in carbonate reservoirs for flow-unit targeting: Univ. Texas Austin Bureau of Economic Geology, final technical report prepared for U.S. Department of Energy under contract no. DE-FC26-01BC15351

Ruppel SC Jones RH 2006 Key role of outcrops and cores in carbonate reservoir characterization and modeling, Lower Permian Fullerton field, Permian Basin, USA. In: Harris PM, Weber LJ (eds) Giant hydrocarbon reservoirs of the world—from rocks to reservoir characterization, SEPM/AAPG Core Workshop, AAPG Annual Meeting

Saller AH 1984 Petrologic and geochemical constraints on the origin of subsurface dolomite, Enewetak Atoll: an example of dolomitization by normal seawater. Geology 12: 217–220

Schmoker JW, Halley RB 1982 Carbonate porosity versus depth: a predictable relation for south Florida. AAPG Bull. 66, 12:2561–2570

Scholle PA, Ulmer DS, Melim LA 1992 Late stage calcites in the Permian Capitan Formation and its equivalents, Delaware Basin margin, West Texas and New Mexico: evidence for replacement of precursor evaporites. Sedimentology 39:207–234

Schreiber BC, Friedman GM, Decima A, Schreiber E 1976 Depositional environments of Upper Miocene (Messinian) evaporite deposits of the Sicilian Basin. Sedimentology, 23:729–760

Swart PK, Cantrell DL, Westphal H, Handford CR, Kendall CG 2005 Origin of dolomite in the Arab-D reservoir from the Ghawar Field, Saudi Arabia: Evidence from petrographic and geochemical constraints. J Sediment Research, 75, 3:476–491

Thomeer, JHM 1960 Introduction of a pore geometrical factor defined by the capillary pressure curve: AIME Transactions, v. 219, p. 354–358

Wang FP, Lucia FJ, Kerans C 1994 Critical scales, upscaling, and modeling of shallow-water carbonate reservoirs. Society of Petroleum Engineers, Paper No. SPE 27715, Midland, Texas, pp. 765–773

Wang FP, Lucia FJ, Kerans C 1998 Integrated reservoir characterization study of a carbonate ramp reservoir: Seminole San Andres Unit, Gaines County, Texas. SPE Reservoir Evaluation & Engineering, 1, 3:105–114

Wang, Fred, and Lucia FJ 2004 Reservoir modeling and simulation of Fullerton Clear Fork field, Andrews County, Texas. In Ruppel SC (ed) Multidisciplinary imaging of rock properties in carbonate reservoirs for flow-unit targeting: Univ. Texas Austin Bureau of Economic Geology, final technical report prepared for U.S. Department of Energy under contract no. DE-FC26-01BC15351, p. 219–304

Ward WC, Halley RB 1985 Dolomitization in a mixing zone of near-seawater composition, Late Pleistocene, Northeastern Yucatan Peninsula. J of Sedimentary Petrology 55, 5:407–420

Whitaker FF, Smart PL, Jones DG 2004 Dolomitization: from conceptual to numerical models. In Braithwaite CJR, Rizzi G, Darke G (eds) The geometry and petrogenesis of dolomite hydrocarbon reservoirs. London, Geological Society, Special Publications 235, pp 99–139

Chapter 8 Touching-Vug Reservoirs

8.1 Introduction

The three-dimensional spatial distribution of petrophysical properties is controlled by two geological processes, depositional and diagenetic. Although it is clear that the three-dimensional spatial distribution of petrophysical properties is initially controlled by the spatial distribution of depositional textures, it is also clear from numerous reservoir studies that the petrophysical properties found in carbonate reservoirs are significantly different from those of modern carbonate sediment. Diagenesis typically reduces porosity, redistributes the pore space, and alters permeability and capillary characteristics.

The basic diagenetic processes discussed herein are (1) calcite cementation, (2) mechanical and chemical compaction, (3) selective dissolution, (4) dolomitization, (5) evaporite mineralization, and (6) dissolution, collapse, and fracturing. Each of these processes can be identified by a specific fabric, and how they overprint and modify depositional textures is a key issue in predicting and mapping the distribution of petrophysical properties within a carbonate reservoir.

A key question in mapping diagenetic effects is the degree of conformance between diagenetic products and depositional patterns. If the transport of material in and out of the system is not an important factor in producing the diagenetic product, the product will generally conform to depositional patterns. However, if the transport of ions in and out of the system by fluid flow is required to produce the diagenetic product, then the product may not conform to depositional patterns. In this case, knowledge of the hydrological system may be required to map the diagenetic products, including the source of the fluid and the direction of fluid flow.

Diagenetic processes are grouped according to their conformance to depositional patterns because of our focus on mapping and predicting the distribution of petrophysical rock-fabrics. Cementation, compaction, and selective dissolution form the first group, reflux dolomitization and

evaporite mineralization form the second group, and dissolution, collapse brecciation, and fracturing make up the third group.

As discussed in Chapter 6, the products of cementation, compaction, and selective dissolution can normally be linked to depositional textures. In Chapter 7, we discussed reflux dolomitization and evaporite mineralization, two processes that require fluid flow for the introduction of magnesium and sulfate into the system, and, therefore, their patterns may not be linked to depositional patterns. Dolomitization may increase the particle size, significantly modifying the pore-size distribution of the sediment and smoothing out important petrophysical differences found in depositional textures. Predolomite diagenetic history may significantly alter the permeability structure and result in dolomitizing waters following diagenetic rather than depositional flow paths. Spatial patterns of gypsum and anhydrite show little linkage to depositional facies patterns, even though sulfate commonly selectively occludes pore space in grainstones.

In this chapter we will discuss dissolution, collapse brecciation, and fracturing. Dissolution may be fabric selective or non-fabric selective dissolution, but *the key to this fabric is that associated fracturing and karst processes enhance permeability beyond that expected from matrix fabrics.* We will organize our discussion into small-scale touching vugs, associated with fabric dissolution, and large-scale touching vugs, associated with karst processes. Small-scale touching vugs include microfractures related to overburden compaction. Microfracturing increases the connection between separate vugs and enhances permeability. This fabric is normally contained within a permeability sample and can be characterized using core samples.

Large-scale touching vugs encompass a large variety of voids including simple fractures, fault breccia, dissolution enlargement of fractures, dissolution of bedded evaporite minerals, cavern formation at any scale, and associated collapse, fracturing, and brecciation. These fabrics are normally larger than core samples and have little relationship to rock fabrics. As a result, their petrophysical properties cannot be accurately characterized by core measurement, and model construction is difficult.

Most commonly, reservoirs that have permeability higher than can be expected from matrix fabrics are assumed to be fractured reservoirs (see Aguilera (1979) for descriptions of fractured reservoirs). Carbonate reservoirs with unusually high permeability, however, have a more complicated pore structure than simple fractures. The pore space is typically found in solution enlarged fractures, interconnected vug networks with a wide range of sizes and shapes, and collapse breccias. In general, these pore types are thought to be related to flow of near-surface ground

water, perhaps controlled by fractures, a diagenetic environment herein referred to as the meteoric or karsting environment. Some non-fabric dissolution and brecciation, however, is thought to be associated with deep fluid movements and unrelated to surface events (Dravis and Muir 1993, Wierzbicke and Dravis 2006). Deep dissolution is suggested to be related to "thermochemical sulfate reduction," a process of producing sulfuric acid by the reduction of sulfate minerals or the H_2S in hydrocarbons (Heydari and Moore 1989; Kaufman et al. 1990). Movements of these burial fluids are thought to be focused along fracture and fault zones and are often referred to as "hydrothermal diagenesis" (Evans and Smith 2006) In this chapter, we will deal only with the meteoric environment, although the reservoir properties resulting from dissolution, collapse, and fracturing in both the meteoric and "burial" environment are likely to be similar.

8.2 Small-scale dissolution, collapse, and microfracturing

Small-scale dissolution is generally associated with dissolution of aragonite grains or gypsum/anhydrite crystals. In rare cases, the centers of dolomite crystals are selectively dissolved. This dissolution can occur within the meteoric environment associated with fresh water or in the burial environment. The dissolution molds are susceptible to collapse due to the increase in overburden pressure as burial depth increases. The collapse of the grain molds fractures the grains and the surrounding mud matrix, creating an interconnection of microfractures and grain molds. This is a small-scale touching-vug system and enhances permeability without changing porosity significantly. A small-scale touching-vug pore type, the Idd el Shargi field, was discussed in Chapter 6.

The conversion of gypsum to anhydrite results in a 40% volume loss. This conversion is controlled by temperature and the salinity of the formation water (see Chapter 7), and in West Texas appears to occur at around 4,000 ft. Overburden pressure causes the resulting voids to collapse, fracturing the surrounding sediment. These fractures are typically filled with anhydrite as part of the conversion and collapse process. However, if the anhydrite is later selectively dissolved, the resulting vugs and fractures will form a small-scale touching-vug system.

8.2.1 Effects on Petrophysical Properties

Small-scale dissolution and microfracturing is on a scale that can be analyzed using core material. The process generally enhances permeability

with little change in porosity (see Chapter 6, Idd el Shargi field). Class 3 mud-dominated packstones may plot in the class 2 field and class 2 grain-dominated packstones in the class 1 field. An example from the Sacroc Pennsylvanian field, West Texas, shows that samples without microfracturing plot in the class 2 field, whereas the samples with microfracturing plot in the class 1 field (Fig. 1). The permeability is enhanced by a factor
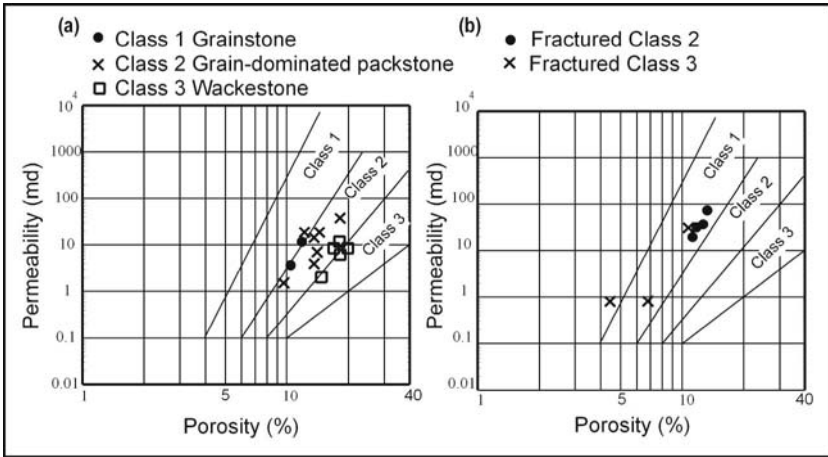
Fig. 8.1. Cross plot of porosity and permeability from the Sacroc (Pennsylvanian) field in West Texas showing the (a) fabrics without microfractures plot in the class 2 field with class numbers decreasing from wackestone to grainstone and (b) fabrics with microfractures plot in the class 1 field

of 5to10 over the matrix permeability. An example in the South Cowden Permian field, West Texas, shows that medium crystalline dolowackestones and grain-dominated packstones plot in the class 2 field as predicted, whereas the permeability for samples with microfractures are enhanced by a factor of 5. Therefore, the dissolution, collapse, and fracturing at the grain scale can be assumed to enhance permeability 5to10 times over what would be expected for matrix permeability with the same porosity.

8.2.2 Small-scale touching vug reservoirs

In Chapter 6 we discussed the Idd el Shargi field in Oman and showed how small-scale touching vugs composed of grain molds connected by compaction fractures enhanced the permeability of a mud-dominated packstone. The grain molds are constrained to a specific depositional environment, and the distribution of the touching vugs can be predicted by knowing the distribution of that environment. In this chapter we will discuss

another example of small-scale touching vugs in the South Cowden dolostone reservoir in West Texas, where microfractures are related to anhydrite emplacement and dissolution. A study of similar touching vugs related to anhydrite dissolution has been published by Dehghani et al. (1999).

South Cowden Grayburg Reservoir

The South Cowden Grayburg reservoir is an example of a reservoir with enhanced permeability related to small-scale touching vugs composed of grain molds and microfractures. The South Cowden field is located in Ector County, Texas (Fig. 2) and produces from Grayburg dolostones and
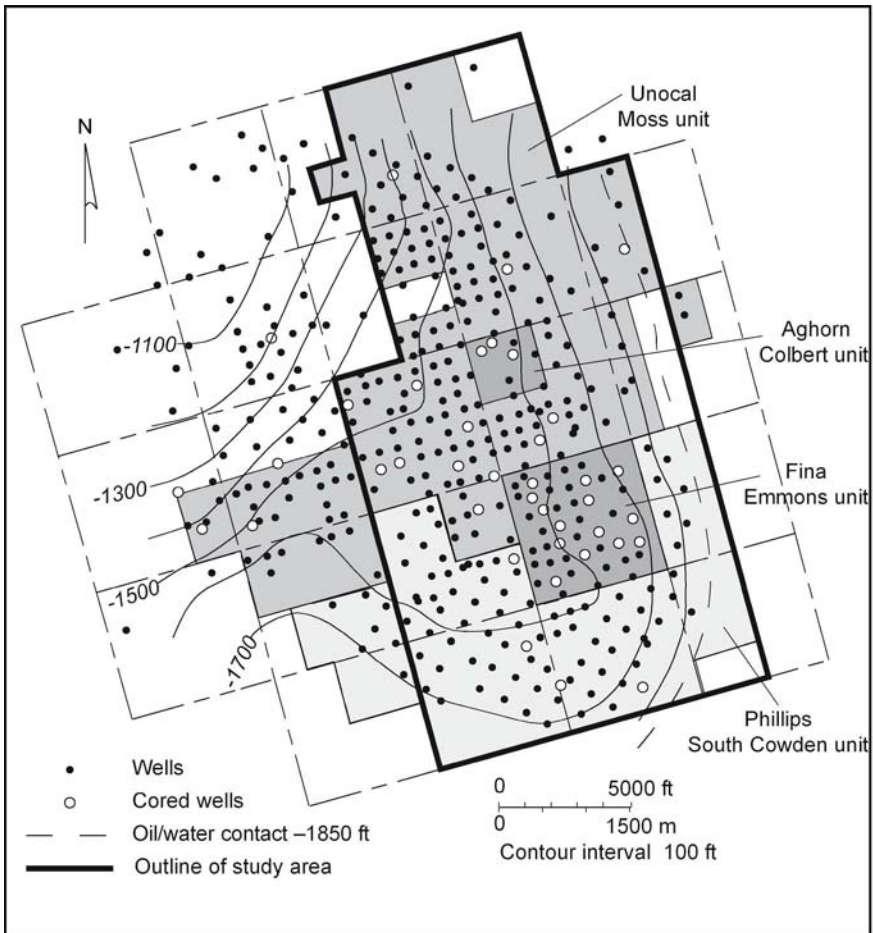
Fig. 8.2. Location map of South Cowden field showing production units, study area, and structure

sandstones at a depth of 4,000 to 5,000 ft. Development was initiated in 1948, and the field was unitized in 1962 for the purpose of conducting waterflooding operations. A map of cumulative production from the original development wells shows large differences in production, with production decreasing updip to the west due to a porosity pinchout and downdip to the east due to decreasing pay thickness and increasing water production (Fig. 3). Lucia and Ruppel (1996) and Saller and Henderson (1998) have equated the loss of porosity updip to overdolomitization.
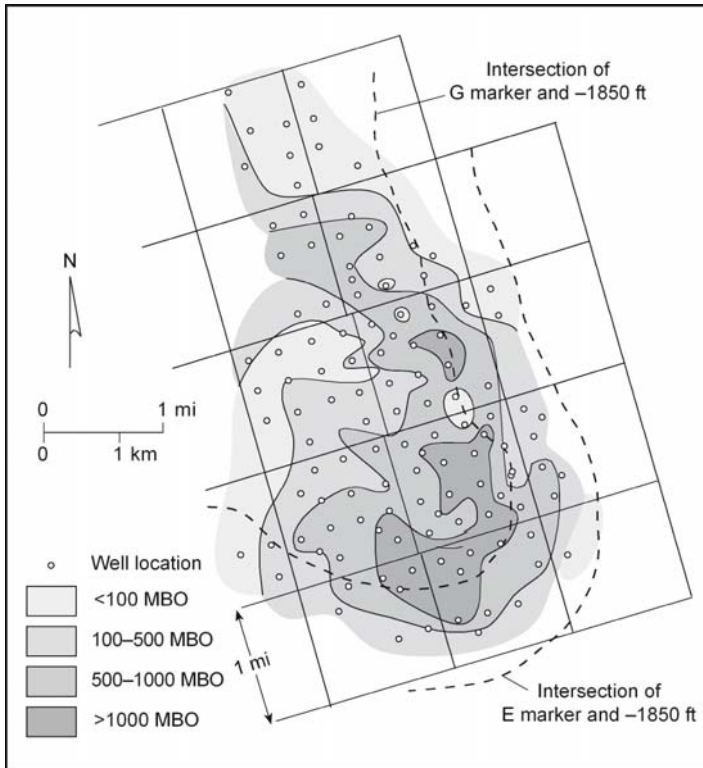
Fig. 8.3. Isopach map of cumulative production from original development wells in the study area

The Grayburg has been divided into four high-frequency sequences. The productive interval is located in Grayburg sequences 3 and 4, which are divided into 11 high-frequency cycles (Fig. 4). The cycles are correlated using the gamma-ray and porosity logs. The cycles are composed of a lower low-porosity silty dolostone or sketetal-peloid mud-dominated dolostone, and an upper more porous grain-dominated dolopackstone. Each cycle is divided into two flow layers based on these
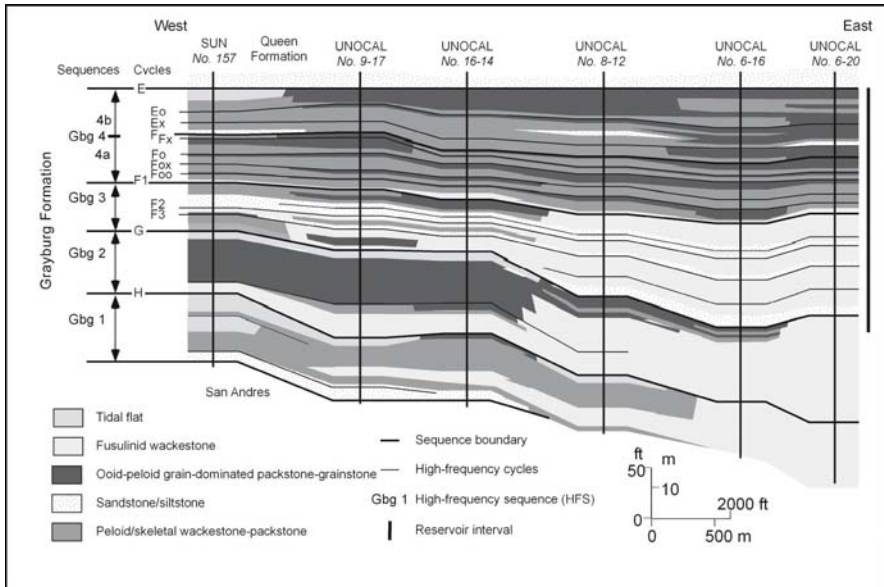
Fig. 8.4. Stratigraphic cross section of South Cowden field showing high-frequency sequences and cycles

fabric changes.

Dolomitization has played a large role in the petrophysics of this reservoir. Dolomitization has increased in particle size in the mud-dominated fabrics by replacing the lime mud with medium-size dolomite crystals. The lime mud was a class 3 fabric, and the dolomitized fabric was a class 2 fabric. As shown in Figure 5a, the result of dolomitization is that the permeability can be estimated from one class 2 porosity transform. Anhydrite is found in the form of nodules, poikilotopic crystals, and pore-filling crystals. Pore-filling crystals fill intergrain, grain mold, and fracture pore space. Interestingly, the anhydrite has been dissolved in the most productive area of the field. The removal is evidenced by the presence of large molds of anhydrite nodules, and fusulinid molds and microfractures lined with calcite that has replaced a small part of the anhydrite. This is mostly likely related to the migration of burial fluids out of the Midland Basin.

Anhydrite dissolution has enhanced permeability by a factor of 5 over matrix permeability (Fig. 5b) by dissolving the pore-filling anhydrite from microfracture and grain molds creating a small-scale touching-vug system. This enhancement is the cause for the areas of high production illustrated in Figure 3. It was possible to map the general area of enhancement using
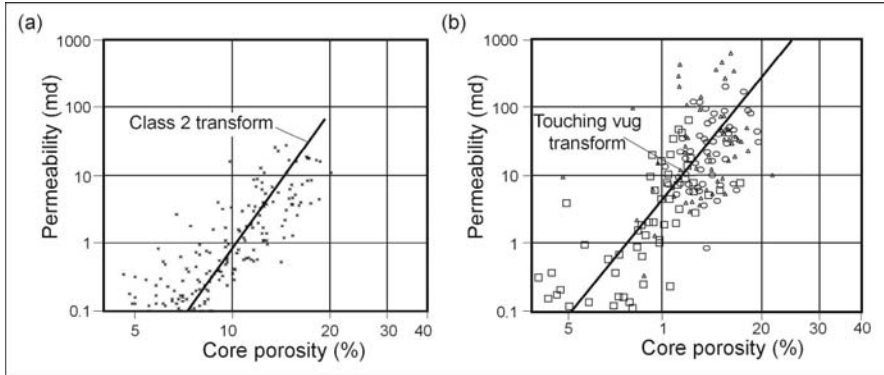
Fig. 8.5. Cross plot of porosity and permeability core values from **(a)** interparticle porosity and **(b)** small scale touching-vug porosity showing the improved permeability in the touching-vug pore system

cross plots of porosity and travel time. The sonic response in the area of dissolved anhydrite has a much lower slope than do areas where the anhydrite is present or partially dissolved (Fig. 6).
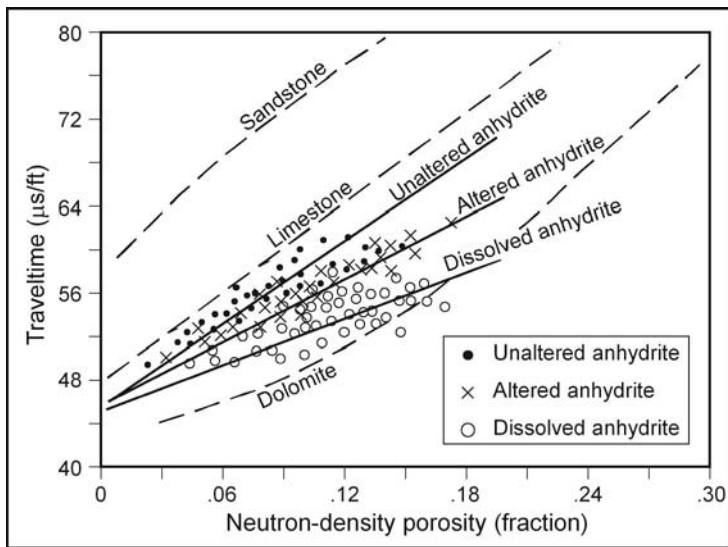
Fig. 8.6. Cross plot of transit time, from acoustic logs, and porosity, from neutron and density logs, showing the unique signature of the touching-vug pore system found in the dissolved anhydrite area

The sonic tool was useful for identifying zones of dissolved anhydrite and identifying general patterns of dissolution. Well data demonstrated the presence of pillars of unaltered anhydritic dolostone a few hundreds of feet

in diameter within the general area of dissolution. Also it is clear that the low permeability barriers to cross flow in the unaltered areas are not present in the dissolution areas.

However, there was not enough well control to build a robust map of the dissolution area. An attempt to use seismic amplitude data to map the high porosity was made and the results appeared to coincide with the areas of high production (Fig. 7). The map suggests a n orthogonal fracture pat-
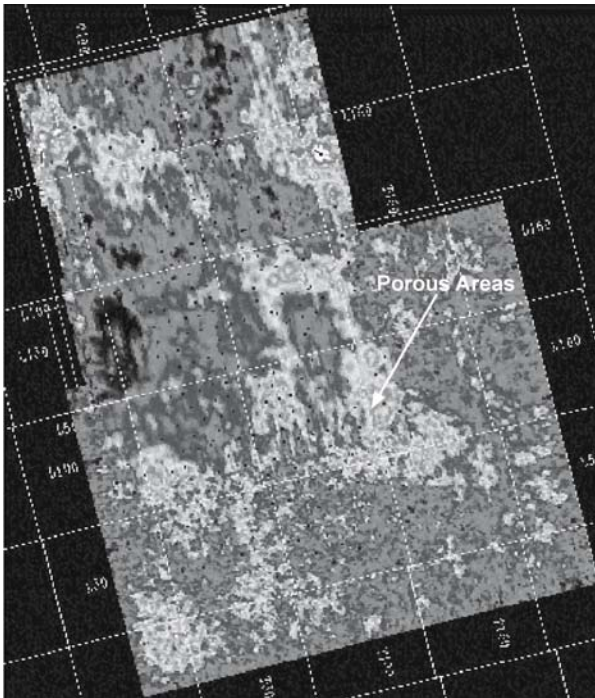
Fig. 8.7. Seismic map of South Cowden reservoir showing rectilinear porosity patterns

tern that controlled the flow of burial fluids and resulting anhydrite dissolution. A map of this type could not have been made with well control and demonstrated the power of seismic data that is correlated with a geologic/petrophysical model.

8.3 Large-scale dissolution, collapse, and fracturing

Large-scale dissolution is a characteristic process associated with major fresh water aquifers, the meteoric diagenetic environment (Fig. 8).
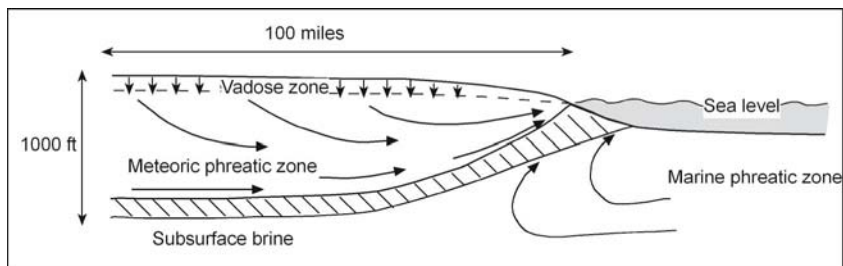
Fig. 8.8. The meteoric-groundwater environment showing groundwater zones, mixing zone, and fluid flow directions. Dissolution is known to be concentrated in the vadose zone, the upper levels of the meteoric phreatic zone, and in the mixing zone

A common dissolution product in this environment is cave development, and many reservoirs are known to produce from intervals with paleocaves (Loucks, 1999). Meteoric water falling on a land surface will enter the groundwater system and flow toward the sea. Between the earth's surface and the water table, the pore space is partially saturated with capillary-held water except during heavy rains or floods. This zone of partial air saturation is called the *vadose zone*. Flow in this zone occurs during rainfall and flooding, is focused at fracture intersections and dolines, and is dominantly in a downward direction. Below the water table, the pore space is 100% saturated with water and is called the *phreatic zone*. Flow in this zone can have both a lateral and a downward component and is focused along fractures and in dissolved passageways.

    The location of the boundary between the vadose and phreatic zone is not constant but moves up and down based on the balance between rainfall recharge, evapotranspiration, and discharge into bodies of water. The thickness of the vadose zone is dependent upon topography. In mountainous topography the vadose zone can extend to a depth of over 1000 ft, whereas in flat country it is typically a few feet to 200 ft thick. Most reservoirs are found in the passive margin tectonic environment where exposure surfaces have only a small amount of relief. Therefore, we will focus our remarks on meteoric diagenetic environments associated with surfaces that have little topography.

    Studies of karsting and modern caves have focused on the vadose zone. Karsted landscapes are characterized by internal drainage into dolines or sink holes formed by concentrated dissolution, perhaps at the intersection of fracture systems. Dolines lead to underground passages that may contain underground streams and are commonly floored by cave sediment and collapse breccia. These caves are concentrated in the vadose and upper phreatic zones. Little is known about the extent of modern caves below the

water table, but geological studies suggest that they may extend hundreds of feet below the water table.

The geochemistry and hydrology of the ground water system are key to understanding the origin and distribution of touching-vug pore systems. Both dissolution and precipitation occur in this environment, removing carbonate from some areas and precipitating carbonate in other areas through a complicated geochemical and hydrological system. Porosity is lost due to pendulous and meniscus cements that form in capillary trapped water of the vadose zone, and sparry cements form from ground water in the vadose zone.

Undersaturated meteoric water is characteristic of the meteoric diagenetic environment, and dissolution is focused in the vadose, high phreatic, and mixing zones. Because rain water is undersaturated, it initially dissolves carbonates in the vadose and upper phreatic zones. Geochemical studies have shown that the mixing of two waters saturated with calcite at differing CO_2 partial pressures can produce solutions that are undersaturated with calcite, and thus gain a capacity to dissolve calcite (Plummer 1975). Sea water is supersaturated with $CaCO_3$, but when mixed with more dilute meteoric ground water in the mixing zone it may become undersaturated and produce cavernous pore space (Fig. 9; Plummer 1975). Studies of the Florida Aquifer
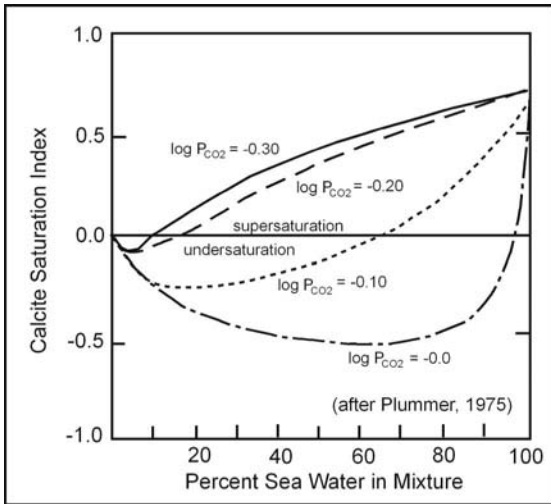
Fig. 8.9. Saturation index of calcite in mixtures of solutions saturated with calcite at differing CO_2 partial pressures and 25 °C and modified seawater. (Plummer 1975)

and coastal caves in Yucatan, Mexico, have demonstrated limestone dissolution at the mixing zone between sea water or subsurface brine and fresh water of the aquifer (Stoessell et al. 1989).

The geometry of touching-vug pore systems in the meteoric environment is controlled by preexisting tectonic fracture patterns, the location of the vadose/phreatic contact, the geometry of the mixing zone, and lithology. Depositional textures have little control on the distribution of large-scale dissolution; however, beds of soluble minerals, such as the evaporite minerals anhydrite, gypsum, or halite, can be selectively dissolved in the ground water environment, forming cave systems (Warren et al. 1990). Also, limestone beds may be preferentially dissolved over dolomite beds in strata where these two lithologies are interbedded.

Cave maps commonly show that fracture systems exert a strong control on cave geometry. Fractures are a common feature of carbonate rocks and are formed in response to stress, which can be generated in many ways. Three common stress regimes are tectonic, geopressure, and the formation of large voids (caves). Tectonic fractures form in response to the bending and braking of strata, and fracture distribution can be related to bending moments and distance from faults. In some instances, fracture density is related to lithology; for instance, dolomite tends to be more fractured than limestone. Geopressure fractures are formed when pore fluids are trapped and cannot be expelled as overburden pressure increases. As the pore pressure approaches overburden pressure, fracture pressure is reached and the rock breaks. Fractures form in the roofs of large caves as burial increases the overburden pressure to a point where the roof fails and collapse breccia forms. Fracture distribution is directly related to cave distribution and indirectly related to tectonic fractures and the water table.

Massive dissolution and karsting can be directly associated with subaerial exposure surfaces because these surfaces are the point of entry of the water into the ground water system. In the reflux dolomitization model, identifying supratidal surfaces and evaporite lagoons as the point of entry of the dolomitizing water is important for predicting dolomite patterns and dolomite porosity. Similarly, identifying the point of entry of the meteoric ground water system is important for predicting the distribution of massive dissolution products such as caves, collapse breccias, and fractures.

A review of sequence stratigraphy studies suggests that karsting is not well developed at the boundaries of high-frequency cycles. Small karst pits filled with overlying sediment may be found at exposure surfaces bounding high-frequency sequences and composite sequences (Kerans et al. 1994). Massive dissolution effects, however, appear to be associated with second- order unconformities, exposure surfaces with millions of years missing (Budd et al. 1995).

Identifying the surface to which the formation of collapse breccia and caverns is linked can be difficult because massive dissolution can form hundreds of feet below a subaerially exposed surface. There is no typical

vertical succession of karst fabrics that can be used to identify the karst surface, and one-dimensional data, such as vertical cores, may have undisturbed strata between the karsted surface and the first underlying collapse breccia. The tendency for observers to place the surface of exposure immediately above collapse breccias has led to a misinterpretation that major dissolution occurs at cycle boundaries. Outcrop observations, however, do not confirm this conclusion.

In summary, the formation of caves and cavern systems by massive dissolution initiates a series of events that have an important effect on reservoir geometry (Fig. 10). The first is the importation of sediment into the caves by flowing surface water. This sediment can be deposited in the
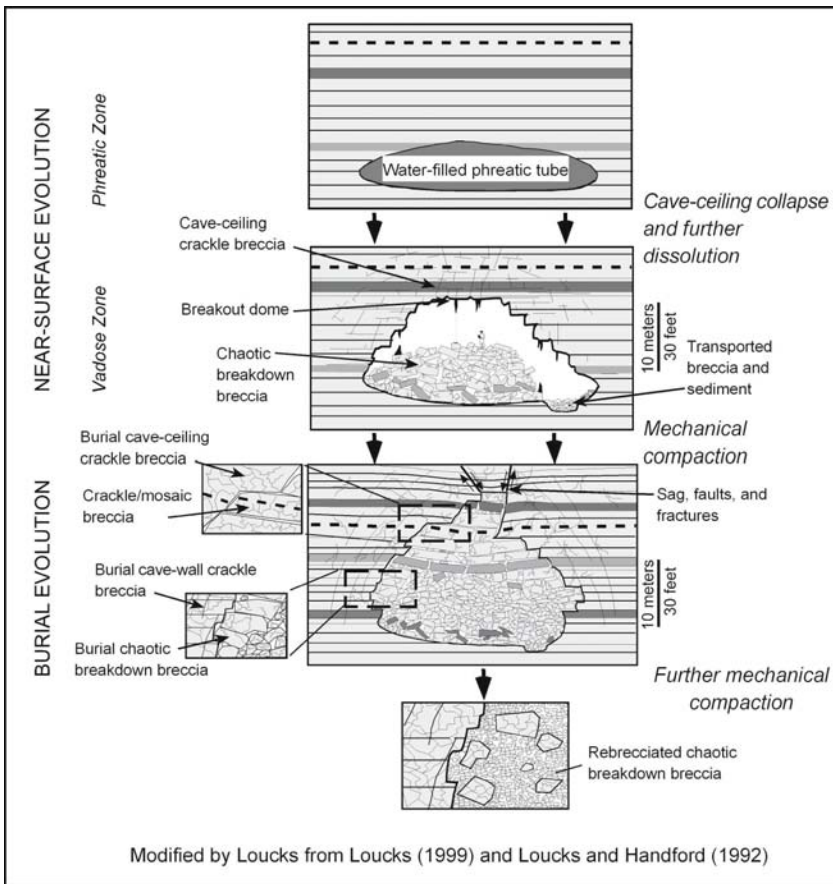
Fig. 8.10. Schematic diagrams showing evolution of cave-related breccias. (Loucks and Handford 1992)

vadose caves or may filter down through the fractures and passages in the phreatic zone. Large caves cannot support themselves for long periods of time and are destroyed by roof collapse. Roof collapse can occur during the time of exposure and can continue after exposure as overlying sediment is deposited and the overburden pressure increases. The history of collapse is often very complicated and extends over hundreds of millions of years (Loucks and Handford 1992).

Products of collapse important for reservoir description are fractures and collapse breccia; the formation of fracture porosity and interbreccia-block pore space referred to as touching-vug pore types. The geometry of collapse breccia will follow the pattern of major cave development. Fracture porosity will be concentrated in the failed roof and flanks of the cavern system (Loucks and Handford 1992).

The distribution of petrophysical properties in the massive dissolution, collapse, and fracture environment is controlled by preexisting fracture patterns, meteoric flow regime, and stratum lithology (Fig. 11). Massive
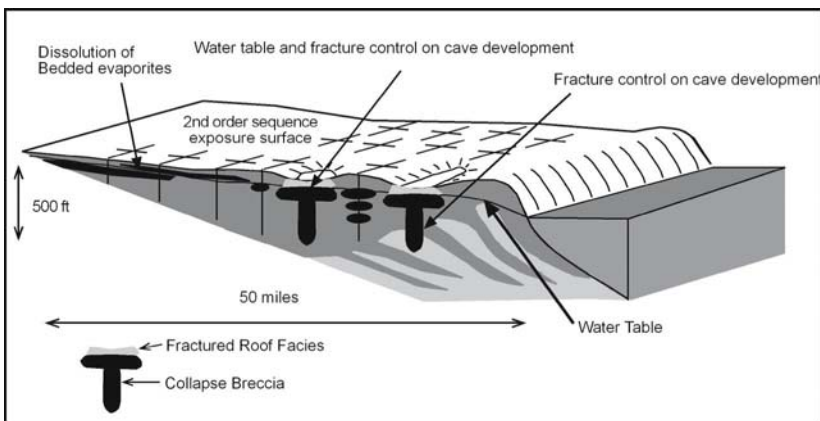
Fig. 8.11. Patterns of touching-porosity formed by massive dissolution, cavern development, and collapse. Geometry of touching-vug bodies is controlled by strataform evaporite bodies, water table, and precursor fracture patterns

dissolution creates large, connected voids herein referred to as touching vugs. If the vugs are large enough to form caverns and caves, they can collapse, fracturing the overlying roof and forming a collapse breccia with interbreccia-block porosity. Cavern development and collapse can produce a vertical sequence of fracture and breccia types (Kerans 1988). Fracture breccia, mosaic breccia, or crackle mosaic are characteristic of the collapsed roof. Chaotic breccia with open interclast pore space or filled with internal sediment are characteristic of the collapsed cavern. Open and

sediment-filled vugs and small caverns are characteristic of strata below and adjacent to the collapsed caverns.

8.3.1 Effects on Petrophysical Properties Distribution

Large-scale dissolution creates a pore system that cannot be related to interparticle or separate-vug porosity, and is referred to as a touching-vug pore system. In addition, touching-vug pore systems have little relationship to depositional patterns, which make them difficult to model. Although matrix porosity may be quite high, the fluid flow is concentrated in the touching-vug system because the pore sizes are typically very large and transmit fluid easily (Fig. 12). Studies of the Edwards Aquifer in Texas have shown
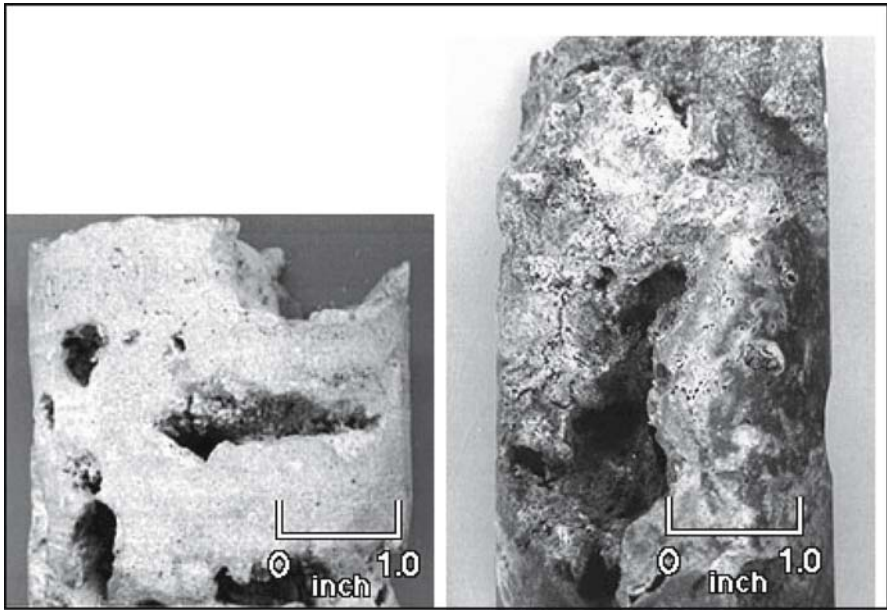
Fig. 8.12. Examples of cavernous porosity observed in cores. **A** Miami Oolite from the Miami aquifer, Miami, Florida. **B** Niagaran (Silurian), Michigan pinnacle reef

that flow in fractures and caves (touching vugs) is more than 100 times higher than flow in the matrix (Hovorka and Mace 1998). Touching-vug systems typically control fluid flow because of their wide conduits, but they contribute less than 1% to reservoir porosity. A study of modern cave systems has shown that cave pore space occupies less than 1% of the country rock (Sassowsky 2004) Most of the reservoir pore space is located in ma-

trix pore types, creating a bimodal pore system where most of the storage is in the matrix and most of the flow capacity is in the vug system.

The petrophysical properties of touching-vug reservoirs are difficult to characterize because the size and shape of the vugs are often larger than those of core samples. Typically, however, porosity and permeability cross plots using data from whole-core analyses show a scatter of high to low permeability in the < 6% porosity range (Fig. 13). The most useful data are
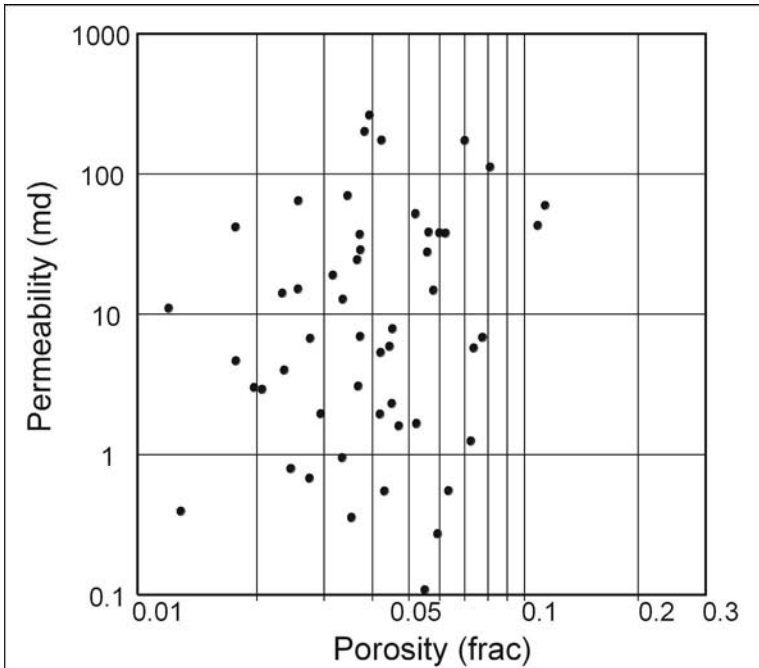
Fig. 8.13. Cross plot of porosity and permeability from touching-vug porosity found in the Sacroc (Pennsylvanian) field, West Texas show scattered high and low permeability and low porosity values typical of some touching vugs

derived from production data using well tests and production/injections logs. These data usually suggest that much higher permeability than calculated for matrix permeability is required to match production of injection rates. An example from the Cogdell Pennsylvanian reservoir in West Texas shows all the injection entering a 20-ft interval that has an average porosity of 7% and not entering a higher porosity zone below (Fig. 14). The estimated matrix permeability from this zone is between 6 and 0.2 md. A permeability of 50 md is calculated from the injection data, and a fiftyfold enhancement in permeability. It is not uncommon for production
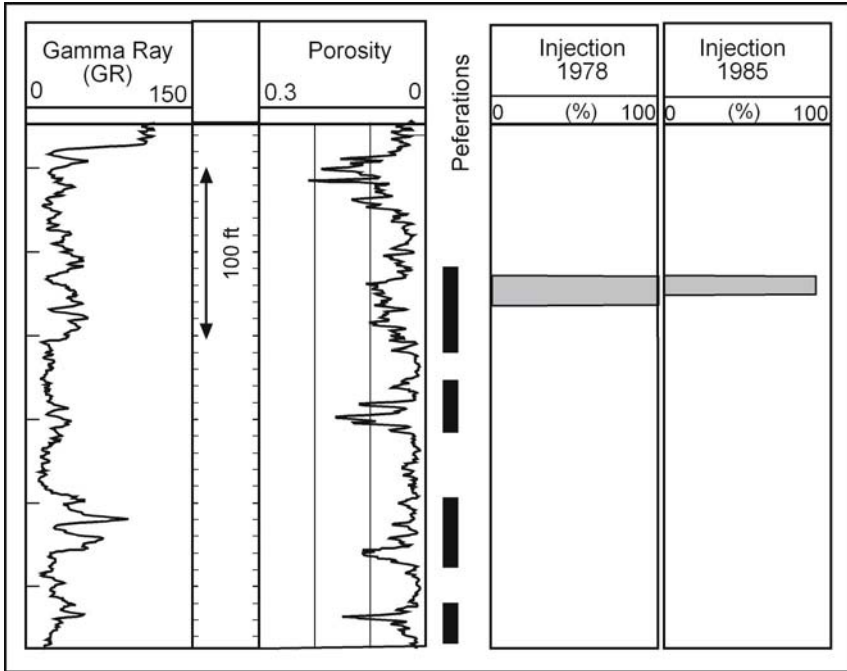
Fig. 8.14. Illustration of an injection profile showing all fluid being injected into a 20-ft interval of low porosity suggesting a touching-vug pore system

tests to calculate Darcy permeability where matrix permeability is a few tens of millidarcys. Water saturations are considered to be very low because of the large pore size, and transition zones are very thin. Therefore, although touching-vug reservoirs often have lower porosity than do other carbonate reservoirs, the large-scale dissolution process results in excellent permeability and low initial water saturation despite the low porosity.

8.3.2 Large-scale touching-vug reservoirs

The massive dissolution diagenetic environment commonly is a late diagenetic event and follows cementation, compaction, selective dissolution, reflux dolomitization, and sulfate mineralization. Therefore, massive dissolution reservoirs often retain some of the rock fabrics from these earlier diagenetic events. Two San Andres fields from West Texas are presented as examples of the combination of depositionally-controlled petrophysical distribution and massive-dissolution-controlled brecciation, collapse, and fracturing. A Mississippian reservoir from Wyoming is pre-

sented as an example of a petrophysical distribution controlled by collapse-fracture-controlled late dolomitization. Although we focus on hydrocarbon reservoirs, some of the most interesting "reservoir" examples are lead and zinc mines found in the Ordovician of Missouri, USA, and in the Devonian of western Canada.

San Andres Fields, West Texas

Although many San Andres fields in West Texas produce from interparticle and separate-vug pore systems, some of the major fields have an overprint of caverns and fractures that have a major effect on fluid flow. Two of the reservoirs are the giant Yates field, with 4 billion barrels of oil originally in place, and the interesting Taylor Link field, with 50 million barrels in place. These two fields are only about 15 miles apart and have had a similar depositional and diagenetic history. The *Yates field* is divided into a lower package of low-energy open-ramp facies and an upper package composed of three to four upward-shallowing high-frequency sequences (Tinker and Mruk 1995). The upper three HFSs are composed of 13 upward shallowing high-frequency cycles. The top of the San Andres is a significant karst surface.

An extensive Yates field is dolomite, there is good conformance between depositional textures and reservoir quality in the Yates field, with grainstones and grain-dominated packstones having the highest matrix porosity (Tinker and Mruk 1995). The depositional textures have a predictable relationship to the Permian paleogeography of the region, with grainstones concentrated at the ramp crest and mud-dominated fabrics and peritidal sediments concentrated in the middle and inner ramp.

An extensive fracture network overprints the matrix porosity. The fractures important to reservoir performance are believed to have formed early in the life of the reservoir and act as conduits for solution enlargement during post San Andres karstification. Fracture patterns are predictable because they have a well-defined orthogonal NW-SE and NE-SW orientation (Fig. 15). Numerous caves have been mapped using bit drops and caliper logs, and these caves are found hundreds of feet below the San Andres top (Fig. 16). There is some indication that cave formation occurred in response to freshwater lenses that developed during exposure of each of the four HFSs. The Yates field is relatively shallow, and most caves have not undergone mechanical collapse.

The *Taylor Link field* is similar to the Yates field in that the matrix petrophysical properties conform well to depositional textures and the fractures do not (Lucia et al. 1992). The field is composed of an upper
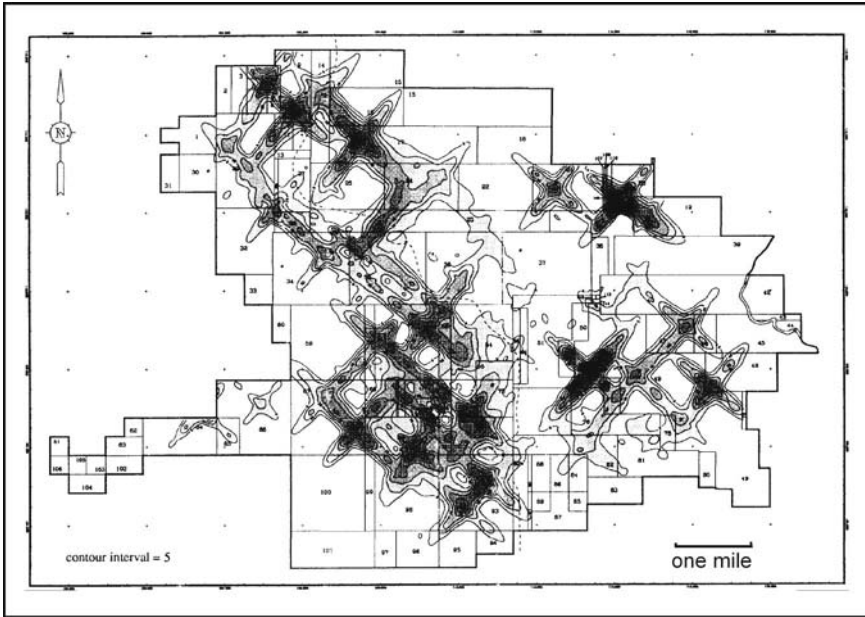
Fig. 8.15. Isopach of the number of fractured feet in a 20 ft slice map of the Yates San Andres field showing NW-SE and orthogonal NE-SW trends imposed on data (Tinker and Mruk 1995)
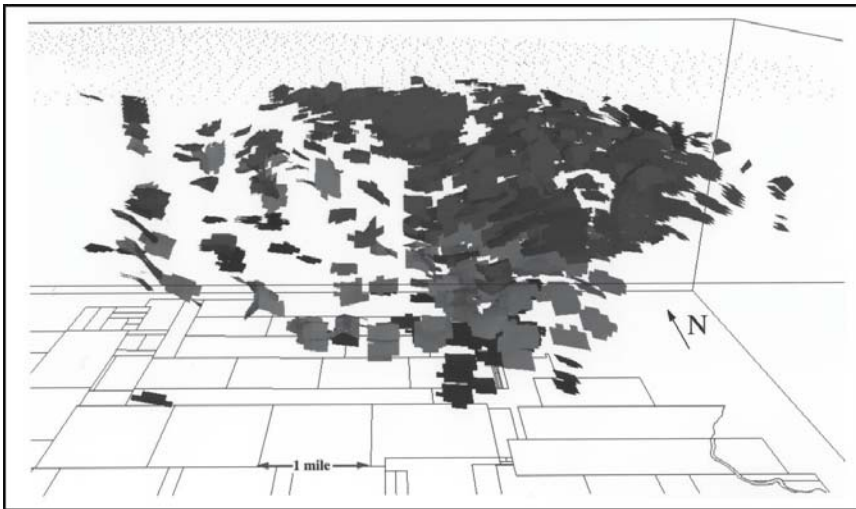
Fig. 8.16. Three-dimensional diagram showing distribution of caves in the Yates San Andres field. (Tinker and Mruk 1995)

dolograinstone unit that is about 60 ft thick and probably represents an amalgamation of several upward-shoaling cycles. The pore space is between ooid grains, and the porosity permeability transform for this facies is within the class 1 field (Lucia 1995). The lower unit is a fusulinid fine crystalline dolowackestone with scattered fusumolds. Fractures and large circular vugs are concentrated in the dolowackestone. Fracture types include simple fractures, solution-enlarged fractures, and micro-breccia and associated fractures.

Core analyses show highest porosity values in the dolograinstone facies, whereas permeability values are as high in the dolowackestone as in the dolograinstone facies (Fig. 17). This is due to fracture porosity in the
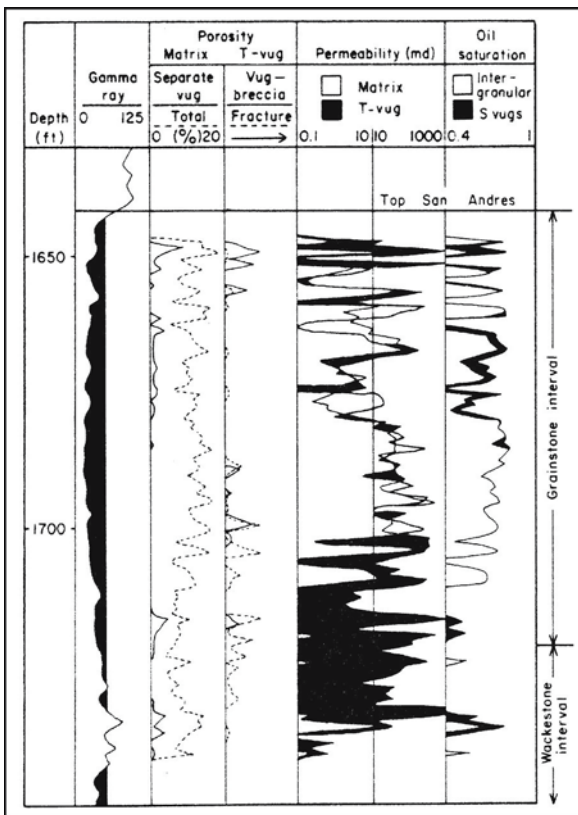
Fig. 8.17. Depth plot from a well in the Taylor Link San Andres field showing matrix and fracture permeability. Fracture permeability is shown in *black* as the difference between matrix permeability estimated from fabric analysis and total permeability from core measurements. (Lucia et al. 1992)

wackestone. An estimate of the fracture permeability was obtained by estimating the matrix contribution to total permeability using the porosity-permeability transform for a grainstone and comparing the values with core values, values that include both matrix and fracture permeability. Results show that all the permeability in the grainstone interval (about 20 md) can be attributed to intergrain porosity, whereas all the permeability in the wackestone (about 20 md) can be attributed to fracture porosity. Fracture porosity is estimated at 1%.

A reservoir model of the Taylor Link reservoir (Fig. 18) shows the
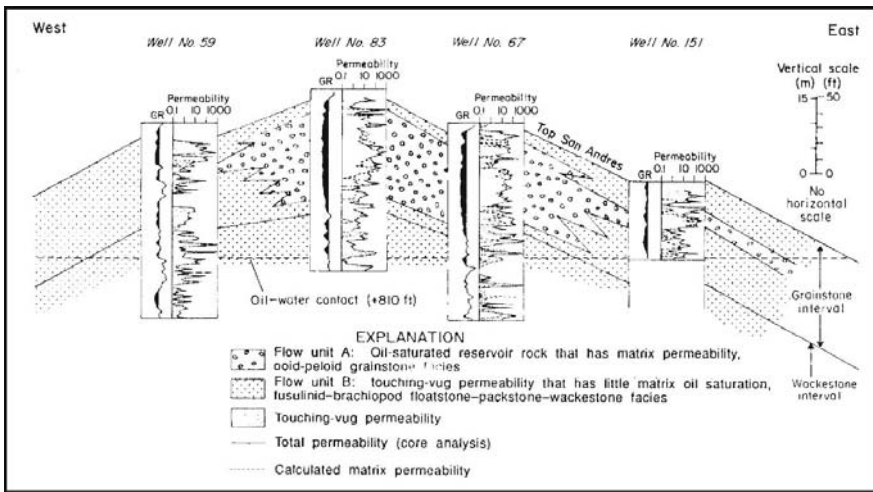
Fig. 8.18. Northwest-southeast cross section of the Taylor-Link San Andres reservoir showing distribution of ooid grainstone rock-fabric facies and fractured fusulinid wackestone facies. (Lucia et al. 1992)

upper unit composed of a porous and permeable grainstone facies that grades laterally into low-porosity fractured wackestone. The lower unit is composed entirely of low-porosity fractured wackestone. It has little porosity or oil saturation, but it has fracture permeability and is a thief zone.

Elk Basin Mississippian Reservoir

The Elk Basin field produces from the Mississippian Madison Group and is located in the north end of the Big Horn basin on the border between Wyoming and Montana. Reservoir rocks were deposited on a shallow carbonate shelf in an upward-shoaling sequence from mud-dominated to grain-dominated sediments. Evaporite beds capped several of these cycles.

At the end of Madison deposition, the Madison was exposed subaerially, and an extensive karst surface formed during Late Mississippian and Early Pennsylvanian time. The evaporite beds were dissolved to form stratiform breccias and caverns, and vertical caverns were formed, probably along fracture planes (Fig. 19). During deposition of the overlying Pennsylvanian
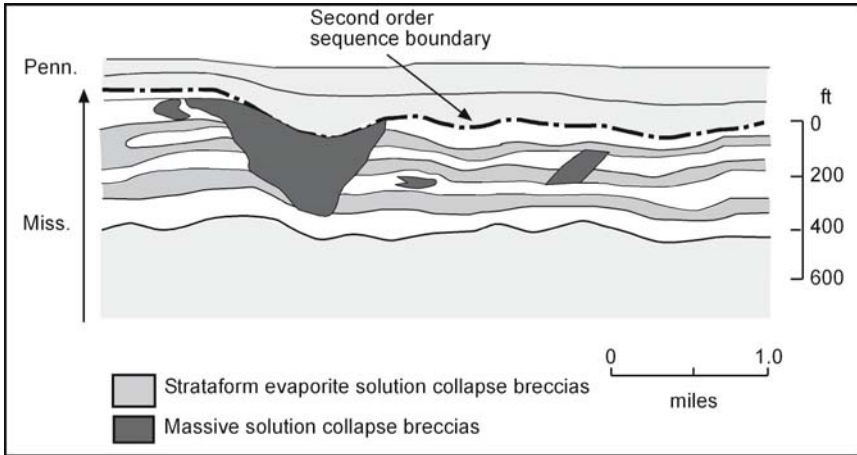
Fig. 8.19. Cross section of the Elk Basin (Mississippian) field, Wyoming, showing massive breccias that cross cut stratigraphy and stratiform collapse breccias formed by dissolution of evaporite beds (After McCaleb and Waynam 1969)

sediments, the cavities were partially filled with a mixture of clay and sand. Collapse of the caverns resulted from burial. As a result of infill and collapse, large areas of the Elk Basin field are isolated from each other.

A excellent outcrop analog has been described by Sonnenfeld (1996) and related to the Elk Basin field. Exposure time is estimated at 10-20 million years, typical of a second-order sequence boundary. Small-scale karst features are found capping the upper two high-frequency (third-order) sequences. Anhydrite beds are common in much of the area but are absent in the area of the Elk Hills field. This is attributed to efficient dissolution of anhydrite by undersaturated meteoric water in the Elk Hills area. The massive dissolution produced a stratiform cave system that later collapsed, forming extensive stratiform collapse breccia composed of a suite of breccia fabrics ranging from chaotic, to mosaic, to crackle (Fig. 20). Cave collapse triggered a stoping process in overlying strata, which propagated upward to the Mississippian unconformity. The vertical breccias are possibly guided by preexisting fractures spaced about 200 ft apart. A late dolomitization event overprints the vertical breccias and mosaic and fracture breccia of the stratiform roof facies.

Reservoir quality is concentrated in dolostone and collapse fractures of the roof facies. Limestone rarely has more than 2% porosity, and evaporite solution collapse breccias are flow barriers because they are argillaceous. Beds of peritidal sediments and associated reflux dolomite are typically porous and permeable, forming laterally continuous flow units. Late dolo-
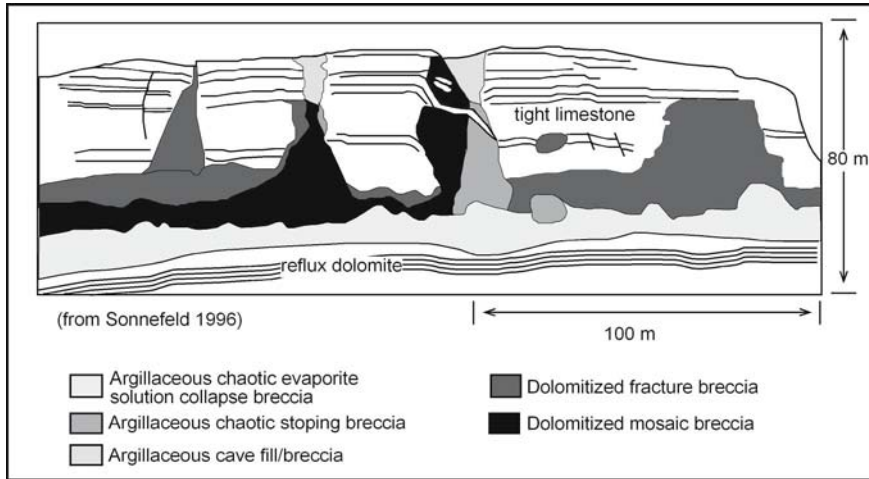
Fig. 8.20. Sketch of Madison outcrop, Wind River Gorge showing distribution of collapse breccia. (Sonnenfeld 1996)

mitization controlled by collapse brecciation patterns also produces reservoirquality dolostones. However, their pattern will be nonstratiform and laterally discontinuous because of the irregular distribution of the collapse brecciation and fracturing.

Ellenburger Lower Ordovician Fields

Ellenburger (lower Ordovician) reservoirs in the Permian Basin of West Texas and New Mexico are classified as fractured reservoirs, and the fractures are a product of massive dissolution and collapse. An outcrop analog to these reservoirs is found in the Franklin Mountains, El Paso, Texas. Major collapse breccias are associated with the second-order sequence boundary between the lower Ordovician El Paso Group and the upper Ordovician Montoya Group, which has an estimated time gap of 30 million years. Extensive field mapping of the El Paso Group has demonstrated that a large cavern system was formed in the upper 300 m (1000 ft) of the El Paso Group (Fig. 21). In the upper 75 m (250 ft), the El Paso caverns were tabular and horizontal and were formed near the phreatic-vadose interface.
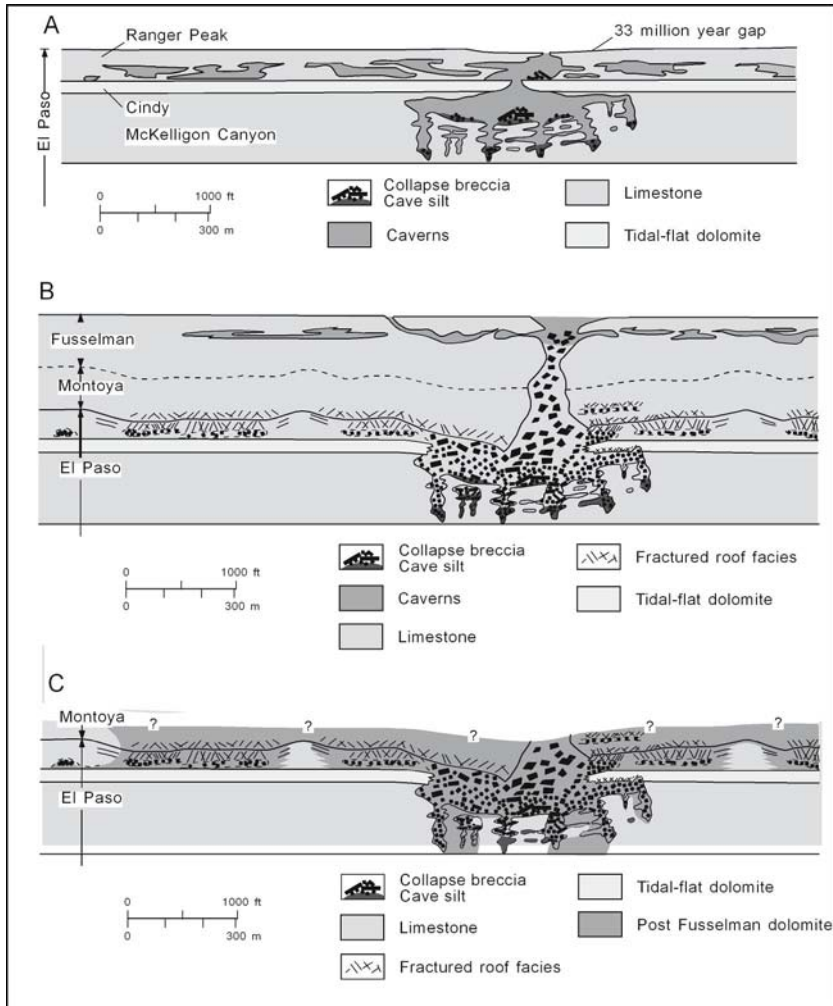
Fig. 8.21. Reconstruction of El Paso Caverns. **A** penecontemporaneous dolomiti-zation of the Cindy Formation and development of tabular, laterally continuous caverns in the Ranger Peak Formation and vertical, laterally discontinuous caverns in the McKelligon Canyon Formation. **B** Collapse of the El Paso caverns showing collapse of the Montoya, development of breccia pipes up into the Fusselman Formation, and development of caverns in the Fusselman Formation. **C** Late-stage dolomitization of the El Paso and Montoya Groups controlled by fluid flow through collapse breccia, fractures, and into adjacent carbonates. (Lucia 1995)

These caverns were discontinuous but extended for thousands of feet later-ally. In the lower 225 m (750 ft), the caverns were linear and vertical and

were formed in the deep phreatic zone along vertical fractures spaced 900 m (3000 ft) apart. These caverns were also discontinuous, extending laterally along the precursor fractures for several kilometers and perpendicular to the fracture trend for hundreds of meters (Fig. 22). Collapse of the El Paso Caverns formed a cave roof fracture system in the overlying Montoya Group and megacollapse breccias in the El Paso Group. Collapse brecciation formed fractures in the overlying Ordovician and Silurian strata,
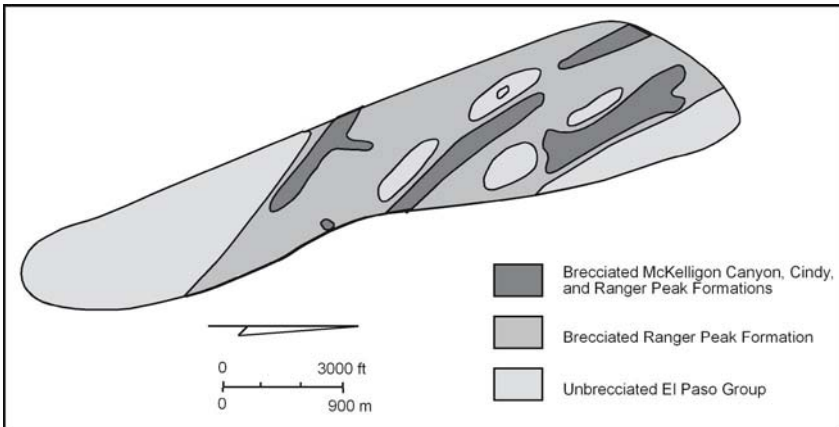
Fig. 8.22. Map view showing a reconstruction of the collapse breccia in the southern Franklin Mountains, El Paso, Texas. (Lucia 1995)

which were sites of later dissolution and collapse brecciation. A late dolomitization event converted much of the fractured and brecciated strata to dolomite, and dolomite cement filled much of the fracture and breccia pore space.

In the subsurface Ellenburger reservoirs, collapse breccias can be found as far as 1000 ft below the exposure surface at the top of the Ellenburger. The upper 300 ft, however, is of most interest because that is where most of the reservoirs are found for trap considerations. These reservoirs have been described by Kerans (1988, 1989) as having a fractured roof facies, a cave fill facies, and a cave floor breccia facies. Laterally persistent caverns have floor breccias formed during cave development that are overlain by clastic sediments of the Simpson Formation that were washed into the resulting caves during transgression (Figs. 23-25). Later collapse produced extensive fracturing and brecciation, producing a vertical sequence of intact cave floor, cave floor breccia, cave fill breccia, and cave roof breccia.

The cave fill breccia forms a reservoir barrier separating an upper and lower reservoir. SP and gamma-ray logs are used to identify the cave filling clastic sediment and map the upper and lower reservoir. These fields have
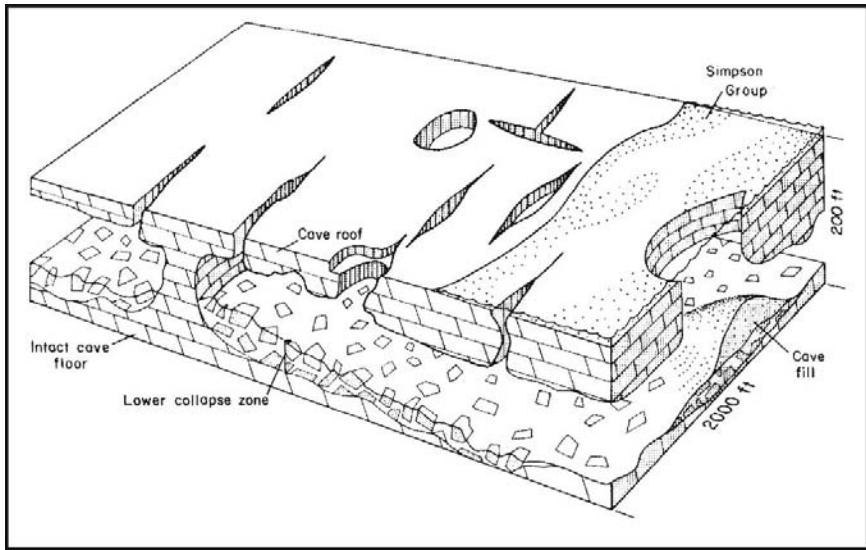
Fig. 8.23. Schematic block diagram showing a laterally extensive cave system with collapse breccias lining the cave floor. (Kerans 1989)
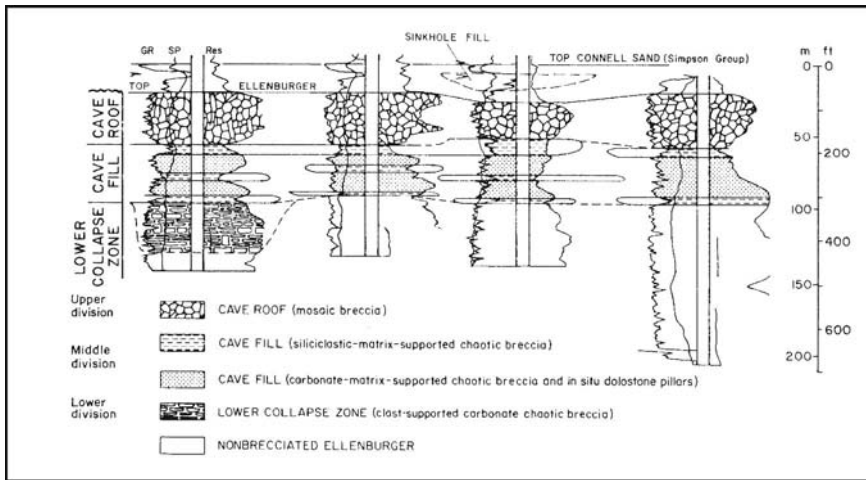
Fig. 8.24. Cross section from the Emma Ellenburger field, Andrews County. West Texas, illustrating the fractured cave-roof facies, laterally persistent cave fill facies, and laterally discontinuous collapse-breccia facies. (Kerans 1989)
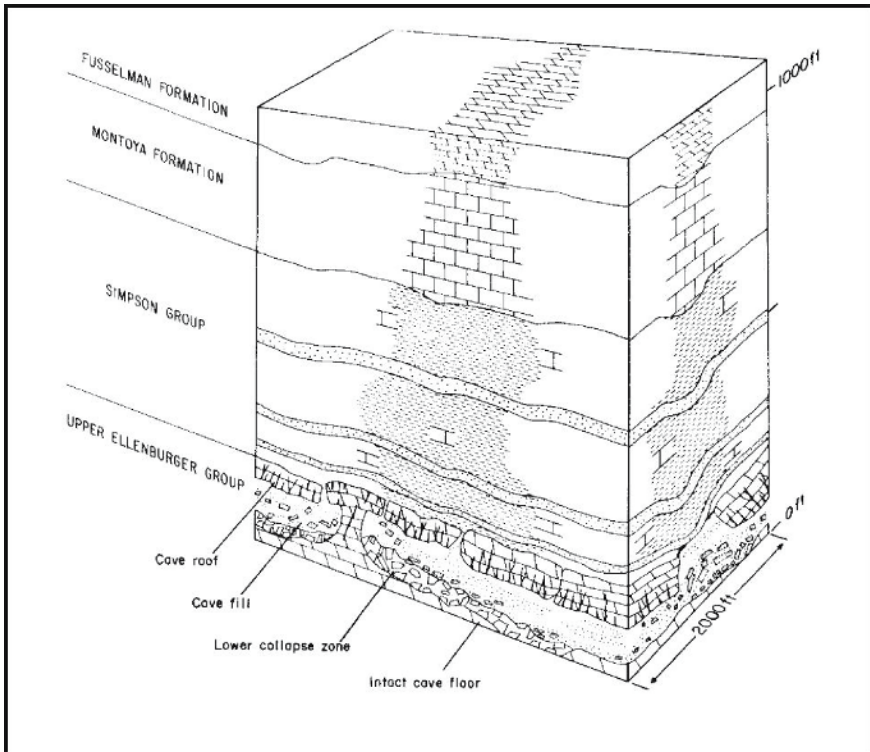
Fig. 8.25. Cartoon of cavern development and collapse in Lower Ordovician El-
lenburger fields of West Texas showing cave facies (Kerans, 1989)

bottom water drives, and initial development wells were completed in the
upper reservoir only to control water coning. However, the recognition of a
cave fill reservoir barrier and observation that water inflow was edge water,
not bottom water (Ader 1980), initiated a redevelopment program to deepen
wells to recover hydrocarbons in the lower reservoir.

Silurian Reef Fields

The Northern Michigan Reef belt produces from Silurian pinnacle reefs.
The reefs are located parallel to and basinward of a massive shelf-edge reef
complex. Reefs are found about every 1.5 square miles within the reef belt
and average about 80 acres in size and 400 ft in height. These reefs were
initiated in deep water with deposition of a mud mound facies and grew up
into shallower water, where corals and stromatoporoids formed the main
constructional facies. A flanking crinoidal facies is present seaward, and
an algal restricted marine facies is found behind the coral-stromatoporoid

facies. After it formed, the reef was exposed subaerially, and massive dissolution occurred (Fig. 26). After deposition of thick salt beds adjacent to
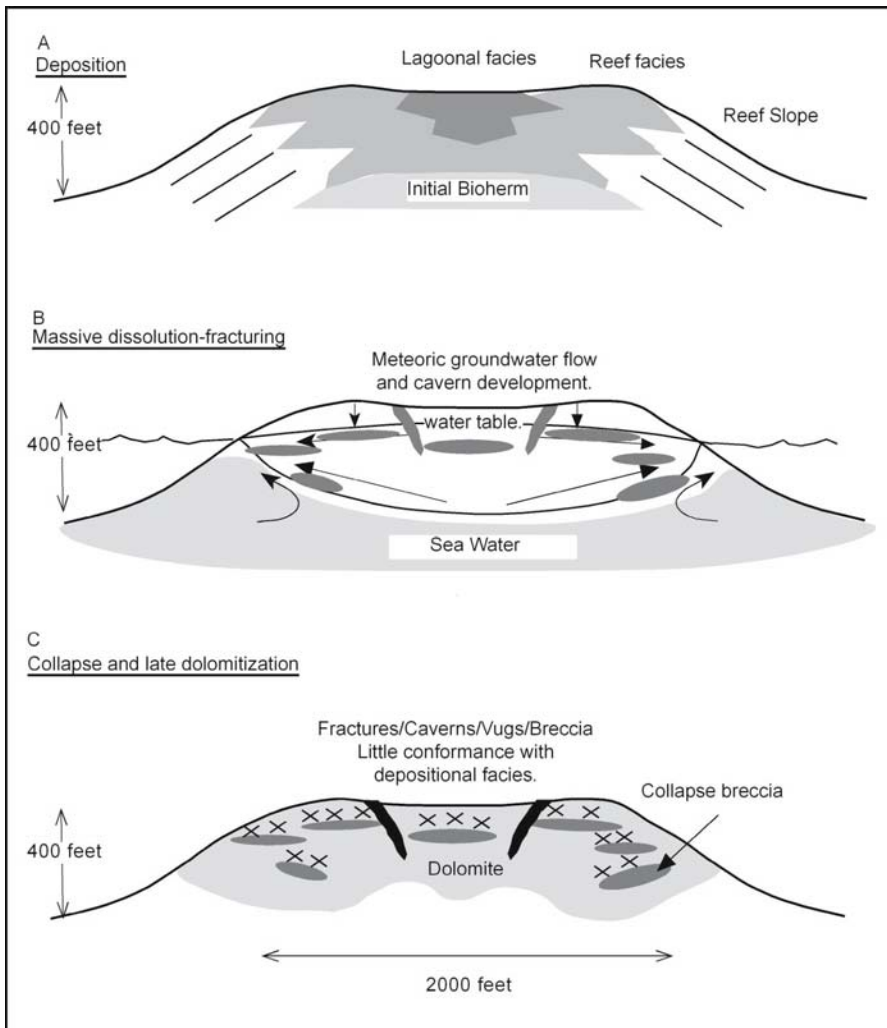
Fig. 8.26. Massive dissolution in Silurian pinnacle reefs, Michigan.   **A** Reef growth started with a marine cemented bioherm on which corals and stromatoporoids grew and developed a reef margin, slope, and interior lagoon. **B** A freshwater lens developed during the subaerial exposure phase resulting in massive dissolution and the formation of caverns and associated enlarged fractures. **C** Collapse of the cave system with burial produced collapse breccias and fractures. (Modeled after Sears and Lucia 1980)

the reefs, the basin returned to normal marine conditions, and a carbonate tidal flat sequence was deposited over and around the reefs. Dolomitization occurred at this time. With burial, salt-saturated waters were compacted out of the salt basin and into the reefs, occluding much of the porosity in the more basinward reefs with halite (Caughlin et al. 1976; Sears and Lucia 1980).

The massive dissolution is typical of small buildups and large sea-level changes. The sea-level changes were probably related to evaporative drawdown of the restricted Michigan Basin rather than to eustasy. A local rather than regional ground-water system was developed within each buildup, and the associate massive dissolution formed caverns and enlarged fractures, which were later dolomitized. Small bit drops that occurred while developing these reservoirs attest to the fact that some small caverns are still present.

References

Ader JC 1980 Stratification testing results in revised concept of reservoir drive mechanism, University Block 13 Ellenburger Field. J Pet Technol 32, 8:1452-1458

Aguilera R 1979 Naturally fractured reservoirs. Petroleum Publishing, Tulsa, Okla

Back W 1963 Preliminary results of a study of calcium carbonate saturation of a ground water in Central Florida: Int Assoc Sci Hydrol VIIIe, Annee 3, pp 43-51

Budd DA, Saller AH, Harris PA (eds) 1995 Unconformities and porosity in carbonate strata. AAPG Mem 63, 313 pp

Caughlin WG, Lucia FJ, McIver NL 1976 The detection and development of Silurian reefs in Northern Michigan. Geophysics 41, 4:646-658

Choquette PW, James NP 1984 Introduction. In: James NP, Choquette PW, (eds) Paleokarst. Springer-Verlag, Berlin, Heidelberg, New York, pp 1-24

Davies RD, Smith LB 2006 Structurally controlled hydrothermal dolomite reservoir facies: an overview. AAPG Bull 90, 11:1641-1690

Dehghani K. Harris PM, Edwards, KA, Dees, HT 1999 Modeling a vuggy carbonate reservoir, McElroy Field, West Texas. AAPG Bull 83, 1:19-43

Dravis J J, Muir ID 1993 Deep-burial brecciation in the Devonian Upper Elk Point Group, Rainbow Basin, Alberta, Western Canada. In: Fritz RD, Wilson JL, Yurewicz DA, (eds) Paleokarst related hydrocarbon reservoirs. SEPM Core Workshop 18: pp 119-167

Heydari E, Moore CH 1989 Burial diagenesis and thermochemical sulfate reduction, Smackover Formation, southeastern Mississippi salt basin. Geology 17, 12:1080-1084

Hovorka SD, Mace RE 1998 Permeability structure of the Edwards aquifer, South Texas – Implications for aquifer management. The University of Texas, Bureau of Economic Geology, Report of Investigations No. 250, 55 pp

Kaufman J, Meyers WJ, Hanson GN 1990 Burial cementation in the Swan Hills Formation (Devonian), Rosevear Field, Alberta, Canada. J Sediment Petrol 60, 6:918-939

Kerans C 1988 Karst controlled reservoir heterogeneity in Ellenburger Group carbonates of West Texas. AAPG Bull 72, 10:1160-1183

Kerans C 1989 Karst-controlled reservoir heterogeneity and an example from the Ellenburger Group (Lower Ordovician) of West Texas. The University of Texas at Austin, Bureau of Economic Geology, Report of Investigations No. 186, 40 pp

Kerans C, Lucia FJ, Senger RK 1994 Integrated characterization of carbonate ramp reservoirs using outcrop analogs. AAPG Bull 78, 2:181-216

Loucks RG 1999 Paleocave carbonate reservoirs: Origins, burial-depth modifications, spatial complexity, and reservoir implications. AAPG Bull 83, 11:1795-1834

Loucks RG, Handford CR 1992 Origin and recognition of fractures, breccias, and sediment fills in paleocave-reservoir networks. In: Candelaria MP, Reed CL, (eds) Paleokarst, karst-related diagenesis and reservoir development: examples from Ordovician-Devonian age strata of West Texas and the Mid-Continent. Permian Basin Section-SEPM Publ 92-33, Midland, Texas, pp 31-44

Lucia FJ 1970 Lower Paleozoic history of the western Diablo Platform of West Texas and south central New Mexico. Geologic Framework of the Chihuahua Tectonic Belt, West Texas Geol Soc Publ, Midland, Texas

Lucia FJ, Ruppel SC 1996 Characterization of diagenetically altered carbonate reservoirs, South Cowden Grayburg reservoir, West Texas. SPE paper 36650

Lucia FJ, Kerans C, Vander Stoep GW 1992 Characterization of a karsted, high-energy, ramp-margin carbonate reservoir: Taylor-link West San Andres Unit, Pecos County, Texas. The University of Texas at Austin, Bureau of Economic Geology, Report of Investigations No, 208, 46 pp

Lucia FJ 1995 Lower Paleozoic development, collapse, and dolomitization, Franklin Mountains, El Paso, Texas. In: Budd DA, Saller AH, Harris PA, (eds) Unconformities and porosity in carbonate strata. AAPG Mem 63:279-300

Maiklem WR 1971 Evaporative drawdown - a mechanism for water-level lowering and diagenesis in the Elk Point Basin. Bull Can Petrol Geol 19, 2:487-503

McCaleb JA, Wayhan DA 1969 Geologic reservoir analysis, Mississippian Madison Formation, Elk Basin Field, Wyoming, Montana. AAPG Bull 51:2122-2132

Plummer FN 1975 Mixing of sea water and calcium carbonate ground water: In: Whitten EHT (ed) Quantitative Studies in Geological Sciences. GSA Mem 112:219-236

Saller AH, Henderson N 1998 Distribution of porosity and permeability in platform carbonates: Insights from the Permian of West Texas. AAPG Bull 82, 8:1528-1551

Sassowsky ID 2004 Detailed analogs for Paleokarst reservoirs: Promise and problems (abs). AAPG Annual Convention Abstracts Volume, v. 13, p. A123

Sears SO, Lucia FJ 1980 Dolomitization of Northern Michigan Niagaran reefs by brine refluxion and freshwater/seawater mixing. In: Zenger DH, Dunham, JB, Ethington RL, (eds) Concepts and models of dolomitization. SEPM Spec Publ 28:215-236

Sonnenfeld M D 1996 An integrated sequence stratigraphic approach to reservoir characterization of the Lower Mississippian Madison Limestone, emphasizing Elk Basin Field, Bighorn Basin, Montana. Unpubl PhD Dissertation, Colorado School of Mines, Golden, Colorado, 438pp

Stoessell RK, Ward WC, Ford BH, Schuffert JD 1989 Water chemistry and $CaCO_3$ dissolution in the saline part of an open-flow mixing zone, coastal Yucatan Peninsula, Mexico. GSA Bull 101, 2:159-169

Tinker SW, Mruk DH 1995 Reservoir characterization of a Permian giant: Yates field, West Texas. In: Stoudt EL, Harris PM, (eds) Hydrocarbon reservoir characterization: Geologic framework and flow unit modeling. SEPM Short Course 35:51-128

Warren JK, Havholm KG, Rosen MR, Parsley MJ 1990 Evolution of gypsum karst in the Kirshberg Evaporite member near Fredericksburg, Texas. J Sedimentary Petrology 60, 5:721-734

Wierzbicke R, Dravis JJ 2006 Burial dolomitization and dissolution of Upper Jurassic Abenaki platform carbonates, Deep Panuke reservoir, Nova Scotia, Canada. AAPG Bull 90, 11:1843-1861

Subject Index